Université Lille 1 Sciences et Technologies

THÈSE

Presentée pour obtenir le grade de :

Docteur de l'Université de Lille 1

Spécialité:

Sciences de la Matière, du Rayonnement et de l'Environnement

Soutenue publiquement le 9 juillet 2015 par

Anton Fedarenka

Titre :

The utilization of ground-based polarimetric measurements for improving retrieval of aerosol microphysics

Jury :

Rapporteurs :	Aliaksandr SINYUK
	Jean-Claude ROGER
Examinateurs :	Alexander KOKHANOVSKY
	Carlos TOLEDANO
Directeurs :	Oleg DUBOVIK
	Philippe GOLOUB

Laboratoire d'Optique Atmosphérique
U.F.R de Physique Fondamentale
Université Lille 1 Sciences et Technologies
59655 Villeneuve d'Ascq, France

Acknowledgements

I would like to express my deepest appreciations and respects to many people for their help and support that made this work possible.

First of all, I would like to thank my supervisors Oleg Dubovik and Philippe Goloub for wise guidance and persistent help in scientific and personal problems.

I am grateful to CIMEL company in the person of its director Didier Crozel as well as Nord-Pas de Calais Region for financial support of my work.

I sincerely appreciate the significant contribution of Zhengqiang Li to the matter of my study.

I am thankful to my colleagues Andrei Holdak, Tatiana Lapionak, Pavel Litvinov, Yevgeni Derimian, Luiz Gonzalez, Luc Blarel and Thierry Podvin for participation in my work and essential advices. I also thank my friends and fellow students Yana Karol and Anton Lopatin for diverse help and support.

Special thanks to Marie-Lyse Liéevin and Ann Priem for all the help with French bureaucratic runaround.

I express my warm thanks to Alexander Lapionak as well as Konstantin Zabalkansky for their help and assistance in my life in France.

Finally, I would like to thank all staff of LOA for their hospitality and friendliness that I was surrounded during my work in Lille.

I am also deeply appreciative to Anatoly Chaikovsky and the staff of Laboratory of Scattering Media of Institute of Physics of National Academy of Sciences of Belarus for advices and the possibility to finish my thesis in comfortable scientific environment.

Abstract

The use of polarimetric observations in addition to the observations of total atmospheric radiance is widely expected for aerosol characterization using remote sensing measurements. However, the polarimetric observations from ground have not yet been as widely developed as in remote satellite sensing and, at present, there is rather limited experience in using ground-based measurements of polarization for aerosol characterization. In order to explore the potential of ground-based passive polarimetry for aerosol remote sensing, a new sun-photometer CIMEL CE318-DP enabling multi-wavelength polarization characteristics of the downward field radiation has been developed. Such instruments were deployed at several sites of AErosol RObotic NETwork (AERONET).

The thesis presents the efforts on including the polarimetric data to the routine inversion of the ground-based observations and analysis of the obtained advantages in retrieval results. In order to process large amount of polarimetric data a data preparation tool was developed. It is based on AERONET inversion code adapted for inversion of both intensity and polarization measurements.

To assess the relevance of the polarization measurements for aerosol retrieval results, both synthetic simulated data and the real field measurements were processed and analyzed using developed routine. The sensitivity study has been carried out using simulated data based on five main aerosol models: desert dust, urban industrial, urban clean, biomass burning and maritime aerosols. The test investigated the effects of polarization data applying in presence of random noise, bias in optical thickness measurements and pointing errors. The results demonstrate the advantage of polarization data utilization in the cases of aerosols with pronounced concentration of fine particles for all considered errors. The polarimetric data revealed minor sensitivity to the coarse mode dominated aerosols as desert dust.

Further, the AERONET extended data sets observations were processed. The data for three observation sites have been investigated: GSFC, USA (clean urban aerosol dominated by fine particles), Beijing, China (polluted industrial aerosol characterized by pronounced mixture of both fine and coarse mode) and Dakar, Senegal (desert dust dominated by coarse particles). The results of the study revealed considerable advantages of polarimetric data utilization in the case of industrial pollution (Beijing). The use of polarization improves the retrieval of the particle size distribution by decreasing overestimated fine mode and increasing the coarse mode. Furthermore, it increases underestimated real part of the refractive index and the fraction of spherical particles due to high sensitivity of polarization to particle shape. The results for the desert dust did not indicate significant improvements from additional use of polarization measurements. The inversions of GSFC data take a middle position.

Thus, the analysis of large amount of processed polarimetric observations by ground-based sun-photometer as well as sensitivity study demonstrates a significant value of polarimetric data for improving aerosol characterization. This approach is especially beneficial for aerosol types with pronounced fine fraction or complex aerosol contained fine and coarse modes both, such as observed over Beijing and likely other regions with the presence of heavy pollution.

Résumé

Plusieurs études ont montré que l'utilisation d'observations polarimétriques, en complément, des observations de luminances atmosphériques, améliorent la caractérisation des aérosols, par télédétection. Paradoxalement, il s'agit principalement d'observations réalisées depuis l'espace, comme les missions POLDER. A l'inverse les observations polarimétriques au sol sont encore peu répandues, en dehors de celles réalisées par le Service d'Observation PHOTONS, composante française du réseau international AERONET (AErosol RObotic NETwork). Afin d'explorer le potentiel de la polarimétrie passive au sol pour la télédétection des aérosols, nous avons utilisé la version polarisée (CE318-DP) du photomètre développé par CIMEL Advanced Monitoring, version permettant la mesure de la polarisation du rayonnement de ciel à plusieurs multi-longueur. Ces instruments ont été déployés sur plusieurs sites de AERONET.

La thèse présente l'analyse des données polarimétriques et paramètres aérosols restitués par inversion. Afin de pouvoir traiter de manière automatisée l'ensemble des données polarimétriques disponible, un outil de préparation de données a été développé. Nous avons ensuite adapté le code d'inversion utilisé par le système de traitement AERONET pour réaliser l'inversion simultanée des luminances totales et luminances polarisées mesurées par le C318-DP.

Pour établir l'intérêt des mesures de polarisation, nous avons débuté notre travail par une étude de sensibilité théorique. L'étude de sensibilité a été réalisée en utilisant des données simulées pour une base de cinq principaux modèles d'aérosols: la poussière désertique, industrielle et urbaine, urbains propres, combustion de la biomasse et des aérosols maritimes. Nous avons évalué l'effet d'un bruit aléatoire, d'un biais sur les mesures d'épaisseur optique aérosols et des erreurs de pointage de l'instrument. Les résultats démontrent clairement l'avantage d'utiliser la polarisation dans le cas de concentrations importantes en particules fines. A l'inverse, la polarisation s'est révelée moins sensible à la présence d'aérosols dominés par les grosses particules (poussière désertique).

Dans un second temps, les données de trois sites d'observation ont été traitées et analysées : GSFC, USA, (aérosol urbain dominé par les particules fines) ; Beijing, Chine, (aérosols industriels pollués caractérisés par un mélange prononcée à la fois en mode fin et grossier) et à Dakar, Sénégal, (poussières désertique dominées par des particules grossières). Les résultats de l'étude ont révélé des l'intérêt d'utiliser la polarisation dans le cas de la pollution industrielle (Beijing), correction de biais affectant les deux modes de la distribution de taille des particules.

Notre approche corrige, de plus, la sous-estimation de la partie réelle de l'indice de réfraction et de la fraction de particules sphériques, et cela en raison de la haute sensibilité de la polarisation à la forme des particules. Pour les aérosols désertiques, nous ne constatons pas d'amélioration significative par rapport à l'inversion standard AERONET (sans polarisation). Les résultats obtenus pour le site de GSFC occupent une position médiane.

Nos résultats montrent finalement la valeur ajoutée apportée par les données polarimétriques pour améliorer la caractérisation des aérosols. Cette approche est particulièrement bénéfique pour les types d'aérosols avec une fraction fine prononcée ou les aérosols de mélange comme ceux présents, en abondance, dans de vastes régions d'Asie.

Contents

Chapter 1

Introduction

1.1 Atmospheric aerosols

Atmospheric aerosol is generally defined as a suspension of liquid and solid particles in the air, with particle radii varying from a few nm to larger than $100\,\mu m$. The most evident examples of aerosols in the atmosphere are clouds, which consist primarily of condensed water with particle diameters on the order of approximately $10\,nm$. In atmospheric science, however, the term aerosol traditionally refers to suspended particles that contain a large proportion of condensed matter other than water, whereas clouds are considered as separate phenomena. As another examples can be called haze, smoke, smog etc.

A human interacts with aerosol all his life: breathes it, creates new particles. More than 50% of technological processes produce the aerosols. Despite these, a concentration of the aerosol particles in the atmosphere does not exceed the concentration such rare inert gas as xenon. Even in very dusty regions an amount of aerosol particles is less than 10^{-6} of air mass in which they are contained. And it is three to four orders smaller than the mass fraction of water vapor. Nevertheless, impact of the aerosols on environment is very important and includes direct health effects, acid deposition and the Earth radiation balance changing.

The interaction of the aerosols with water vapor plays an important role in atmospheric processes. Fist of all, the aerosol particles act as condensation nuclei for cloud formation that has a great influence on climate and radiation balance of the planet (Boucher, 1999; Lohmann et al., 2003; Lohmann and Feichter, 2005; Lohmann and Hoose, 2009). In absence of this process, clouds might occur in the atmosphere only at high altitude due to condensation of water vapor on the ions. Besides, the size and composition of aerosol particles can be changed due to water absorbing by particles or conversion of water from a gaseous state into aerosol. The transformation depends on numerous factors as concentration of aerosol and water vapor, ambient temperature and relative humidity, intensity and spectrum of incident solar radiation, physical and chemical properties of aerosol particles. This effect strongly affects on the variability of aerosol optical properties. It should be mentioned, that the mechanisms of the growth of aerosol particles is not clear when the humidity changes, especially when it is quite far from saturation.

The described aerosol impact on cloud formation and their properties is so-called aerosol indirect effect (Ramanathan et al., 2001; Kaufman et al., 2002). The direct effect consists in iteration of aerosol particles with solar and thermal radiation. In general, both of them lead to cool the atmosphere-surface system. Indeed, clouds and aerosols first cool the surface and atmosphere reflecting sunlight. However, aerosol further cool the surface but warm the atmosphere absorbing radiation. Moreover, the absorption leads to modifying the temperature and humidity profiles that is so-called semi-direct effect.

Fig. 1.1 shows the sign and the intensity of radiative forcing of the main constituents of the atmosphere (on Climate Control , IPCC; IPCC, 2007; Forster et al., 2007; Hansen et al., 2011). In total, the aerosols have cooling effect ($-0.5W/m^2$ for direct and $0.7W/m^2$ for indirect effects in average) but the uncertainty in cooling effect estimation is high and a level of scientific understanding ("Level of Scientific Understanding", LOSU) is low. It is also shown, that increasing of greenhouse gas emissions in the troposphere due to human activities leads to a positive radiative forcing estimated at about $2.99W/m^2$ (from 2.62 to 3.56) (with $1.66 \pm 0.17W/m^2$ of carbon dioxide, $0.48 \pm 0.05W/m^2$ of the methane, $0.16 \pm 0.02W/m^2$ of nitrous oxide, $0.34 \pm 0.03W/m^2$

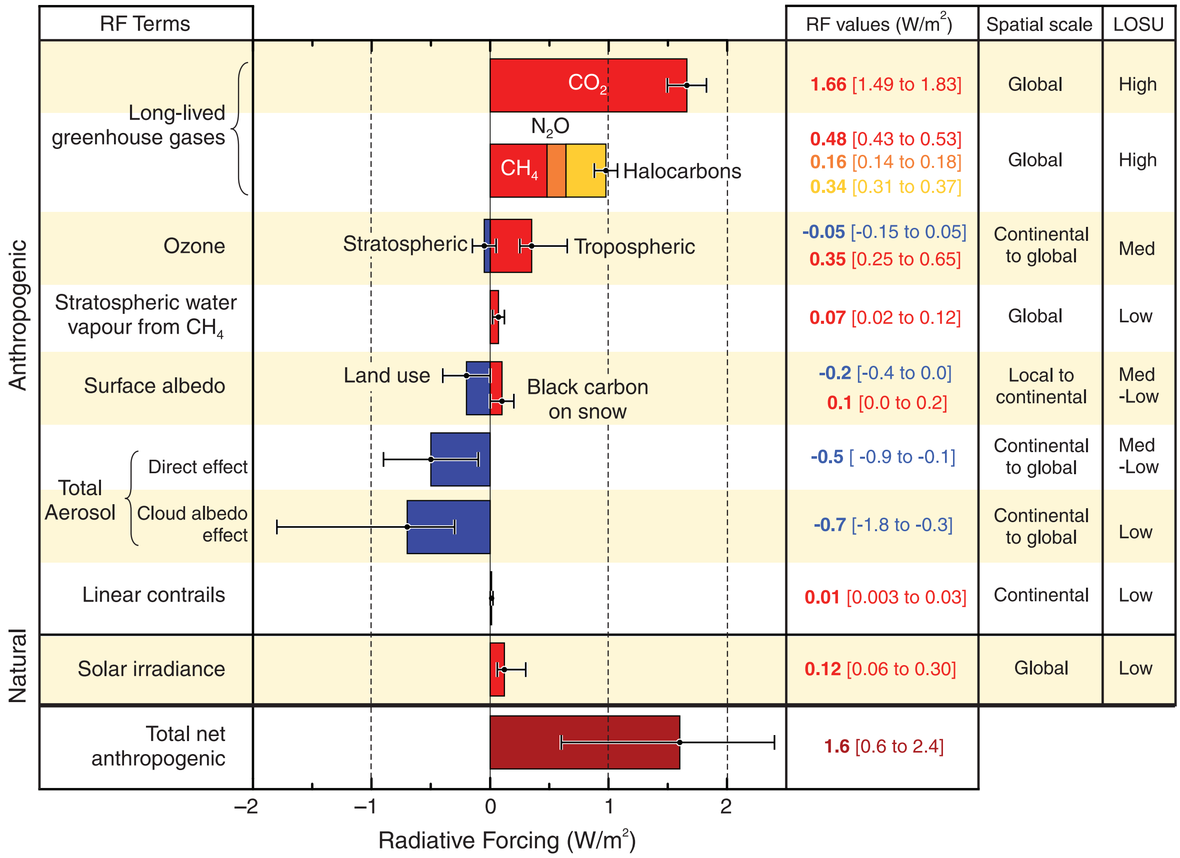

FIGURE 1.1: Global average radiative forcing in 2005 with respect to all important agents and mechanisms, together with the typical geographical extent (spatial scale) of the forcing and the assessed level of scientific understanding (LOSU); according to IPCC2007 (Forster et al., 2007)

of the halocarbon and $0.35W/m^2$ (from 0.25 to $0.65W/m^2$) of ozone). The radiative forcing due to greenhouse gas emissions is estimated with a high LOSU, apart from an "average" level for ozone. In total, the radiative forcing caused by the emission of anthropogenic greenhouse gas and aerosols is considered positive to $1.6W/m^2$ (from 0.6 to $2.4W/m^2$) demonstrating the significant influence of human activities on warming.

Furthermore, the phenomena of atmospheric electricity are closely related to the presence of atmospheric aerosol particles. J. Frenkel suggested that the oriented adsorption of water molecules can cause charged particles (Frenkel, 1944). Also, the adhesion of light ions to aerosol particles leads to a decrease in the conductivity of air. Moreover, collecting the charge of definite sign on large aerosol particles ($R > 0.1\ \mu m$) could lead to the formation of a large volume charge in the air.

It should be emphasized that the role of aerosol in atmospheric processes and the contribution to the radiative budget depend primarily on microphysical characteristics of the aerosol particles, i.e their size, shape and chemical composition. For example, the initial charge of the drops and electrical properties of the air are determined by the content of the ions with the radius $0.001 < R < 0.055$ μm. In the optics of atmospheric aerosol larger particles comparable to the wavelength of the radiation have major influence on the processes of scattering and absorption of radiation. For the processes of cloud formation the presence of atmospheric cloud condensation nuclei and sublimation, which have a particle size $R > 1\mu\ m$ is important. These particles also determine the rate of precipitation (Junge, 1963). Another good example is black carbon or soot that have strongly absorbing characteristics and, consequently, heats the atmosphere, whereas aerosols generally are highly reflective. Therefore the accurate investigation of the aerosol properties have a great importance to understand the climate effects. In turn, the aerosol microphysical characteristics are determined by the aerosol origin.

Aerosol origin

Atmospheric aerosol particles originate from a wide variety of natural and anthropogenic sources.There are two ways of aerosols appearance in the atmosphere: the particles can be directly emitted as liquids or solids (primary particles) from sources such as biomass burning, incomplete combustion of fossil fuels, volcanic eruptions, and wind-driven or traffic-related suspension of road, soil, and mineral dust, sea salt, and biological materials (plant fragments, microorganisms, pollen, etc.), or formed in the atmosphere from precursor gases such as SO_2, NO_x, NH_3 and non-metal volatile organic compound precursors (secondary particles) by gas-particle transformation processes through the phenomena of nucleation, condensation or adsorption (Hoffmann et al., 1997; Kamens and Jaoui, 2001). Submicron aerosol fraction originated mainly from the secondary sources is approximately a half of mass of aerosol matter in the atmosphere. The precursor gas can come from emissions from the soil (e.g. due to the use of fertilizers), vegetation (biogenic VOC) or human activities (combustion of fossil fuels in energy production, transport, industrial activities, etc.).

The total aerosol mass is dominated by aerosols produced from the surface due to natural processes such as the volcanic emissions, biomass burning, the action of the wind (sea spray aerosol, desert dust), etc. However, anthropogenic emissions of both primary particles and precursor gases contribute significantly to the total aerosol load. Moreover, a bulk of fine particles having an impact on health, environment and climate as carbon soot and sulfates, are derived from anthropogenic emissions.

Some aerosol sources are contributed by natural and anthropogenic factors both (biomass burning and soil dust emissions). Often it is hard to distinguish between anthropogenic and natural contribution of these sources.

1.2 Motivation

The time spent in the atmosphere by aerosol particles is a complex function of its physical and chemical characteristics (particle size, hydroscopic properties, etc), meteorological conditions, time and location of its release. The lifetime of greenhouse gases such as carbon dioxide or methane (CO_2 or CH_4) is about 100 years and them spatial distribution over the world is quite uniform. Unlike this, the lifetime of tropospheric aerosol is estimated to be order of days to week. Due to short lifetimes together with mostly indefinite aerosol sources with numerous complex characteristics, the aerosol is highly variable in both space and time. All these facts cause the specificity of the methodology of the aerosol climate impact study. Namely, each model aiming to produce a realistic description of the aerosol properties and climate impact must use the results of regular and global measurements of the aerosol parameters.

Remote sensing allows to obtain a global information of aerosol and clouds properties. Remote sensing methods could be divided into active (lidars) and passive (radiometers) techniques. Corresponding measurements can be carried out either from space (space-borne instruments) or ground (ground-based instruments). Also there exist airborne instruments taking a middle position. Each technique and instrument has its own field of application as well as scope and limitations. For example, space-borne instruments implement global monitoring of large areas and produce wide spectrum of information concerning various regions over the world. But, at the same time, satellite observations generally have low resolution and precision of the measurements. Detailed review of the satellite systems could be find in Kaufman et al. (2002). Lidars measure the vertical profile of extinction coefficient but has limitation in quantitative measurements because the lidar equation cannot be solved without an assumption on aerosol optical characteristics or some additional constraints such as independent optical depth measurements.

The most simple and useful devices are ground-based instruments. They do not conduct the monitoring of the big areas as a satellite devices, but provide high quality and resolution of the measurements of a chose region.

Due to the large spatial and temporal variability of the aerosol there was a need for the implementation of global ground-based observations. The AERONET program (Holben et al., 1998), initiated by NASA and LOA in the 90's, is the most extended and well-established network of ground-based solar radiometers. The data provided by AERONET are currently used by a wide community for aerosol characterization, satellite and model validation and synergetic utilization with other instrumentation (lidar, in-situ, radiation, etc.). The network is equipped by the sun-radiometers provided by CIMEL company, Paris, France.

The interpretation of the measured characteristics of radiation relies on a complex inverse method (inversion code) aiming on providing detailed information on aerosol properties integrated over the column such as size distribution, refractive index, chemical composition, particle shape (mainly in case of large particles), absorption, scattering properties, lidar ratio. A first generation of the inversion code was developed by Dubovik and King (2000) and is extensively used in the framework of the AERONET.

In order to efficiently retrieve aerosol microphysical parameters by any inversion methods the total number of input measured information should exceed the number of required unknowns. How it was been mention by Michael Mishchenko in several studies (Mishchenko et al., 1997, 2000, 2007, 2010, etc.), more often than not, the requisite number of unknown model parameters exceed the number of independent measurements, thereby making the inverse problem ill-posed. First of all, it concerns the measurement techniques based on the radiance intensity observations only. The one way to ameliorate the ill-posed nature of the inverse problem is to increase the number of independent measurements per scene location until it significantly exceeds the number of unknown model parameters. Then, the retrieval procedure based on a minimization technique is likely to become stable and yield a unique solution.

There are several well-known methods to increase a body of data provided by passive measurements (Mishchenko et al., 2007):

- to measure not only the intensity, (i.e., the first Stokes parameter, I), but also the one or more other remaining Stokes parameters describing the polarization state of the reflected radiation (i.e., Q, U, and V; Hansen and Travis 1974);
- to increase the number of spectral channels and the total spectral range covered;
- to increase the number and range of viewing directions from which a scene location is observed;
- to improve the measurement accuracy, especially for polarization

Z. Li showed previously a few notable improvements of aerosol retrieval that the use of additional polarimetric measurements of diffuse radiation brings (Li et al., 2009). This technique is already well exploited in satellite observations (Dubovik et al., 2011). However, multi-wavelength polarization information is rarely available (or at only one wavelength) and is not considered in AERONET system.

1.3 Objectives

The developing of new CIMEL CE318-DP sun-photometer allows to improve the quality and accuracy of ground-based observations by applying of additional polarimetric measurements of diffuse radiation for the inversion. Together with high resolution and accuracy of these measurements as well as big amount of the sites over the world in AERONET system (Holben et al., 1998), the application of this technique can significantly decrease uncertainties in aerosol properties determination and its climate impact.

The main enhancement of the new CIMEL sun-photometer is a new scheme of a measurement mechanism. It organizes as a system of two paired independently rotating wheels one from which is a set of polarizers and another one is a set of filters. Thus it provides a possibility to measure the polarized radiance at all available wavelengths that significantly increases the information content of data provided by a single photometer. Further this instrument will be called DWP-photometer (Double Wheel Polar).

Nonetheless, the measured data from DWP-photometer have not been systematically processed yet and have not been used for operational retrieval into framework of the AERONET. In order to process them the data preparation tool for the retrieval was developed. The program have been designed for semi-operational processing of the data independent of an observation geometry using AERONET inversion code adapted for inversion of both intensity and polarization measurements (Dubovik et al., 2006).

In order to estimate a contribution of polarized measurements to inversion results the observed data for several regions with different aerosol types have been processed. The data were considered, inverted and analyzed with and without applying polarimetric measurements. To operationally increase the quality of the measurements and, consequently, the accuracy of the inversion results, a data quality check routine was developed as a part of the whole data preparation tool. This function removes physically unrealistic measured values (sharp peaks, for example) from initial data set before the inversion procedure conducting. It allows to consider with acceptable precision even the observations obtained for imperfect measurement conditions.

Moreover, some studies have been carried out over synthetic data to investigate a sensitivity of the polarimetric data to the traits of the key aerosol types. The usage of the simulated data for analysis was obligatory since a deficit of the real data due to low propagation of the DWP-photometer – only few sites over the world are equipped by the new instrument at present time.

Chapter 2

Aerosol properties and remote sensing

2.1 Properties of aerosols

Generally, atmospheric aerosols can be described by two sets of properties: physical and optical. The first one characterizes the shape, size and structure of aerosol particles, while the second set describes the interaction of the aerosol with radiation (refraction, reflection, extinction, etc). Obviously, optical properties of aerosol are defined by physical properties and number of its particles, which in turn may be identified by optical aerosol properties observation.

2.1.1 Aerosol physical properties

The properties of the aerosols in the atmosphere depend directly on the source, formation mechanism of the particles and the transformations they undergo in the atmosphere.

Shape and size of the particles

Liquid aerosols particles are mostly spherical in the atmosphere conditions, whereas the shape of solid aerosol particles is very variable and may be irregular (crystalline, aggregate, fractal, amorphous).

Nevertheless, to simplify the aerosol behavior analysis an equivalent (effective) diameter is often used, which is defined as the diameter of a sphere that has the same value of a particular physical property as that of the irregular particle. These are equivalent mass diameter, equivalent volume diameter, equivalent optical diameter, equivalent aerodynamic diameter etc. For example, equivalent mass diameter is a diameter of a sphere of the same material that has the same mass as the irregular particle, and equivalent aerodynamic diameter is defined as the diameter of a sphere of unit density ($1g/cm^3$) that has the same settling velocity in air as the particle under consideration. The second one is widely used in atmospheric science and can be written as $d_a = d_p\sqrt{\rho}$, where d_p is a physical diameter and ρ is a density of the particle.

Suitable for the characterization of the size of a population of aerosols, the *size distribution* is used to quantify the number of particles of a certain radius. This distribution presents one or more modes. The aspect of a multi-modal distribution of aerosols in the troposphere has been shown by Jünge (1955) and more recently updated by Whitby (1978).

Fig. 2.1 represents the most commonly observed aerosol modes according to the equivalent aerodynamic particle diameter for the range between 0.01 and 100 μm. These are so called "Aitken" mode, A), accumulation (B) and coarse mode (C). Aitken (A) and accumulation (B) modes can be grouped into a single mode called "fine".

The smallest particles with diameters not exceeding 0.01 μm (not shown in Figure 2.1) are known as ultrafine particles (also called nucleation mode). They are thought to be generated by gas-to-particle conversion processes. Because of their very small size and mass, they are difficult to study with the available measurement techniques. These particles are only observed as a distinct mode at their source and have a very short lifetime, some times on the order of minutes, due to their rapid coagulation or random impaction onto surfaces.

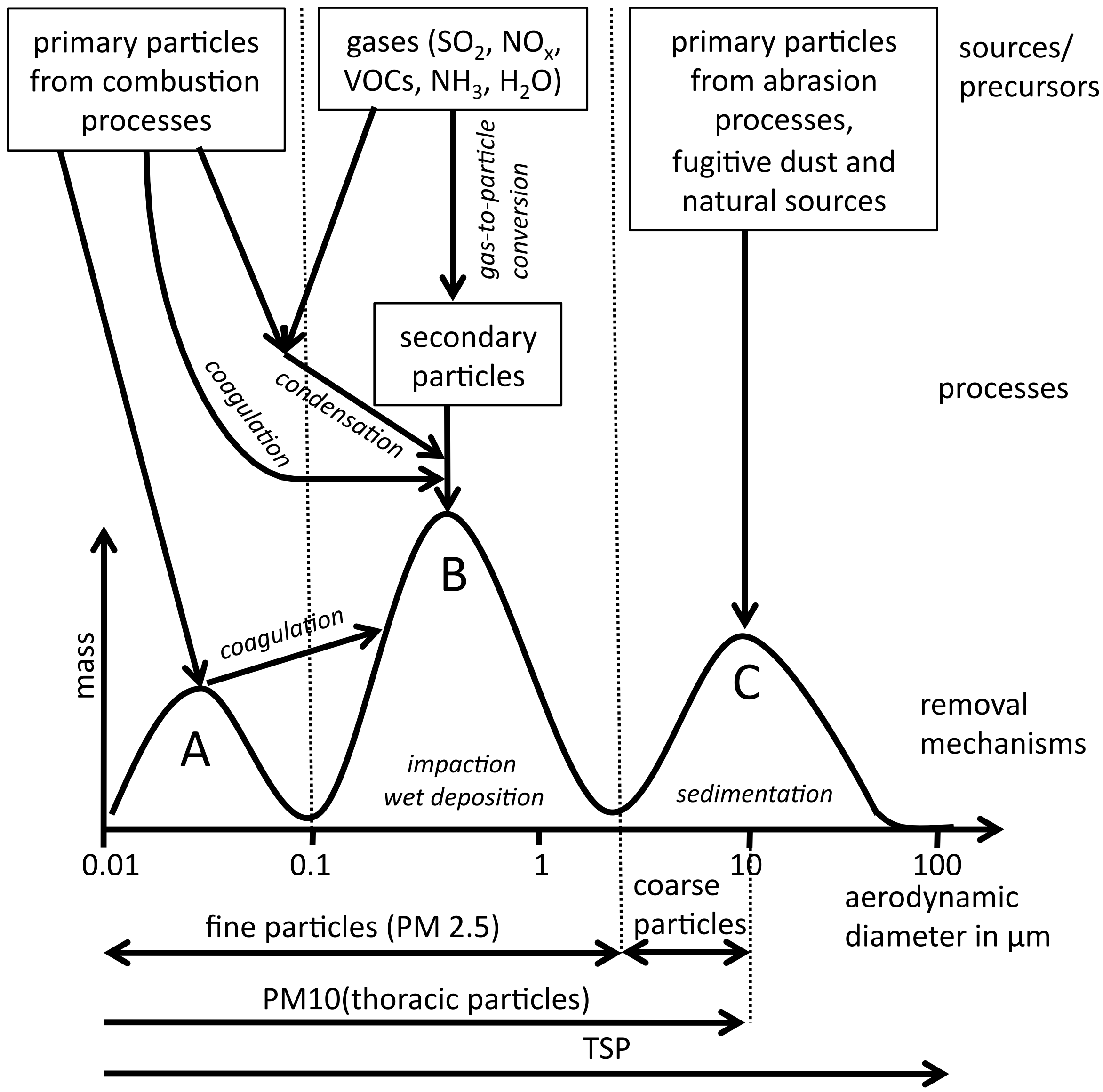

FIGURE 2.1: Schematic view of the size ranges of atmospheric aerosols in the vicinity of the source and the principal processes involved A: Aitken mode; B: accumulation mode; C: coarse particles (modified from Kacenelenbogen (2008)

The Aitken mode (A) particles, extending from 0.01 to 0.1 μm in diameter, are formed from ambient-temperature gas-to-particle conversion as well as condensation of hot vapor during combustion processes. These particles act as nuclei for the condensation of low-vapor pressure gaseous species, causing them to grow into the bigger mode. The lifetime of these particles is short, as they are lost principally by coagulation with larger particles.

The accumulation mode (B) represents a physical particle radius between 0.1-1.0 μm. They come from the aggregation of smaller particles, from the condensation of gases or the re-evaporation of droplets. Aerosols of this type are of great importance from the climate viewpoint because their interaction with the light is maximal (since their size is of the order of the solar spectrum) and their presence time in the atmosphere is the longest.

Finally, the coarse mode (C) corresponds to particles of radius more than 1 *mum*. These particles are mainly produced by mechanical processes and introduced directly into the atmosphere from both natural and anthropogenic sources. Because of their relatively large size, coarse particles settle out of the atmosphere in a reasonably short time by sedimentation, except on windy days, where fallout is balanced by re-entrainment.

Both the nucleation and Aitken mode particles account for the majority of atmospheric particles by number, but due to their small sizes, they rarely account for more than a few percent of the total mass. Hence the toxicological effects are determined primarily by the number of particles, rather than their mass, these small particles could ultimately prove to be of high importance. The accumulation mode particles generally account for a significant fraction of the total aerosol mass and have the greatest surface area. This makes these particles to be very important to gas phase deposition and atmospheric heterogeneous chemistry. Most of the aerosol mass is found in the coarse mode, where large particles contribute significantly to the optical properties of atmospheric aerosols. All these modes, in general, originate separately, are transformed separately, are removed from the atmosphere by different mechanisms, have different lifetimes, have different chemical composition and have different optical properties. Therefore, the distinction of particles between nucleation, Aitken, accumulation and coarse modes is a fundamental one in any discussion of the physics, chemistry, or measurement of aerosols.

Mathematically, the lognormal distribution can well characterize a population covering a wide range of sizes. Variation in the number of particles n as a function of the natural logarithm of the radius r can be written then

$$n(r) = \frac{dN}{d\ln r} = \frac{n_0}{\sigma_0\sqrt{2\pi}}\exp[-\frac{(\ln r - \ln r_0)^2}{2\sigma_0^2}] \tag{2.1}$$

where $n(r)$ is the number of particles, the natural logarithm of the radius is between $\ln r$ and $\ln r + d\ln r$, r_0 is the modal radius, σ_0 is the standard deviation of the natural logarithm of the radius (the width of the distribution) and n_0 is the number of particles in the mode considered.

A multi-modal distribution is simply described by a sum of log-normal distributions. The most used is bi-modal lognormal size distribution.

It is not always correct to use the distribution of the number of particles. The distribution of the surface is better if we are interested in the chemical reactions in which aerosols participate. If one seeks to evaluate the mass of aerosols, the distribution of volume V will be interesting. This can be written

$$\frac{dV}{d\ln r} = \frac{V_0}{\sigma_3\sqrt{2\pi}}\exp[-\frac{(\ln r - \ln r_3)^2}{2\sigma_3^2}] \tag{2.2}$$

where r_3 and σ_3 are defined in the same way as above, and V_0 is the volume concentration of particles. Knowing that the radius of the modal distribution of the n-th power of the radius is given for the log-normal $r_0\exp(-n\sigma_0^2)$ and the standard deviations remain unchanged ($\sigma_3 = \sigma_0$), we pass from modal radius distribution volume for that of the distribution of the number by

$$r_0 = r_3\exp(-3\sigma_0^2) \tag{2.3}$$

Thus r_3 is higher than r_0. This fact means the shift of volume distribution towards larger particles which contribution is dominated .

Chemical composition

The chemical composition of ambient aerosol particles has a critical importance for identification of their sources and prediction of the impact on various atmospheric processes and human health. Chemical composition of aerosols depends on sources of emission and transformations they undergo in the atmosphere. According to on Climate Control (IPCC) atmospheric aerosols are generally composed of variable amounts of sulphate, ammonium, nitrate, sodium, chloride, trace metals, crustal elements, water and carbonaceous material.

Carbonaceous aerosol components count for a large fraction of air particulate matter. Traditionally the total carbon content divided into an organic carbon fraction and a black carbon (elemental carbon, graphitic carbon or soot). Black carbon is emitted directly into the atmosphere, predominantly from combustion processes. Particles containing organic carbon can be not only directly emitted into the atmosphere (for e.g. from biomass burning and combustion), but they can also be formed by nucleation or condensation of products of photochemical degradation of volatile organic compounds (VOCs). This is called secondary organic aerosol (SOA). VOCs can come from the vegetation (terpenes, limonene, etc.) or be derived from anthropogenic sources (benzene, toluene, etc.) (Hoffmann et al. (1997), Kamens and Jaoui (2001)).

Crustal materials originate from soil dust and windblown minerals and are contained mostly in the coarse particle fraction. Their composition varies greatly according to local geology and surface conditions.

The main source of *chlorides* is sea spray, even at distant locations from the coast. Sea salt particles cover a wide size range ($0.05 < d < 10\mu m$), and have a correspondingly wide range of atmospheric lifetimes. This aerosol is dominant contributor to both light scattering and cloud nuclei. It is very efficient cloud condensation nuclei, making them an important part of aerosol indirect effects (Gong et al. (1998)). Chlorides also enter atmospheric particles as a result of ammonia neutralization of vapor of hydrochloric acid, which is emitted from such anthropogenic sources as power stations and incinerators.

The *sulphate* components are derived mainly from the atmospheric oxidation of anthropogenic and natural sulphur-containing compounds, such as sulphur dioxide (SO_2) and dimethyl sulphide respectively. Sulphates in aerosol particles are present as sulphuric acid, ammonium sulphate, and intermediate compounds, depending on the availability of gaseous ammonia to neutralize the sulphuric acid formed from SO_2 (Adams et al. (1999)). The chemical pathway to convert the precursors to sulphates is important because it influences on radiative effect. Most SO_2 is converted to sulphates either in the gas phase or in cloud droplets that later evaporate (Weber et al. (1999)).

Nitrate are formed mainly from the oxidation of atmospheric nitrogen dioxide (NO_2) and are not considered in assessments of the radiative effects of aerosols because they cause only 2% of the total direct forcing (Andreae (1995)). They are important only at a regional scale (ten Brink et al. (1996)).

Accurate determination of the chemical composition of air particulate matter is a formidable analytical task. Minute sample amounts are usually of several main constituents and hundreds of minor and trace constituents. Moreover, the composition of the individual particles can be fairly uniform (internally mixed aerosols) or very different from the ensemble composition (externally mixed aerosols), depending on the particle sources and atmospheric aging processes involved (coagulation, gas-particle partitioning, chemical reactions).

2.1.2 Aerosol optical properties

Microphisical characteristics of aerosol and its concentration define the interaction of the incoming radiation with the aerosol layer or, in another words, the aerosol optical properties. A parallel light beam passing through a layer of aerosol particles is attenuated by absorption and scattering. The main optical properties of aerosol determining its radiation effects are the aerosol optical depth and extinction coefficient, complex refractive index, Ångström parameter, single scattering albedo and the phase matrix. All these parameters are spectral dependent except the Ångström parameter.

2.1.2.1 Refractive index

The refractive index is one of a major optical properties of the aerosol that is involved in the extinction of light. Its complex value is determined as:

$$m = n + ik \tag{2.4}$$

where $n = Re(m)$ is the real part and $k = Im(m)$ is the imaginary part of the complex refractive index. The real part $Re(m)$ defines the speed of propagation in the medium and provides information on the deflection of light by the particles. This is generally between 1.33 (aerosols saturated water) and 1.55 (mineral aerosol), but can reach 1.75 in the visible range for soot particles. The imaginary part $Im(m)$ is connected to the absorption properties of aerosols. It is 0 for purely scattering aerosols (such as sea salt) and 0.66 for the most absorbing aerosols such as soot particles.

2.1.2.2 Aerosol optical depth and extinction coefficient

The aerosol optical depth shows the attenuation of radiation by aerosol particles containing in the atmosphere. From the Bouguer-Lambert-Beer law, the Sun irradiance $E(\lambda)$ at wavelength λ is written (Bohren and Huffman, 1998):

$$E(\lambda) = E_0(\lambda)e^{-\tau(\lambda)m} \tag{2.5}$$

where $E_0(\lambda)$ is the extraterrestrial Sun irradiance; m is an airmass proportional to $1/cos(\theta_s)$ when refraction is neglected; θ_s is a solar zenith angle; $\tau(\lambda)$ is the spectral total optical depth of the atmospheric column that is the sum of aerosol extinction, gaseous absorption and molecular (Rayleigh) scattering optical depths:

$$\tau(\lambda) = \tau^a_{ext}(\lambda) + \tau^m_{scat}(\lambda) + \tau^g_{abs}(\lambda) \tag{2.6}$$

The aerosol optical depth $\tau^a_{ext}(\lambda)$ (AOD) is the sum of the depths of optical absorption and scattering: $\tau^a_{ext} = \tau_{scat} + \tau_{abs}$ represents the extinction of radiation by aerosol layer integrated along the atmospheric column, i.e.

$$\tau^a_{ext}(\lambda) = \int_0^\infty \sigma^a_{ext}(\lambda)dz \tag{2.7}$$

where σ^a_{ext} is the *extinction coefficient* that is defined as the fraction of intensity lost from a collimated beam per unit of layer thickness at the given wavelength λ (units of m^{-1}). In turn, it can be determined as

$$\sigma_{ext}(\lambda) = \int_0^\infty \pi r^2 Q_{ext}(m, r, \lambda)n(r)dr \tag{2.8}$$

where $n(r)$ is the size distribution of a set of particles; Q_{ext} is extinction efficiency factor and depends on the refractive index m, the particle size r and the wavelength λ.

As in the case of the extinction optical thickness one can write:

$$\sigma_{ext} = \sigma_{scat} + \sigma_{abs} \tag{2.9}$$

2.1.2.3 Single Scattering Albedo

The relative contribution of absorption to the extinction by aerosol particles is usually expressed by aerosol *single-scattering albedo* ω_0, which is defined as the ratio between particle scattering and particle extinction coefficients:

$$\omega_0(\lambda) = \frac{\sigma_{scat}}{\sigma_{ext}} \tag{2.10}$$

Evidently, higher the absorption is, smaller is ω_0. Single scattering albedo is anticorrelated with the imaginary part of the refractive index. For a non-absorbing aerosol (for which the imaginary part of the refractive index is equal to 0), $\omega_0 = 1$.

Most of the absorption in the aerosol compound is due to presence of black carbon ($\omega_0(550nm) = 0.15 \div 0.30$) (Bond and Bergstrom, 2006) and to absorbing mineral dust ($\omega_0(550nm) = 0.75 \div 0.99$) (Tanré et al., 2001) whereas other species such as sulphates, organic carbon and sea salt are predominantly non absorbing ($\omega_0(550nm) = 0.98 \div 1$) (Penner et al., 2001; Cooke et al., 1999; Hess et al., 1998).

2.1.2.4 Ångström parameter

The wavelength dependence of $\tau^a(\lambda)$ can be characterized by the Ångström parameter α (Ångström, 1929), which is a coefficient of the following regression:

$$\tau^a(\lambda) = \tau^a(\lambda_0)\left(\frac{\lambda}{\lambda_0}\right)^{-\alpha} \tag{2.11}$$

The value of the Ångström exponent provides information on the particle size (Schuster et al., 2006): the smaller the aerosol particles, the larger the Ångström coefficient.

In the case of molecules (Rayleigh scattering), AOD approximately follows a law λ^{-4}. Regarding aerosols, the Ångström parameter ranges from 0 (very large particles, for example, desert dust) to 3 (very fine particles like urban pollution aerosol). Note that a population of large particles whose number is distributed on a single mode can have a slightly negative Ångström parameter.

2.1.2.5 Phase matrix

The angular distribution of the scattered electromagnetic wave in the far field, where the distance between the scattering particle and the observation location is much larger than wavelength, is characterized by the *phase matrix* $\mathbf{P}(\Theta)$. Electromagnetic radiation can be described as a four element vector or *Stokes vector* (van de Hulst, 1957). It is a very effective tool for scattering problem solution. Stokes formalizm is discussed in detail in the chapter 4.

The phase matrix specifies the directionality of scattering, and transformation matrix from the incident Stokes vector $\mathbf{I}_i$ to the scattered vector $\mathbf{I}_s$:

$$\mathbf{I}_s \propto \mathbf{P}(\Theta)\,\mathbf{I}_i, \tag{2.12}$$

where Θ is the scattering angle. The element $P_{11}(\Theta)$ of the phase matrix is called the scattering phase function and for non-polarized light satisfies the following normalization condition:

$$\frac{1}{2}\int\limits_0^{\pi} \sin(\Theta)\, P_{11}(\Theta)\, d\Theta = 1. \tag{2.13}$$

Generally, $\mathbf{P}(\Theta)$ is a 4x4 element matrix. In certain conditions, it can be reduced to six individual elements, rather than the full sixteen, thus transforming Equation 2.12 into:

$$\begin{pmatrix} I_s \\ Q_s \\ U_s \\ V_s \end{pmatrix} \propto \begin{pmatrix} P_{11}(\Theta) & P_{12}(\Theta) & 0 & 0 \\ P_{12}(\Theta) & P_{22}(\Theta) & 0 & 0 \\ 0 & 0 & P_{33}(\Theta) & P_{34}(\Theta) \\ 0 & 0 & -P_{34}(\Theta) & P_{44}(\Theta) \end{pmatrix} \begin{pmatrix} I_i \\ Q_i \\ U_i \\ V_i \end{pmatrix}, \tag{2.14}$$

Such reduction could be made under one of the following conditions:

- a group of randomly oriented particles, each with a plane of symmetry (such as spheres or spheroids),
- a group of randomly oriented particles with an equal number of mirror particles,
- a group of particles that are much smaller than the wavelength of radiation so the theory of Rayleigh scattering can be used to determine the scattering matrix.

For homogeneous or radially inhomogeneous spheres (as particles of higher symmetry), the scattering matrix has only four independent elements (since $P_{11}(Q) = P_{22}(Q)$ and $P_{33}(Q) = P_{44}(Q)$).

2.2 Aerosol impact on climate and human health

2.2.1 Radiative impact

The atmospheric aerosols influence significantly on the radiative balance of the Earth that is a relation between a part of solar energy absorbed by Earth-atmosphere system and the part reradiated back to the space. This impact could be subdivided into three distinct groups including direct, indirect and semi-direct effects, shown in detail in figure 2.2.

Direct aerosol effect is any interaction of atmospheric aerosol with solar and terrestrial radiation, such as scattering and absorption. The magnitude of the radiation

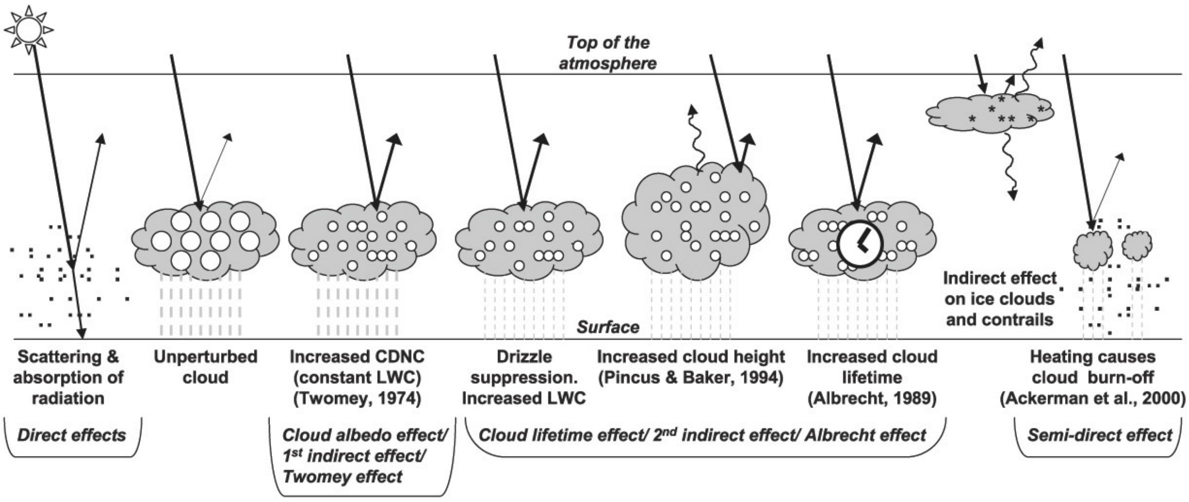

FIGURE 2.2: Schematic diagram showing the various radiative mechanisms associated with cloud effects that have been identified as significant in relation to aerosols; modified from Haywood and Boucher (2000).

forcing of the direct effect could be both positive and negative and depends on aerosol single scattering albedo and on the albedo of underlying surface (Haywood and Shine, 1995; Haywood and Boucher, 2000). Generally, the aerosols reflect solar radiation which cools the atmosphere. However, some types of aerosols, such as black carbon, for example, strongly absorb the radiation and, as a result, warm the atmosphere and cool surface at the same time. But the total radiative effect of aerosols is negative (fig. 1.1).

Indirect effects occur due to the aerosol particles acting as cloud condensation nuclei and thus affecting cloud formation and properties. Clouds reflect solar radiation that leads to cooling of the atmosphere. When aerosol concentration increases, the fine aerosol particles decrease the sizes of drops or ice crystals in clouds by 20-30% for constant liquid water content (Boucher, 1999; Lohmann et al., 2003; Lohmann and Feichter, 2005; Lohmann and Hoose, 2009). It increases clouds reflectance and cools the atmosphere and surface still more. This is so-called Twomey effect (Twomey, 1974, 1977b). Presence of aerosols also increases of the cloud height (Pincus and Baker, 1994) and affects the cloud lifetime (Albrecht, 1989).

Semi-direct effect consists in modification of the atmospheric temperature profile by absorbing aerosols, that affects the conditions of cloud formation (Ackerman et al., 2000). The impact of absorbing aerosols depends on their altitude (Koch and Del Genio, 2010) and the local meteorological conditions.

2.2.2 Impact on human health

Except the radiative balance influence and climate forcing effects, the atmospheric aerosols have a direct impact on human health. Even presence of a tiny amount of the aerosol toxic matter in the air significantly decrease its suitability for breathing. They negatively impact on lung functions, increase the outbreak of asthma and the death number due to cardiovascular diseases (Liao et al., 1999; Donaldson et al., 2001). Aerosol particles can contain toxic compounds, radioactive elements, allergens, mutagens or carcinogens, such as polycyclic aromatic hydrocarbons and heavy metals, which can reach the lungs, where they are absorbed in the blood and tissues. The most dangerous for health are the finest particles with diameter less than 2.5 microns since they can penetrate deeply the respiratory system and reach the lung alveoli.

Health effect of air pollution were sometimes dramatic in the past. The first evident event that showed the relationship between particulate air pollution and health impacts took place in Glasgow in 1909 when nearly 1000 deaths were attributed to the sharp increase in concentrations of sulphur dioxide and particulate matter caused by very stable meteorological conditions. The term "smog" (smoke contraction of smoke and fog, mist) was used for the first time to characterize this episode. There were several other tragic events of the same nature, such as Donora (USA) on 26-31 October 1948 (20 dead). The most infamous episode of aerosol pollution is The Great Smog in London that had 4000 deaths between 5 and 9 December 1952. More recent research suggests that the total number of fatalities was considerably greater, at about 12,000 During the episode, the particle concentrations reached $3000\mu g/m^3$ (Davis et al., 2002).

These health crises relating to the excessive use of fossil fuels (especially coal), lead to developing policy for reducing emissions of gaseous and particulate pollutants in most industrialized counties. However, the use of fossil fuels in huge megalopolises in India, China or Africa still make the alarming pollution in these regions.

The efforts recently undertaken in industrial countries to reduce aerosol pollution, lead to decrease of aerosol concentration to a few tens of micrograms per cubic meter (in daily average) in major agglomerations of Western Europe. However, there is no threshold concentration of fine particles in ambient air below which there would be no health impact (see InVS/Afsse, 2005; Mullot et al., 2009) and the influence on the health of low to moderate concentrations events is not recognized. The experts from AFSSET specify that frequent exposure at moderate levels are more dangerous than occasional exposure of peak concentrations. According to them, only 3% of health impacts would be caused by high concentrations of particles.

2.3 Aerosol observations

Optical technics of atmospheric aerosol remote sensing could be devided into active and passive. Passive measurements consist in registration of natural radiation that is interacted with aerosols in the atmosphere. Reflected or scattered sunlight is the most common source of radiation measured by passive sensors. The examples of passive instruments are radiometers and polarimeters.

Active instruments emit radiation by itself that is backscattered by aerosol then detected and analized by a instrument sensor. LiDARs (LIght Detection And Ranging) systems are widely used examples of active remote sensing. LiDAR technique allows the measurements of the delay time between emission and return of laser pulse, providing information about the aerosol altitude and location.

Both active and passive instruments can be also classified by the place of location: surface of the Earth, space or atmosphere. So these are grond-based, satellite or airborn instruments correspondingly. All these methods and instruments have its own scope and limitations as well as advantages. Let us consider all of them in detail.

2.3.1 Ground-based remote sensing

Observations by ground-based instruments provide detailed and accurate (Nakajima et al., 1996; Dubovik and King, 2000) but cover only local area nearby the observation site. In order to obtain such data at extended geographical scales, the ground-based observations are often collected within observational networks employing identical instrumentation and standardized data processing procedures. At present, there are a number of global and regional networks conducting both passive and active ground-based observations. Aerosol data collected by the networks provide highly valuable information for monitoring of aerosol that is widely used for validating satellite observations and constraining aerosol properties in climate simulation efforts (Kinne et al., 2003, 2006; Textor et al., 2006; Koch et al., 2009).

Sun photometers

The solar radiometers historically known as sun photometers probably are the most widespread passive instruments for aerosol monitoring. Depending on the model, they can conduct the measurements of direct Sun irradiance, diffuse sky radiance or both on only one wavelength or for several spectral channels. Some instruments have an additional ability to measure the polarization of radiation and, technically, can be also considered as polarimeters. The examples of sun photometers used in ground-based remote sensing are MFRSR, POM-1, POM-2 and series of CIMEL radiometers that are particularly described in the next chapter. The most known networks of photometers are South-Eastern SKYNET (Nakajima et al., 2007) equipped by POM-1 and POM-2, and global AERONET (Holben et al., 1998) network discussed in chapter 3 too.

Lidars

LIDAR is a technology to obtain information about distant objects using active optical systems based on the reflection and backscattering of the light in the transparent or semi transparent media. LIDAR works precisely as RADAR: a pointed beam from the light sourse is reflected from the targets, returned to the source and registered by a reciever. The response time is directly proportional to the distance to the target. The main difference between RADAR and LIDAR is that radar uses radio waves that effectively reflected from the large metallic targets, while LIDAR uses light that is scattered by any media allowing both to measure the distance to the transparent targets and analyse the intensity of the light scattered by them. It allows to retrieve the aerosol parameters together with its vertical profile. Thus, the LiDAR systems are efficient and widely used tools for realtime monitoring of aerosols or gases that can be single- or multi-wavelength.

As well as in the case of groun-based photochemic observations, regular monitoring of the state of the atmosphere are carried out in the framework of international lidar and combine lidar-photometer. For instance, regional EARLINET – European Aerosol Research Lidar Network (Bösenberg, 2000), ADNET – Asian Dust Network(Murayama and et al., 2000), MPL-Net – Micro Pulse Lidar Network (Welton and et al., 2002), ALiNe – The Latin America Lidar Network (Antuña et al., 2006), Cis-Linet – CIS Lidar Network (Chaikovsky et al., 2006) and global lidar network GALION – GAW Aerosol Lidar Observation Network (Bösenberg and Hoff, 2007; Wandinger et al., 2004).

2.3.2 Satellite observations

Space-born instruments are the main tool of global monitoring of aerosol and cloud distribution. In contrast with ground-based measuremets, satellite remote sensing performs the aerosol observations on large spatial scales but with low resolution.

Space-born passive instruments measure the radiance scattered by aerosols and clouds in the satellite direction or reflected from the ground. Examples of such sensors are MODIS – MODerate resolution Imaging Spectro-radiometer (Remer et al., 2005), MISR – Multiangle Imaging Spectro-Radiometer (Diner et al., 1998), POLDER – Polarization and Directionality of the Earth's Reflectance (Deschamps et al., 1994), AVHRR – Advanced Very High Resolution Radiometer (Stowe et al., 1992), TOMS – Total Ozone Mapping Spectrometer (Herman et al., 1997), OMI -Ozone Monitoring Instrument (Levelt et al., 2006), SEVIRI - Spinning Enhanced Visible and Infra Red Imager (Sun and Pinker, 2007), etc.

The active remote sensing is also now carried out from the space. As the examples, we can list the next lidars: LITE - Lidar In-space Technology Experiment (Winker et al., 1996), GLAS - Geoscience Laser Altimeter System (Schutz et al., 2005), CALIOP - Cloud-Aerosol Lidar with Orthogonal Polarization (Winker et al., 2010). They are collecting essential information about aerosol vertical distributions.

Furthermore, the synergy between active and passive satellite systems results in the constellation of six afternoon-overpass spacecrafts, the so-called A-Train (Stephens

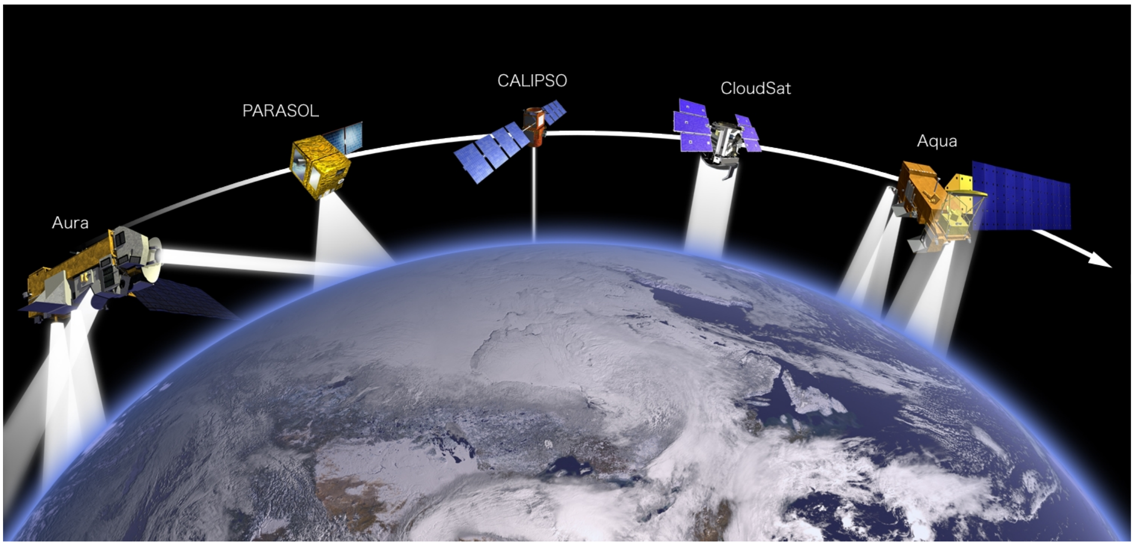

FIGURE 2.3: The constellation of spacecraft that overfly the Equator at about 1:30 PM, the so-called A-Train consists of four satellites with one no longer in the constellation (PARASOL).

et al., 2002). This system allows to conduct near simultaneous (within 15-minutes) measurements of aerosols, clouds, and radiative fluxes in multiple dimensions with sensors in complementary capabilities (Pelon et al., 2011). It is a set of four satellites (illustrated in the Figure 2.3) Aqua (with 6 instruments including MODIS), Aura (4 instruments including OMI), CALIPSO (3 instruments including CALIOP), CloudSat.

2.3.3 Airborne instruments

Airborne instruments are installed on aircrafts. Using this technique, the photometric observations can be carried out on different altitude during the flight. It allows to directly measure the vertical profile of AOD at different wavelengths (Matsumoto et al., 1987; Schmid et al., 2003; Asseng et al., 2004; Zieger et al., 2007; Karol et al., 2013). This possibility can be used, for example, to validate ground-based or space-born lidar measurements. Several airborn sun photometers were recently developped and shortly describe below.

These are the 6- and 14-channel NASA Ames Airborne Tracking Sunphotometer AATS-6 (Matsumoto et al., 1987) and AATS-14 (Schmid et al., 2003) that measure the transmission of the solar beam in 6 or 14 spectral channels. The spectral range is $380 \div 1021\ nm$ for AATS-6 and $354 \div 2139\ nm$ for AATS-14.

The systems FUBISS-ASA (Free University Berlin Integrated Spectrographic System Aureole and Sun Adapter) and FUBISS-ASA2 measures simultaneously the direct solar irradiance and the aureole around the sun in two different angles ($4°$ and $6°$). The spectra are measured with three spectrometers in the range of $400 \div 1000\ nm$ for FUBISS-ASA (Asseng et al., 2004) and $300 \div 1700\ nm$ for FUBISS-ASA2 (Zieger et al., 2007) on 256 spectral channels simultaneously.

And, finally, PLASMA system (Photomètre Léger Aéroporté pour la Surveillance des Masses d'Air) developped in the Laboratory of Atmospheric Optics, Lille University of Sciences and Technologies. The instrument conducts the direct Sun measurements over a wide spectral range ($340 \div 2250\ nm$) on 14 spectral channels (Karol et al., 2013). The main advantage of PLASMA is its small size and lightness. The weight of the optical head (mobile part) is 3.5kg and the weight of the electronic modules is around 4kg. So that it can be easily installed on a small airplane or an automobile (Karol et al., 2013).

Chapter 3

Aerosol observations by ground-based Sun/sky-radiometers

3.1 AERONET network (overview, aerosol products: direct sun observations and retrievals)

As it was mentioned above, the ground-based radiometers provide high spectral and temporal resolution image of aerosol distribution that is highly desirable to validate and augment the global data produced by satellite instruments since the development of accurate dynamical picture of aerosol loading, transport and transformation is highly important for understanding aerosols influence on climate forcing. As an answer to this challenge, the global AErosol RObotic NETwork (AERONET; Holben et al., 1998) has been established.

AERONET program was started by the National Aeronautics and Space Administration (NASA) in the 90's, in collaboration with PHOTONS (Laboratoire d'Optique Atmosphérique-LOA, University of Lille), as a federation of networks with regional or national extent deployed on ground in the form of stations for monitoring atmospheric aerosols. The aims of the AERONET project are the characterization of the aerosol properties and validation of satellite measurements providing reliable monitoring of global aerosol optical and microphysical properties as well the synergy with other instrumentation (lidar, surface radiation, in situ aerosol, etc.). The AERONET Synergy Tool, available at the AERONET website, is an example of integration of the AERONET observations with satellite data (MODIS, MISR, OMI, AIRS) lidar data from MPLNET, incoming solar radiation (SolRAD), back-trajectories, aerosol models (GOCART, NOGAPS), etc. The approximate total number of permanent sites is currently over 200 and around 50 sites are seasonal (like in the Amazon site where photometers are not installed during the rainy season). Fig. 3.1 presents the overall distribution of all available stations measuring network AERONET.

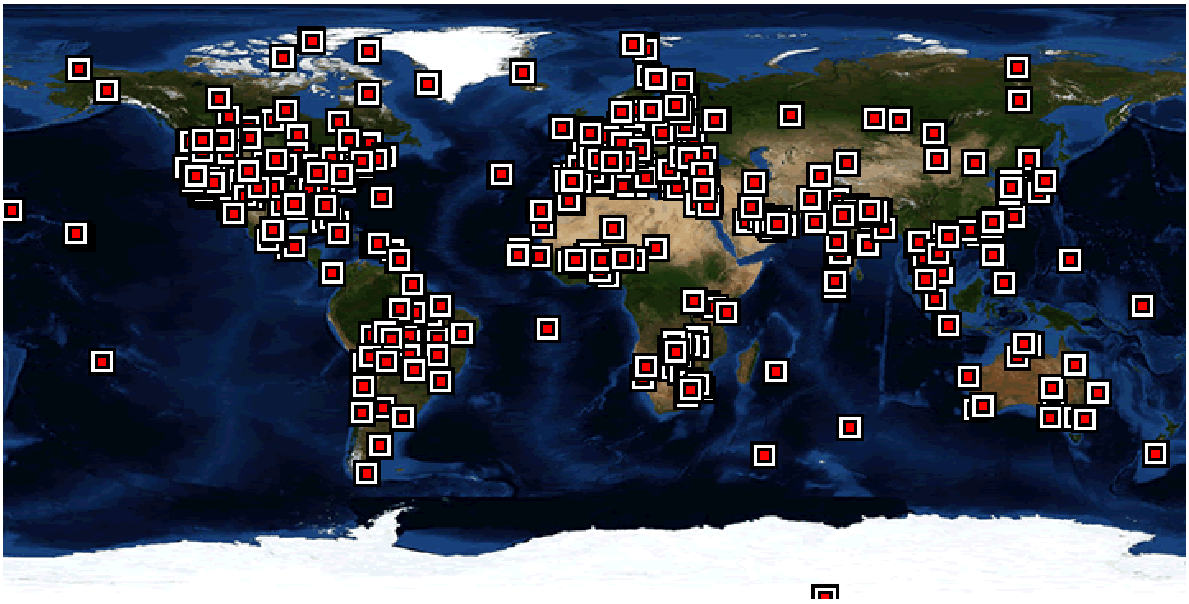

FIGURE 3.1: Distribution of AERONET stations in the world (September 2014)

The network are managed simultaneously in the United States by NASA (GSFC) and in Lille by the Laboratory of Atmospheric Optics (LOA). LOA also ensures the calibration, on-site installation and maintenance of several sites (including Europe and Africa).

3.1.1 General description of the AERONET basic instrument

The standard AERONET instrument is a portable automatic Sun and sky radiometer CIMEL CE318 developed by CIMEL Electronique company, Paris, France. This instrument equipped with 8 or 9 spectral channels covering the spectral range 340-1640 nm.

It has approximately a 1.2° full angle field of view and two detectors for measurement of direct sun, aureole, and sky radiance. The 33 cm collimators were designed for 10^{-5} straylight rejection for measurements of the aureole 38 from the sun. The robot-mounted sensor head is parked pointed nadir when idle to prevent contamination of the optical windows from rain and foreign particles. The Sun/aureole collimator is protected by a quartz window allowing observation with a UV enhanced silicon detector with sufficient signal-to-noise for spectral observations between 300 nm and 1020 nm. The sky collimator has the same field of view, but an order of magnitude larger aperture-lens system allows better dynamic range for the sky radiances. The components of the sensor head are sealed from moisture and desiccated to prevent damage to the electrical components and interference filters. Eight ion-assisted deposition interference filters are located in a filter wheel which is rotated by a direct drive stepping motor. A thermistor measures the temperature of the detector allowing compensation for any temperature dependence in the silicon detector (Holben et al., 1998).

The sensor head is pointed by stepping azimuth and zenith motors with a precision of 0.058. A microprocessor computes the position of the Sun based on time, latitude, and longitude, which directs the sensor head to within approximately 18 of the Sun, after which a four-quadrant detector tracks the Sun precisely prior to a programmed measurement sequence. After the routine measurement is completed, the instrument returns to the "park" position awaiting the next measurement sequence. A "wet sensor" exposed to precipitation will cancel any measurement sequence in progress (Holben et al., 1998).

3.1.2 Measurement concept

The measurement sequence is standardized within AERONET. The photometer provides direct Sun and angular measurements of sky radiance distribution in almucantar (a circle on the celestial sphere parallel to the horizon with constant zenith angle equal to solar zenith angle) and solar principal plane configurations (see fig. 3.2). The philosophy is to acquire aureole and sky radiances observations through a large range of scattering angles from the Sun.

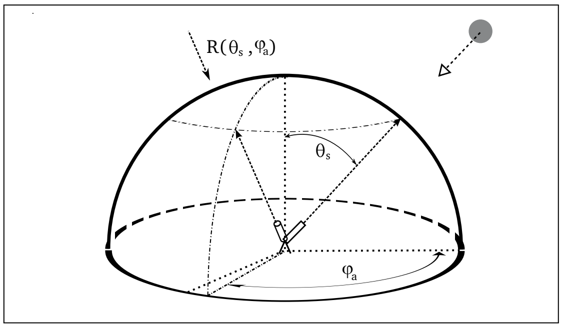

a)

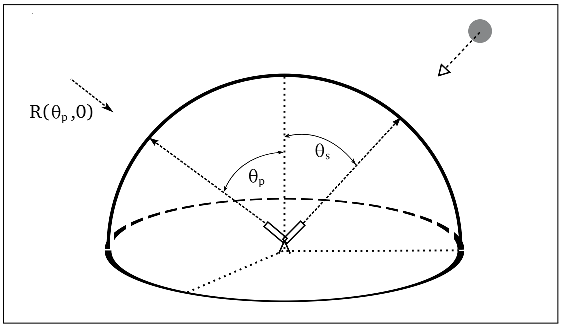

b)

FIGURE 3.2: Description of the geometries followed within AERONET: almucantar conducted with $\theta_s = const$ (a) and solar principal plane conducted with $\varphi_a = const$ (b).

An almucantar is a series of measurements taken at the elevation angle of the Sun for specified azimuth angles relative to the position of the Sun. The range of scattering angles decrease as the solar zenith angle decreases; thus almucantar sequences made at an optical airmass of 2 or more achieve scattering angles of 120° or larger. The standard principle plane sequence measures in principal plane of the Sun where all angular distances from the Sun are scattering angles regardless of solar zenith angle. Generally, principal plane observations are made hourly when the optical airmass is less than 2.

The preprogrammed sequence of measurements starts at an air mass of 7 in the morning and ends at an air mass of 7 in the evening (approximately 8° solar elevation). It consists of a series of direct sun and sky radiance measurements at fix solar elevations during sunrise and sunset (called "Langley sequence"). For solar zenith angles below 60° (air mass of 2), direct Sun measurements are performed every 15 minutes and sky radiances are acquired every hour in the almucantar and principal plane configurations. A sequence of three such direct Sun measurements are taken 30 seconds apart creating a triplet observation per wavelength. The time variation of clouds is usually greater than that of aerosols causing an observable variation in the triplets that can be used to screen clouds in many cases. Additionally the 15 minute interval allows a longer temporal frequency check for cloud contamination. There is an operational cloud-screening algorithm in AERONET, fully described by Smirnov et al. (2000).

Independently of the version, all instruments operating within AERONET are equipped at least with the spectral channels 440, 670, 870, 936 nm and 1020 nm that is the core of AERONET measurement protocol. Apart from these, each version may have additional channels, such as 500 nm, 1640 nm, ultraviolet (340, 380 nm) or polarized channels.

Measured data are automatically transmitted from the memory of the sun photometer via the Data Collection Systems (DCS) to the geostationary satellites and then retransmitted to the ground receiving station in GSFC.

The calibration is carried according to a strict protocol, which is the base of the data quality assurance in the network. The instruments are calibrated before and after deployment in the field. The operation period is approximately 1 year. The field instruments are calibrated by comparison with master instruments (so-called intercalibration method) for which high operating standards is applied. Master instruments are calibrated at high altitude stations (Manua Loa Observatory in Hawaii, USA, and Izaña in Canary Islands, Spain). In detail calibration procedure is discussed in chapter 5.

3.1.3 Aerosol products

AERONET employed a series of processing algorithms provided information about aerosol loading (optical thickness) and retrieval of aerosol microphysical characteristics. Aerosol parameters are inverted by standard AERONET retrieval algorithm initially developed by Dubovik and King (2000). Retrieved data includes size distribution of aerosol particles, complex refractive index and fraction of spherical particles. Additionally, some optical characteristics are calculated on the basis of the retrieved properties including single scattering albedo, phase function, spectral and broad-band fluxes. Particularly the inversion process is described in chapter .

All the measured and recalculated data are stoked in AERONET database in a unique format. The archival system allows the user community to access either the raw or processed data via internet for examination analysis, and/or reprocessing as needed. The archival browse algorithms are known as “demonstrat”, which graphically provides access to all aspects of the database. Data for export may be selected by location, time, and the type of raw or processed data desired. The data may be e-mailed directly during a "demonstrat session" or may be downloaded to any computer with Internet access through the AERONET homepage using a guest account.

3.2 Advanced AERONET instrumentation: DWP Cimel sun-photometer

Different versions of the instrument exist within the network: analog photometers (standard and polarized versions with 8 channels), digital photometers with 8 spectral channels (standard and polarized), the Short Wave Infrared (SWIR, also called "extended" instruments with 9 channels). By default, all instruments operating within AERONET are five spectral channels: 440, 670, 870, 936, 1020 nm. But each version can be equipped additionally by 500 nm, 1640 nm, ultraviolet (340, 380 nm) or polarized channel. But only single polarization wavelength at 870 mn is available for these instruments. This disadvantage has been removed by developing a new modification of CIMEL radiometer that is Dual Wheel Polar (DWP) sun-photometer CE318-DP.

The main improvement of the new DWP instrument is rotating-wheel technique consisting in combining the rotation of two independent polarizer and filter wheels that allows to measure the polarization at all spectral channels. CE318-DP is equipped by two parallel optical paths with different detectors: silicon and InGaAs. The silicon path covers 8 wavelengths centered at 340, 380, 440, 500, 675, 870, 936 and 1020 nm whereas the InGaS detector provides another two middle infrared channels (1020 and 1640 nm). The instrument provides the direct-Sun, angular sky radiance and polarization measurements. The observations can be conducted either by pre-defined or user-assigned sequences. Like other CE318 versions, it is fully automatic and autonomous in the field because it is powered by a solar panel. The measured data are transferring through the satellite or directly to a PC.

Further the measurements conducted by the photometer are described in detail.

3.2.1 Direct-Sun measurements

According to the Bouguer-Lambert-Beer law (eq. 2.5) a filtered detector measures the spectral extinction of direct beam radiation. That is, an instrumental digital signal $DN(\lambda)$ measured by photometer at spectral channel λ can be interpreted as

$$DN(\lambda) = DN_0(\lambda) exp[-\tau(\lambda)m] f_{es} \tag{3.1}$$

where $DN_0(\lambda)$ is a calibration coefficient which is an instrumental signal at the top of the atmosphere, i.e. with $\tau = 0$ (see section 5.2.1 in chapter 5); f_{es} is the Sun-earth distance correction factor, m is optical airmass. Clearly, the measurements of $DN(\lambda)$ with known calibration coefficients $DN_0(\lambda)$ produce the total optical depth that. In turn, if aerosol absorption and molecular scattering are known from extra measurements or some other sources, the required aerosol optical depth (AOD) can be easily obtained.

3.2.2 Sky radiance measurements

The angular measurements of sky radiance intensity are carried out in almucantar geometry for low Sun elevation angles or, equivalently, for large airmass ($m \geq 2$), and, conversely, in principal plane geometry for high Sun elevation angles or for small airmass ($m \leq 2$).

In the almucantar configuration (see fig. 3.2a) the sun-photometer keeps the zenith angle constant (equal to the solar zenith angle θ_s). The instrument makes a direct Sun measurement, and then it covers the whole range of azimuth angle φ_a, starting at 3° and finishing at 180° . The movement is done first towards right measuring the diffuse sky radiance $R(\theta_s, \varphi_a)$, and then, after pointing the Sun again, is repeated towards the left. The observation angles are the same for both branches (table 3.1). The final radiance values used for retrieval are obtained making an average between them. The sequence is repeated for each spectral channel. The entire measurement takes about 5 minutes.

In the principal plane geometry (fig. 3.2b) the azimuth angle remains constant (precisely, $\varphi_a = 0°$ or $180°$) and the instruments, after a direct Sun measurement, take the sky radiance measurements from the different scattering angles (table 3.1).

Geometry of observations	Measurements angles
Almucantar	$0°, 3.0°, 3.5°, 4.0°, 5.0°, 6.0°, 6.0°, 7.0°, 8.0°, 10.0°, 12.0°, 14.0°, 16.0°, 18.0°, 20.0°, 25.0°, 30.0°, 35.0°, 40.0°, 45.0°, 50.0°, 60.0°, 70.0°, 80.0°, 90.0°, 100.0°, 120.0°, 140.0°, 160.0°, 180.0°$
Solar Principle Plane	$-6.0°, -5.0°, -4.0°, -3.5°, -3.0°, -2.5°, -2.0°, 0°, 2.0°, 2.5°, 3.0°, 3.5°, 4.0°, 5.0°, 6.0°, 6.0°, 8.0°, 10.0°, 12.0°, 14.0°, 16.0°, 20.0°, 25.0°, 30.0°, 35.0°, 40.0°, 45.0°, 50.0°, 55.0°, 60.0°, 65.0°, 70.0°, 80.0°, 90.0°, 100.0°, 110.0°, 120.0°, 130.0°, 140.0°, 150.0°$

TABLE 3.1: Observation angles of sky radiance measurements in different geometries: Azimuth angles relative to the solar position in almucantar geometry (towards right and left sides from the Sun) and scattering angles relative to the zenith solar position (negative values means below the Sun) in solar principal plane. The double observation at 6° indicates the change from Aureole to Sky channels.

3.2.3 Polarization measurements

As well as sky radiance measurements, polarization observations are conducted by angular measurements of scattering light in almucantar or principal plane geometry but with a polarizer applying. Radiance is measured for 3 relative orientations of polarizer axis $(-60°, 0°, 60°)$ that are called polarized units (PU). So we have 3 values (L_{p1}, L_{p2}, L_{p3}) at each observation angle. Polarization measurements are performed at the same geometry but for different angles (see table 3.2).

Geometry of observations	Measurements angles
Almucantar	$30.0°, 35.0°, 40.0°, 45.0°, 50.0°, 60.0°, 70.0°, 80.0°, 90.0°, 100.0°, 120.0°, 140.0°, 160.0°, 180.0°$
Solar Principle Plane	$-85.0°, -80.0°, -75.0°, -70.0°, -65.0°, -60.0°, -55.0°, -50.0°, -45.0°, -40.0°, -35.0°, -30.0°, -25.0°, -20.0°, -15.0°, -10.0°, -5.0°, 5.0°, 10.0°, 15.0°, 20.0°, 25.0°, 30.0°, 35.0°, 40.0°, 45.0°, 50.0°, 55.0°, 60.0°, 65.0°, 70.0°, 75.0°, 80.0°, 85.0°$

TABLE 3.2: Observation angles of polarization measurements in different geometries. Angles are azimuth positions relative to the Sun for almucantar (towards right and left sides from the Sun) and are zenith angles for principal plane.

In contrast to sky radiance measurements, polarization is not measured at aureole area. Furthermore, in principal plane geometry the measurements are conducted for the zenith angles (table 3.2) independently of the current Sun position whereas in the case of Sun radiance observations the scattering angles relative to the Sun zenith angle.

Chapter 4

Retrieval of the aerosol properties

4.1 Modeling of aerosol Polarimetry observations

In addition to irradiance and frequency, a monochromatic (i.e., time-harmonic) electromagnetic wave has a property called its *state of polarization*. Polarization is very important property since two waves with identical frequency and irradiance, but different polarization, can behave quite different.

The plane monochromatic electromagnetic wave is given by

$$\begin{aligned} \mathbf{E}(\mathbf{r}, t) &= \mathbf{E_0} \exp(i\mathbf{k} \cdot \mathbf{r} - i\omega t) \\ \mathbf{H}(\mathbf{r}, t) &= \mathbf{H_0} \exp(i\mathbf{k} \cdot \mathbf{r} - i\omega t) \end{aligned} \tag{4.1}$$

where $\mathbf{E}$ is the electric and $\mathbf{H}$ the magnetic field, $\mathbf{E_0}$ and $\mathbf{H_0}$ are their amplitudes, t is time, $\mathbf{r}$ is the position vector, ω is the angular frequency and $\mathbf{k}$ is the real-valued wave vector.

The polarization of electromagnetic wave is associated with motion of the real electric field vector $Re(\mathbf{E})$. For plane monochromatic wave it is

$$\begin{aligned} Re(\mathbf{E}) &= Re[(\mathbf{A} + i\mathbf{B}) \exp(ikz - i\omega t)] \\ &= \mathbf{A} \cos(kz - \omega t) - \mathbf{B} \sin(kz - \omega t) \end{aligned} \tag{4.2}$$

where $k = 2\pi/\lambda$ is the wave number.

In each particular plane ($z = 0$, for instance) we have

$$\mathbf{E}(z=0) = \mathbf{A}\cos\omega t + \mathbf{B}\sin\omega t \tag{4.3}$$

Thus, during each time interval $2\pi/\omega$, the tip of the real electric field vector $Re(\mathbf{E})$ describes an ellipse in the plane normal to the propagation direction. If $\mathbf{A} = 0$ (or $\mathbf{B} = 0$), the ellipse degenerates to a straight line, and the wave is *linearly polarized*; the vector $\mathbf{B}$ then specifies the direction of polarization. If $|\mathbf{A}| = |\mathbf{B}|$ and $bfA \cdots B = 0$ the ellipse is a circle and the wave is *circularly polarized*. In general, a monochromatic wave of the form 4.2 is *elliptically polarized*.

Since the electric vector is transverse, it may be represented as a superposition of two orthogonal components:

$$\mathbf{E} = Re(E_{\parallel}\hat{e}_{\parallel} + E_{\perp}\hat{e}_{\perp}) \tag{4.4}$$

where $\hat{e}_{\parallel}$ and $\hat{e}_{\perp}$ are the "horizontal" and "vertical" orthogonal axes respectively. $E_{\parallel}$ and $E_{\perp}$ are the complex, oscillating functions defined as

$$\begin{aligned} E_{\parallel} &= A_{\parallel}e^{i\delta_{\parallel}}, \\ E_{\perp} &= A_{\perp}e^{i\delta_{\perp}}, \end{aligned} \tag{4.5}$$

where $A_{\dots}$ denotes the component of electro-magnetic amplitude, $\delta_{\dots}$ is the phase.

Now we can determine the *Stokes parameters* that are very useful especially in the scattering problems.

$$\begin{aligned} I &= E_{\parallel}E_{\parallel}^{*} + E_{\perp}E_{\perp}^{*} = A_{\parallel}^{2} + A_{\perp}^{2}, \\ Q &= E_{\parallel}E_{\parallel}^{*} - E_{\perp}E_{\perp}^{*} = A_{\parallel}^{2} - A_{\perp}^{2}, \\ U &= E_{\parallel}E_{\perp}^{*} + E_{\perp}E_{\parallel}^{*} = 2A_{\parallel}^{2}A_{\perp}^{2}\cos\delta, \\ V &= -iE_{\parallel}E_{\perp}^{*} - E_{\perp}E_{\parallel}^{*} = 2A_{\parallel}^{2}A_{\perp}^{2}\sin\delta, \end{aligned} \tag{4.6}$$

where the $\delta = \delta_{\parallel} - \delta_{\perp}$ is the phase difference and * denotes the complex conjugate complex value.

They are real numbers that satisfy the relation

$$I^2 = Q^2 + U^2 + V^2 \tag{4.7}$$

The firs one, I, represents the intensity, which is equal to the energy flow per unit area (Wm^{-2}). The other parameters have the same dimension.

However, the well-defined ellipse of polarization exists only for strictly monochromatic wave for which the time dependence is $\exp(-i\omega t)$. Obviously, it is the theoretical approximation and the time dependence of the actual light is different. A more appropriate description of the real electromagnetic radiation is a quasi-monochromatic beam:

$$E(\mathbf{r}, t) = \mathbf{E_0}(t) \exp(i\mathbf{k} \cdot \mathbf{r} - i\omega t), \qquad \mathbf{E_0}(t) = E_{\parallel}(t)\hat{e}_{\parallel} + E_{\perp}(t)\hat{e}_{\perp} \tag{4.8}$$

i.e., the complex amplitudes $E_{\parallel}$ and $E_{\perp}$ are the functions of time varying slowly over time intervals of the order of the period $2\pi/\omega$. However, for time intervals long compared with the period, the amplitudes fluctuate in some manner either with some correlation or independently of each other. If $E_{\parallel}(t)$ and $E_{\perp}(t)$ are completely uncorrelated, the beam is unpolarized. It is so-called natural light (e.g. solar light). If $E_{\parallel}(t)$ and $E_{\perp}(t)$ are completely of partially correlated, the light is fully or partially polarized respectively.

The Stokes parameters of quasi-monochromatic beam are obtained as

$$\begin{aligned}
I &= \left\langle E_{\parallel}E_{\parallel}^* + E_{\perp}E_{\perp}^* \right\rangle, \\
Q &= \left\langle E_{\parallel}E_{\parallel}^* - E_{\perp}E_{\perp}^* \right\rangle, \\
U &= \left\langle E_{\parallel}E_{\perp}^* + E_{\perp}E_{\parallel}^* \right\rangle, \\
V &= -i\left\langle E_{\parallel}E_{\perp}^* - E_{\perp}E_{\parallel}^* \right\rangle
\end{aligned} \tag{4.9}$$

where $\langle ... \rangle$ denotes time averaging over a time interval much longer than $2\pi/\omega$. And now we have

$$I^2 \geqslant Q^2 + U^2 + V^2 \tag{4.10}$$

The equal sign holds if the light is polarized; $Q = U = V = 0$ for natural or unpolarized light. In all other cases light is partially polarized and can be represented as a combination of natural unpolarized and completely polarized components. In the

Stokes formalism it is

$$\{I, Q, U, V\}^T = \{I_{nat}, 0, 0, 0\}^T + \{I_{pol}, Q, U, V\}^T \tag{4.11}$$

where T denotes transposition. So it leads naturally to the notion of *degree of polarization*:

$$P = I_{pol}/I = \sqrt{Q^2 + U^2 + V^2}/I \tag{4.12}$$

as well as the *degree of linear polarization* (DOLP)

$$DOLP = \sqrt{Q^2 + U^2}/I \tag{4.13}$$

and the *degree of circular polarization* that is defined as V/I. The relationship between Q and U can be described by the polarization angle, χ, which is the angle between the polarization direction and $\mathbf{I}$:

$$\chi = \frac{1}{2}\tan^{-1}\frac{U}{Q} \tag{4.14}$$

Since more than one value of χ satisfies equation 4.14, the convention that is used (Hansen and Travis, 1974) is to select the value in the interval $0 \leqslant \chi \leqslant \pi$ for which $\cos 2\chi$ has the same sign as Q.

It should be mentioned, that solar light scattered in the atmosphere is partial linear polarized whereas the Stokes parameter V is negligibly small. Hence the atmospheric studies usually deal with the DOLP of the measured radiation. In order to characterize the degree of asymmetry in the directional distribution of the electric vector in the figure plane, we can also define the so-called signed degree of linear polarization as

$$P = \frac{I_{\parallel} - I_{\perp}}{I} = \frac{I_{\parallel} - I_{\perp}}{I_{\parallel} + I_{\perp}} \tag{4.15}$$

where $I_{\parallel}$ and $I_{\perp}$ are the intensity components with real electric vector oscillations perpendicular and parallel to the scattering plane, respectively. The scattering plane is defined to include both the vectors pointing in the incident and scattering directions. This definition allows negative values of P if $I_{\perp} < I_{\parallel}$ which means that oscillations of the real electric fields in the scattering plane dominate those in the perpendicular plane and conversely.

Polarization is indeed quite a sensitive function of particle microphysical characteristics and can change not only its absolute value but even the sign with minute variations in particle size and/or refractive index. Therefore an investigation of these parameter are considerably challenging for improving of our knowledge about aerosol structure.

4.2 Inversion of observations

Scattering and absorption of the incoming solar light by the atmospheric aerosol particles modify the observed direct and diffuse radiation. Therefore, the observations of the scattered solar light can be used for aerosol characterization by means of inverting the properties of atmospheric aerosol from the measured radiation field. The inverse algorithm usually includes two complementary modules: "forward model" that is capable to accurately simulate observations if properties of the atmosphere are known, and "numerical inversion" that implements fitting of the observations by "forward models".

The operational inversion algorithm employed by AERONET network was initially developed by Dubovik and King (2000) with some improvements added later and described by Dubovik et al. (2002a); Dubovik (2004); Dubovik et al. (2006, 2011); Sinyuk et al. (2007). The algorithm inverts the direct and diffuse radiation measured by AERONET CIMEL sun/sky-radiometers and derives a large number of the aerosol microphysical and optical parameters characterizing properties of aerosol in the total atmospheric column. The set of the retrieved parameters includes volume particle size distribution, complex refractive index and fraction of spherical particles. Additionally, some optical characteristics are calculated on the basis of the retrieved properties including single scattering albedo, phase function, spectral and broad-band fluxes, etc.

4.2.1 Forward model

Photometric and polarimetric parameters of atmospheric radiation can be modeled by solving the radiative transfer vector equation for a plane-parallel atmosphere. The scattering properties of the atmosphere are described by the extinction optical thickness τ_{ext}, single scattering albedo ω_0 (ratio of the scattering optical thickness τ_{scat} to τ_{ext}) and the scattering matrix $P(\Theta)$. As it was mentioned above (see eq. 2.6), these characteristics include three main components: gaseous absorption ($\omega_0^{gas} = 0$), molecular scattering ($\omega_0^{mol} = 1$), and aerosol scattering and absorption. In the case of ground-base observations molecular scattering can be calculated from the surface pressure at the time of measurements. The strong gaseous absorption can be avoided by instrumental design and the weak one (minor ozone absorption, for example) can be accounted for using known models e.g. (e.g. SA, 1976; ISA, 1975; ICA, 1993; Tomasi et al., 1998) or climatology data as well as using available information from ancillary observations. Thus, the Stokes vector of scattered light I_s depends primarily on the aerosol contribution to the single scattering properties of the atmosphere, i.e.

$$I_s = I(\tau_{ext}^a; \omega_0^a; P^a(\Theta)) \tag{4.16}$$

In turn, these properties are determined by aerosol microphysics: particle size, shape and composition (refractive index).

In the retrieval aerosol is modeled as mixture of spherical and non-spherical particles. Original Dubovik and King (2000) algorithm did not take aerosol particle non-sphericity into account, and used spherical particle approximation. However, the studies by Dubovik et al. (2000, 2002a, 2006) revealed the important effect of non-spherical particles on the retrieval, and demonstrated that a mixture of polydisperse randomly oriented homogeneous spheroids (e.g. Mishchenko et al., 1997) can be used as a reliable model of the non-spherical mineral dust – one of the most common type of non-spherical aerosol. Of course, there is not evident reason to expect non-spherical aerosol particles to be perfect spheroids, and, indeed, microphotographs of natural aerosols show a great variety of shapes, often different from spheroids. However, all existing numerical methods that could provide computations of scattering properties of the particles of more realistic geometrical shapes, such as the discrete dipole approximation (e.g., Draine and Flatau, 1994) and the finite difference time domain technique (e.g., Yang et al., 2000) require excessive computer resources. This is why the spheroid approximation remains appealing from an operational perspective. Moreover, the following considerations can be listed as further motivations for the utilization and exploration of spheroid models (under Dubovik et al., 2006):

- A spheroid is the simplest non-spherical shape that can generalize the spherical shape (a sphere is a particular case of spheroid with an axis ratio $\varepsilon = 1$). Accordingly, conventional spherical models of atmospheric aerosol can be easily generalized in terms of a model of randomly oriented spheroids with only one extra characteristic – the distribution of axis ratios (assuming, as the first-order approximation, that shape is independent of size).

- The scattering of electromagnetic radiation by spheroids can be accurately simulated with the T-matrix method that provides an exact solution for light scattering by randomly oriented spheroids with different sizes, axis ratios, and complex refractive indexes (Mishchenko et al., 1996; Mishchenko and Travis, 1998; Mishchenko et al., 2000).

- The observations of scattering by non-spherical aerosol show a considerable degree of averaging of contributions from individual particles with different orientations, shapes, and compositions. Hence one can expect (Mishchenko et al., 1997) that specific shape details of a single particle may be insignificant after such an averaging and that scattering by an ensemble of particles can be approximated by that of a mixture of simplified particles (such as spheroids).

The utilization of this model has significantly improved the AERONET operational retrieval of aerosol with pronounced coarse mode fraction (Reid et al., 2003; Eck et al., 2005; Dubovik et al., 2006). The same model has been shown to reproduce adequately the ground-based polarimetric observations of non-spherical desert dust (Li et al., 2009).

Figure 4.1 demonstrates the differences in phase function (left side) and degree of linear polarization (right side) calculated from spheroid and spherical models. The evident conclusion is the fact that degree of linear polarization (DOLP) cannot be correctly fitted using spherical model only. The differences in phase function are mainly situated at bigger angles that have important meaning for lidar measurements.

Thus, present AERONET retrieval algorithm (see Dubovik et al., 2006, 2011) describes aerosol as a mixture of two components spherical and non-spherical. Both components have the homogeneous with index of refraction that is the same for particles of all sizes. Also, both components have the same volume size distribution of particle. The

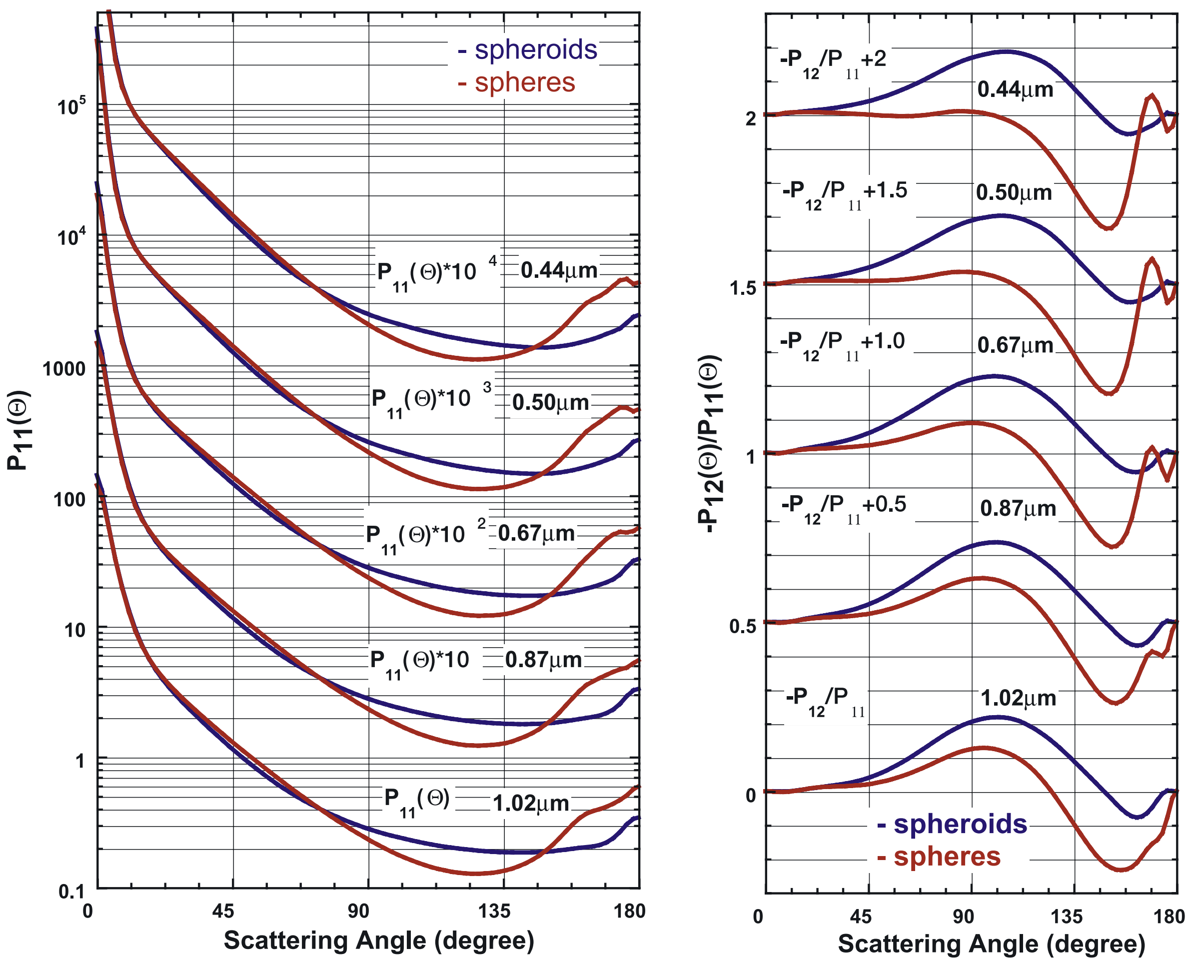

FIGURE 4.1: Comparison of desert dust phase function and degree of linear polarization simulated with spheroids and spherical aerosol model with the same size distribution and complex refractive index, taken from Dubovik et al. (2006).

spherical component is modeled by an ensemble of polydisperse homogeneous spheres whereas the non-spherical component is represented by ensemble of randomly oriented spheroids (ellipsoids of revolution). In contrast with spheres describing by radius only, the shape of spheroids is described by two parameters: radius of the volume-equivalent sphere and the axis ratio $\varepsilon = a/b$, where a is the axis of spheroid rotational symmetry and b is the axis perpendicular to the axis of spheroid rotational symmetry.

According to this model, the non-spherical component have additionally size-independent distribution of shapes and the modeling of the aerosol scattering matrix $P_{ij}(\lambda, \Theta)$ and total aerosol optical thickness of extinction and scattering $\tau_{ext/scat}(\lambda)$ of non-spherical aerosol can be written as the following:

$$\tau_{scat}(\lambda)P_{ii'}(\Theta) = \int\limits_{\ln r_{min}}^{\ln r_{max}} \int\limits_{\ln \varepsilon_{min}}^{\ln \varepsilon_{max}} \frac{C_{ii'}(\lambda,\Theta,n,k,r)}{\nu(r)} \frac{dn(\varepsilon)}{d\ln\varepsilon} \frac{dV(r)}{d\ln r}\, d\ln\varepsilon\, d\ln r \tag{4.17}$$

$$\tau_{ext/scat} = \int\limits_{\ln r_{min}}^{\ln r_{max}} \int\limits_{\ln \varepsilon_{min}}^{\ln \varepsilon_{max}} \frac{C_{ext/scat}(\lambda,n,k,r)}{\nu(r)} \frac{dn(\varepsilon)}{d\ln\varepsilon} \frac{dV(r)}{d\ln r}\, d\ln\varepsilon\, d\ln r \tag{4.18}$$

where $C_{ext}(\lambda, n, k, r)$, $C_{scat}(\lambda, n, k, r)$ and $C_{ii'}(\lambda, \Theta, n, k, r)$ denote, respectively, the cross sections of extinction, scattering and directional scattering corresponding to matrix elements $P_{ii'}(\Theta)$, λ is wavelength, n and k – real and imaginary parts of the refractive index and $\nu(r)$ is the volume of particle with radius r. $dV(r)/d\ln r$ denotes volume size distribution of particles:

$$V(r_1, r_2) = \int\limits_{r_1}^{r_2} \frac{dV(r)}{dr}\, dr = \int\limits_{\ln r_1}^{\ln r_2} \frac{dV(r)}{d\ln r}\, d\ln r \tag{4.19}$$

where $V(r_1, r_2)$ is the total volume of particles with radii between r_1 and r_2.

To reduce a computation time the retrieval algorithm by Dubovik and King (2000) uses precomputed look-up tables (or kernels) of aerosol scattering properties that are defined as follows:

$$K^{\varepsilon}_{...}(\lambda, k, n, r_p, \varepsilon_k) = \int\limits_{\ln r_p - \Delta \ln r}^{\ln r_p + \Delta \ln r} \int\limits_{\ln \varepsilon_k - \Delta \ln \varepsilon}^{\ln \varepsilon_k + \Delta \ln \varepsilon} \frac{C^{\varepsilon}_{...}(\lambda, \kappa, n, r_p, \varepsilon_k)}{v(r)} A_k(\varepsilon)\, B_p(r)\, d\ln\varepsilon d\ln r, \tag{4.20}$$

$A_k(\varepsilon)$ and $B_p(r)$ are the functions providing correspondingly the interpolation of shape and size distributions between the selected points ε_k and r_i. In studies by Dubovik et al. (2002b, 2006), the coefficients $A_k(\varepsilon)$ were assumed as rectangular, and $B_p(r)$ as trapezoidal functions (Dubovik et al., 2000).

The size distribution is retrieved in the range of size $0.05\mu m \leq r \leq 15\mu m$ for 22 logarithmically equidistant bins. It should be note that no assumption of the size distribution shape used, i.e. neither number of aerosol modes nor their shape is prescribed. However, some smoothness constraints are used in order to avoid unrealistic oscillations.

The real $n(\lambda)$ $(1.33 \leq n(\lambda) \leq 1.6)$ and imaginary $k(\lambda)$ $(0.0005 \leq k(\lambda) \leq 0.5)$ parts of the refractive index are retrieved on the wavelengths corresponding to measurements.

The laboratory measurements by Volten et al. (2001) reveal the limited sensitivity to the minor details of axis ratio distribution $dN(\varepsilon_k)/d\ln\varepsilon$. Therefore, it was demonstrated that AERONET retrieval might rely on assumption that shape distribution of the non-spherical fraction of any tropospheric aerosol is the same. Based on this conclusion, $dN(\varepsilon_k)/d\ln\varepsilon$ obtained by Dubovik et al. (2006) from fitting Volten et al. (2001) measurements was employed as shape distribution for non-spherical fraction:

$$\frac{dN(\varepsilon_k)}{d\ln\varepsilon} = \begin{cases} 0, & 0.7 < \varepsilon < 1.44 \\ const, & \varepsilon \leq 0.7;\ \varepsilon \geq 1.44 \end{cases} \tag{4.21}$$

Hence, the integration over ε in Eq. 4.20 can be done once and for all and, modeling of aerosol optical properties $\tau_a(\lambda)$, ω_0^a, $P_{ij}^a(\lambda,\Theta)$ is implemented in the retrieval in a following form:

$$\begin{gathered}\tau_{scat}(\lambda)\, P_{ij}(\lambda,\Theta) = \\ \sum_{p=1,\ldots,N_r} \Big(C_{sph} K_{ij}^{sph}(\lambda,\kappa,n,r_p) + (1-C_{sph})\, K_{ij}^{nons}(\lambda,\kappa,n,r_p) \Big),\end{gathered} \tag{4.22}$$

and

$$\begin{gathered}\tau_{ext/scat}(\lambda) = \tau_{ext/scat}^{sph}(\lambda) + \tau_{ext/scat}^{nons}(\lambda) = \\ \sum_{p=1,\ldots,N_r} \Big(C_{sph} K_{ext/scat}^{sph}(\lambda,\kappa,n,r_p) + (1-C_{sph})\, K_{ext/scat}^{nons}(\lambda,\kappa,n,r_p) \Big),\end{gathered} \tag{4.23}$$

where

$$K_{\ldots}^{sph}(\lambda,n,\kappa,r_p) = \int\limits_{\ln r_p - \Delta\ln r}^{\ln r_p - \Delta\ln r} \frac{C_{\ldots}^{sph}(\lambda,\kappa,n,r)}{v(r)} B_k(r)\, d\ln r, \tag{4.24}$$

and

$$K_{\ldots}^{nons}(\lambda,n,\kappa,r_p) = \int\limits_{\ln r_p - \Delta\ln r}^{\ln r_p - \Delta\ln r} B_p(r) \int \frac{C_{\ldots}^{sph}(\lambda,\kappa,n,r)}{v(r)} \frac{dN(\varepsilon)}{d\ln\varepsilon}\, d\ln\varepsilon\, d\ln r. \tag{4.25}$$

where C_{sph} is the fraction of the spherical particles included in the set of retrieved parameters.

As a result, all parameters determining the scattering radiation field is expressed through retrieved aerosol properties.

In the original AERONET inversion algorithm by Dubovik and King (2000) the solution of the radiative transfer equation in scalar approximation was implemented using Discrete-Ordinate approach by Nakajima et al. (1983). Later, the possibility of using vector solution of radiative transfer equation was also included (see Dubovik et al. (2006, 2011); Li et al. (2009)) by employing Successive Order of Scattering radiative transfer code (Lenoble et al. (2007)). Correspondingly this modification allowed for inversion of not only intensity observations and also polarimetric.

The vertical distribution of aerosol is assumed homogeneous in inversion of radiation intensity in the almucantar and bi-layered in inversion of principle plane. If vector radiative transfer code is use, the 50-layer approximation of atmosphere is used.

4.2.2 Numerical inversion

The inversion is implemented as statistically optimized fitting accounting for different levels of accuracy in the data. Theoretically, the best fit of the measurements gives the correct solution of the problem. However, often several different combinations of aerosol parameters produce nearly the same radiation distribution that leads to non-unique or highly unstable solution in presence of even minor noise in the measurements (Dubovik, 2004).

The inversion algorithm by Dubovik and King (2000) suggests to utilize additional a priori assumptions on smoothness of the retrieved parameters in order to constrain and stabilize the solution. Specifically, smoothness constraints are applied on several retrieved characteristics: on size distribution variability with size and on spectral variability of both real and imaginary parts of the refractive index. The smoothness of the retrieved characteristics is enforced by limitations on the derivatives of correspondent retrieved functions. The a priori constraints are inverted together with the real measurements.

Formally, the retrieval algorithm (Dubovik and King, 2000; Dubovik, 2004; Dubovik et al., 2008) is designed as a multi-term least-square method (LSM) providing a numerical solution of the following system of equations:

$$\begin{cases} \mathbf{f}^* = \mathbf{f}(\mathbf{a}) + \Delta\mathbf{f} \\ \mathbf{0}^* = (\Delta\mathbf{a})^* = \mathbf{S}\mathbf{a} + \Delta(\Delta\mathbf{a}) \\ \mathbf{a}^* = \mathbf{a} + \Delta\mathbf{a}^* \end{cases} \tag{4.26}$$

Here $\mathbf{f}^*$ is a vector of combined measurements, $\Delta\mathbf{f}$ is a vector of measurement uncertainties, $\mathbf{a}$ is a vector of unknowns. The second line of this equation system represents the a priori smoothness constraints on retrieved characteristics that are applied for eliminating the unrealistic solutions. The matrix $\mathbf{S}$ is composed of coefficients for calculating m-th differences (numerical equivalent of the derivatives) of retrieved parameters. $\mathbf{0}^*$ is a zero vector allowing to eliminate the strongly oscillating solutions with high derivatives. $\Delta(\Delta\mathbf{a})$ is the vector of the uncertainties characterizing the deviations of the differences from the zeros. The third line in eq. 4.26 consists of the vector of a priori estimates a^* and the vector of the uncertainties in a priori estimates $\Delta\mathbf{a}^*$. Table 4.1 contains the definitions of each element of the vectors $\mathbf{f}^*$ and $\mathbf{a}$. In addition, Table 4.1 shows the variability ranges allowed for each retrieved parameter.

TABLE 4.1: Description of the elements of the measurement vector $\mathbf{f}^*$ and the vector of unknowns ($\mathbf{a}$)

$\mathbf{f}^*$ – vector of measurements		
$\{f^*_\tau\}_i = \ln(\tau(\lambda_i))$, where $\tau(\lambda_i)$ is a total optical thickness obtained from AERONET observations		
$\{f^*_I\}_i = \ln(I(\Theta_j;\lambda_i))$, where $I(\Theta_j;\lambda_i)$ is total radiance observed by photometer		
$\{f^*_P\}_i = \ln(P(\Theta_j;\lambda_i))$, where $P(\Theta_j;\lambda_i) = \frac{\sqrt{Q^2(\Theta_j;\lambda_i)+U^2(\Theta_j;\lambda_i)}}{I(\Theta_j;\lambda_i)}$ is degree of linear polarization		
$\mathbf{a}$ – vector of unknowns		
Notation	Definition	Variability limits
a_V	$\{a_V\}_i = \ln\left(\frac{dV(r_i)}{d\ln r}\right), i = 1, ..., N_r$	$0.000005 \le \frac{dV(r_i)}{d\ln r} \le 0.03$
a_n	$\{a_n\}_i = \ln(n(\lambda_i)), i = 1, ..., N_\lambda$	$1.33 \le n(\lambda_i) \le 1.6$
a_k	$\{a_k\}_i = \ln(k(\lambda_i)), i = 1, ..., N_\lambda$	$0.0005 \le k(\lambda_i) \le 0.1$
a_{sph}	$a_{sph} = \ln(C_{sph})$	$0.001 \le C_{sph} \le 1.0$

The retrieval methodology uses the assumption of log-normal error distribution. Indeed, the normal or Gaussian distribution is the most appropriate function for describing random noise. The log-normal noise distribution implies that the logarithms of the observed positively defined values are normally distributed. So the inversion procedure uses the logarithmic transformation for both measured $\mathbf{f}$ and retrieved $\mathbf{a}$ parameters. Correspondingly, the uncertainties $\Delta\mathbf{f}$, $\Delta\mathbf{a}*$, $\Delta(\Delta\mathbf{a})$ are assumed normally distributed.

Since the properties of the observation noise is known, the statistically optimum solution of the equation system (4.26) can be found by fitting the expected error distribution. To evaluate the fit accuracy the probability density function (PDF) is used as a function of modeled errors.

The principle of multi-term least-square method (LSM) is based on the fact that the errors characterizing the different sets of the inverted data are statistically independent. Correspondingly, the joined PDF of all fitted data is a product of the PDF of all independent vectors of inverted data:

$$P(f_1(a), \dots, f_k(a) | f_1^*, \dots, f_k^*) = \prod_k P(f_k(a) | f_k^*) \tag{4.27}$$

Correspondingly, according to the well-known method of maximum likelihood (MML), the best estimation of the unknowns corresponds to the maximum of the above likelihood function. Thus, assuming that PDFs of each vectors described by Gaussian distribution function, the maximum of joint PDF corresponds to the minimum of least squares that is provided by the solution of multi-term LSM equation:

$$\begin{gathered}\Psi\left(\mathbf{a}^p\right) = \Psi_f\left(\mathbf{a}^p\right) + \Psi_\Delta\left(\mathbf{a}^p\right) + \Psi_a\left(\mathbf{a}^p\right) = \\ \tfrac{1}{2}\left(\left(\Delta\mathbf{f}^p\right)^T \mathbf{W}_f^{-1} \Delta\mathbf{f}^p + \gamma_\Delta (\mathbf{a}^p)^T \boldsymbol{\Omega} \mathbf{a}^p + \gamma_a (\mathbf{a}^p - \mathbf{a}^*)^T \mathbf{W}_a^{-1}\left(\mathbf{a}^p - \mathbf{a}^*\right)\right).\end{gathered} \tag{4.28}$$

The minimum could be obtained by iterative procedure:

$$\mathbf{a}^{p+1} = \mathbf{a}^p - t_p \Delta\mathbf{a}^p, \tag{4.29}$$

where $\mathbf{a}^p$ is the p-th solution of so called normal system:

$$\mathbf{A}_p \Delta \mathbf{a}^p = \nabla \Psi \left(\mathbf{a}^p \right), \tag{4.30}$$

where $\mathbf{A}_p$ is the Fisher Matrix and the right side represents the gradient $\nabla \Psi \left(\mathbf{a}^p \right)$:

$$\nabla \Psi \left(\mathbf{a}^p \right) = \mathbf{K}_p^T \mathbf{W}_f^{-1} \Delta \mathbf{f}^p + \gamma_\Delta \mathbf{\Omega} \mathbf{a}^p + \gamma_a \mathbf{W}_a^{-1} \left(\mathbf{a}^p - \mathbf{a}^* \right), \tag{4.31}$$

$$\mathbf{A}_p = \mathbf{K}_p^T \mathbf{W}_f^{-1} \mathbf{K_p} + \gamma_\Delta \mathbf{\Omega} + \gamma_a \mathbf{W}_a^{-1}, \tag{4.32}$$

where $\Delta \mathbf{f}^p = f\left(\mathbf{a}^p \right) - \mathbf{f}^*$ and $\mathbf{K}_p$ is the Jacobi matrix of the first derivatives $\frac{\partial f(\mathbf{a}^p)}{\partial a_i}$.

It should be noted that Fisher Matrix $\mathbf{A}_p$ can be considered as so-called Hessian matrix of second-order partial derivatives of the quadratic form $\Psi \left(\mathbf{a}^p \right)$ (see for e.g. Bevington, 1969; Tarantola, 2005). Correspondingly, Eq. 4.30 can be also written as follows:

$$\left(\nabla \nabla \Psi \left(\mathbf{a}^p \right) \right) \Delta \mathbf{a}^p = \nabla \Psi \left(\mathbf{a}^p \right), \tag{4.33}$$

where $\nabla \nabla^T \Psi \left(\mathbf{a}^p \right)$ is the matrix with the elements $\left\{ \nabla \nabla^T \Psi \left(\mathbf{a}^p \right) \right\}_{ji} = \left. \frac{\partial^2 \Psi(\mathbf{a})}{\partial a_j \partial a_i} \right|_{\mathbf{a}=\mathbf{a}^p}$.

$\mathbf{W}$ are the weighting matrices, defined by Dubovik et al. (2000) as follows:

$$\mathbf{W}_{\dots} = \frac{\mathbf{C}_{\dots}}{\varepsilon_{\dots}}, \tag{4.34}$$

where $\varepsilon_{\dots}^2 = \{ \mathbf{C}_{\dots} \}_{11}$ are the first diagonal elements of the corresponding covariance matrices $\mathbf{C}_{\dots}$ and $\gamma_{\dots}$ are Lagrange multipliers, defined by Dubovik (2004):

$$\gamma_\Delta = \frac{N_f \varepsilon_f^2}{N_\Delta \varepsilon_\Delta^2} \quad and \quad \gamma_a = \frac{N_f \varepsilon_f^2}{N_a \varepsilon_a^2} \tag{4.35}$$

where $N_{\dots}$ are the sizes of corresponding vectors. The Lagrange multiplier determines the contribution of appropriate "a priori" component in the retrieval solution.

Equation 4.35 is written under an assumption that increasing the number of measurements in the coordinated set of remote sensing observations inevitably will decrease the accuracy of each single measurement in this observation set. For example, if a sun-photometer takes one single observation, the expected variance of measurement error is

$\varepsilon^2_{f,N}$. If the same sensor makes N_f space- and/or time-coordinated observations the variance of the error in each single observation increases by the factor N_f, i.e. $\varepsilon^2_{f,N} \sim N_f \varepsilon^2_{f,1}$. This increase can be explained by the fact that the consistency of the N_f coordinated observations should be assured by controlling relations between the N_f observations. The control of each of those relationships introduces a random error $\varepsilon^2_{f,N}$, correspondingly the error variance of a single measurement in dimensional observation increases in N_f times.

The coefficient t_p in Eq. 4.29 is adjusted to provide the monotonic decrease of $\Psi\left(\mathbf{a}^p\right)$, i.e.

$$\Psi\left(\mathbf{a}^{p+1}\right) < \Psi\left(\mathbf{a}^p\right). \tag{4.36}$$

If all assumptions are correct, the minimum value of the above quadratic form can be theoretically estimated as follows:

$$\Psi\left(\mathbf{a}\right) \approx \left(N_f + N_\Delta + N_{a^*} - N_a\right)\varepsilon^2_f. \tag{4.37}$$

So, if the measurement error ε^2_f is known, the equation 4.37 can be used to verify the inversion consistency. Namely, if iteration procedure cannot achieve the expected minimum it can indicate the presence of unidentified biases or inadequacy in the assumptions made.

It should be noted that the control of "measurement residual" $\Psi_f\left(\mathbf{a}^p\right)$ (the first term of quadratic form in Eq. 4.28) is a very useful tool for diagnostics of the retrieval dynamics. Specifically, the final value of $\Psi_f\left(\mathbf{a}^p\right)$ should be close to the level of the expected measurement noise. Indeed, if the algorithm has found the right solution, the value of the total residual $\Psi\left(\mathbf{a}^p\right)$ should be rather small and determined mainly by the random errors of observations. The contributions of the a priori residual terms in Eq. 4.28 should not be significant, because generally the weights of a priori terms $\Psi_\Delta\left(\mathbf{a}^p\right)$ and $\Psi_a\left(\mathbf{a}^p\right)$ are minor compared to the weight of the "measurement residual" term $\Psi_f\left(\mathbf{a}^p\right)$.

It should be noted that the multi-term LSM concept allows application of several a priori constraints at the same time. Indeed, AERONET algorithm uses simultaneously the smoothness constraints on variability of particle size distribution and spectral dependencies of real and imaginary parts of the refractive index. Similarly, the recent AERONET like multi-term LSM algorithm developed by Dubovik et al. (2011, 2014) for inverting PARASOL/GRASP satellite observations applies even larger number of a priori constraints. Over land, the PARASOL/GRASP retrieves simultaneously properties of aerosol and surface. Correspondingly, the a priori constraints are applied on the retrieved parameters of both aerosol and surface. Moreover, PARASOL/GRASP uses new multi-pixel retrieval approach where the retrieval is conducted for a several observations over different pixels, and some constraints on inter-pixel variability of the retrieved properties are applied additionally. The application of multiple a priori constraint is very straightforward in the frame of the multi-term LSM, while is not naturally assumed in the majority of known widely used inversion approaches suggested by textbooks (e.g., Tarantola, 2005; Rodgers, 2000; Twomey, 1977a, etc.).

Chapter 5

Development of automated DWP Cimel data processing

5.1 Introduction

The Dubovik and King (2000) inversion code is employed for operational processing of AERONET observations. The processing includes a preliminary stage of the data preparation where the observations are verified, translated in standard format and complemented some ancillary information as required for inversion code applying. Then the observations are massively processed and the retrieval products are stored into AERONET database and displayed on the website. This procedure is very well established for standard intensity observations. However, utilization of the polarimetric data obtained by dual-polar Cimel radiometers is not yet fully operationalized because the data preparation stage is not yet fully established. Therefore, as part of the current study we have developed the data preparation routine to implement semi-operational processing of the polarization observations.

The software allowing automatized preparation of the dual-polar Cimel radiometer observations for inversion has been developed. The program creates the input files for both almucantar and solar principle plane (spp) viewing configurations with and without polarimetric data applying. The organigram in figure 5.1 shows data flow of this program. The main parts of the data preparation procedure are represented on the organigram and discussed in details in following sections.

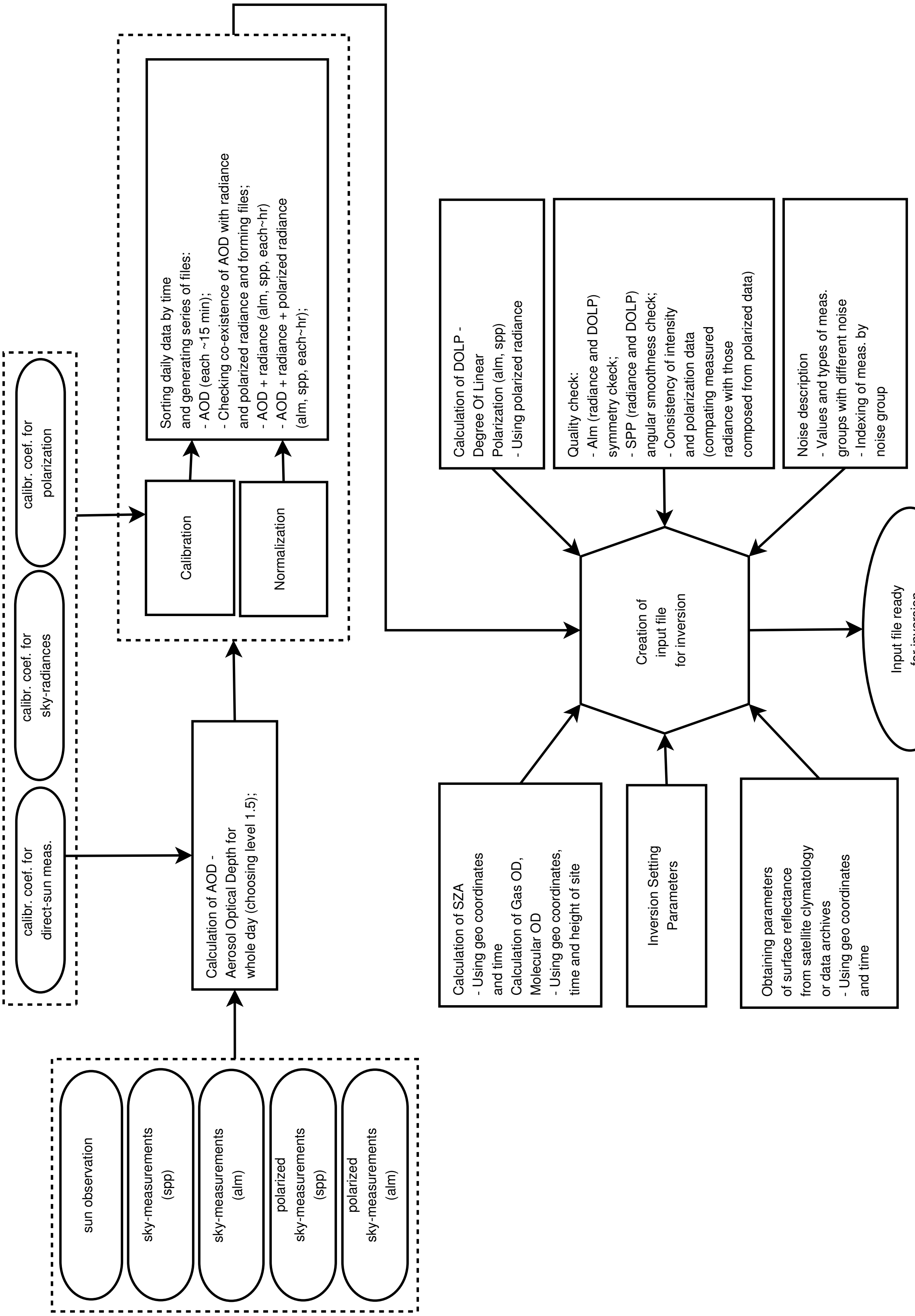

Figure 5.1: Organigram of the program to create the input file for inversion

5.2 Raw data pre-processing and DOLP calculation

According to AERONET measurement protocol the measurements are performed for the airmasses less than 7, i.e. they starts at an air mass of 7 in the morning and ends at an air mass of 7 in the evening. Direct Sun measurements are conducted every 15 minutes and the angular measurements of diffuse radiance intensity and polarization are acquired every hour in both almucantar and principal plane configurations when the solar zenith angle is less than 60°.

The results of Sun radiation measurements are values of signal obtained from sun-photometer detectors. These values are separated by days, detector type, filters, polarizers etc. and stored into database (in this study we used PHOTONS database, at LOA, University Lille-1). As a result we have daily sorted raw data files separated by the type of observations. These files include the following data: the direct Sun measurements, the measurements of intensity or polarization of diffuse sky radiance registered for solar principal plane or almucantar configurations. The raw data must be calibrated to obtain physically reasonable values. Usually the calibration of sun-photometers is performed regularly for all instruments and the calibration coefficients are also stored into the PHOTONS database. The program finds required file in the database (accordingly to the number of the instrument), extracts corresponding calibration coefficients by comparison of observation and calibration dates and applies them to the raw data (see section 5.2.1). To use these calibrated data in inversion process several other procedures must be applied: sorting daily data by time and generating series of files, normalization to the value of solar irradiance, calculation of the aerosol and total optical depth from direct Sun measurements and sorting diffuse sky and polarization data in groups corresponding to different observation periods. The calculation of the solar zenith angle is made once for each observation series (for each wavelength). Zenith and azimuth angles are calculated each time for every single measurement.

There are three data levels used in AERONET. The level 1.0 means unscreened data, i.e. the measurements were obtained during imperfect conditions or cloud screening procedure cannot be applied. The data of level 1.5 are cloud screened and can be used in inversion process. The level 2 means manually checked data. The calibrated data are separated on two levels: 1.0 and 1.5. The developed program uses the data of level 1.5 only.

Once the raw observations are pre-processed, they are included in the input file inverted by the Dubovik and King (2000) retrieval algorithm. In addition to observations, the input files include inversion settings, various ancillary and a priori information about observations and inversion procedure.

5.2.1 Calibration

5.2.1.1 Calibration of direct-Sun measurements

The purpose of the calibration of the direct-Sun measurements is to determine $DN_0(\lambda)$ coefficient in Eq. 3.1 for each spectral channel.

Two methods of Sun-photometer calibration are used within AERONET system as routine procedures (Holben et al., 1998): Bouguer-Langley or, simply, Langley method (Shaw et al., 1973) and intercalibration with master instrument (Lenoble et al., 2011).

The first one consists in measuring of the solar irradiance for a large range of the solar zenith angles. Following a linear dependence of $\ln DN(\lambda)$ versus airmass m (eq. 5.1), $DN_0(\lambda)$ can be derived by extrapolation of the line obtained to $m = 0$.

$$\ln(DN(\lambda)) = \ln(DN_0(\lambda)) - \tau(\lambda)m \tag{5.1}$$

Usually measurements are made during the day for the airmass range between 5 and 2. To eliminate time-changing drifts in atmospheric properties the procedure is performed on high-altitude mountain observatories known to present excellent optical conditions (Manua Loa, Hawaii, USA; Izaña, Tenerife, Spain).

The intercalibration technique based on comparison of the co-located measurements of the instrument undergoing calibration and well calibrated one (master instrument). Required spectral calibration coefficients $DN_0^{field}(\lambda)$ can be found as

$$DN_0^{field}(\lambda) = DN_0^{master}(\lambda)\frac{DN^{field}}{DN^{master}} \tag{5.2}$$

Calibration of the master instrument is performed by Langley method with an accuracy about 0.5%, whereas intercalibration of the field instruments gives 1-2% of uncertainty. A 1% error in calibration coefficient leads to inaccuracy $\Delta AOD \approx 0.01$ at $m = 1$ with the error decreasing by a factor of $1/m$ as airmass increases. Thus, the facts described above yield an AOD error about $0.002 < \Delta AOD < 0.009$ for the master instrument and about $0.01 < \Delta AOD < 0.02$ for the field instrument (Eck et al., 1999).

5.2.1.2 Calibration of sky-radiance measurements

A laboratory calibration procedure is used to determine the calibration coefficients needed to convert sky measurements from digital counts to units of radiance ($\mu W/cm^2/sr/nm$).

The sky radiance measurements are performed by sun-photometer with two different gains depending on the angular distance from the Sun. The area with the angular distance less than 6° is called "Aureole" and more than 6° is so called "Dark sky". Due to more intensive radiance in the aureole region, low gain is used there (close to the Sun). So aureole and sky channels have independent calibration coefficients. Therefore at 6° the observations are made twice with both gains to fulfill consistency check of the angular data (see section 5.5).

The sky radiance calibration is made with calibrated spectral radiance source (integrating sphere). In the calibration procedure, the photometer is placed against the sphere port and measures the radiance by aureole and sky channels both. The calibration coefficients can be calculated as the ratio between the radiance of the integrating sphere at each wavelength and the corresponding photometer raw signal:

$$A(\lambda) = \frac{L(\lambda)}{DN(\lambda)} \tag{5.3}$$

where $L(\lambda)$ is the radiance of the calibration source on the λ wavelength band and $DN(\lambda)$ is the measured response for that wavelength band.

The accuracy of calibration coefficients is mainly driven by the accuracy of integrating sphere that is $\pm 5\%$. So it can be no better than $\sim 5\%$.

5.2.1.3 Calibration of polarization measurements

Generally, polarization calibration is more complex than radiance calibration but, in principal, it is conducted by the same way. The integrating sphere is used as uniform radiance source to determine a transmittance of each polarizer. In order to evaluate and quantify the DOLP degradation due to decline of polarizers, POLBOX device is applied. POLBOX system is a stack of parallel glasses with known refractive index that cab be rotated. It produces a linearly polarized light with tunable DOLP from 0 to 0.57 with an accuracy of ~ 0.0015. POLBOX can also be rotated around its horizontal axis to change the direction of polarization. This capability is used to check an individual efficiency of each polarizer. Initially, the system was designed in LOA for calibration of POLDER.

The calibration of polarization channels consists in comparison of reference polarized light with measured one. The DOLP of measured radiation is determined as

$$DOLP^{CIMEL} = \frac{2\sqrt{P_1^2 + T_{12}P_2^2 + T_{13}P_3^2 - T_{12}P_1P_2 - T_{13}P_1P_3 - T_{12}T_{13}P_2P_3}}{P_1 + T_{12}P_2 + T_{13}P_3} \tag{5.4}$$

where P_k $(k = 1, 2, 3)$ are the raw signal of 3 polarized channel placed on 60° to each other, $T_{12} = P_1/P_2$ and $T_{13} = P_1/P_3$. T_{12} and T_{13} are normalization coefficients to compensate the inter-filter transmission difference, because for a natural light each polarized channel should measure the same signal and DOLP equals 0.

On the other hand, the DOLP of radiation produced by POLBOX can be calculated from the equation:

$$DOLP^{POLBOX} = \frac{A\cos^2(2\alpha) + B\cos(2\alpha) + C}{D\cos^2(2\alpha) + E\cos(2\alpha) + F} = \eta DOLP^{CIMEL} \tag{5.5}$$

where $A, B, \dots F$ are polynomial expression of the refractive index n of the optical plates averaged over the filter bandwidth, α is the angle between the optical planes, and η is required DOLP calibration coefficient.

Full calibration of DOLP can be performed in two steps: (a) calibration of R_{12} and R_{13} in order to correct the difference between the intensity responses of three polarization units and (b) correction of the possible systematic bias in $DOLP^{CIMEL}$ associated with polarizing efficiency.

Laboratory T_{12} and T_{13} tuning is traditionally performed by using an integrating sphere as a non-polarized light source to characterize the transmittance difference between different polarizers. Calibration coefficient η can be derived as a degradation coefficient of the linear dependence $DOLP^{CIMEL}$ versus $DOLP^{POLBOX}$.

In practice, transmittance coefficients are combining with η to produce a single coefficient for each polarizer. That is, finally we have three calibration coefficient each one for appropriate polarized unit. The application of the coefficient to the measured digital number directly provides polarized radiance.

The maximum uncertainty of DOLP measurements is estimated to be less than 0.0085 (i.e. 0.0015 of the POLBOX, 0.004 remaining errors after applying the η coefficient, and an extra 0.003 as a maximum estimation for the possible low signal biases in the field).

It should be mentioned that reference partly polarized radiance with certain DOLP can be obtained as reflected solar light. As well as nonpolarized light is direct solar beam. This is so-called "vicarious calibration method" presented by Li et al. (2010). The method have a number of significant advantageous comparing with standard calibration procedure. First of all, it is expected to facilitate polarization calibration instead of using complex and expensive laboratory devices. Second, the DOLP of reflected light can be changed in wide range from 0 to 1 whereas maximum of DOLP produced by POLBOX is 0.57. Indeed, the light reflected at the Brewster's angle is perfectly polarized. This feature is important since the accuracy of η determination reveals the exponential dependence on DOLP value (Li et al., 2010). Namely, $\Delta\eta$ decreases with DOLP increasing and increases fast for $DOLP < 0.2$ and $DOLP \to 0$. Therefore, as reported by Li et al. (2010), the accuracy of DOLP measurements can be improved from 0.0085 to ~ 0.005 by vicarious method employing. Unfortunately, we did not utilize this technique in current study since it is not integrated in the data processing system. But we plan to use it in future work.

5.2.2 Normalization and sorting daily data

Calibration procedures provide sky radiance, I ($\mu W/cm^2/sr/nm$), whereas inversion code requires dimensionless values that is a normalized radiance, i.e. $L = \pi I/E_0$, where E_0 is the spectral solar irradiance which depends on wavelength (see table 5.1).

Table 5.1: The values of solar irradiance (E_0) used to normalize sky-radiance measurements

$\lambda(nm)$	$E_0(\mu W/cm^2/sr/nm)$
340	100.68
380	117.59
440	186.87
500	196.18
670	149.42
870	95.56
1020	69.87
1640	22.83

In addition, the time variation of $E_0(\lambda)$ due to variation of Sun-Earth distance is taken into account by using the equation:

$$L(\lambda) = \frac{\pi I(\lambda)}{E_0 f_{es}}, \quad f_{es} = 1 + 0.033cos(2\pi * J_{julien}/365) \tag{5.6}$$

where J_{julien} is an absolute number of the day of the year. The procedure of radiance normalization is included in the data preparation program.

Usually, during a day, the Sun-photometer makes several sets of measurements and all of them are stored in the same appropriate file. One of the major assumptions of the AERONET retrieval is homogeneity of aerosol in time and space for one set of observation. In other words, it is assumed the same aerosol was observed in all measurements included into the input file containing the data of single observation in full set of angles and wavelength ranges. Obviously, it is assumed that AOD, radiance and polarized data must be measured in short period of time, the direct Sun, diffuse sky and polarization measurements are not affected by variations of aerosol. The program sorts the daily data of direct-Sun, sky and polarization observations by time and generates series of files corresponding the single set of measurements for all wavelengths and angle range. Then it checks a co-existence of AOD, sky and polarized radiance data (if polarimetric data are used) and forms the input file for these measurements.

5.2.3 DOLP calculation

Following Malus' law, when a partially polarized beam of light passes through a linear polarizer, the measured value (e.g. the radiance of the light that passes through) is

$$L_p = \frac{1}{2} I^{in}_{nat} + I^{in}_{pol} cos^2(\theta) \tag{5.7}$$

where I^{in}_{nat} is a natural incoming light; I^{in}_{pol} is a polarized incoming light; θ is the angle between the plane of polarization of the input light and the axis of the polarizer.

As it already was mentioned in the sections 3.2.3 and 5.2.1.3, the DWP-photometer performs the polarization observations by placing three polarizers under 60° between each other sequentially in the light path. After calibration of the measured signals, the degree of the linear polarization is calculated directly as

$$DOLP = \frac{2\sqrt{L^2_{p1} + L^2_{p2} + L^2_{p3} - L_{p1}L_{p2} - L_{p1}L_{p3} - L_{p2}L_{p3}}}{L_{p1} + L_{p2} + L_{p3}} \tag{5.8}$$

where L_{pi} ($i = 1 \div 3$) are the radiances of three polarized units which refer to a combination of the polarizer and filter. Hence, we calculate the angular and spectral distribution of DOLP used in retrieval.

Furthermore, the total sky radiance can be recalculated from polarized radiance as

$$I_{rec} = \frac{L_{p1} + L_{p2} + L_{p3}}{3} \tag{5.9}$$

where I_{rec} is the total radiance recalculated from polarimetric measurements. This option is important in the data quality control procedure (see section 5.5).

5.3 Observational geometry settings

The inversion code requires zenith and azimuth angles of each direct-Sun and angular measurement of diffuse radiance intensity and polarization. Additionally it needs the scattering angles of angular measurements of intensity and polarization of sky radiance in almucantar configuration. As it was mentioned previously (see sections 3.2.1-3.2.3), once the data are pre-processed, we have date and time of each direct-Sun measurement as well as time of each series of sky or polarization measurements for full angle range and for each wavelength. We know also scattering angles of sky-radiance observations in solar principal plane, azimuth angles of sky and polarization observation in almucantar and zenith angles of polarization observations in principal plane (see tables 3.1, 3.2).

Thus in order to create an input file for retrieval code the next values need to be calculated:

- solar zenith angles of each direct-Sun measurement
- azimuth angles of angular measurements in solar principal plane
- zenith angles of sky-radiance measurements in solar principal plane
- scattering angles of sky-radiance and polarization measurements in almucantar

Actually, all these calculations require preliminary determination of the solar zenith angle corresponded to the actual measurements. Its quantity is computed using available date, time and geographical coordinates of the observation site.

Then, the zenith angles of sky measurements in solar principal plane is determined as $\theta_j = \varphi_j - \theta_s$, where φ_j is the scattering angle (tab. 3.1) and θ_s is solar zenith angle. In this case, as well as in the case of polarization observations in principal plane (i.e. for zenith angles from the table 3.2), azimuth angle of the measurements equals 0° if θ_j is negative (towards the Sun), and 180° if θ_j is positive (against the Sun). Obviously, zenith angle of the angular measurements in almucantar equals Sun zenith angle. At last, scattering angles of angular observations in almucantar geometry is determined as (Nakajima et al., 1996)

$$cos(\varphi_j) = cos^2(\theta_s) + sin^2(\theta_s)cos(\phi_j) \tag{5.10}$$

where φ_j is the scattering angle in almucantar and ϕ_j is the azimuth of the observation angle (tables 3.1-3.2 for almucantar).

The method is realized using dynamic 3-dimensional arrays that allows for using one function to calculate all required angles in different configurations (almucantar and principal plane) instead of using different functions for different geometries. This solution simplifies the program structure and allows to easily adapts the function to process the data of the other complex geometries that can bring improvements into remote aerosol observations.

5.4 Setting assumptions for surface reflectance

An accurate accounting of the Earth surface reflection is an important part of the aerosol properties retrieval from the measurements of downward radiation. Although less affected than upward radiances (studied by space-born instruments) by surface reflectivity, surface reflection properties must be as correctly as possible accounted for when sun-photometer sky-radiance and polarization are interpreted.

The radiative transfer model used in the retrieval accounts for intrinsic reflectance properties of the surface using the bidirectional reflectance distribution function (BRDF). BRDF is defined as a ratio of the radiance reflected by infinitesimal surface area to the infinitesimal solid angle to the irradiance illuminating that surface within an infinitesimal solid angle, i.e.

$$BRDF(\theta_s, \theta_v, \phi_0, \phi_v, \lambda) = \frac{dL(\theta_s, \theta_v, \phi_0, \phi_v, \lambda)}{dE_0(\theta_s, \phi_0, \lambda)} \tag{5.11}$$

where θ_s and θ_v are solar and viewing zenith angles, respectively; ϕ_0 and ϕ_v are solar and viewing azimuth angles, respectively; λ is wavelength of the incoming and reflected radiation; L is observed reflected radiance and E_0 is incoming irradiance.

Integrating BRDF over zenith and azimuth angles, the bihemispherical reflectance (BHR) also called integral surface albedo is defined:

$$BHR(\lambda) = \int_0^{\pi/2}\int_0^{2\pi}\int_0^{\pi/2}\int_0^{2\pi} BRDF(\theta_s, \theta_v, \phi_0, \phi_v, \lambda)\cos(\theta_v)\sin(\theta_v)\cos(\theta_s)\sin(\theta_s)d\theta_v d\phi_v d\theta_s d\phi_0 \tag{5.12}$$

Surface BRDF is a theoretical function that cannot be derived directly from the observations. Estimation of the appropriate BRDF values relies on the surface reflectance model producing the BRDF quantity according with satellite measurements. In this study we use kernel-driven Ross-Li model (Ross, 1981; Li and Strahler, 1992; Wanner et al., 1995). Generally, the kernel-driven models are defined as a linear combination of kernels represented the reflectance behavior of a particular surface type multiplied to weighting coefficients. In the case of Ross-Li model it is

$$BRDF(\theta_s, \theta_v, \phi, \lambda) = f_{iso}(\lambda) + f_{vol}(\lambda)K_{vol}(\theta_s, \theta_v, \phi) + f_{geo}(\lambda)K_{geo}(\theta_s, \theta_v, \phi) \tag{5.13}$$

where K_{vol} and K_{geo} are the volumetric and geometric scattering kernels, respectively, f_{iso}, f_{vol} and f_{geo} are the isotropic, volumetric and geometric scattering parameters. ϕ is a difference of azimuth angles ($\phi = \phi_v - \phi_0$).

The original algorithm by Dubovik and King (2000) used only the integral albedo in Lambertian approximation (angular independent ground reflectance) in order to account for the surface reflection in sun-photometers data inversion. The values of the surface albedo were fixed constant for most of observational sites. However, later it was shown by Sinyuk et al. (2007), though the effect of surface reflection of transmitted radiation measured on the ground is not very strong, the accurate accounting for both surface reflectance time and angular variability can be important for the achieving accurate aerosol retrieval. Therefore, in present operational AERONET data processing, the variability of surface reflectance is assumed using MODIS observations. The examples of time variability of the surface albedo for Lille, Dakar, Beijing and GSFC are shown in the figure 5.2. Elevation of the albedo for Lille, GSFC and Beijign sites on $841 - 876nm$ is produced by vegetation canopy.

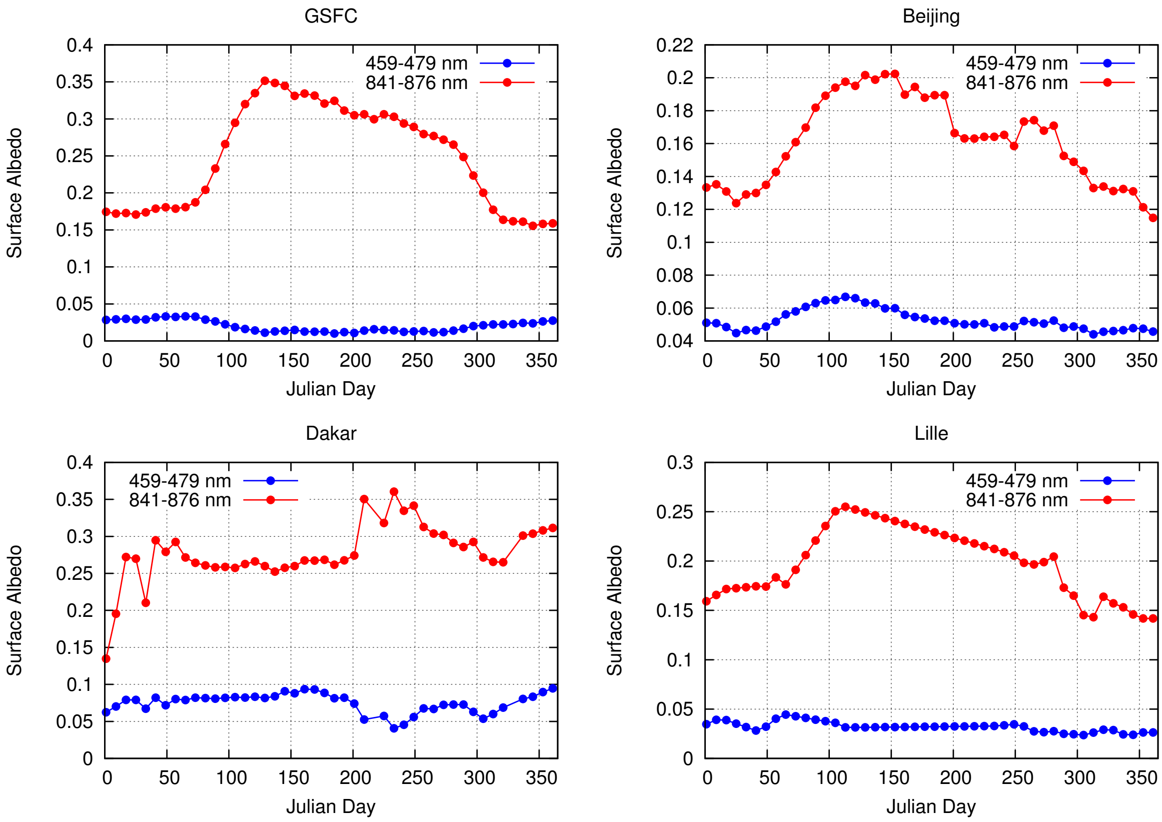

FIGURE 5.2: Variability of the integral surface albedo in GSFC, Beijign, Dakar and Lille during the year at 440 and 870 nm according to the MODIS climatology

The directional behavior of the surface reflectance is modeled using Ross-Li model (Ross, 1981; Li and Strahler, 1992; Wanner et al., 1995). In present study the three BRDF scattering parameters of Ross-Li model (i.e. $f_{iso}, f_{vol}, f_{geo}$) is used as input parameters for inversion. We access the data using previous work of Gonzalez et al. (2010), based on accumulation of MODIS data into a global map of BRDF parameters. The required data are downloaded from the Internet using geographical coordinates and the date of observation. Downloaded file contains the list of the BRDF parameters and surface albedo for the region 10×10 km around observation point and appropriate coordinates for each data set. The surface reflectance parameters are measured in spectral bands ranging from 459 nm to 2155 nm with a spatial resolution of 500 meters and a temporal resolution of 8 days. A developed program downloads corresponding file, looks for the area with coordinates the nearest to observation point and extract the data set in routine regime. Since the MODIS spectral channels do not coincide with sun-photometer wavelength, the needed BRDF parameters are achieved by a linear interpolation.

5.5 DWP Cimel data quality check routine

This step is very important for assuring the high quality of the observations, because possible cloud contamination may introduce significant inhomogeneity in the observation and lead to decrease of accuracy or to complete failure of the aerosol retrieval. The AERONET cloud-screening procedure is described in details by Smirnov et al. (1998).

The cloud screening function is used to filter the measured data, i.e. it removes the data that correspond to bad measurement conditions (e.g. the measurements contaminated by clouds or other disturbances). Thus, it amends initial data set and, correspondingly, improves the inversion results.

The program makes a several important procedures of eliminating cloud contamination that includes: symmetry check of almucantar measurements, angular smoothness check by second derivatives of principal plane measurements and check of consistency of radiometric and polarization data (i.e. compatibility of the measured radiances with those composed from polarization data). The detailed description is provided below.

One of the most important steps of Smirnov et al. (1998) cloud-screening procedure is the symmetry check of the radiance measured in the Solar almucantar. Specifically, assuming atmosphere homogeneous, a symmetry of the measurements in almucantar relative to the solar position allows checking for the data quality by comparison of the left and the right almucantar branches with each other. Namely, the procedure compares appropriate data measured at the same azimuth angles symmetrically about solar principal plane. If a difference between couple of points is more than 20%, it removes these data from a vector of measurements. Finally, if after applying of the symmetry check function a total number of points is less than 10 at least in one measurement vector, program do not consider this case at all.

The check of consistency of radiometric and polarimetric data consists in comparison of measured intensity of sky radiance and a radiance recalculated from polarimetric data (eq. 5.9). The difference between them cannot be more than 20% too.

For the observations in principle plane the symmetry check cannot be performed. Due to this fact, the observations in principle plane were considered unreliable. As a result, the retrievals from principle plane were not included into operational AERONET products and hardly were used in any climatology analyses or validation efforts. At the same time, the observations in principle plane can provide valuable aerosol information especially for the observations corresponding to high sun position (see detailed analyzing in Torres et al., 2014). Moreover, most observations of polarization were conducted in principle planes. Therefore, in current efforts we have added additional cloud-screening steps that expected to select the reliable observations during principle plane scans. Specifically, for the measurements in solar principal plane configuration the angular smoothness check of the data quality is used. The method is based on the consideration of the angular measurements as describing some function and its second derivatives investigation. The limitations on the variation of the derivatives are widely used for smoothing retrieved continues functions in the remote sensing (see discussion in Dubovik, 2004). It is also used to eliminate cloud-contaminated values of AOD in screening procedure by Smirnov et al. (1998). The sign and value of the second derivative is sensitive to the form of the function. It is assumed that the second derivative reacts to abrupt changes of the function (sharp picks for sure).

In current screening procedure we rely on the fact that a regular distribution of sky measurements should be smooth for consecutive angles. Therefore, any unevenness indicates low quality of the data due to bad measurement conditions and should be removed from consideration.

The derivatives can be approximated by differences between values of the function $y(x_i)$ in n discrete points x_i (Dubovik, 2004):

$$\frac{dy(x_i)}{dx} \approx \frac{\Delta^2 y(x_i)}{\Delta_1 x_i} = \frac{y(x_i + \Delta x_i) - y(x_i)}{\Delta_1 x_i} = \frac{y(x_{i+1}) - y(x_i)}{\Delta_1 x_i};$$

$$\frac{d^2 y(x_i)}{dx^2} \approx \frac{\Delta^2 y(x_i)}{\Delta_2 x_i} = \frac{\Delta^1 y(x_{i+1})/\Delta_1 x_{i+1} - \Delta^1 y(x_i)/\Delta_1 x_i}{(\Delta_1 x_{i+1} + \Delta_1 x_i)/2} =$$

$$= \frac{(y_{i+2} - y_{i+1}/x_{i+2} - x_{i+1}) - (y_{i+1} - y_i/x_{i+1} - x_i)}{\frac{1}{2}\left((x_{i+2} - x_{i+1}) + (x_{i+1} - x_i)\right)} \tag{5.14}$$

So using the eq. (5.14) we can quantify the second derivatives for each group of three points. To determine the threshold of the quality check function applying the next inequality is used:

$$N^2 = \frac{1}{n}\sum_{i=1}^{n}\left(\frac{\Delta^2 y(x_i)}{\Delta_2 x_i}\right)^2 \quad < \quad \varepsilon \tag{5.15}$$

where N^2 is a norm, ε is a limitation. If the norm exceed the limit, the same value is calculated n times more. Every calculation is performed for $n-1$ points by sequentially removing each measurement. Further, the function searches the result with the smallest norm, the corresponding removed point is assumed as contaminated one and is deleted from inverted data. The procedure repeats until the norm becomes less than the limit value. As well as for almucantar geometry, the final number of points in the vector of measurements must be at least 10, otherwise the corresponding case does not considered.

Some examples of the results of the angular smoothness check method utilization are represented in the figure 5.3. Different plots represent the application of the cloud screening function to the same data but with different limitations. The stronger limits produce the smoother curves. But in the case of very strong limitation it is possible to lose some "good" points as it is seen on the fig. 5.3f. Thus, one important task is to find an optimum value ε.

In order to keep all good "clear" data, the measurements of radiance intensity are separated into two parts with scattering angles more and less than 40° and different limits are applied to different parts since second derivatives vary a lot for small scattering angles (generally $< 40°$) and, inversely, quite flat for large angles.

In the case of application of the cloud screening function to polarization data a single limit ε for all data is used.

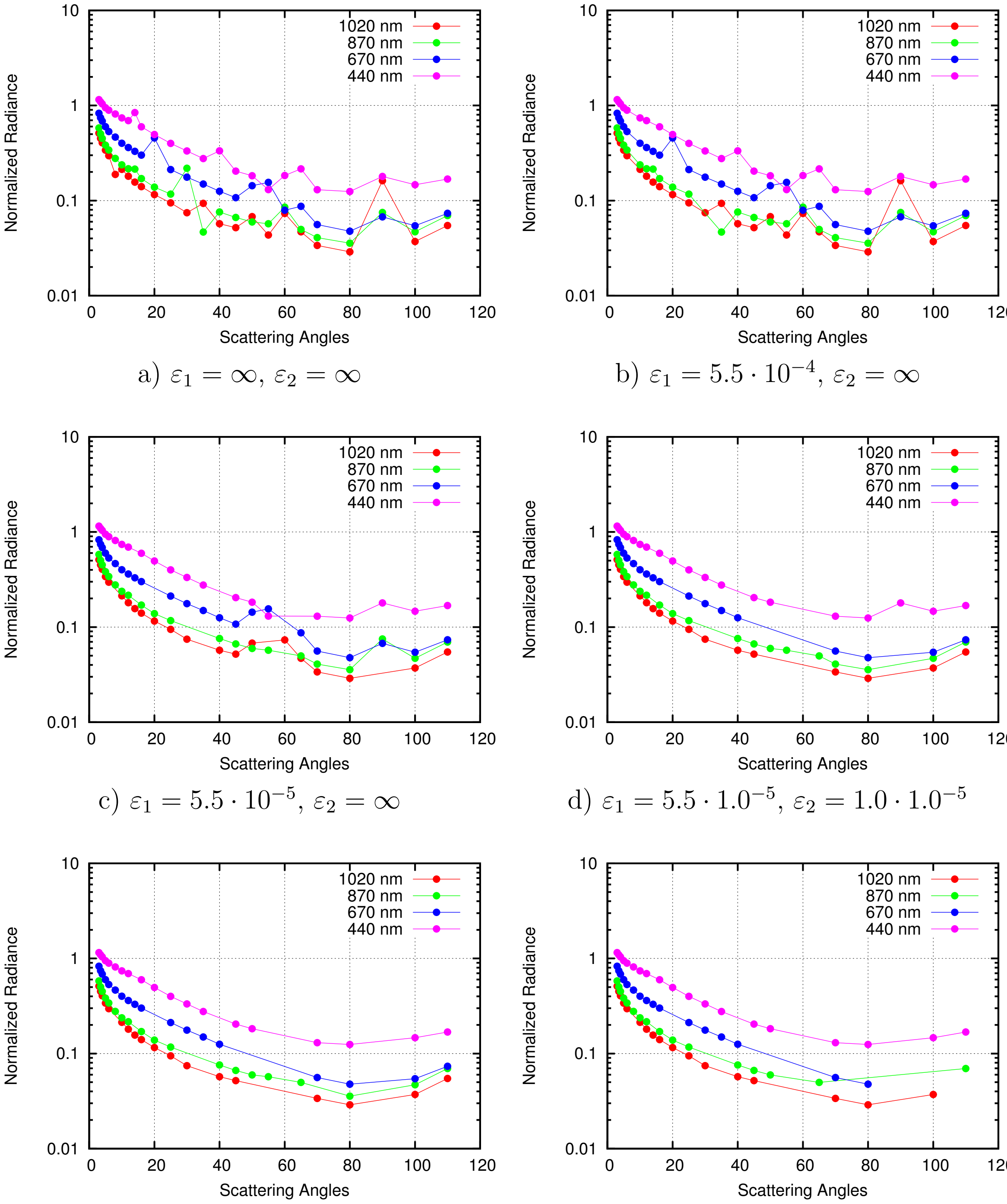

a) $\varepsilon_1 = \infty$, $\varepsilon_2 = \infty$

b) $\varepsilon_1 = 5.5 \cdot 10^{-4}$, $\varepsilon_2 = \infty$

c) $\varepsilon_1 = 5.5 \cdot 10^{-5}$, $\varepsilon_2 = \infty$

d) $\varepsilon_1 = 5.5 \cdot 1.0^{-5}$, $\varepsilon_2 = 1.0 \cdot 1.0^{-5}$

e) $\varepsilon_1 = 5.5 \cdot 1.0^{-5}$, $\varepsilon_2 = 1.0 \cdot 2.5^{-6}$

f) $\varepsilon_1 = 5.5 \cdot 1.0^{-5}$, $\varepsilon_2 = 1.0 \cdot 1.0^{-6}$

FIGURE 5.3: The illustration of quality check function applying for observation in solar principle plane. Different plots correspond to the different limits ε_1 and ε_2

Chapter 6

Data processing, generating and analysis of retrieval results

6.1 Sensitivity analysis of accuracy improvements in aerosol retrievals from polarimetry measurements

Instrumental errors are inevitable in measurement process. Even the data obtained form well calibrated instrument are affected by random noise. During the exploitation the devices are dynamically degrading that can lead to appearance of systematic offsets in radiance measurements or possible loss in precision of angle pointing. Hence, the increase of stability of the inversion process to the measurement errors is very important and highly desirable.

The improvement of the retrieval accuracy is usually associated with enhancement of the information content of the processed data, that can be achieved by increasing the number of independent measurements, by adding the measurements with essentially different sensitivities to the parameters to be retrieved. In this regard, the purposes of the sensitivity test proposed here is an estimation of the improvements in the retrieval of aerosol parameters achieved by utilization of the measurements of polarization in addition to radiometer total intensity observations.

Moreover, in the case of the measured data analysis the accuracy of the inversion results can be determined only indirectly. Namely, one can judge about the success of the retrieval mainly by analyzing the goodness of the real measurements fit recalculated by forward model calculations from retrieved aerosol characteristics. The current analysis has been carried out with the data simulated by forward model for the specified aerosol parameters. In a contrast, the numerical experiment with synthetic data simplifies the further analysis because it allows the direct comparison of the retrieved parameters with the assumed values. Considering obtained effects in detail we can conclude how the inclusion of the additional data affects the retrieval of the particular aerosol parameter.

Moreover, some important aerosol types cannot be analyzed because of rare propagation of the DWP photometer. Thus, the second purpose of the sensitivity test is to consider the results of polarization data applying for these aerosols. Obviously, the current study cannot replace the real data analysis but it can essentially expand our knowledge concerning the efficiency of polarization observations in different regions.

6.1.1 Description of the chosen aerosol models

In this study we have analyzed five main aerosol types covered most of the possible aerosol conditions observed over the world: desert dust, biomass burning, urban clean, urban industrial and maritime aerosols. Long-term measurements of AERONET network show that these aerosol types in their pure forms are observed at the following sites: Solar Village (Saudi Arabia), Mongu (Zambia), Goddard Space Flight Center (Maryland, USA), Mexico (Mexico), Lanai (Hawaii, USA). All these examples are fully described and parametrized in the article by Dubovik et al. (2002a). This work was chosen to obtain microphysical and optical parameters of the considered aerosols.

The particle volume size distribution is modeled by a bimodal lognormal size distribution as follows:

$$\frac{dV(r)}{d\ln r} = \sum_{i=1}^{2} \frac{C_{V,i}}{\sqrt{2\pi}\sigma_i} \exp\left[-\frac{(\ln r - \ln r_{V,i})^2}{2\sigma_i^2}\right] \tag{6.1}$$

where $C_{V,i}$ denotes the particle volume concentration, $r_{V,i}$ is the median radius, and σ_i is the standard deviation. According to many studies (Whitby, 1978; Shettle and Fenn, 1979; Remer and Kaufman, 1998), the bimodal lognormal function is the most appropriate model for aerosol particle size distributions. Indeed, practically all observed size distributions have bimodal structure with quite wide local minimum with low values of $dV(r)/d\ln r$ around $0.6\mu m$.

The fraction of spherical particles, that is one of the parameters retrieved by AERONET, is assumed as 0% for desert dust (all the particles are considered to be non-spherical) and for the rest of the cases as 100% (considering all the particles as spheres).

Mexico - Urban industrial aerosol

The site is located in high-populated and polluted Mexico city (19.33N, 99.18W, Elevation: 2268 m). The aerosol has the highest absorption among the urban aerosols with mean value of the refractive index imaginary part of $\langle k \rangle = 0.014$.

The size distribution is the function of the aerosol optical depth at 440 nm. The values of the size distribution in grid-points is computed by formula 6.1. Table 6.1 contains the expressions used to calculate the parameters for fine and coarse modes together with corresponding values of the complex refractive index.

TABLE 6.1: Optical properties of aerosol in Mexico (after Dubovik et al., 2002a)

Range of optical thickness; $\langle \tau \rangle$	$0.1 \leq \tau(440) \leq 1.8$; $\langle \tau(440) \rangle = 0.43$
n; k	1.47 ± 0.03; 0.014 ± 0.006
$r_{V_f}(\mu m)$; σ_f	$0.12 + 0.04\tau(440) \pm 0.02$; 0.43 ± 0.03
$r_{V_c}(\mu m)$; σ_c	$2.72 + 0.60\tau(440) \pm 0.23$; 0.63 ± 0.05
$C_{V_f}(\mu m^3/\mu m^2)$	$0.12\tau(440) \pm 0.03$
$C_{V_c}(\mu m^3/\mu m^2)$	$0.11\tau(440) \pm 0.03$

Mongu - Biomass burning aerosol

The AERONET station Mongu (15.25S, 23.15E, Elevation: 1107 m) is located in the airport of Mongu, the capital of the western region in Zambia. The aerosol in this region contains a lot of high-absorbing smoke due to the savanna burning annually from July to November.

Concentrations and radii of both modes of the size distribution are the functions of the aerosol optical depth at 440 nm (table 6.2). The values of the complex refractive index do not depend on the aerosol optical depth. The imaginary part is one order of magnitude higher than for other aerosol types.

TABLE 6.2: Optical properties of aerosol in Mongu (after Dubovik et al., 2002a)

Range of optical thickness; $\langle\tau\rangle$	$0.1 \leq \tau(440) \leq 1.5$; $\langle\tau(440)\rangle = 0.38$
n; k	1.51 ± 0.01; 0.021 ± 0.004
$r_{V_f}(\mu m)$; σ_f	$0.12 + 0.025\tau(440) \pm 0.01$; 0.40 ± 0.01
$r_{V_c}(\mu m)$; σ_c	$3.22 + 0.71\tau(440) \pm 0.043$; 0.73 ± 0.03
$C_{V_f}(\mu m^3/\mu m^2)$	$0.12\tau(440) \pm 0.04$
$C_{V_c}(\mu m^3/\mu m^2)$	$0.09\tau(440) \pm 0.02$

GSFC - Urban clean aerosol

The AERONET calibration center at NASAs Goddard Space Flight Center in Greenbelt, Maryland (38.99N, 76.84W, Elevation: 87 m) is located 20 km from Washington inside the Boston-Washington megalopolis which is a heavily urbanized area. The aerosol in GSFC has the lowest absorption values of the urban aerosol.

Concentrations and radii of both modes of the size distribution are the functions of the aerosol optical depth at 440 nm (table 6.3). The values of the real part of the refractive index also depends on $\tau(440)$ and the imaginary part is very low ($\langle k\rangle = 0.003$) as the aerosol is slightly absorbing.

TABLE 6.3: Optical properties of aerosol in GSFC (after Dubovik et al., 2002a)

Range of optical thickness; $\langle\tau\rangle$	$0.1 \leq \tau(440) \leq 1.0$; $\langle\tau(440)\rangle = 0.24$
n; k	$1.41 - 0.03\tau(440) \pm 0.01$; 0.003 ± 0.003
$r_{V_f}(\mu m)$; σ_f	$0.12 + 0.11\tau(440) \pm 0.03$; 0.38 ± 0.01
$r_{V_c}(\mu m)$; σ_c	$3.03 + 0.49\tau(440) \pm 0.021$; 0.75 ± 0.03
$C_{V_f}(\mu m^3/\mu m^2)$	$0.15\tau(440) \pm 0.03$
$C_{V_c}(\mu m^3/\mu m^2)$	$0.01 + 0.04\tau(440) \pm 0.01$

Solar Village - Desert dust aerosol

Solar Village (24.9N, 46.40E, Elevation: 790 m) is an important solar powered electricity generating system situated in the Arabian desert approximately 50 km northwest of Riyadh. The aerosol registered in this site present optical properties representative of the so-called pure desert dust, without contamination by urban pollution.

Concentrations and radii of both modes of the size distribution are the functions of the aerosol optical depth at 1020 nm (table 6.4). The values of the imaginary part of the refractive index at other wavelengths (340, 380, 500, 550, 1240, 1640, 2250 nm) were computed by the linear interpolation.

Table 6.4: Optical properties of aerosol in Solar Village (after Dubovik et al., 2002a)

Range of optical thickness; $\langle\tau\rangle$	$0.1 \leq \tau(1020) \leq 1.5$; $\langle\tau(1020)\rangle = 0.17$
n	1.56 ± 0.03
$k(440/670/870/1020)$	$0.0029/0.0013/0.001/0.001 \pm 0.001$
$r_{V_f}(\mu m)$; σ_f	0.12 ± 0.05; 0.40 ± 0.05
$r_{V_c}(\mu m)$; σ_c	2.32 ± 0.03; 0.60 ± 0.03
$C_{V_f}(\mu m^3/\mu m^2)$	$0.02 + 0.02\tau(1020) \pm 0.03$
$C_{V_c}(\mu m^3/\mu m^2)$	$-0.02 + 0.98\tau(1020) \pm 0.04$

Lanai - Maritime aerosol

The site is situated on the cost of Lanai island (20.74N, 156.92W, Elevation: 20 m) approximately 100 km from Honolulu, Hawaii. The aerosol at that location has very low optical thickness: $\tau(1020)$ varies from 0.01 to 0.2 with mean value of $\langle\tau(1020)\rangle = 0.04$.

The concentration of fine and coarse modes of the size distribution is the function of the aerosol optical depth at 1020 nm (table 6.5). The values of the imaginary part of the refractive index are the lowest among five examples chosen.

Table 6.5: Optical properties of aerosol in Lanai (after Dubovik et al., 2002a)

Range of optical thickness; $\langle\tau\rangle$	$0.01 \leq \tau(1020) \leq 0.2$; $\langle\tau(1020)\rangle = 0.04$
n, k	1.36 ± 0.01; 0.0015 ± 0.001
$r_{V_f}(\mu m)$; σ_f	0.16 ± 0.02; 0.48 ± 0.04
$r_{V_c}(\mu m)$; σ_c	2.70 ± 0.04; 0.68 ± 0.04
$C_{V_f}(\mu m^3/\mu m^2)$	$0.40\tau(1020) \pm 0.01$
$C_{V_c}(\mu m^3/\mu m^2)$	$0.80\tau(1020) \pm 0.02$

6.1.2 Methodology of the sensitivity study

The figure 6.1 represents the principle scheme of the sensitivity study methodology. Firstly we obtain the values of the particle size distribution and complex refractive index for specific optical thickness from the aerosol model. This step is not noted on the diagram.

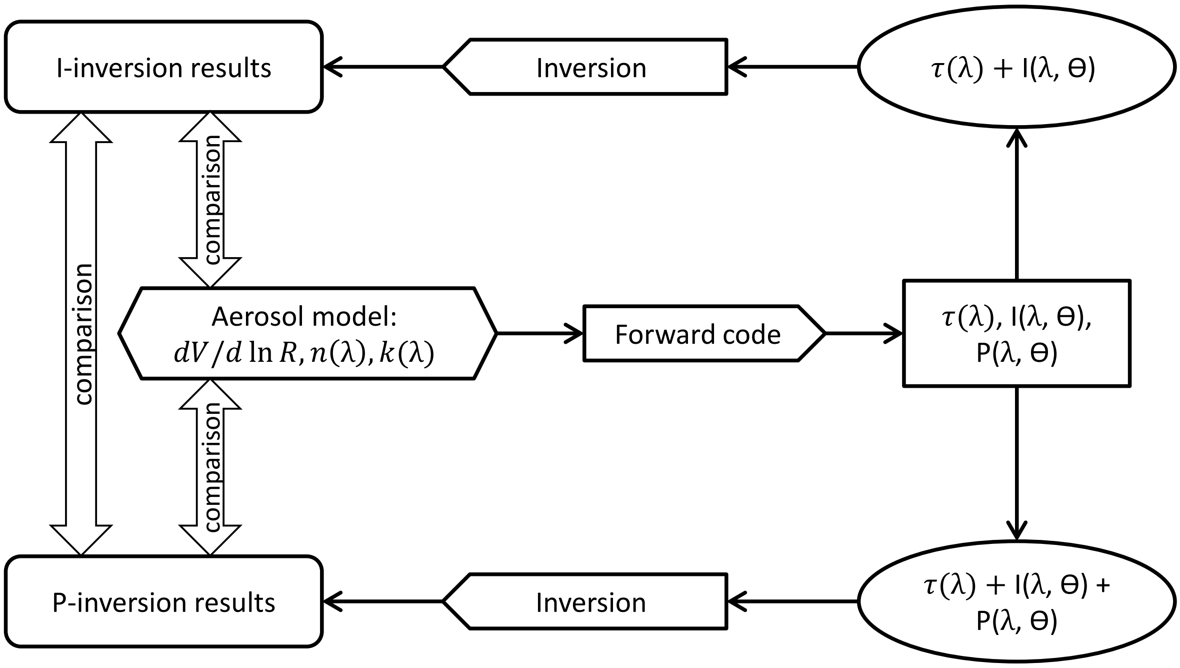

FIGURE 6.1: Scheme of the sensitivity study.

Further, the synthetic data including the aerosol optical thickness, angular distribution of the intensity and DOLP (Degree of the Linear Polarization) of the diffuse radiation corresponding to the geometry and spectral specifications of the real observations are calculated using forward model calculation for the assumed data. The assumed data include parameters of chosen aerosol models: size distributions and complex refractive indices. These parameters are expected to be retrieved. Also, the assumed data include other parameters that are not expected to be retrieved but that need to be defined for reproducing the real observation conditions. For example, it is necessary to define surface reflectance properties, the elevation of the instrument, etc. The simulated data set is modified depending on the investigated error impact. Then, we conduct the inversion twice: first, using only simulated AOD and sky-radiance intensity data (I-retrieval) and, second, using whole simulated data set that includes AOD, sky-radiance and DOLP data (P-retrieval). The results of both inversions are compared with the assumed aerosol characteristics and with each other.

The first part of the test series includes the inversions for an "error free" conditions, i.e. for the data, with no perturbations added intentionally. Therefore, the conditions called here as "error-free" conditions correspond to the tests when neither systematic nor random errors were specifically introduced either in the forward simulations or in the inversion algorithm. At the same time, it should be noted that some minor errors are always present in the radiance modeling used for inversion. These errors are inherent to the inversion algorithm. Thus, the performance of the algorithm in error free conditions shows the stability of the inversion to minor random errors.

The second part of the test considers the situations when the errors are included in the simulated synthetic data.

We consider two types of errors: random and systematic. The random errors were simulated as a normally distributed random noise. The magnitude of the noise was controlled using the value of the standard deviation of the distribution. The following values were used: $\sigma_\tau = 0.005$ and $\sigma_\tau = 0.01$ for AOD data, $1\% \leqslant \sigma_I \leqslant 7\%$ for the sky-radiance data and $1\% \leqslant \sigma_P \leqslant 2\%$ for polarization data.

The systematic errors under study include the pointing error and the biases in measurements of the total optical thickness. The pointing error is modeled by introducing the absolute shifts in zenith (for solar principle plane geometry) angle pointing: $\Delta\phi = \pm 0.5°$. The biases in optical thickness are specified as a wavelengths-independent absolute uncertainty $\Delta\tau = \pm 0.01$ and $\Delta\tau = \pm 0.02$

The study has been carried out for Sun zenith angle of 60° since this position provides the best scattering angle range for all geometries of observation. All data have been simulated for four wavelengths (440, 670, 870 and 1020 nm) that is standard AERONET protocol of the measurements. The Appendix A contains the illustrations of the results obtained.

6.1.3 Sensitivity to the random noises

The sensitivity of the inversion process to instrumental random noise is very important to study in. The accuracy of the direct-sun measurements by CIMEL sun-photometer is 0.01 for standard instrument and 0.005 for master instrument. This values ware taken as standard deviations of the noise added to the optical thickness measurements. Random errors in optical thickness are expected to have equal absolute errors. The standard deviations of the random noise for sky measurements were chosen from 1 to 7%. And random noise of polarization measurements had a standard deviations between 1 and 5%. Random errors in sky and polarization measurements are expected to have equal relative errors.

It should be mentioned that the random noise for DOLP data is expected to be smaller in relative scale than for intensity of sky-radiance. Indeed, the degree of linear polarization is determined as

$$P = \frac{\sqrt{Q^2 + U^2}}{I} \tag{6.2}$$

The DOLP changes in the range from 1 to 0 and for aerosol it usually notably below 1. The DOLP noise level is expected at the level of 1 or 2% (compare P=1, that is taken as 100% of the value).

6.1.3.1 Urban-industrial aerosol (Mexico City model)

Figures A.1 - A.3 in Appendix A represent particle size distribution, complex refractive index, single scattering albedo and percentage of the spherical particles retrieved with and without polarization data applying with random noises added (indicated in the plot legend) for urban-industrial aerosol model. As it is shown in the figure A.1, the model values of the size distribution are perfectly reproduced in noisy free conditions by both inversion scenarios. Other plots in the figure A.1 demonstrate the retrievals of the noisy data.

The following quite clear tendencies can be observed from the results obtained: the noise increasing leads to overestimation of the fine mode volume and shifting of the coarse mode maximum towards smaller radii. At the same time these error efforts decrease with increasing of AOD level. That is the reason why we did not display the results for the cases with AOD values higher than $\tau(440) = 0.8$. Indeed, the displaying of the cases for higher AOD does not result in any new effects but reduces plot readability.

For all considered cases the P-inversions reproduce the modeled size distribution more accurately. As expected, the utilization of the additional polarimetric information affects mainly the fine aerosol mode retrieval. Changes in the coarse mode retrieval are minor.

Figure A.2 presents the retrieval of the complex refractive index and single scattering albedo for the same scenarios with added random noise. It should be mentioned that optical parameters of aerosol are retrieved sufficiently well only for the cases with high optical thickness ($\tau(440) \geqslant 0.4$), as it was observed in previous studies with intensity data only (Dubovik et al., 2000; Torres et al., 2014). Fig. A.2 shows that for low AOD, the P-retrieval fits model data of the real part of the refractive index slightly better in noise free conditions. But, for $\tau = 0.2$, the results of I-retrieval of noisy data are grouped closer to model value. With increasing of optical thickness the P-inversions reproduce the model values of the real part more accurately for all noisy cases considered in this study. However, the figures demonstrate permanent underestimation of the real part at $\lambda = 1020\,nm$ for high AOD ($\tau \geqslant 0.6$). In the case of the I-inversion the underestimation of this parameter is consistently observed at all wavelengths. The retrieval of the imaginary part of the refractive index and single scattering albedo demonstrates minor sensitivity to the adding of polarization data. This is also consistent with the observation of the study by Li et al. (2009).

All the particles for Mexico aerosol model were modeled as spherical. Generally, both inversion types do not demonstrate significant difference in the sphericity retrieval (fig. A.3). At the same time, overall the P-retrieval reproduces this parameter more accurately especially in the cases when the higher noise is added. Similarly to the situation with the retrieval of the other parameters, the main problems in retrieving the sphericity occur for optical thin situation.

6.1.3.2 African savanna aerosol (Mongu model)

African savanna aerosol model reveals generally the same effects of the inversion sensitivity to the additional random noise (fig. A.4 - A.6) as Mexico aerosol. However the effect of polarization data applying is more pronounced for the size distribution fine mode (fig. A.4). Moreover, sphericity is retrieved more correctly than in Mexico case (fig. A.6).

6.1.3.3 Urban-clean aerosol (GSFC model)

In the case of urban-clean aerosol model the effect of the fine mode correction by polarization data applying slightly decreases (fig. A.7).

Optical characteristics have near the same behavior as in two cases considered previously. The part of spherical particles is retrieved more accurately by the P-inversions. At the same time, it should be mentioned that the underestimation of the particle sphericity in the absence of polarization data occurs mainly for high aerosol loading ($\tau \geqslant 0.8$) which is rare for GSFC site.

6.1.3.4 Desert dust aerosol (Solar Village model)

Desert dust aerosol is totally dominated by coarse particles. As it was expected (from studies by Dubovik et al. (2006) and Li et al. (2009)), in this case we have not observed any pronounced advantages from adding of polarimetric data (fig. A.10). The retrieval of the coarse mode reveals pronounced reaction to the increase of the noise level: the maximum of the coarse mode distribution increases significantly and shifts towards smaller particle size. At the same time, the concentration of the particles with radii larger than $2\mu m$ decreases. These effects together lead to the narrowing of the coarse mode distribution (i.e. the width of the retrieved distribution is decreasing).

It can be seen that the P-inversions overestimate the real part of the refractive index for $\tau(1020) = 0.2$ whereas the I-inversions underestimate it (fig. A.11).

The particles of the desert dust aerosol are modeled as non-spherical (i.e. sphericity is 0%). As in previous cases, figure A.12 shows insignificant difference between the I- and P-inversion results with slight advantage of polarization data utilization.

6.1.3.5 Oceanic aerosol (Lanai model)

The oceanic aerosol observed at Lanai, Hawaii, has a very pronounced fraction of coarse particles (sea salt): $C_{V_c}/C_{V_f} \sim 2$, which is higher than for urban–industrial and biomass burning aerosol but lower than for desert dust. The simulated random noise affects the results of the size distribution retrieval by increase of the fine mode volume and the coarse mode maximum (fig.A.13). The coarse mode retrieval reveals quite the same sensitivity to the random noise as in the case of desert dust. Utilization of polarization data improves the retrieval of the fine mode volume and slightly decreases the coarse mode maximum too.

Oceanic aerosol is characterized by low concentration in the atmosphere ($\tau(1020) \leqslant 0.2$). So the inversion of the optical parameters becomes rather more problematic. Study shows underestimation of the refractive index real part by I-inversion and its overestimation by P-inversion type. The observed effects decrease with AOD increasing. It should also be noted that I-inversion is less affected by noise in the Lanai case. The imaginary part of the refractive index and single scattering albedo do not reveal sensitivity to the polarimetric data applying. The reaction of the both retrieval types to the random noises including are overestimation of the imaginary part and underestimation of single scattering albedo.

Oceanic aerosol contains 100% of spherical particles. The retrieval of this parameter from noisy data was the most problematic from all considered aerosol types (fig.A.13).

6.1.4 Sensitivity to the AOD bias

Systematic errors mainly occur because of the following two reasons: the existence of unaccounted instrumental problems (offsets) during the actual registration of Sun-sky radiance or the use of invalid approximations in the theoretical model used for measurement interpretation. These reasons result in simultaneous erroneous estimation of the optical depth, sky radiance, DOLP and pointing error. For example, the offsets in the AERONET radiance measurements can be caused by miscalibrations of the radiometer Sun-sky channels.

In current study the sensitivity of the inversion code to the biases in optical thickness is investigated. It was decided to examine the sensitivity of the retrieval results to a wavelengths-independent absolute uncertainty $\Delta\tau = \pm 0.01$ and $\Delta\tau = \pm 0.02$. We remind the accuracy of the direct-sun measurements by CIMEL sunphotometer is 0.01 for standard instrument and 0.005 for master instrument.

6.1.4.1 Urban-industrial aerosol (Mexico model)

Figures A.16 - A.18 represent the sensitivity of the particle size distribution, the complex refractive index and single scattering albedo to the AOD biases for Mexico aerosol type. Evidently, increase of aerosol loading (i.e. positive shifts in AOD data) leads to the volume of both aerosol modes increasing as well as AOD decrease gives the opposite effect (fig. A.16). The study demonstrates that the utilization of the additional polarimetric information can significantly correct these features especially for the fine aerosol mode.

Figure A.17 demonstrates the underestimation of the refractive index real part by I-inversion for the cases when AOD biases are positive and overestimation of the real part for negative biases. Utilization of the polarimetric data leads to opposite effects: the real part is overestimated when AOD bias is positive and is underestimated when bias is negative. Moreover, the I-inversion results are closer to the model value at large wavelengths whereas the results of P-inversion at short wavelengths. In general, utilization of the additional polarization data improves the retrieval of the refractive index real part for high aerosol loading ($\tau(440) \geqslant 0.8$). The retrieval of the refractive index imaginary part and single scattering albedo is not sensitive to the polarimetric data applying.

It should be noted that the offset in optical thickness (fig. A.17) results in an artificial wavelength dependence of aerosol optical parameters. This can be explained by the fact that the error in optical thickness measurements is assumed wavelength-independent. At the same time, the aerosol optical thickness $\tau(\lambda)$ can be strongly wavelength-dependent, and, thus, the effect of biases inclusion can be different at different wavelengths. The value of the imaginary part of the refractive index defines the magnitude of the aerosol absorption. Therefore the error in $k(\lambda)$ retrieval correlates with the error $\Delta\tau$. That is, an increase or decrease of $\tau(\lambda)$ caused by the presence of the positive or negative bias $\Delta\tau$ is compensated by the inversion code as an artificial increase or decrease of absorption (i.e., $k(\lambda)$). The opposite effect is observed for single scattering albedo. These effects increase together with wavelength since the relative value of the bias is bigger for the larger wavelengths.

As well as for the case of random noise presence, the parameter of particle sphericity is retrieved with minor difference between I- and P-inversion types (A.18). Some differences occur mainly for optical thin conditions.

6.1.4.2 African savanna aerosol (Mongu model)

In this case, the sensitivity of the retrieved parameters to the AOD bias has quite the same characteristics as described for Mexico aerosol model (see fig. A.19 - A.18).

6.1.4.3 Urban-clean aerosol (GSFC model)

In comparison with urban-industrial aerosol model, urban-clean aerosol reveals less sensitivity to the negative AOD bias than to positive one (fig. A.22 - A.24). The size distribution retrieval reveals sensitivity of the fine mode to AOD biases (fig. A.22). However the retrieval results are corrected by utilization of polarization data.

The real part of the refractive index is fitted more correctly by P-inversion (fig. A.23) especially for high aerosol loading. I-inversion demonstrates the underestimation of the real part for $\tau(440) \geqslant 0.8$.

The advantages of polarization data applying for the sphericity retrieval are more pronounced in GSFC case than for Mexico aerosol (fig. A.24).

6.1.4.4 Desert dust aerosol (Solar Village model)

The size distribution retrieval is not sensitive to polarimetric data applying in the case of the coarse mode dominated desert aerosol. Figure A.25 shows that the AOD bias including in the initial synthetic data slightly changes the retrieval of the coarse mode volume by both inversion types.

Generally the retrieval of the optical parameters does not reveal sensitivity to polarization applying. But the real part of the refractive index is retrieved slightly better for $\tau(1020) \geqslant 0.8$ by P-inversion.

The difference in retrieval of the particle sphericity is not significant between two inversion types. However the inversion with the use of polarization information reproduces 0% of spherical particles for the desert dust more correctly (fig. A.27).

6.1.4.5 Oceanic aerosol (Lanai model)

The oceanic aerosol in Lanai is characterized by low optical thickness. Hence the impact of the biases in AOD data on aerosol characterization is more pronounced than for other considered aerosol types (see fig. A.28 - A.30). However the sensitivity of the retrieved characteristics to the biases in optical depth qualitatively remains the same. Utilization of the polarization corrects the fine mode of the size distribution (fig. A.28) and reveals the minor influence on the coarse mode retrieval.

As for other aerosol types, the retrieval with polarization data utilization fits the model value of the refractive index real part more accurately at short wavelengths (fig. A.28). For $\tau(1020) \geqslant 0.12$ P-inversion retrieves the real part with the same precision as I-inversion. The imaginary part of the refractive index and single scattering albedo do not reveal any sensitivity to the additional polarimetric data applying.

The sphericity is also retrieved by P-inversion more correctly (fig. A.30).

6.1.5 Sensitivity to the pointing error

The pointing error is defined as the angle between the direction which the detector should achieve for the measurement conducting and the direction where it is really pointing. Thus, for direct-sun observations pointing error is the angle between the Sun position (correct pointing) and the erroneous pointing direction. For sky-radiance and polarization observations it is the error in the acquisition of the correct zenith and azimuth angles of the measurements.

Consequently, the pointing error can be split in vertical and horizontal error depending on zenith or azimuth coordinates is achieving erroneously. In current study we consider the vertical errors for the data in solar principle plane only.

The CIMEL radiometer sensor head is pointed by stepping azimuth and zenith motors with a precision of $0.05°$ (Holben et al., 1998) for a well-tuned instrument and $\sim 0.25°$ (or $0.5° \div 1.0°$ in the worst case scenario) for a degraded or improperly aligned instrument. The AERONET radiometer has approximately a $1.2°$ full angle field of view. The sensitivity of the inversion process to the pointing errors was investigated for $\Delta\phi = \pm 0.5°$.

6.1.5.1 Urban-industrial aerosol (Mexico City model)

Figure A.31 represents the influence of the pointing error on the particle size distribution retrieval for Mexico City aerosol model. The negative angular shifting ($\Delta\phi = -0.5$) leads to significant overestimation of the coarse mode volume whereas the positive one results in opposite effect. The changes infused into retrieval of the size distribution coarse mode by polarimetric data are negligible.

The fine aerosol mode retrieval also reveals sensitivity to the pointing error but not so pronounced as the coarse mode. In the presence of positive angle shifting the width of the fine mode distribution increases and the maximum shifts towards smaller particles. The volume of the fine mode also increases. The negative pointing error leads to decrease of the distribution width, slight shifting of the maximum towards larger radius and the total volume of fine particles decreasing. As we can see, the utilization of the additional polarimetric data can slightly correct the shape of distribution of fine particles. All these results are in agreement with previous studies by Dubovik et al. (2000) and Torres et al. (2014). Namely, the high sensitivity of the coarse aerosol mode to the errors in angular pointing is explained by very well pronounced forward peak in phase function of large particles. Thus, the aureole part concentrate significant information about aerosol coarse mode. Hence, shift towards Sun ($\Delta\phi = -0.5°$) increases the volume of the coarse mode and, correspondingly, decreases the volume of the fine mode.

The sensitivity of the optical aerosol parameters to the pointing error is presented in the figure A.33. It is shown that the I-inversion underestimates the real part of the refractive index with positive angle bias and overestimates it with negative one. On the contrary, the P-inversion underestimates the real part for positive biases and overestimates it for negative one. In general, the results of I-retrieval fit the model better than P-retrieval results especially at large wavelengths. This effect can be explained by extremely high sensitivity of the real part retrieval to the polarization information applying in the case of aerosols producing the diffuse radiation with high DOLP. Indeed, the pointing error leads to shifting of all angular measurements including polarization data that, in turn, leads to excessive correction of the misestimated real part. Nevertheless, the polarization data decrease the spectral dependence of the real part retrieved.

The retrievals of the refractive index imaginary part and single scattering albedo reveals the minor sensitivity to the pointing error inclusion as well as additional polarization data applying.

The part of spherical particles is retrieved well by both inversion types (fig. A.32). In the case of positive shift in angular pointing, P-inversion reproduces the model more correctly.

6.1.5.2 African savanna aerosol (Mongu model)

In general, the same sensitivity of the retrieval results to the pointing error is observed for aerosol of africal savanna. In this case the additional polarimetric data essentially improve the fine aerosol mode retrieval (fig. A.34).

The retrieval of the optical aerosol characteristics and the part of spherical particles reveals the same sensitivity to the shifts in angular pointing and the same effects of polarimetric data applying as for Mexico case (fig. A.36-A.35).

6.1.5.3 Urban-clean aerosol (GSFC model)

As it was mentioned, biases in angular pointing have an influence primarily on the retrieval of the coarse aerosol mode. Since urban-clean aerosol is strongly dominated by fine particles, the observed sensitivity of the size distribution retrieval to the pointing error is minor. Figure A.31 demonstrates the same impact of the pointing error on size distribution retrieval. Namely, the study reveals slight increasing of the fine mode and decreasing of the coarse mode volume in the case of positive angle shifting and the opposite effects for negative shift. Utilization of the polarimetric data slightly corrects the artefacts for the fine mode.

As in previous case, the real part of the refractive index is underestimated for positive angle shifting and overestimated for negative one (see fig. A.39). However, in this case the P-retrieval results fit the model value more correctly especially at short wavelengths and for positive angular shift. The exception is the results of I-retrieval for high AOD ($\tau(440) \geqslant 0.6$) and negative pointing error.

The imaginary part of the refractive index is underestimated for negative bias in angular pointing and overestimated for positive one (figure A.39). The opposite effect is observed for retrieval of single scattering albedo. Utilization of the additional polarimetric information do not reveal any considerable impact on these results.

Figure A.38 demonstrates that the P-inversion reproduces the sphericity more correctly in the case when $\Delta\phi = 0.5°$. For $\Delta\phi = -0.5°$ the difference between I- and P-retrievals is negligible.

6.1.5.4 Desert dust aerosol (Solar Village model)

The desert dust reveals the highest sensitivity to the errors in angular pointing among all aerosol types under study. This result is in agreement with Dubovik et al. (2000) and

Torres et al. (2014) because desert dust is dominated by the coarse aerosol mode. As it was mentioned above, the phase function of large particles has a very well pronounced forward peak and even minor pointing errors in aureole area can significantly change the retrieval results.

Figure A.40 shows the underestimation of the size distribution coarse mode for $\Delta\phi = 0.5$ and its overestimation for $\Delta\phi = -0.5$ as well as in previous cases.

The real part of the refractive index is overestimated when angular shift is positive and underestimated in another case (fig. A.42). The effects of polarimetric data utilization are minor except slight correction of the real part retrieval at short wavelengths. The imaginary part of the refractive index and single scattering albedo reveal nearly the same sensitivity to the pointing error as in previous cases.

The part of spherical particles is reproduced more correctly by P-inversion (fig. A.41).

6.1.5.5 Oceanic aerosol (Lanai model)

The retrieval of the oceanic aerosol parameters reveals extremely high sensitivity to the bias in angular pointing. As well as desert dust, maritime aerosol is dominated by large particles that determines this sensitivity. However, it containes pronounced fine mode also. In contrast to other considered aerosol models, in this case the errors in angular pointing strongly influence on the retrieval of both fine and coarse mode of the particle size distribution (fig. A.43). In the case of positive angle bias ($\Delta\phi = 0.5$) the results of I-inversion demonstrate significant overestimation of the fine aerosol mode and underestimation of the coarse mode. Negative angle shift ($\Delta\phi = 0.5$) results in opposite reaction. Utilization of the polarimetric data leads to considerable effects also. First of all, the retrieved volume of the fine mode decreases excessively for positive angle bias and increases for negative one as well excessively. The retrieval of the size distribution coarse mode reveals minor sensitivity to the polarimetric information applying.

Unexpectedly, the part of the spherical particles for $\Delta\phi = 0.5°$ is retrieved more correctly by inversion without polazation data applying (see fig. A.44). But for $\Delta\phi = -0.5°$ the effect is opposite.

The pronounced changes are also observed for the retrieval of the aerosol optical parameters. As in the case of urban industrial aerosol (Mexico model), positive angular bias increases the refractive index real part especially at short wavelength whereas negative bias decreases it (fig. A.45). Utiliztioin of the shifted DOLP data results in the real part overestmation for negative angular bias and underestimation for positive one. That is, the use of the shifted polarization data affects the retrieval results contrarily to the angular shift in the radiance intensity measurements. The most accurate characterization of the real part is obtained by I-retrieval at large wavelengths. However, despite the large deviation of the retrieved values from the model, utilization of the polarimetric data significant decreases the wavelength-dependence of the real part retrieved. The refractive index imaginary part and single scattering albedo demonstrate very pronounced but qualitatively identical sensitivity to the pointing error as for other aerosol models under study. The use of the palarization data do not considerably affects on the retrieval of these parameters.

The erroneous corrections of the retrieved aerosol characteristics indicate high sensitivity of the maritime aerosol type retrieval to the polarimetric information applying as well as sensitivity of the polarization data to the angular shifting. Indeed, pronouned sensitivity to the pointing error is compensated by polarimetric information. But the angular shift in DOLP data leads to opposite effect than the same shift in radiance intensity data that, in turn, results in excessive correction of the misestimated parameters retrieved.

6.2 Illustration and analysis of the retrieval results

As a final stage of current study, the developed processing software was applied to the extensive volume of observational data. As a result, for the first time we have generated large data sets of aerosol retrieval from AERONET/PHOTONS polarimetric observations. The results of the retrievals were analyzed with the objective to identify the main

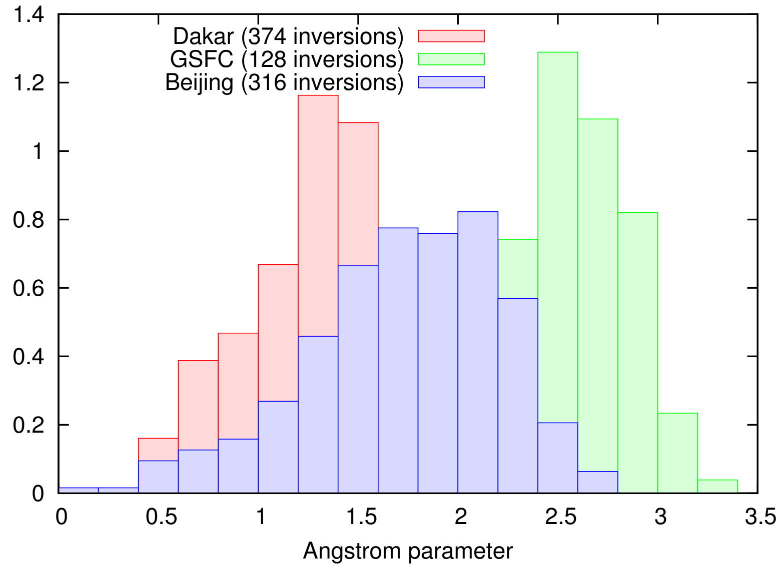

FIGURE 6.2: The distribution of Ångström parameters and total number of inversion results chosen for analysis of influence of polarimetric data utilization.

improvements in the aerosol retrieval obtained due to availability of polarimetric observation in addition to traditional intensity measurements routinely used in AERONET processing.

For inversion we have chosen three sites with different aerosol types: GSFC, USA (measurements during DRAGON campaign (Holben et al., 2011b; Mortier et al., 2012) from July 1 to August 15, 2011, and additionally several months after), Beijing, China (2010-2011) and Dakar, Senegal (2011-2012). For Beijing and Dakar sites the regular AERONET observations were used. All available DWP photometer data with polarization measurements have been collected and processed.

Figure 6.2 represents a normalized histogram (that means a total surface area of each rectangle equal to unity) of angstrom parameters of measurement distribution and total number of inversion results chosen for analysis of the influence of polarimetric data utilization. The histogram clearly illustrates the mentioned previously difference in average particles size of the concerned aerosol types.

In order to estimate the contribution of polarization measurements to retrieval results all inversions were conducted twice: with and without utilization of polarization. As before, index "P-" is used for the retrievals with polarization data applying and index "I-" denotes the retrievals based only on the measurements of radiance intensity. The same indexes we use to mark the values obtained by corresponding retrieval type. For further analysis we have chosen results with final sky error less than 7% for inversions with polarimetric data applying (P-type) and 5% for intensity-only inversions (I-type). Since once polarimetric data are used, the total number of observation increases, the final residual of the sky-radiance measurements fitting is also increases in average (see fig. 6.3). Therefore, the less strong threshold value is used in that case. It can be explained by some inconsistency of intensity and polarization angular measurements leading to increase of the fit discrepancy.

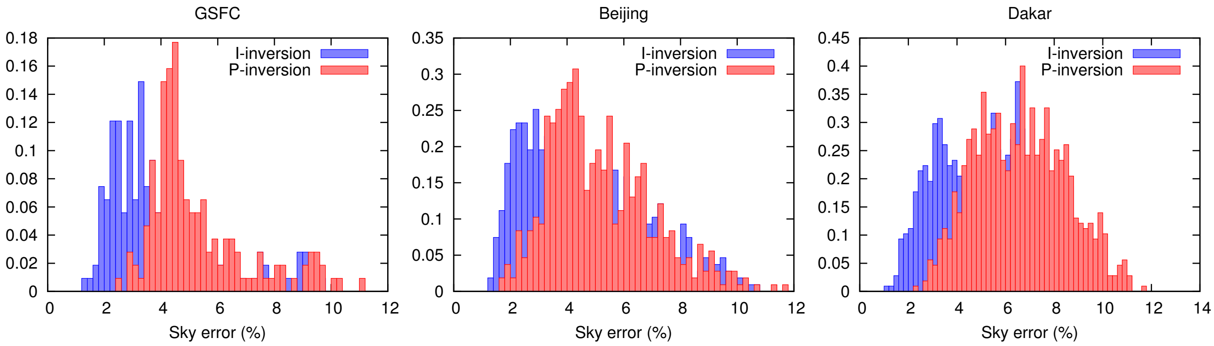

FIGURE 6.3: The distribution of the final residual of sky-radiance measurements fitting for the cases of I- and P-inversion types

In order to clarify whether polarimetric data bring some real improvements to microphysical and optical aerosol properties retrieval or not, we compare the polarization measurements (specifically DOLP calculated from them) with their fits produced by inversion code with and without polarimetric data applying. Clearly, we have used the I-retrieval results as an input parameters in the forward-model calculations to retrieve the DOLP data from them. In other words, DOLP has been recalculated by forward model from the results of I-inversion for the same case and the same angles as the real measurements. The obtained data were compared to both real polarization measurements and their fit acquired from P-inversion. Obviously, the quality of the retrieval is generally characterized by the accuracy of the measurement fitting. Thus, we use a discrepancy between DOLP simulated from I- and P-inversion results and observed data as a measure of the retrieval accuracy. Numerically it can be estimated by a residual calculated as

$$R = \sqrt{\frac{\sum_{i=1}^{n}(DOLP_i^{meas} - DOLP_i^{fit})^2}{n}} \tag{6.3}$$

where R is the residual, $DOLP_i^{meas}$ and $DOLP_i^{fit}$ are the measured and simulated DOLP correspondingly.

Figure 6.4 shows the obtained residuals of I- (blue impulses) and P- (red impulses) fits of DOLP for each inversion versus its respective angstrom parameter. As it is seen, P-inversion fits the real measurements better. The difference between I- and P-fits is more pronounced for larger Ångström parameters that corresponds to the smaller aerosol particles. With increase of the wavelength the less intensity of radiation leads to the signal level decreasing on these channels and, as a result, the error increases for both retrieval types.

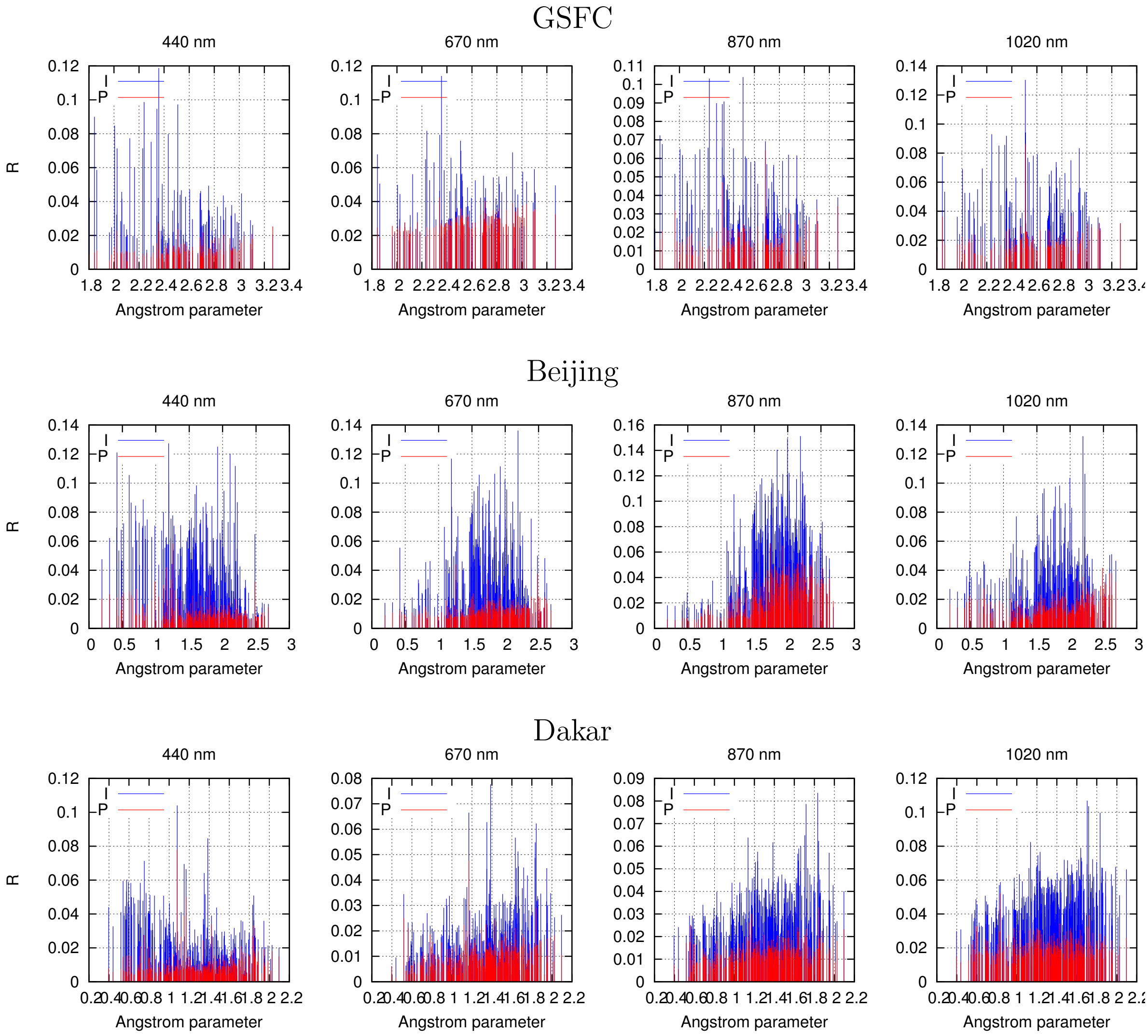

FIGURE 6.4: The residuals of DOLP simulations based on I- and P-inversion results versus Ångström parameter of the observation

In order to estimate the advantage of polarization data use for each studied aerosol type we have calculated the differences between residuals for P- and I-fits of DOLP at $\lambda = 440\ nm$ and $1020\ nm$: $\Delta R(\lambda) = R_I(\lambda) - R_P(\lambda)$. The higher is ΔR, the better is P-inversion in comparison with I-inversion, the more pronounced is its benefit. Table 6.6 represents the percentage of the inversions with $R_P < 0.02$ and different ΔR for two wavelengths. Higher value corresponds to higher sensitivity of the inversion to the polarization measurements. Figure 6.5 expands the context of this table illustrating the same values but for all wavelengths used.

From these values we conclude that the highest influence of applying polarization measurements is for Beijing aerosol type (polluted industrial aerosol with comparable presence of both fine and coarse modes) and the smallest effect is for Dakar aerosol

	GSFC		Beijing		Dakar	
Conditions	440 nm	1020 nm	440 nm	1020 nm	440 nm	1020 nm
$\Delta R > 0$	93.8	69.5	92.7	82.6	96.5	64.2
$\Delta R > 0.01$	56.3	51.6	63.3	51.6	39.8	57.2
$\Delta R > 0.02$	31.2	39.0	46.8	31.0	19.3	44.1
$\Delta R > 0.03$	20.3	25.7	35.8	22.4	7.2	21.1
$\Delta R > 0.04$	9.4	16.4	25.0	11.3	4.3	9.3

TABLE 6.6: Percentage of the inversions corresponded to appropriated ΔR for 440 and 1020 nm. $R_P < 0.02$

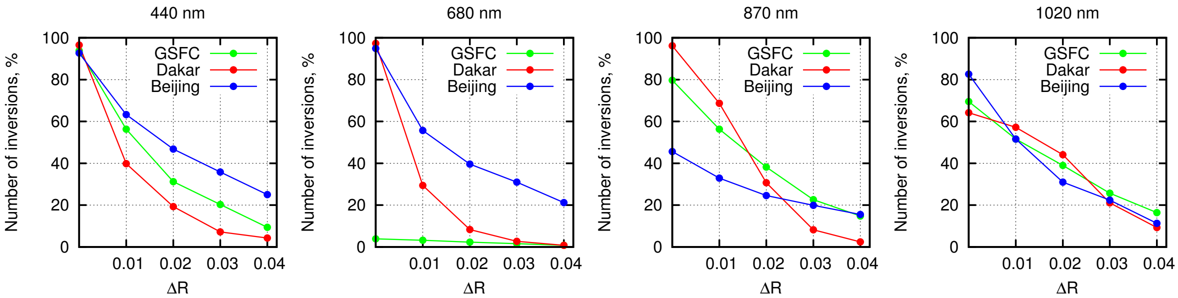

FIGURE 6.5: Percentage of the inversion results versus ΔR for $R_P < 0.02$.

(desert dust aerosol dominated by large particles). GSFC industrial aerosol takes an intermediate position in these statistics due to dominance of small, but mostly spherical particles. Besides, there is some increase of discrepancy between I- and P-fits at large wavelengths, especially at 1020 nm, for Dakar and GSFC cases. Most likely it denotes an augmentation of sensitivity of polarimetric data to aerosol properties with decreasing of size parameter $x = 2\pi a/\lambda$, where a is a particle radius. Indeed, for the particles much smaller than the wavelength ($a \ll \lambda$) the size parameter x is small and we reach the familiar Rayleigh scattering approach (Bohren and Huffman, 1998). For this conditions incident unpolarized light becomes completely polarized at 90°. With size parameter x increasing polarization maximum decreases and shifts towards larger angles. Furthermore, a concomitant of size increasing is more undulations of polarization distribution.

Therefore, the size parameter x decrease leads to the increase of the polarization degree of the scattered light and, accordingly, to the augmentation of useful information that could be obtained from polarimetric observations. This is probably one of the reasons why polarization measurements are more sensitive to aerosol fine mode. Unfortunately, the described effect of polarization sensitivity increasing goes together with general decreasing the signal level at large wavelengths and increasing the instrumental measurement errors. The opposite important mechanism relates to the decrease of the scattered light polarization as a result of the aerosol size parameter increasing. Thus, although the particles of the coarse mode are often non-spherical, they almost do not polarize light since the size parameter is large and, therefore, polarimetric observations do not bring much additional information for the coarse particles.

With the purpose of identifying the influence of the additional polarization information on the retrieval of the microphysical and optical aerosol parameters the differences in the retrievals were visualized in several figures. The average differences between aerosol characteristics (size distribution, refractive index, single scattering albedo) retrieved with and without polarimetric data usage are shown in the figure 6.6. Left side corresponds to the cases with large residual gap between I- and P-fits of DOLP at $\lambda = 440\,nm$ ($\Delta R(440) = R_I(440) - R_P(440) > 0.3$) and the right side represents the minor value of the residual ($\Delta R(440) < 0.2$). The average differences of the size distribution are computed for the data normalized to the total particle volume to eliminate the domination of the cases with high AOD. Since the refractive index and single scattering albedo are retrieved sufficiently well only for the cases with high aerosol loading (Dubovik et al., 2000), the average differences for them were calculated only for $\tau(440) \geqslant 0.4$. The typical examples of the retrieved parameters and corresponding DOLP fits are represented in the figures B.1-B.17 in Appendix B. For example, figures B.1, B.14, B.17 are the instances of the inversion results chosen for the right part of the figure 6.6, and the figures B.4-B.13, B.15 are the instances for its left side.

In agreement with Li et al. (2009) the most pronounced benefits occur for the fine mode of the size distribution, the real part of the refractive index and sphericity. Changes in the imaginary part of the refractive index and single scattering albedo are negligible. Significant changes in particle sphericity even for the cases with lower differences between polarization fits (right part on the fig. 6.6) indicate high sensitivity of DOLP to particle non-sphericity. The decrease of the amount of spherical particles for Dakar site is in agreement with the common expectation that desert dust is dominated by coarse non-spherical particles. A higher density of red impulses on the right part of the figure 6.6 (low $R_I - R_P$ value) for Dakar is explained by larger number of inversion

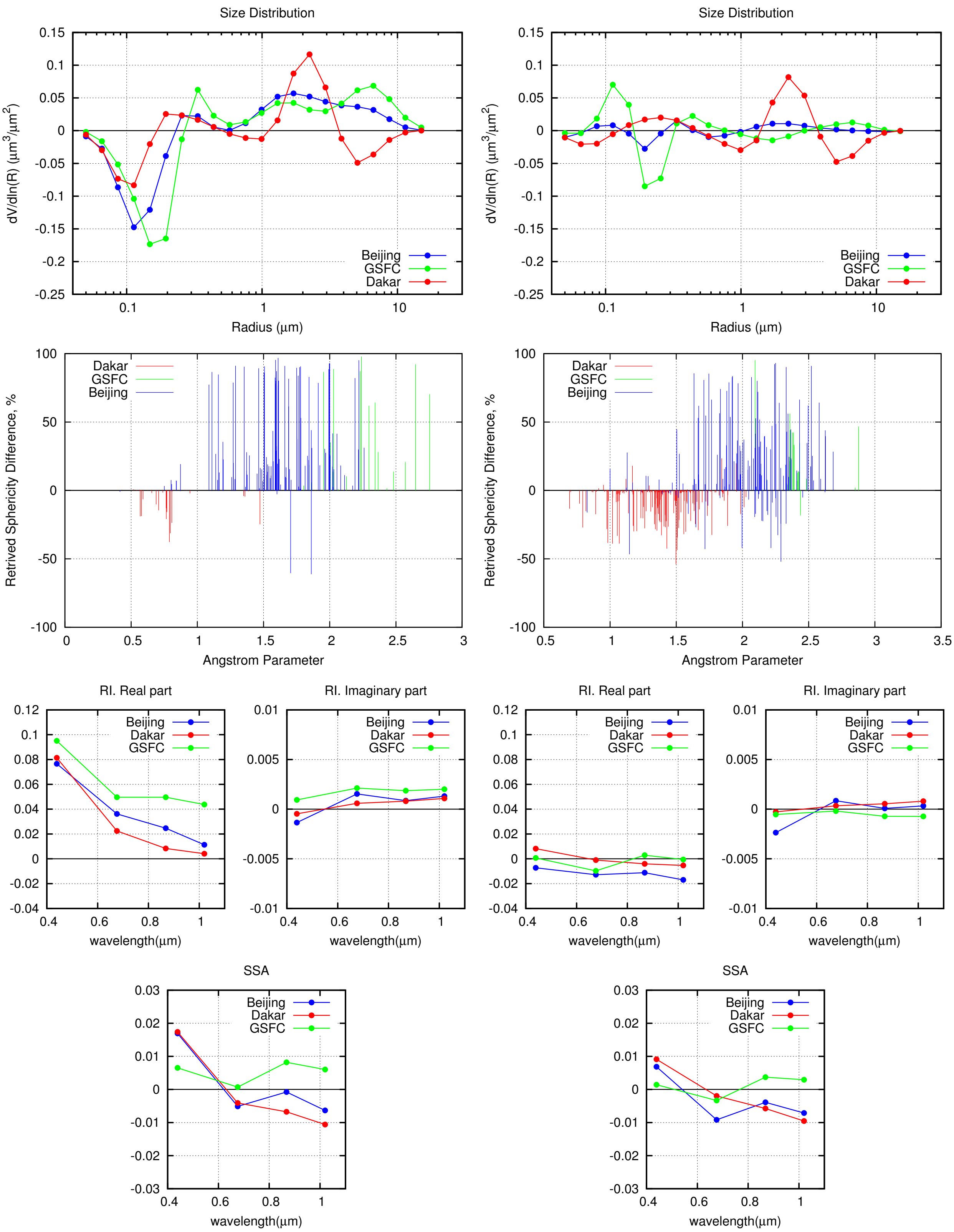

FIGURE 6.6: The average differences between retrievals of the size distribution, the refractive index and single scattering albedo with and without polarimetric data utilization for $\Delta R(440) = R_I(440) - R_P(440) > 0.3$ (left side) and $\Delta R(440) < 0.2$ (right side).

results satisfying these conditions as it was mentioned above. GSFC and Beijing cases show a tendency of the retrieved particle sphericity increase with polarimetric data applying. There is no contradiction between obtained results and theoretical predictions. Actually, a higher percentage of spherical particles for GSFC fine urban aerosol was expected. Beijing industrial pollution consists of both fine and coarse mode particles of various sphericity. It should be noted, that the shape of the fine particles has very minor effect on the scattered light intensity. Thus, in the case of I-retrieval, the inversion code can decrease the particle sphericity. In these regards, the polarization observations add sensitivity to shape of even small particles, therefore P-inversion retrieves sphericity more robustly. All these facts allow us to trust the received results.

The influence of the additional polarimetric data use on the size distribution retrieval appears in decrease of the fine mode volume and its maximum shifting (fig. 6.6 shows an average effect and fig. B.6, B.10 are the examples). The estimation of the coarse mode volume increases especially for the desert dust dominated by large particles (see examples for Dakar in Appendix A). This effect for Dakar site is observed even when the difference between I- and P-fits of DOLP is small ($R_I - R_P < 0.02$; the right part of the figure 6.6). It should be remind, that the conditions on ΔR have been applied only for $\lambda = 440\ nm$. However, the measurements at large wavelengths could be more important for retrieval of the properties of the coarse mode dominated aerosols due to increase of the polarization sensitivity with the size parameter x decreasing that was mentioned above (see figures B.14, B.17 for example). The most expected behavior is detected for Beijing case: for $R_I - R_P > 0.03$ we observe decrease of the fine and increase of the coarse mode retrieved and almost vanishing of these effects on the right side of fig 6.6. GSFC data also have the same trends but stronger curve oscillations for $R_I - R_P < 0.02$ for the fine mode. It results from the fine mode maximum shifting (figures B.1).

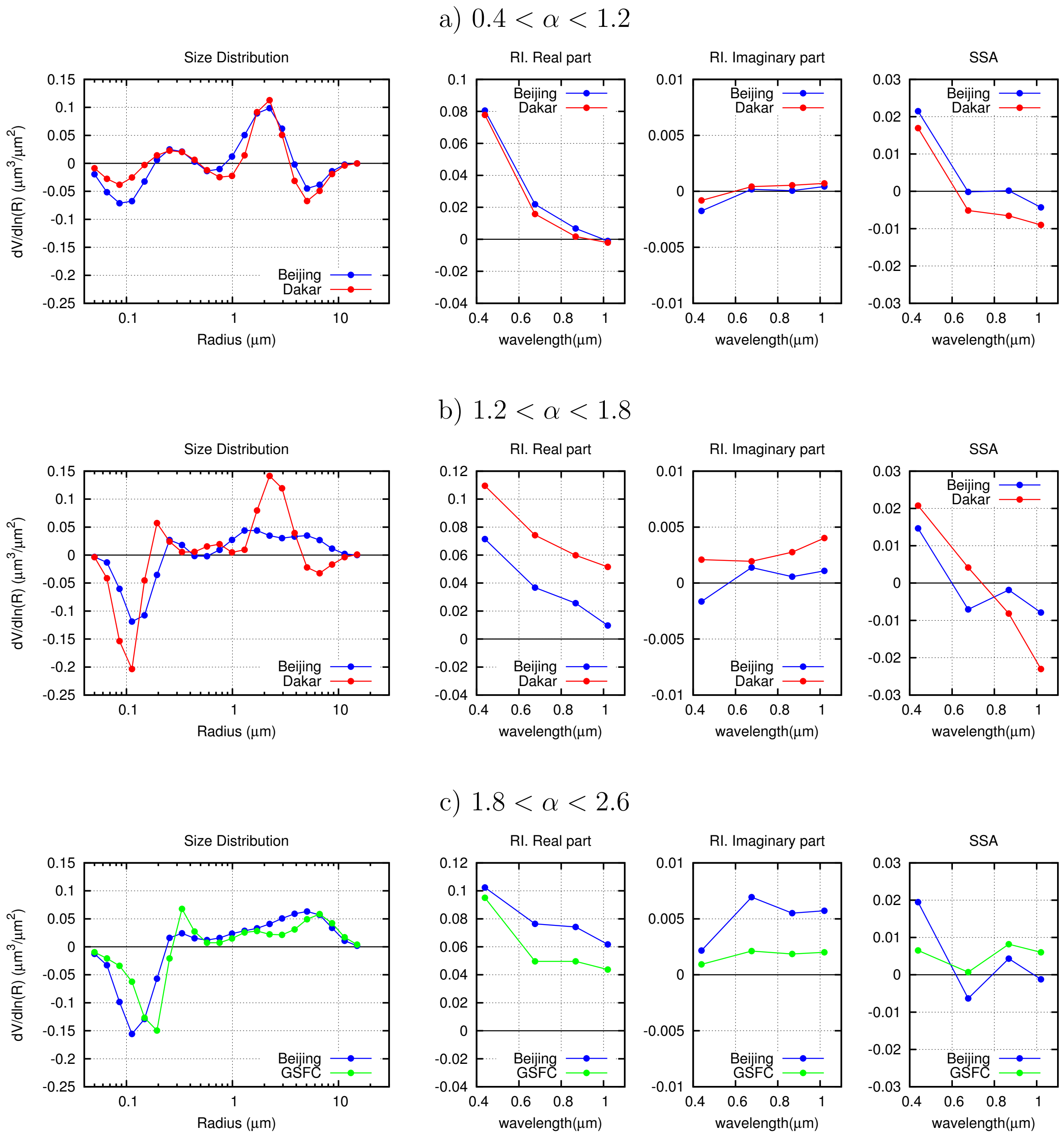

FIGURE 6.7: The average differences between P- and I-retrievals of the particles size distribution, real and imaginary parts of the refractive index and single scattering albedo for different Ångström parameter

Statistical differences between P- and I-retrievals of the refractive index real part have a quite expected shape. Namely, polarimetric data utilization increases underestimated real part especially at short wavelengths, except GSFC case where polarization increases this parameter even at large wavelengths. The estimations of the refractive index imaginary part and single scattering albedo do not show significant changes.

Figure 6.7 demonstrates the same values as the left part of the figure 6.6 (when

$R_I(440) - R_P(440) > 0.03$) but for different Ångström parameter. All inversions were separated into 3 groups: 0.4 < Å < 1.2 (big particles), 1.2 <Å< 1.8 (average size) and 1.8 <Å< 2.6 (small particles). Basically, the picture verifies the fact of increase of polarization sensitivity to aerosol properties with the particle size decreasing. It shows also several features that should be considered. First, there are some advantages of polarimetric data use for the retrieval of the size distribution and the refractive index real part even for coarse particles (0.4 < Å< 1.2) as it is seen from the first line of figure 6.7. The results for the coarse mode dominated aerosol in Dakar and Beijing are enough close to conclude quite identical changes that polarization brings at least for these aerosol types.

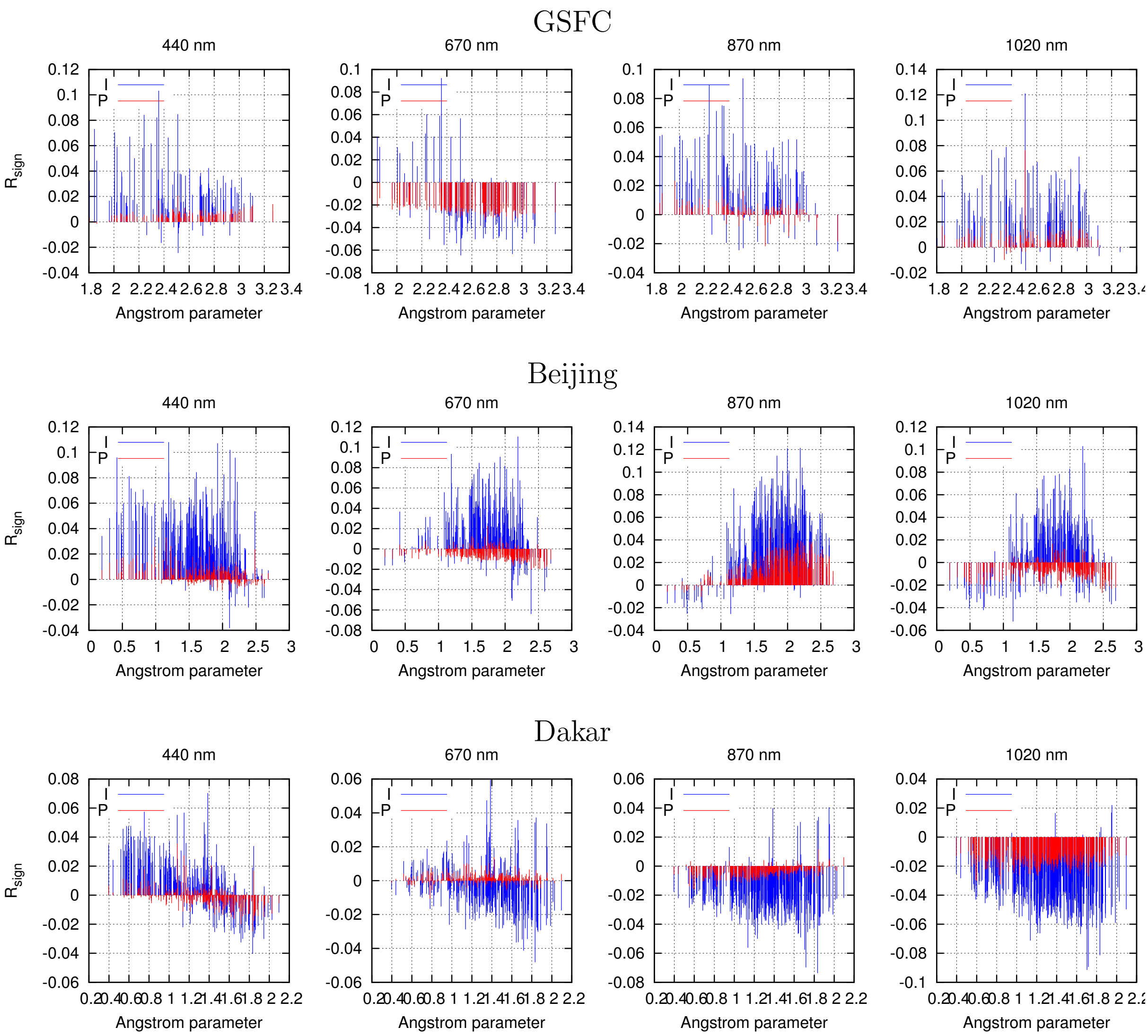

FIGURE 6.8: The relative residuals R_{sign} of DOLP simulations based on I- and P-inversion results versus Ångström parameter of the observations

The examples of the coarse mode dominated aerosols show a tendency of DOLP data underestimation by I-fit at large wavelengths (see examples for Dakar in Appendix A). Figure 6.8 represents the "relative residuals" of I- and P-fits of DOLP obtained simply as $R_{sign} = \sum_{i=1}^{n}(DOLP_i^{meas} - DOLP_i^{fit})/n$ instead of eq. (6.3) to demonstrate a nature of discrepancy (i.e. underestimation or overestimation) between polarization measurements and their fits. For coarse mode dominated aerosol (Dakar case) DOLP data are totally underestimated at 870 and 1020 nm in contrast with GSFC and Beijing. It leads to the coarse mode underestimation and, sometimes, to overestimation of the real part of the refractive index by I-retrieval (see figures B.14, B.16, B.17). The second artifact occurs in contrast with general trend to underestimation of the real part, and appears mainly as a result of the polarimetric data underestimation at large wavelengths (i.e. usually without pronounced discrepancy in the DOLP estimations at short wavelengths). This artifact is observed not often and eliminates in general statistics used for this analysis (figures 6.6, 6.7). To show it other constrains on the residual of the P- and I- DOLP fits and Ångström parameter were applied: $R_I(440) - R_P(440) < 0.02$, $R_I(1020) - R_P(1020) > 0.02$ and $\alpha \leqslant 1.2$ together. The results for Dragon site are represented in the figure 6.9. The average difference in the real part retrieval is negative. The differences of other characteristics have quite the same shape as represented in the figures 6.6 and 6.7.

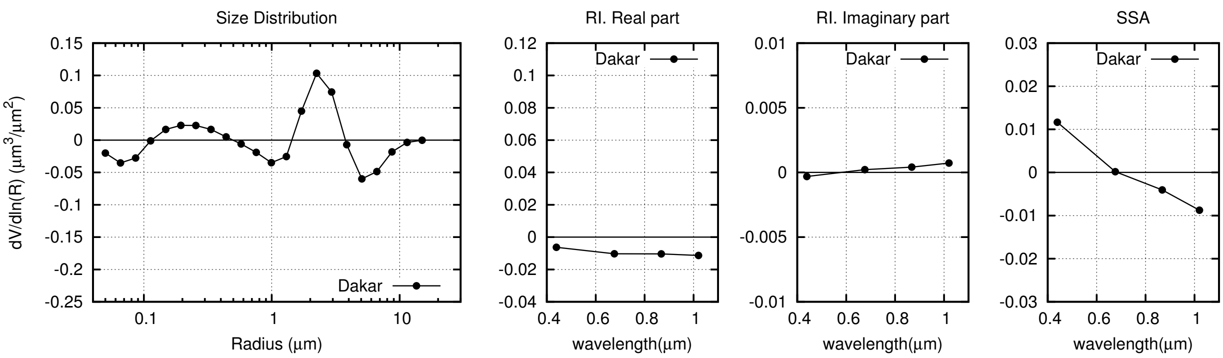

FIGURE 6.9: The average differences between P- and I-retrievals of the size distribution, the refractive index and single scattering albedo for Dakar desert dust. The averaging performed over the cases dominated by large particles ($\alpha < 1.2$), minor difference between I- and P-fits of DOLP at $\lambda = 440nm$ ($R_I(440) - R_P(440) < 0.02$) and significant difference at $\lambda = 1020nm$ ($R_I(1020) - R_P(1020) > 0.02$).

For mid-sized and small particles (second and third lines in the figure 6.7) the difference between I- and P-retrieval results increases. Moreover, except the pronounced improvements in the retrieval of the size distribution and the real part of the refractive index, some changes occur for imaginary part of the refractive index and single scattering albedo.

Moreover, we have obtained a good agreement between the inversions of the data measured in almucantar and principal plane geometries (figures 6.10, 6.11). We have compared only the retrievals without polarization measurements applying since they are not available in almucantar geometry yet. The compared measurements were taken for close observational periods to eliminate the aerosol variability.

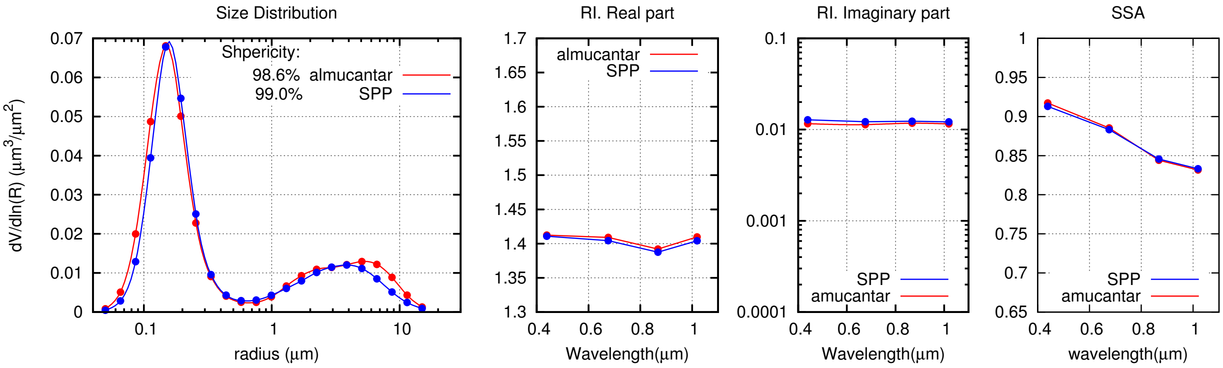

FIGURE 6.10: Comparison of almucantar and solar principal plane data retrieval. 07/11/2011, GSFC, $\theta_s = 39.0°$, $\tau_{440} = 0.43$

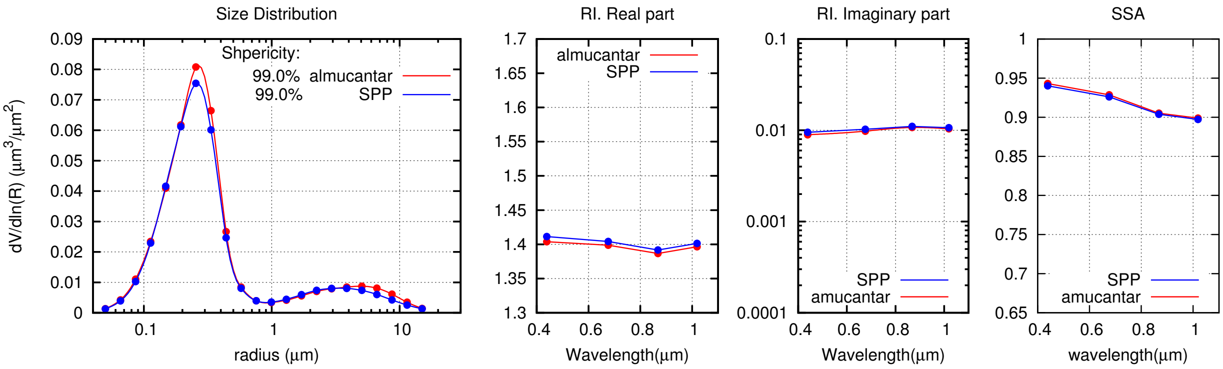

FIGURE 6.11: Comparison of almucantar and solar principal plane data retrieval. 20/11/2011, GSFC, $\theta_s = 40.0°$, $\tau_{440} = 0.67$

In conclusion of the analysis all improvements observed when polarimetric data have been used can be summarized as follow:

- Among three studied aerosol types the utilization of the polarimetric data in retrieval process has been the most beneficial for Beijing aerosol type (industrial pollution). In this case polarization has the largest sensitivity to the particle shape. It is less advantageous for GSFC and Dakar sites due to low DOLP of mainly spherical particles of the urban aerosol (GSFC) and non-spherical coarse particles of the desert dust (Dakar).

- Polarization is extremely sensitive to particle shape. Therefore, the polarimetric data use is beneficial for determination of the particle sphericity. Utilization of the addition polarization measurements increases the part of the spherical particles in Beijing and GSFC cases and decreases it for Dakar aerosol.

- Polarization usually corrects overestimated volume of the fine aerosol mode and underestimated real part of the refractive index (especially at short wavelengths). This appears as probably the most pronounced effect observed due to additional use of polarization data.

- The utilization of polarization can slightly increase the retrieved volume of the aerosol coarse mode. According to our observations it correlates with decrease of the fine mode volume. This effect appears frequently for Dakar and Beijing data.

- The imaginary part of the refractive index and single scattering albedo sometimes can be slightly corrected too. But this feature appears rarely to be statistically not significant.

- DOLP has the largest value for small non-spherical particles. Hence polarimetric data have the most pronounced sensitivity to the fine mode of the size distribution and the real part of the refractive index especially at short wavelengths.

Chapter 7

Conclusions

Inclusion of the polarimetric measurements into protocol of observations produces additional information content that allows to significantly increase the accuracy of aerosol characterization by passive remote sensing. Already widely employed in satellite monitoring, this method was also very promising for ground-based observations, but its implication was pulled back by the absence of reliable devices and appropriate tools for data processing and analysis. This situation has been changed after developing the solar radiometer Cimel CE318-DP registering polarization of radiation in addition to the observation of total atmospheric radiance. This instrument has been elaborated by CIMEL company and have a potential to be widely distributed within AERONET network. This thesis presents the study aimed to fully include the polarization data to the routine inversion of the ground-based observations and analysis of the retrieval results.

In general, the study revealed considerable improvements obtained by the polarization measurements applying for the aerosol characterization by the inversion of ground-based observations. In order to efficiently use the advantages of the new DWP sunphotometer for aerosol remote observations a new software has been developed. The program implements the complex handling of the raw measured data and prepares the input file for inversion procedure in routine regime. It includes data calibration, normalization and sorting daily data. The additional cloud screening procedures have been developed to improve the quality control of the angular measurements of the sky radiance intensity and polarization in both almucantar and principal plane geometries. Moreover, the program conducts the calculation of the DOLP from observed polarized radiance, improved accounting of the surface reflection, calculation of the required zenith, azimuth and scattering angles depending on the observation configuration, introducing various inversion settings parameters, etc. Also the preliminary visualization of the input data and inversion results is available now.

Using this product both synthetic data and the real measurements have been used to investigate the impact of polarization data utilization on the retrieval of aerosol properties. The results of the study are demonstrated and analyzed in chapter 6. The sensitivity test has been conducted using the data simulated on the basis of five main aerosol models. These are desert dust, urban industrial, urban-clean, biomass burning and maritime aerosols. First, undisturbed synthetic data have been processed to verify the accuracy of the inversion code. This step has shown the precise reproducing of the model values by simulated data processing. Further, the sensitivity of the retrieval to polarimetric data applying has been investigated by inversion of synthetic data with included errors and offsets. Random noises, biases in measurements of optical thickness and pointing errors have been considered. The results have revealed the increase of inversion stability in presence of polarization data especially for retrieval of the fine aerosol mode and the real part of the refractive index. This advantages has mainly been observed in the cases of aerosols with pronounced concentration of fine particles for all considered errors. The coarse mode dominated aerosols as desert dust has revealed minor sensitivity to the presence of additional polarimetric information.

However, sensitivity study reveals very high sensitivity of the polarization data to the systematic error in angular pointing. The advantage of polarimetric data utilization for retrieval improvement is ambiguous in the case of erroneous pointing especially for the maritime aerosols. Namely, the polarization utilization results in misestimation of the size distribution fine mode and the refractive index real part. It should be noted, that I-retrieval estimate this parameters erroneously as well. The utilization of additional polarimetric data leads to excessive correction of this values. The most probable reason of this artifact consists in both pronounced sensitivity of the polarization data to the angular shifting and high sensitivity of the retrieved parameters to the polarimetric information applying. Indeed, the bias in DOLP results in opposite effect than the same bias in radiance intensity data that, in turn, leads in excessive correction of the fine aerosol mode and the refractive index real part since high sensitivity of these characteristics to the polarimetric information. Especially this effect is pronounced for the retrieval of the refractive index real part in the cases of urban-industrial and maritime aerosol models. Nevertheless, the use of polarization data essentially decrease the spectral dependence of the real part retrieved. These results indicate importance of the further investigation conducting on the real field measurements for various aerosol types were not considered in current study.

The retrieval of the real field measurements has been performed for extended data set of AERONET observations conducted at three different sites. The measurements form GSFC (DRAGON campaign), Beijing and Dakar have been processed and analyzed. The considered data represent different aerosol types: urban-clean, industrial pollution and desert dust respectively. The retrieval has been carried out for the data measured in different observation geometries (almucantar and solar principal plane) with and without utilization of polarization measurements. The most pronounced sensitivity to the use of polarization data is detected for retrieval of the industrial aerosol properties (Beijign) that results in the notable retrieval improvements. Somewhat less sensitivity is revealed for the cases of clean urban aerosol (GSFC) and desert dust (Dakar). Most likely, the obtained results are determined by differences in typical particle shape and size of considered aerosol types. Beijing industrial pollution contains significant volume of both fine and coarse aerosol modes represented by particles of different shapes whereas GSFC urban aerosol contains mainly small spherical particle and desert dust is the aerosol dominated by coarse non-spherical particles (Dubovik et al., 2002a). According to Li et al. (2009), polarization measurements reveal the high sensitivity to the particle shape of the fine mode that determine their advantage for Beijing data.

Thus, the analysis confirms the expected high sensitivity of polarimetric data to the aerosol particle shape. We receive a correction of non-spherical particle fraction for all aerosols under study. Generally, polarization data utilization increases the amount of non-spherical particles for Dakar data and decreases it in other considered cases.

Evidently, these changes are in a good agreement with the accepted aerosol models (Dubovik et al., 2002a).

The main benefits that polarization brings to aerosol characteristics retrieval are the correction of the overestimated volume of the fine aerosol mode and underestimated real part of the refractive index especially at short wavelengths. These artifacts were previously described by Li et al. (2009). The imaginary part of the refractive index and single scattering albedo can be slightly corrected too, but these features are rarely observed and could be neglected in comparison with other changes. Frequently the retrieved value of the size distribution coarse mode is changed towards increasing. The effect occurs mainly for aerosol containing pronounced coarse mode as in the cases of Beijign and Dakar.

Furthermore, the measurements obtained in almucantar configuration were inverted. Since polarimetric information is not available for observations in almucantar, we compared the retrieval results received for the measurements obtained at close time intervals without use of polarization data. The comparison shows a good agreement between them that indicates the high level of data consistency and accuracy of the methodology applied.

Unfortunately, the polarimetric observations by DWP-photometer is rarely available now and only in solar principal plane configuration. Moreover, such instruments are deployed at few sites of AERONET network. Thus, the further investigations can be focused on the new observation conducting and the analysis of the polarization information utilization for improving characterization of the other aerosol types.

Appendix A

Illustrations of the sensitivity study results

A.1 Sensitivity to the random noises

A.1.1 Urban-industrial aerosol (Mexico model)

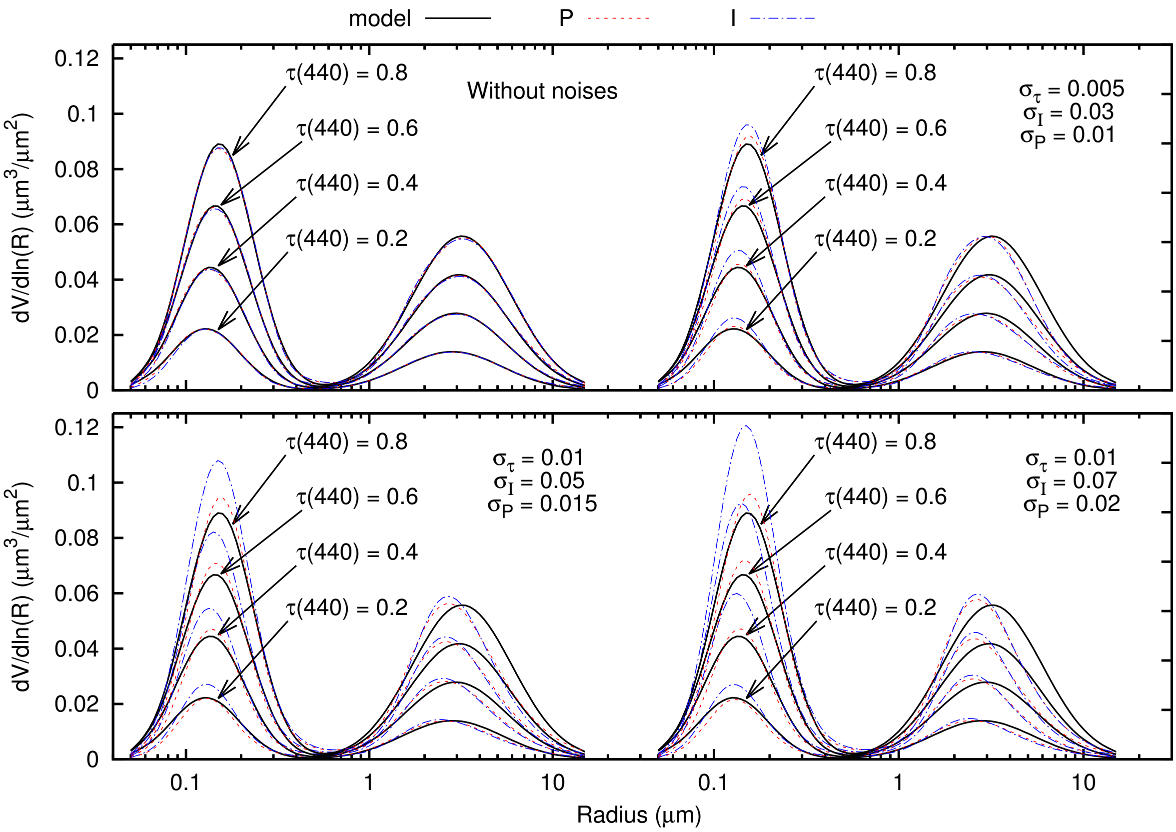

FIGURE A.1: Volume size distribution retrieved with and without polarization data applying for different AOD levels and with different noises added.

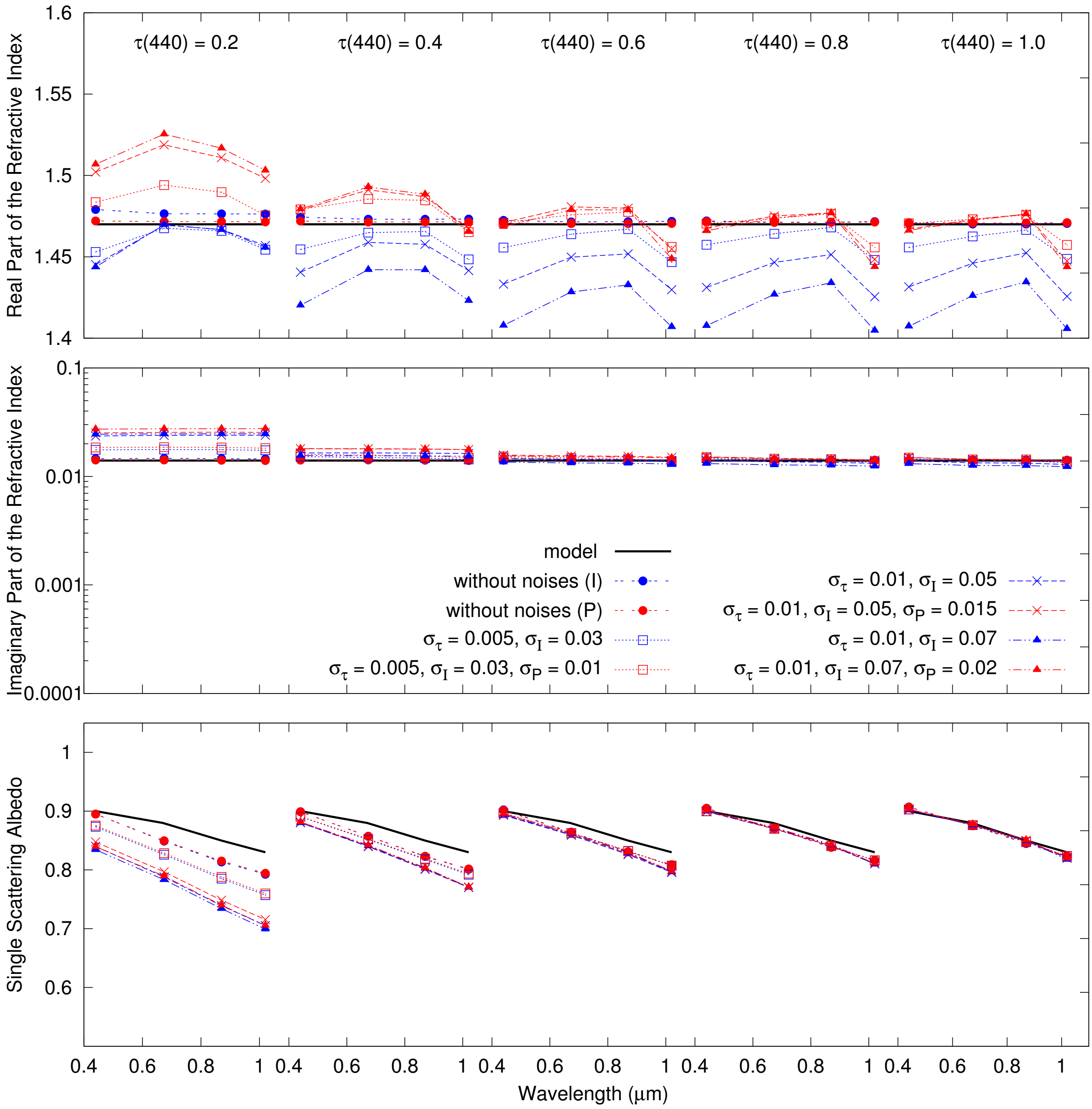

FIGURE A.2: Complex refractive index and single scattering albedo retrieved with and without polarization data applying for different AOD levels and with different noises added.

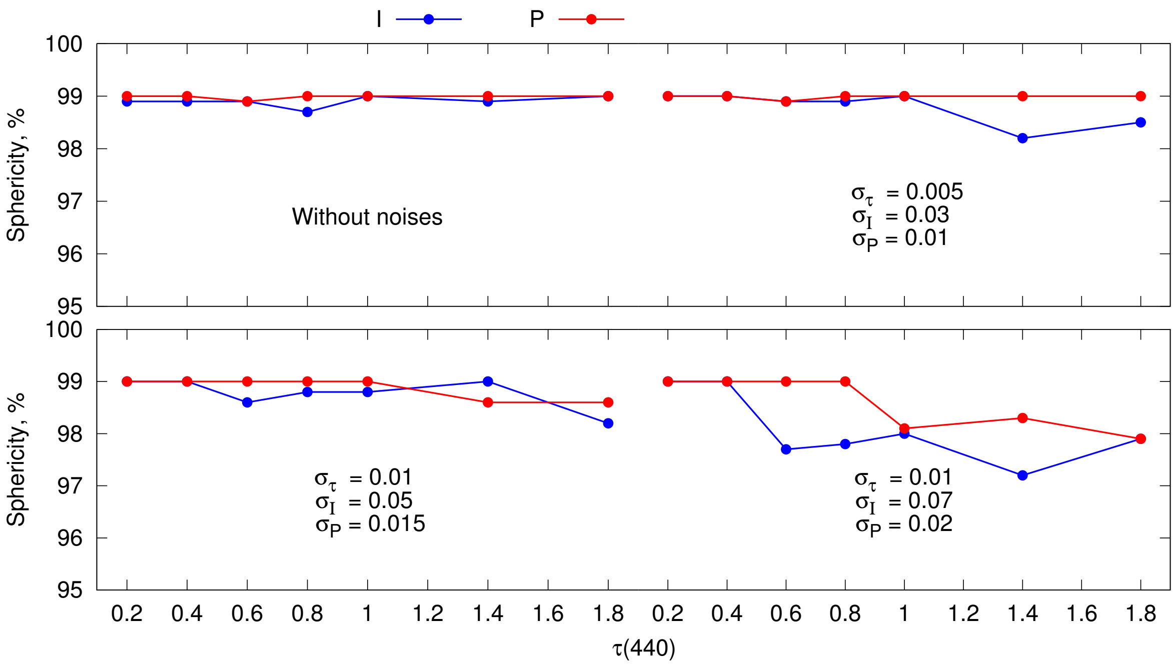

FIGURE A.3: Percentage of the spherical particles retrieved with and without polarization data applying for different AOD levels and with different noises added.

A.1.2 African savanna aerosol (Mongu model)

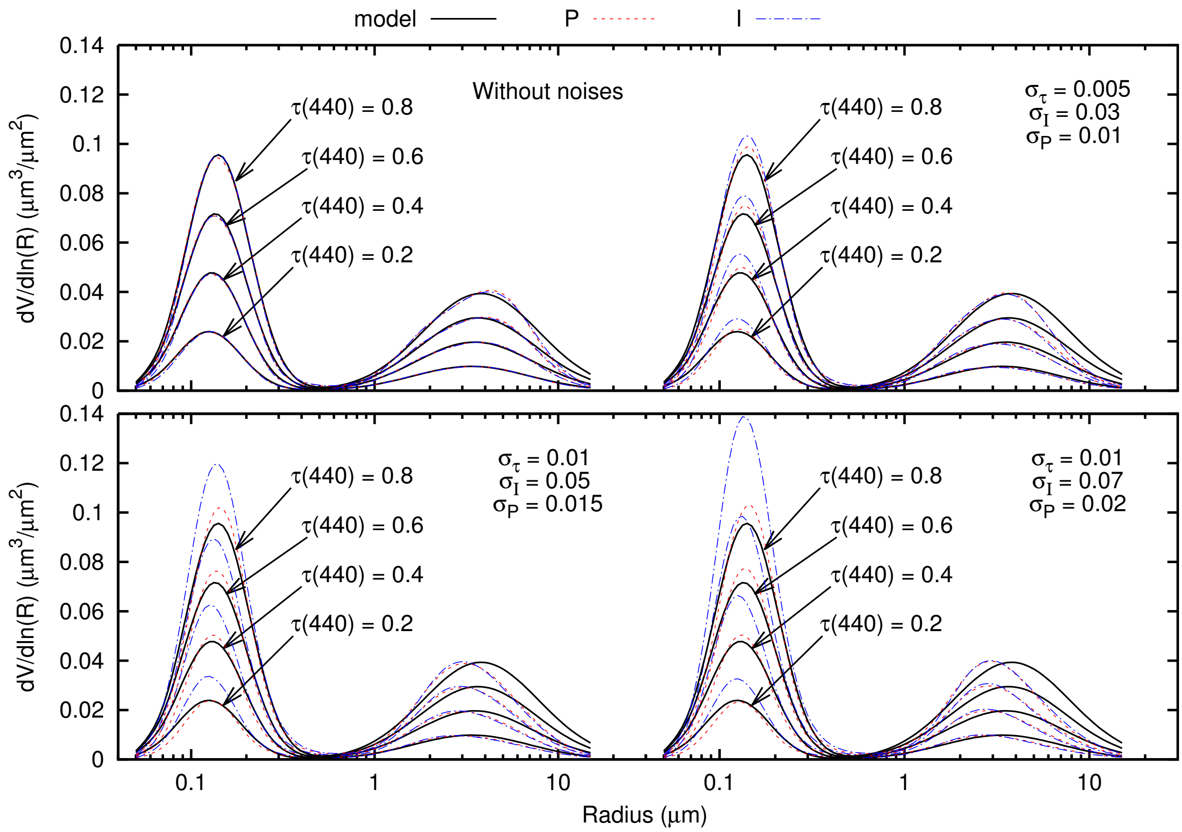

FIGURE A.4: Volume size distribution retrieved with and without polarization data applying for different AOD levels and with different noises added.

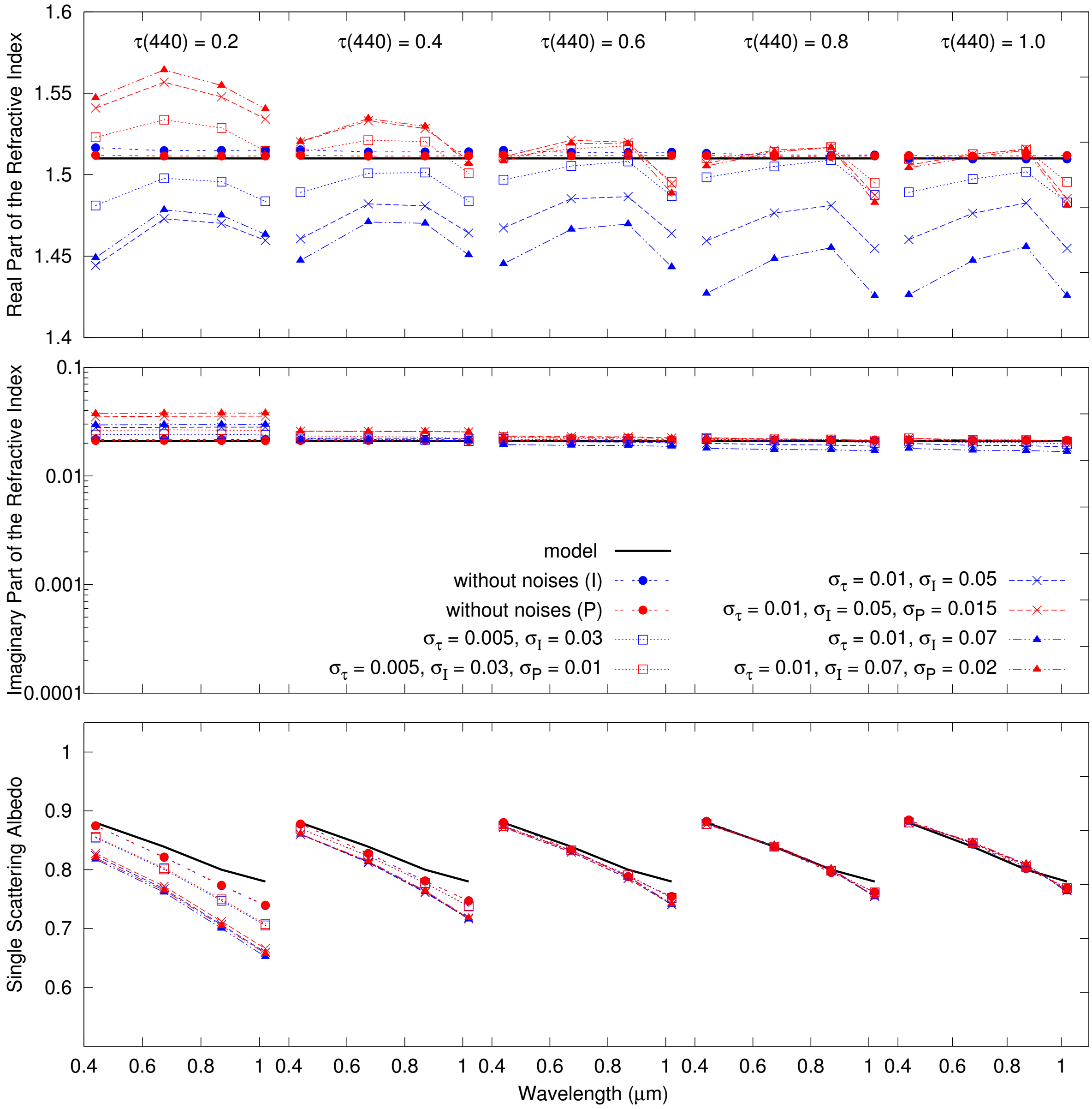

FIGURE A.5: Complex refractive index and single scattering albedo retrieved with and without polarization data applying for different AOD levels and with different noises added.

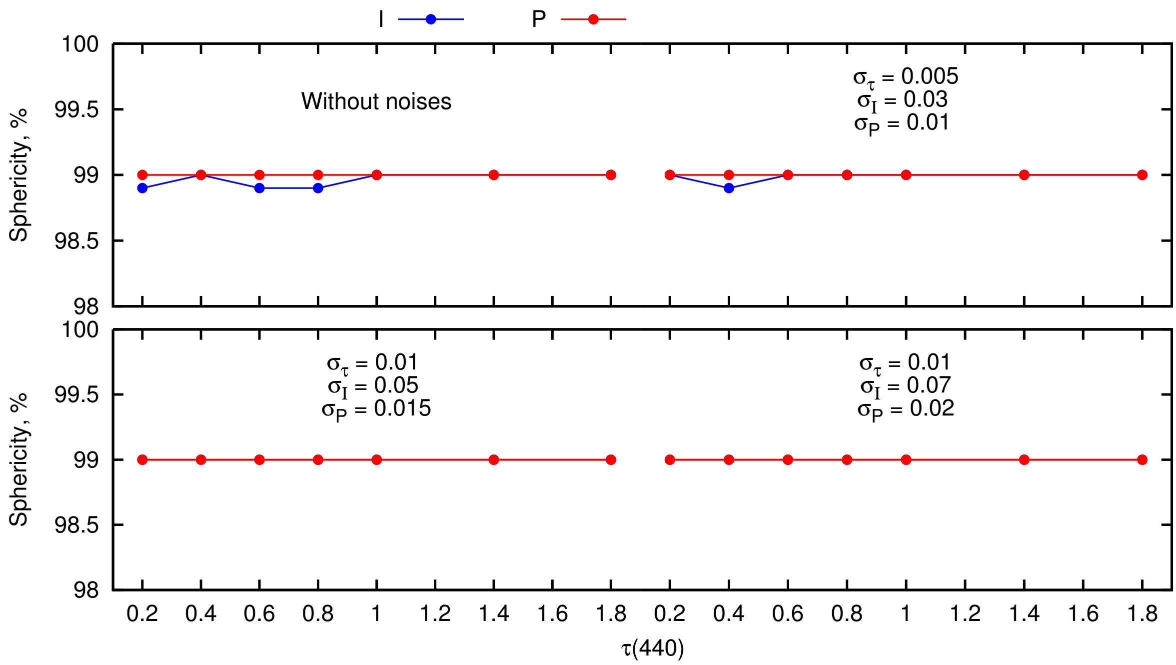

FIGURE A.6: Percentage of the spherical particles retrieved with and without polarization data applying for different AOD levels and with different noises added.

A.1.3 Urban-industrial aerosol (GSFC model)

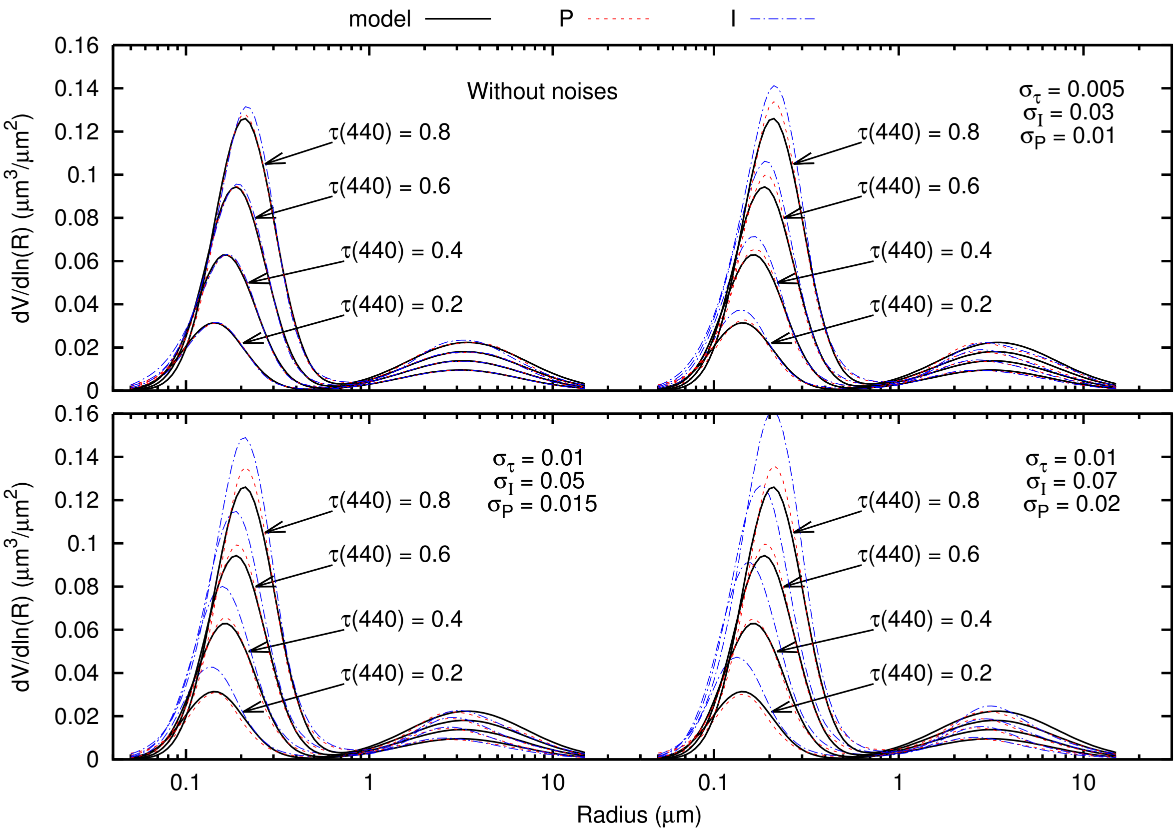

FIGURE A.7: Volume size distribution retrieved with and without polarization data applying for different AOD levels and with different noises added.

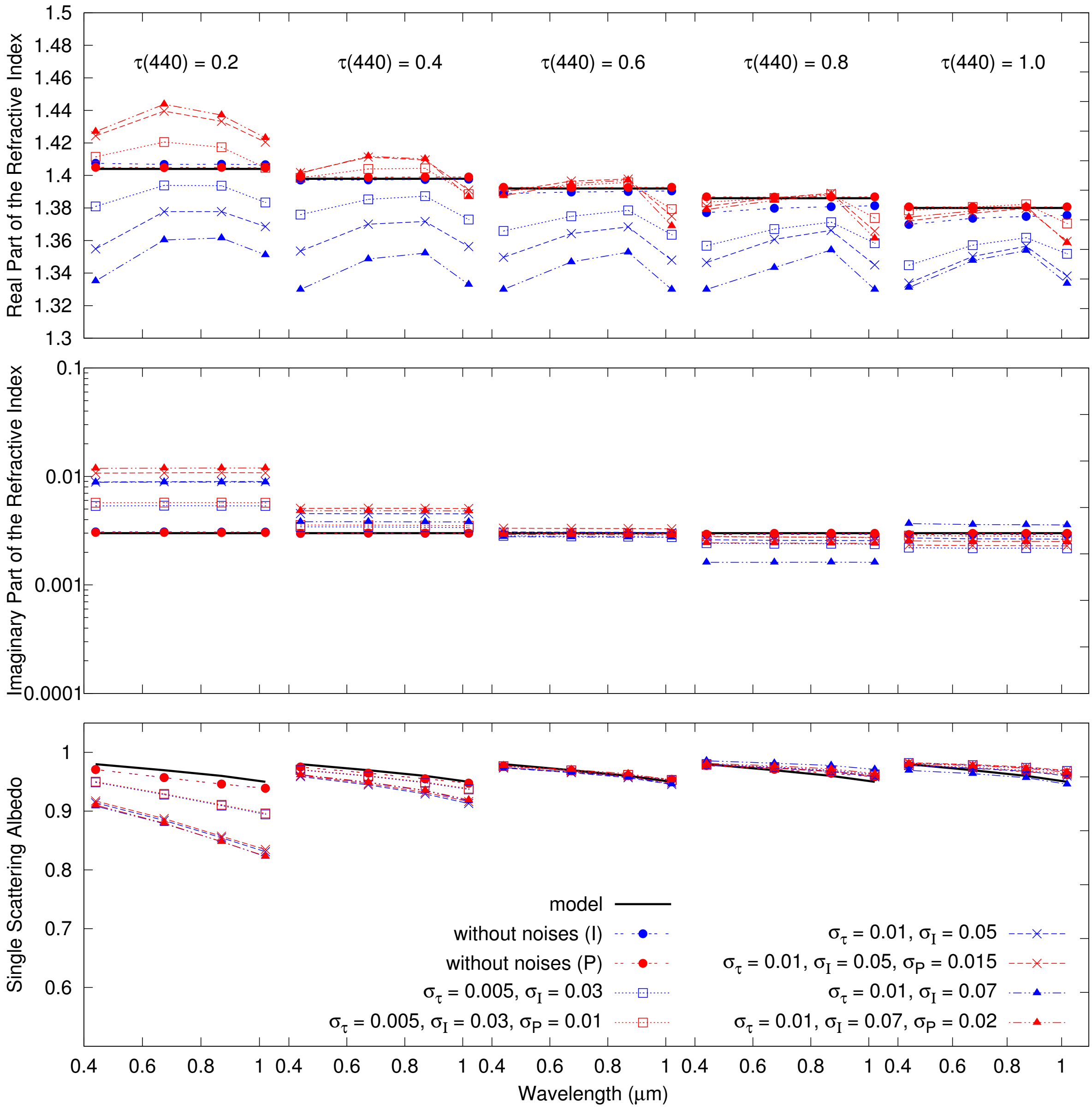

FIGURE A.8: Complex refractive index and single scattering albedo retrieved with and without polarization data applying for different AOD levels and with different noises added.

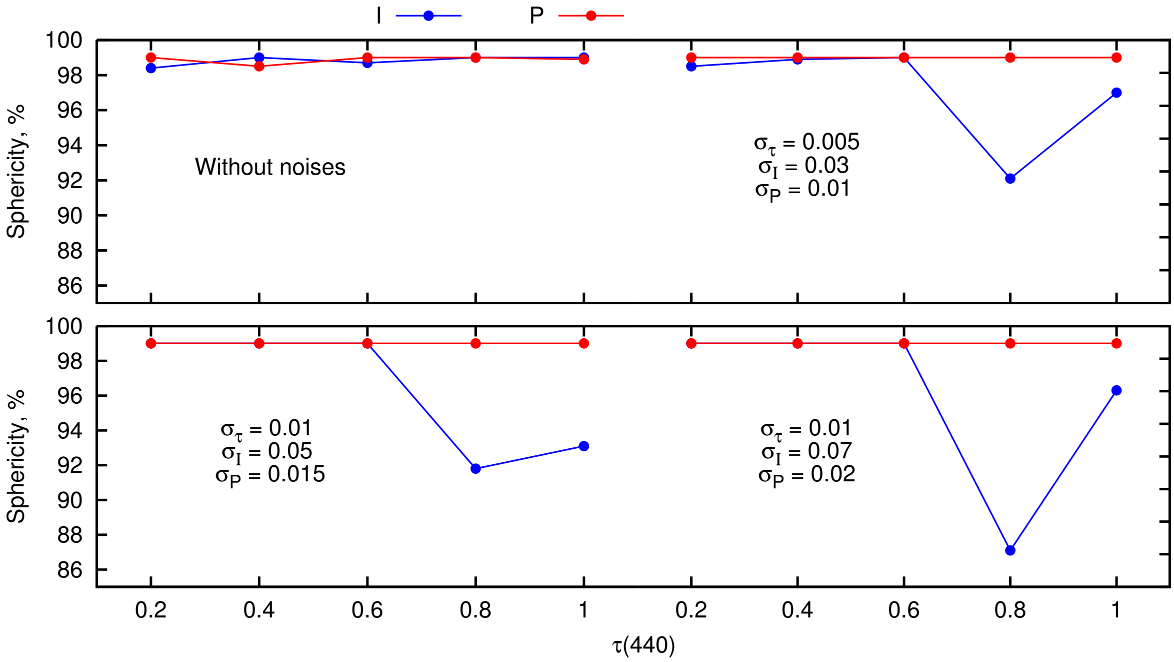

FIGURE A.9: Complex refractive index and single scattering albedo retrieved with and without polarization data applying for different AOD levels and with different noises added.

A.1.4 Desert dust aerosol (Solar Village model)

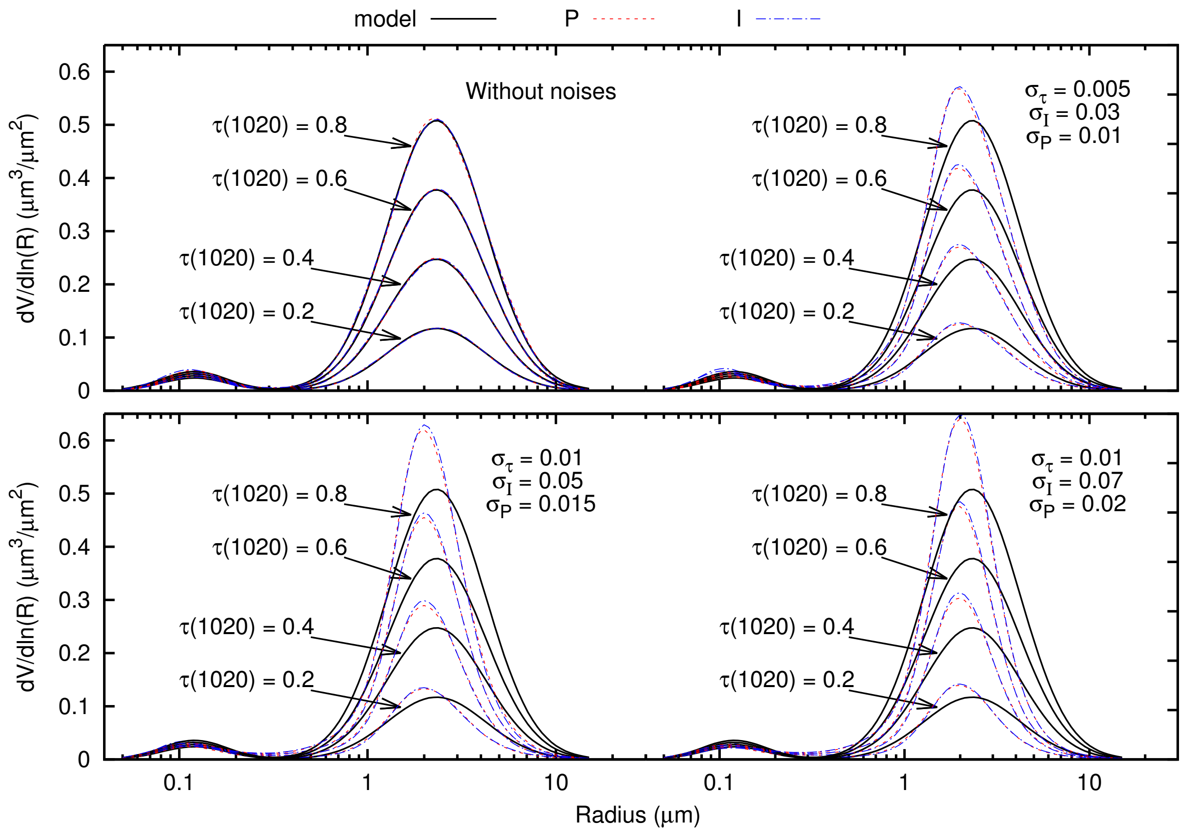

FIGURE A.10: Volume size distribution retrieved with and without polarization data applying for different AOD levels and with different noises added.

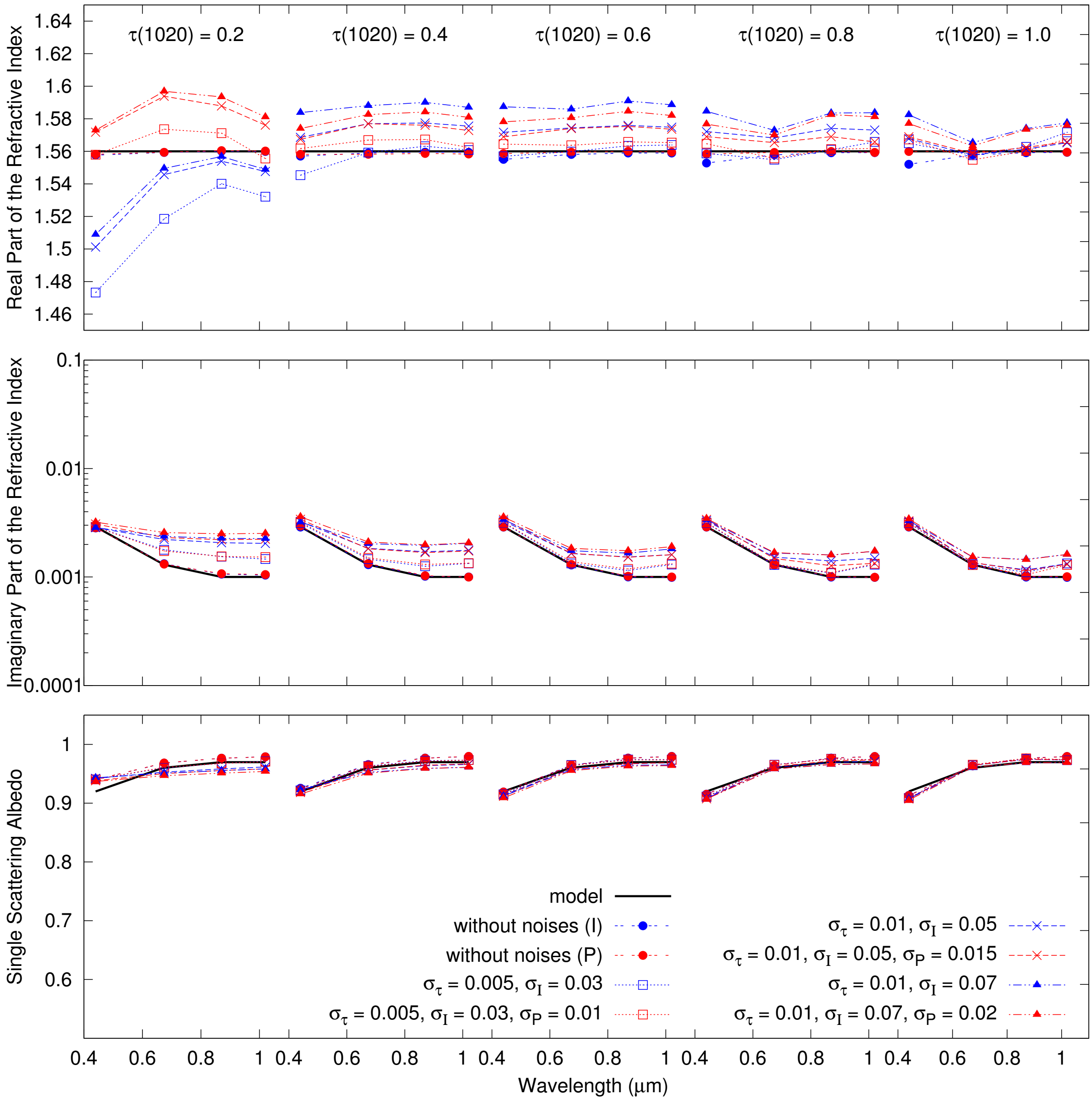

FIGURE A.11: Complex refractive index and single scattering albedo retrieved with and without polarization data applying for different AOD levels and with different noises added.

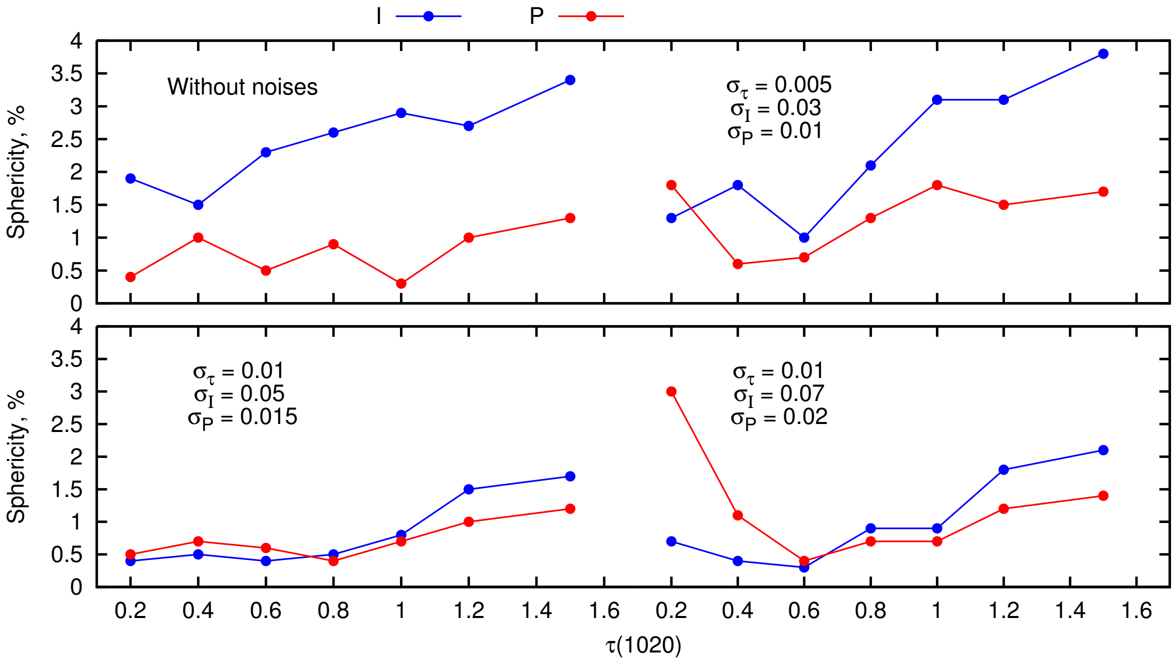

FIGURE A.12: Percentage of the spherical particles retrieved with and without polarization data applying for different AOD levels and with different noises added.

A.1.5 Oceanic aerosol aerosol (Lanai model)

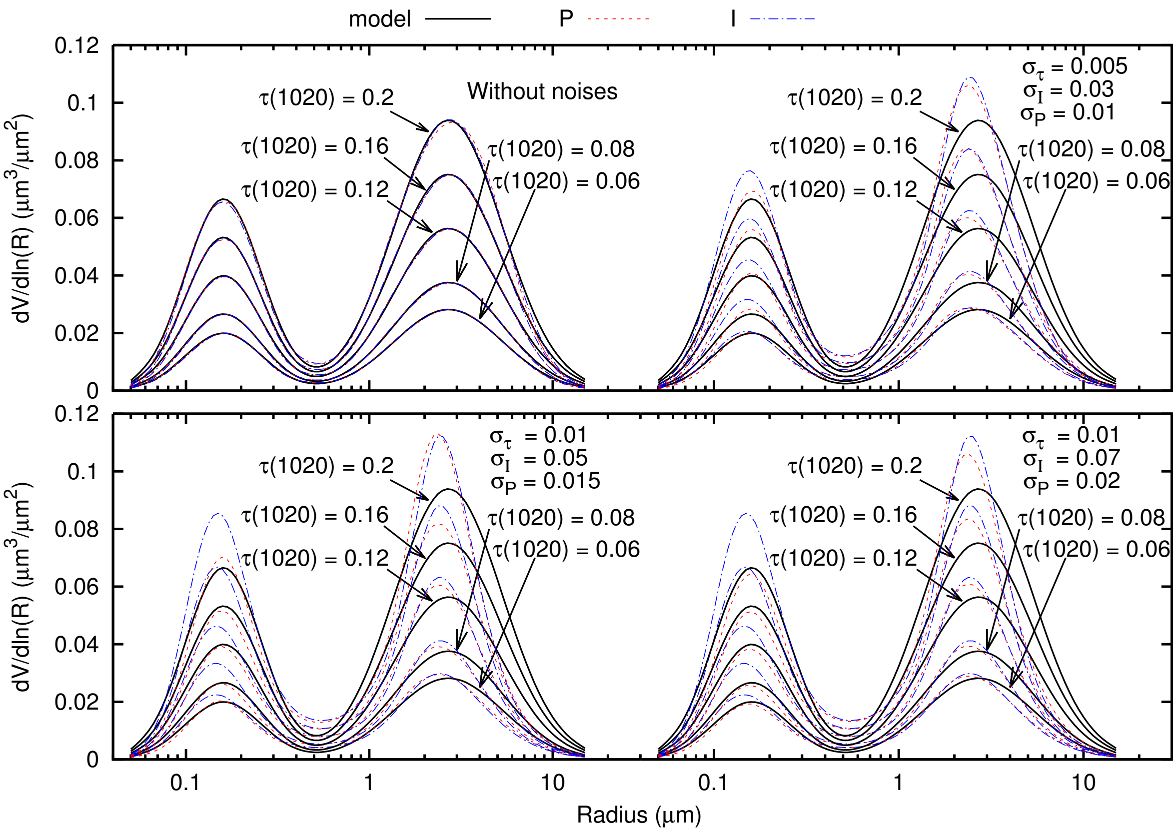

FIGURE A.13: Volume size distribution retrieved with and without polarization data applying for different AOD levels and with different noises added.

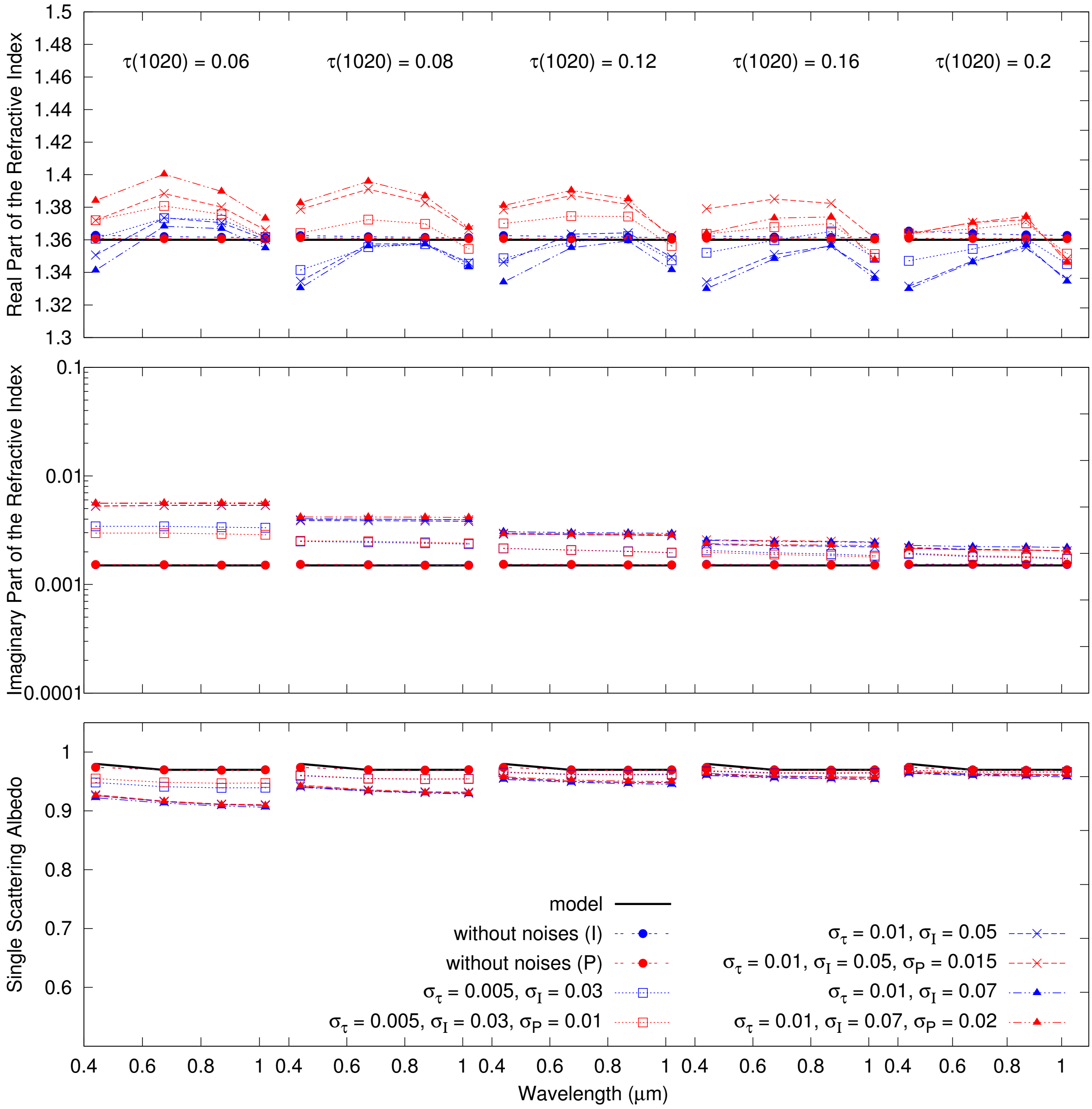

FIGURE A.14: Complex refractive index and single scattering albedo retrieved with and without polarization data applying for different AOD levels and with different noises added.

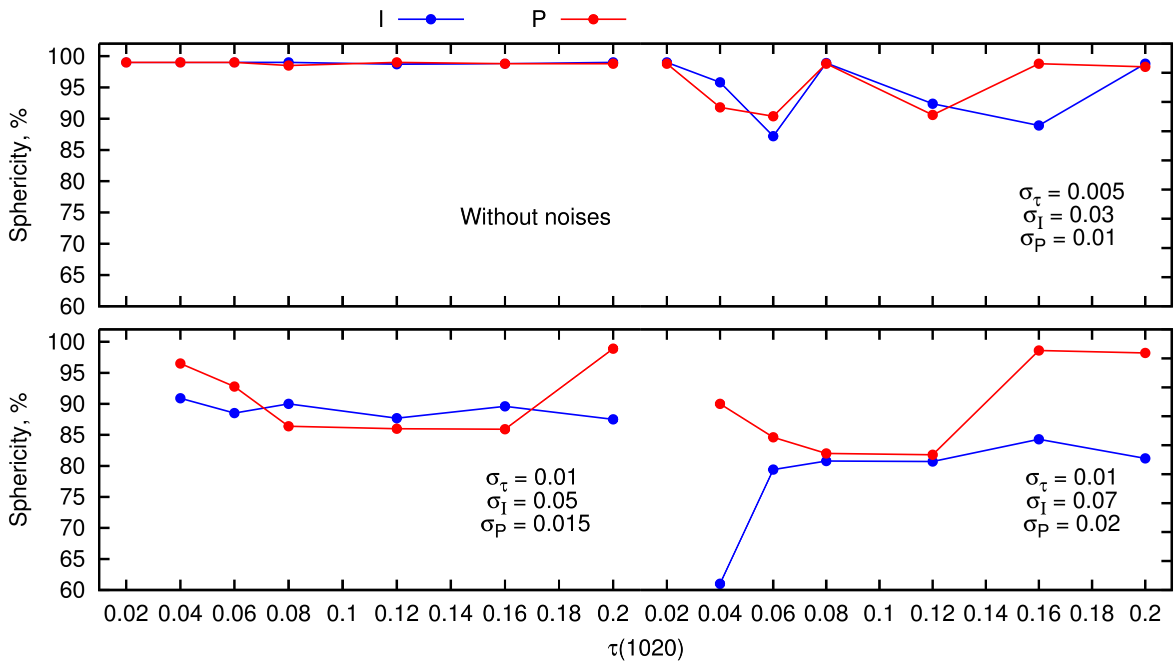

Figure A.15: Percentage of the spherical particles retrieved with and without polarization data applying for different AOD levels and with different noises added.

A.2 Sensitivity to the AOD bias

A.2.1 Urban-industrial aerosol (Mexico model)

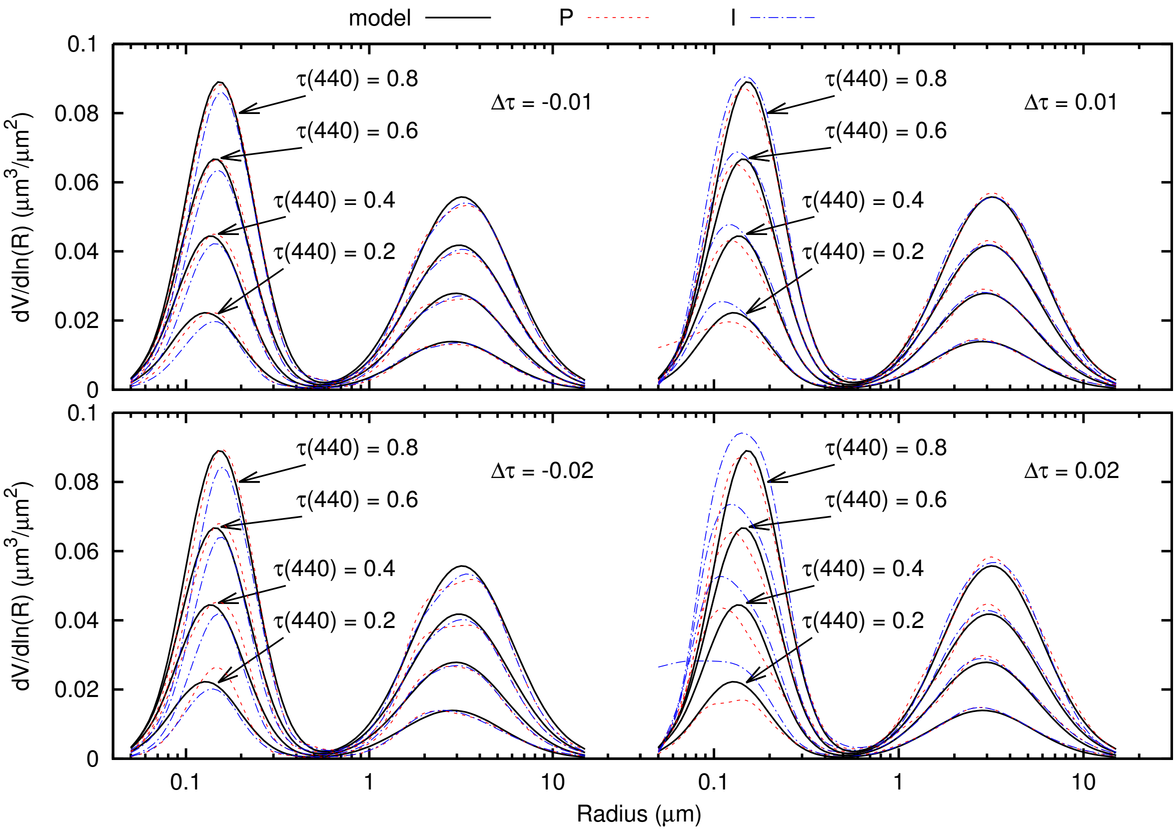

FIGURE A.16: Volume size distribution retrieved with and without polarization data applying for different AOD levels and with different noises added.

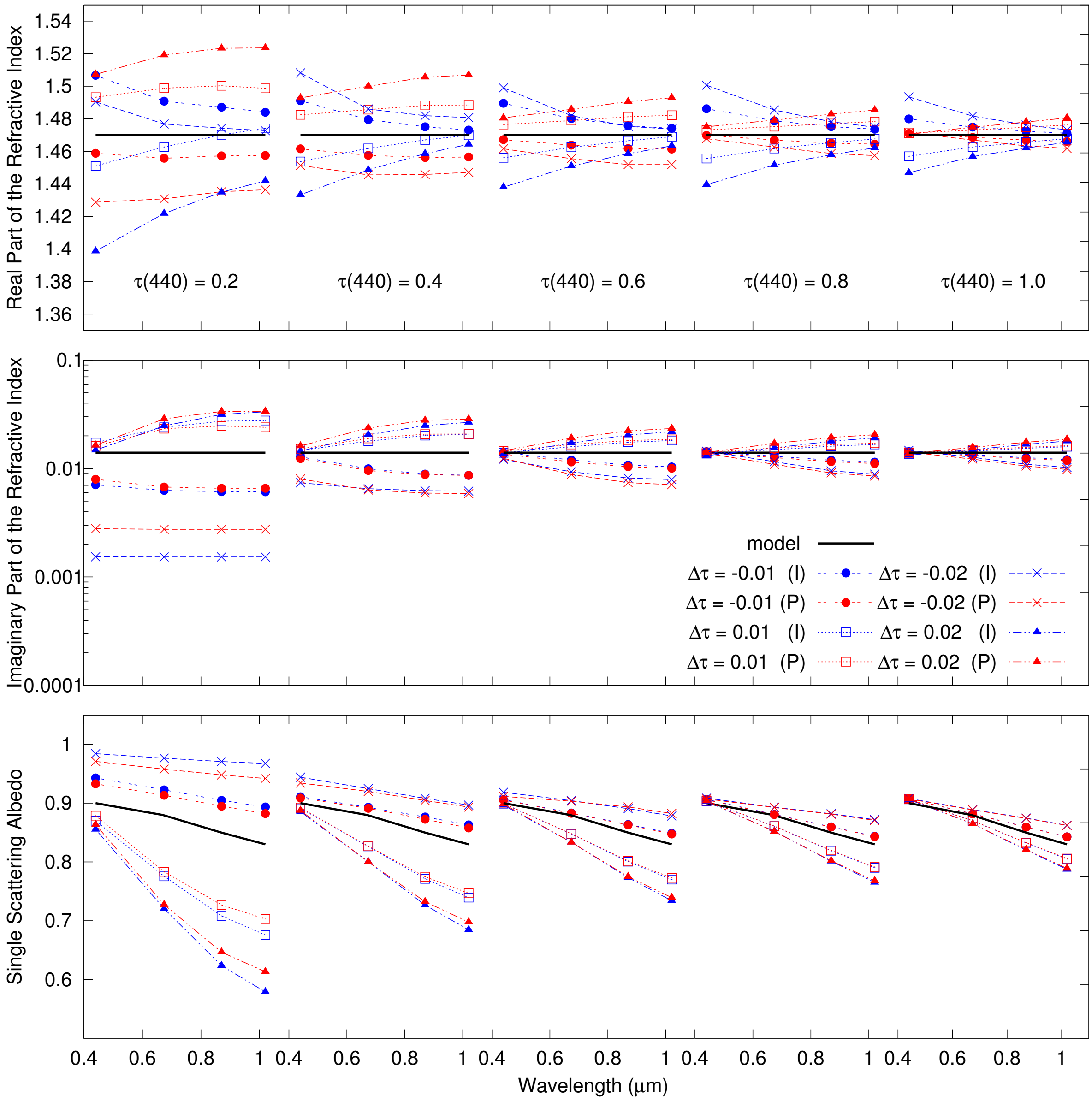

Figure A.17: Complex refractive index and single scattering albedo retrieved with and without polarization data applying for different AOD levels and with different noises added.

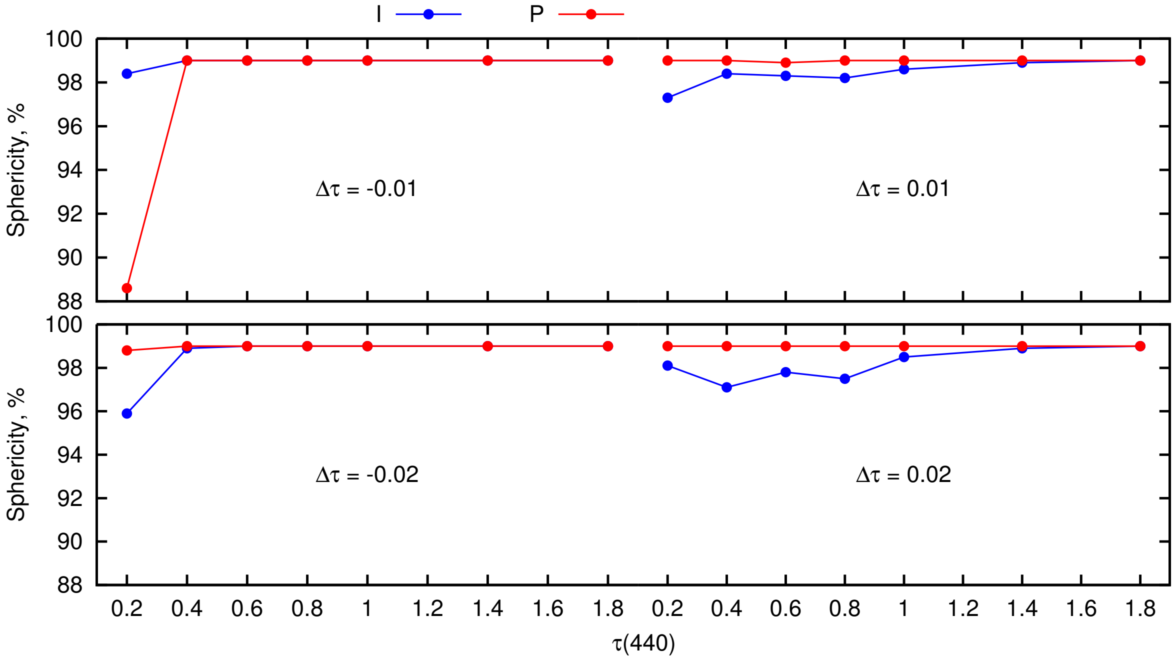

Figure A.18: Percentage of the spherical particles retrieved with and without polarization data applying for different AOD levels and with different noises added.

A.2.2 African savanna aerosol (Mongu model)

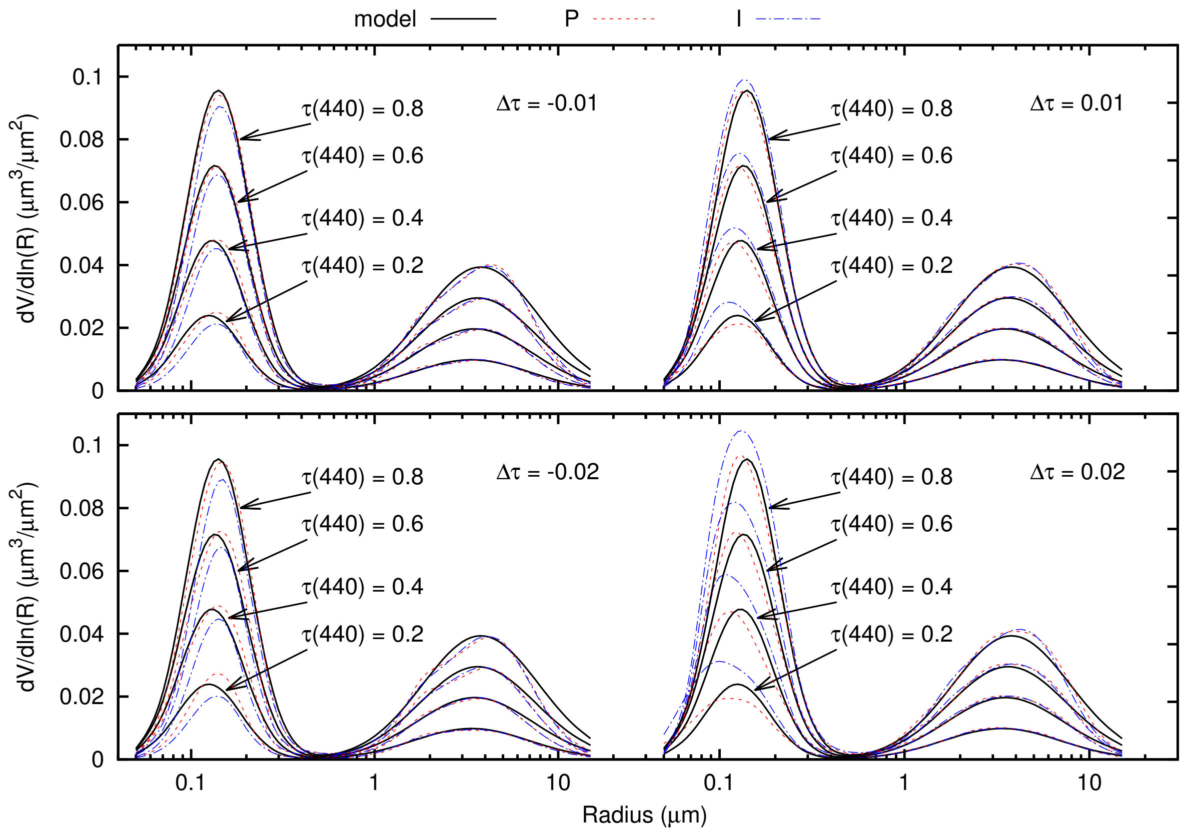

FIGURE A.19: Volume size distribution retrieved with and without polarization data applying for different AOD levels and with different noises added.

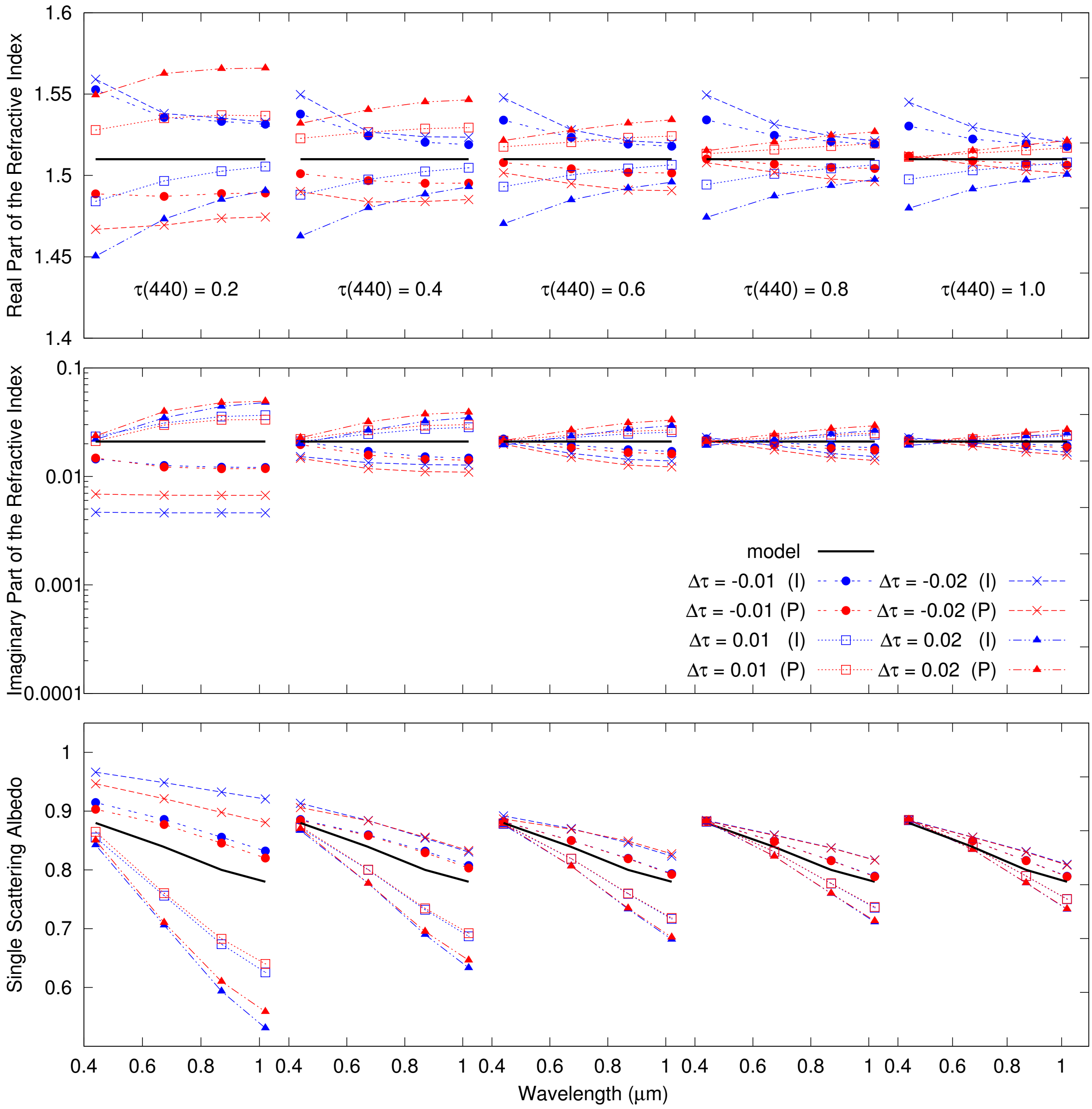

Figure A.20: Complex refractive index and single scattering albedo retrieved with and without polarization data applying for different AOD levels and with different noises added.

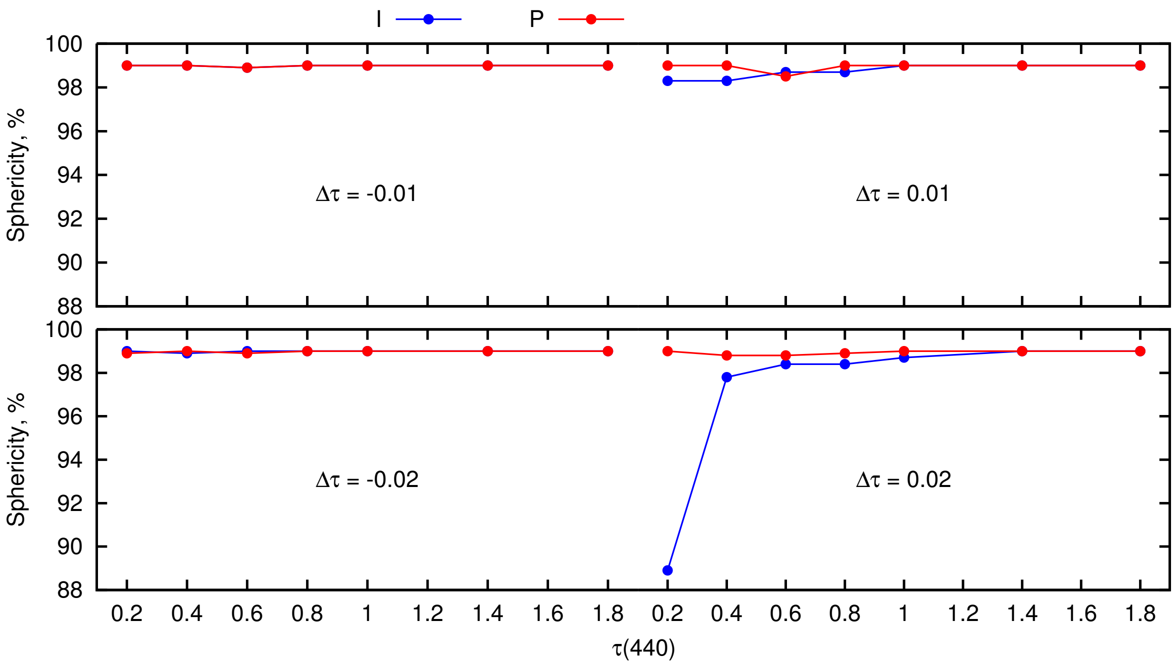

FIGURE A.21: Percentage of the spherical particles retrieved with and without polarization data applying for different AOD levels and with different noises added.

A.2.3 Urban-industrial aerosol (GSFC model)

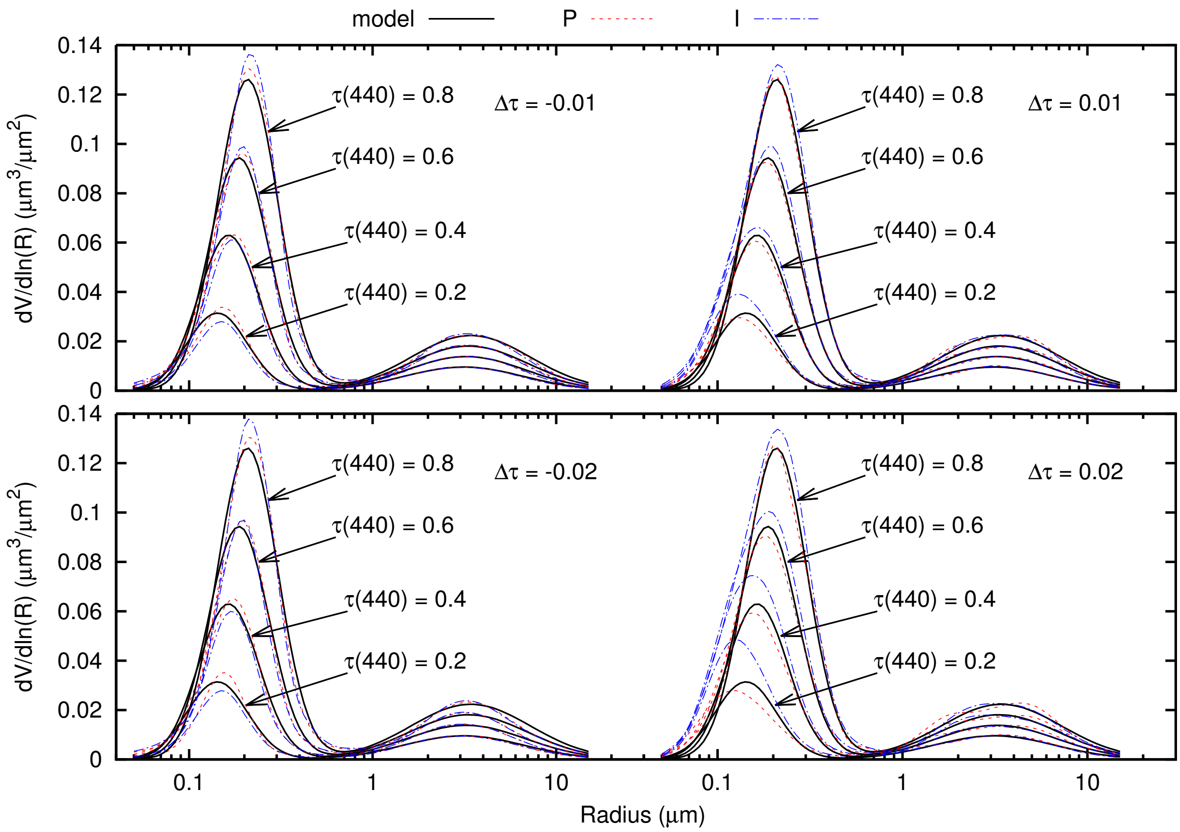

FIGURE A.22: Volume size distribution retrieved with and without polarization data applying for different AOD levels and with different noises added.

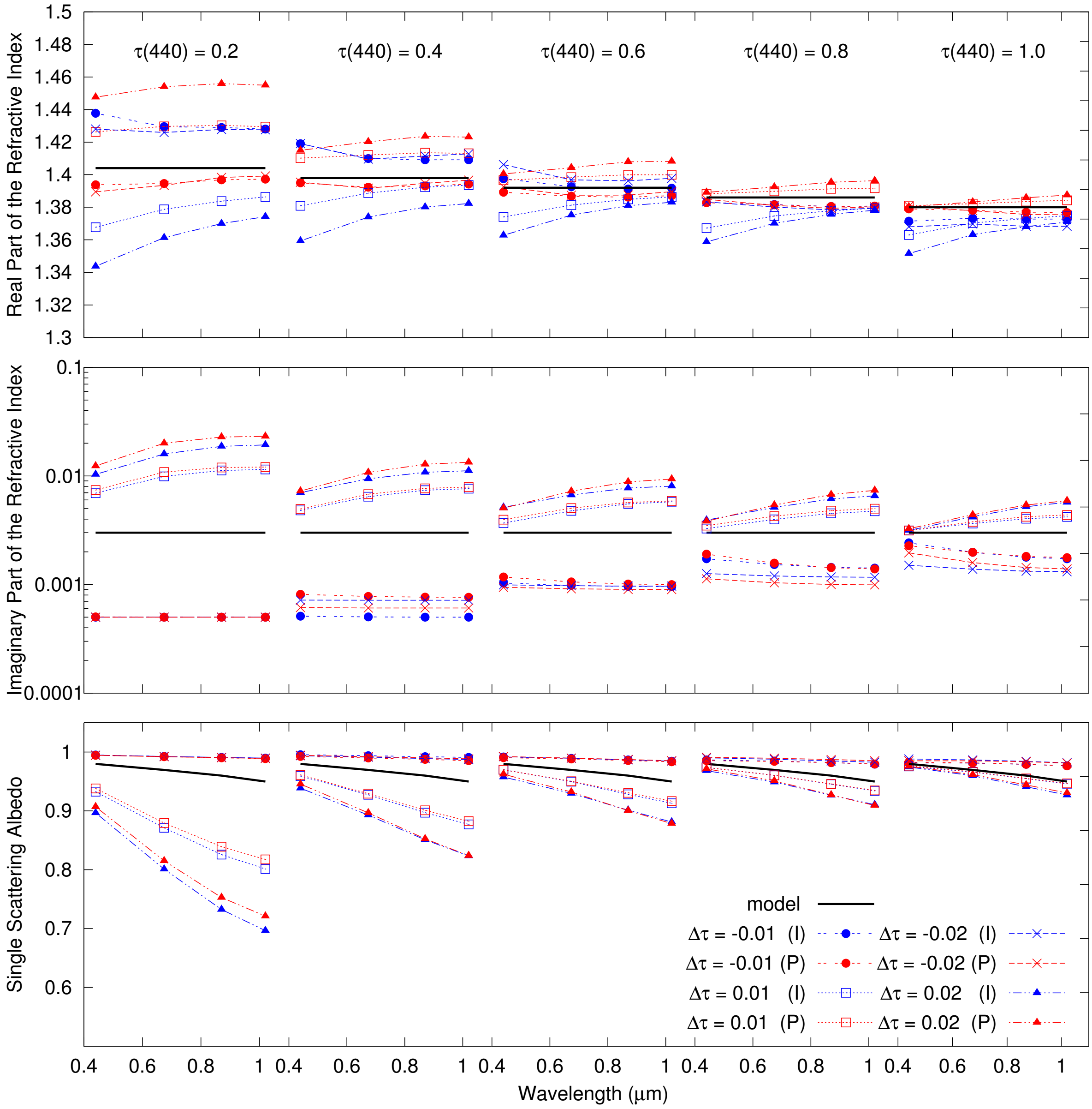

FIGURE A.23: Complex refractive index and single scattering albedo retrieved with and without polarization data applying for different AOD levels and with different noises added.

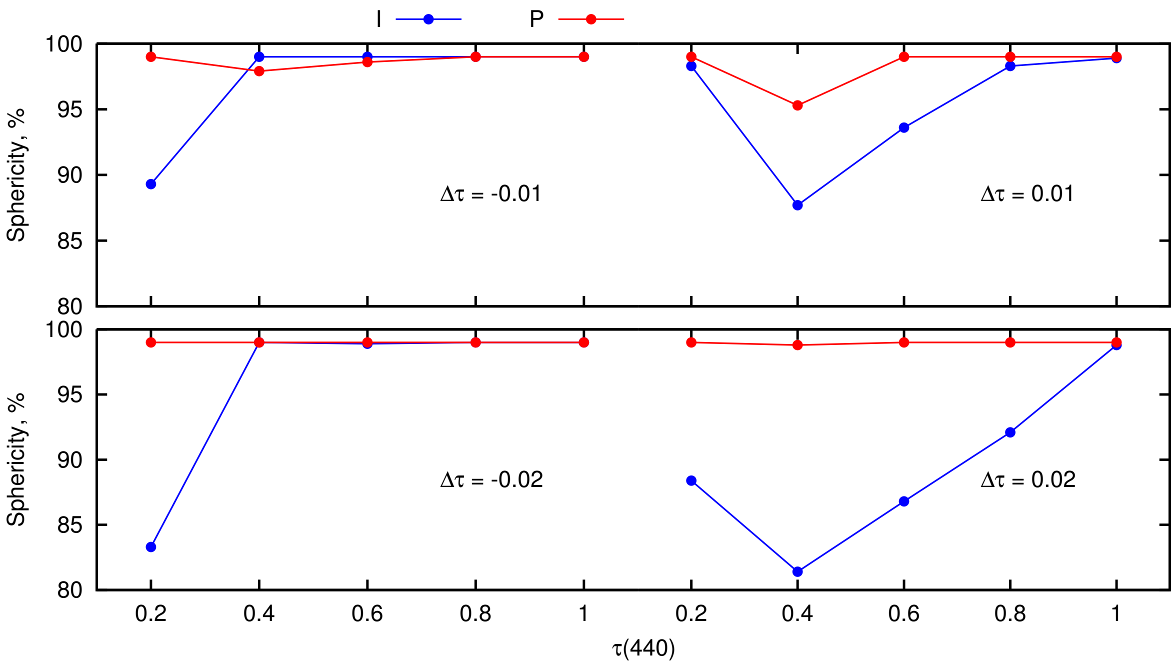

Figure A.24: Percentage of the spherical particles retrieved with and without polarization data applying for different AOD levels and with different noises added.

A.2.4 Desert dust aerosol (Solar Village model)

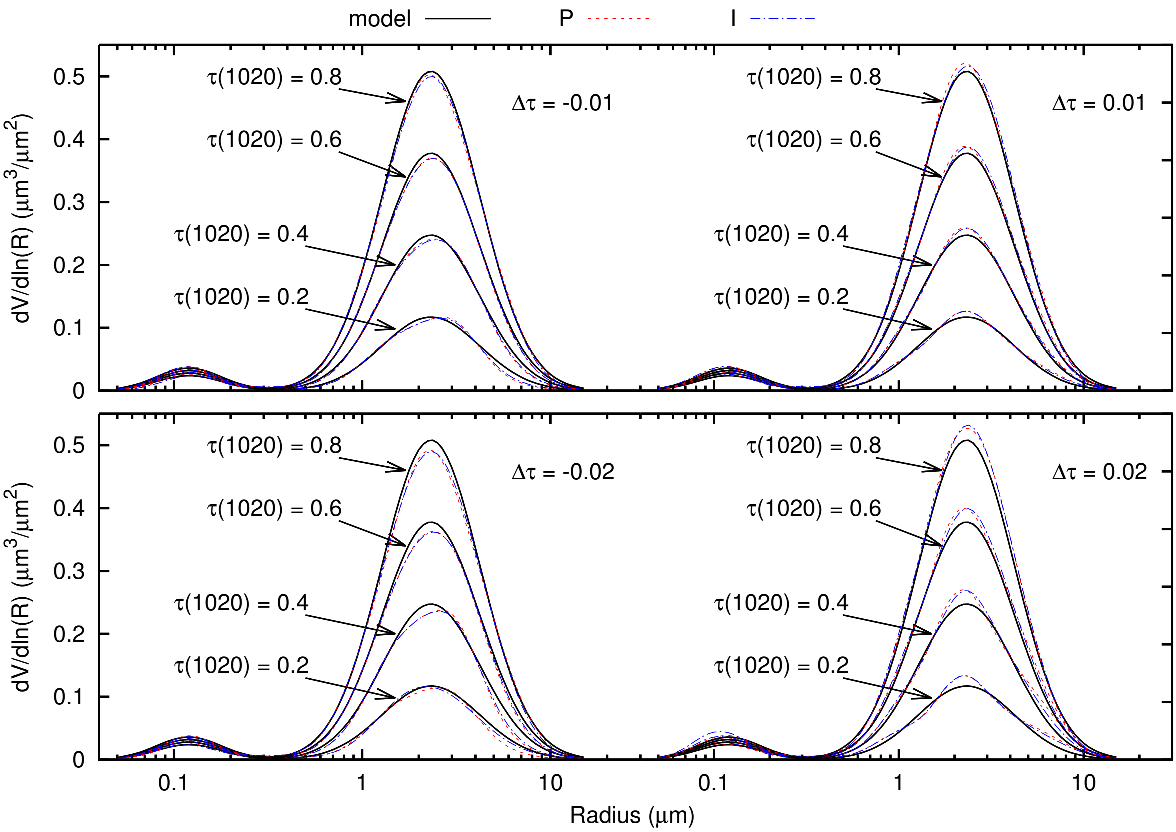

FIGURE A.25: Volume size distribution retrieved with and without polarization data applying for different AOD levels and with different noises added.

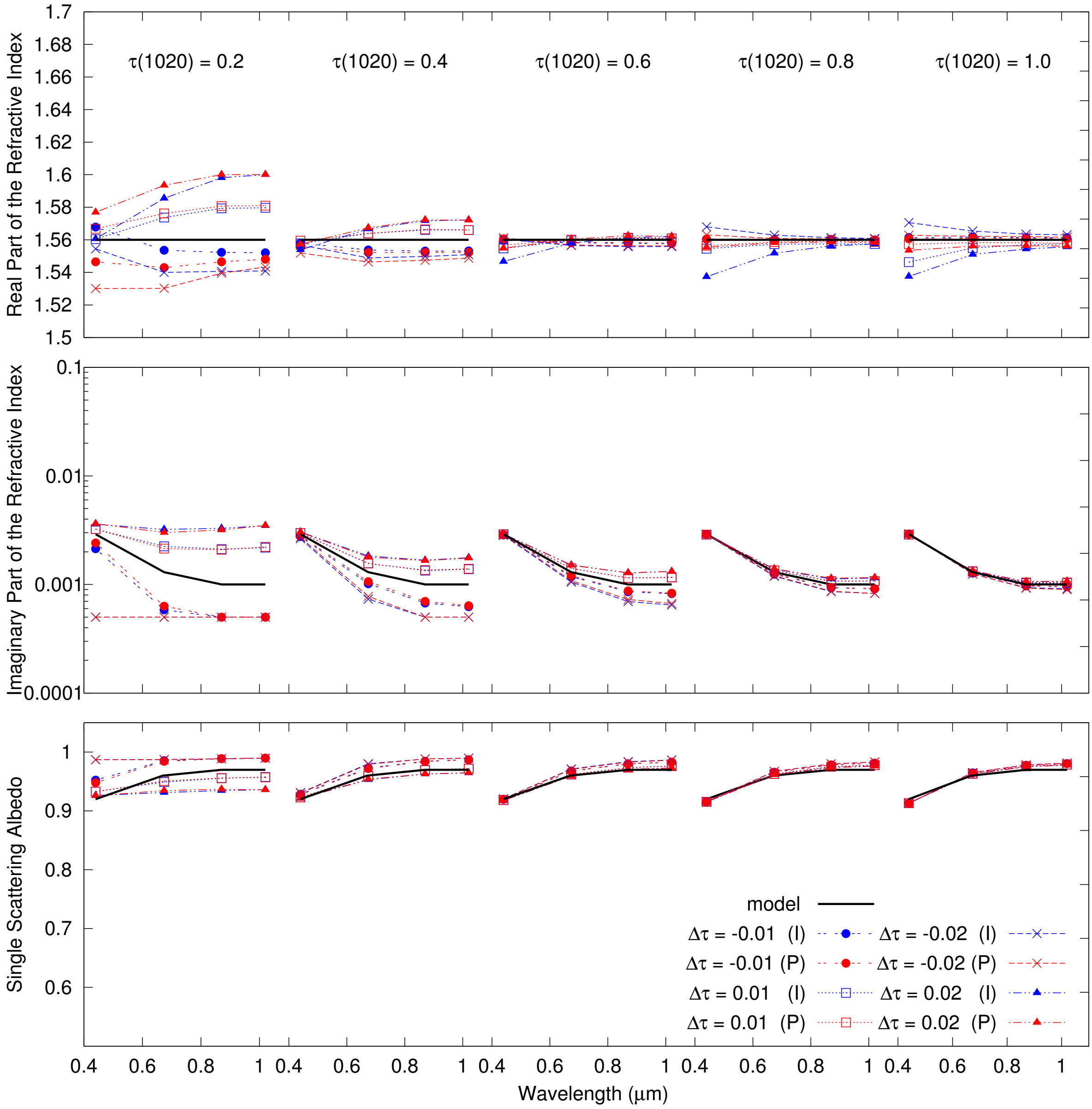

FIGURE A.26: Complex refractive index and single scattering albedo retrieved with and without polarization data applying for different AOD levels and with different noises added.

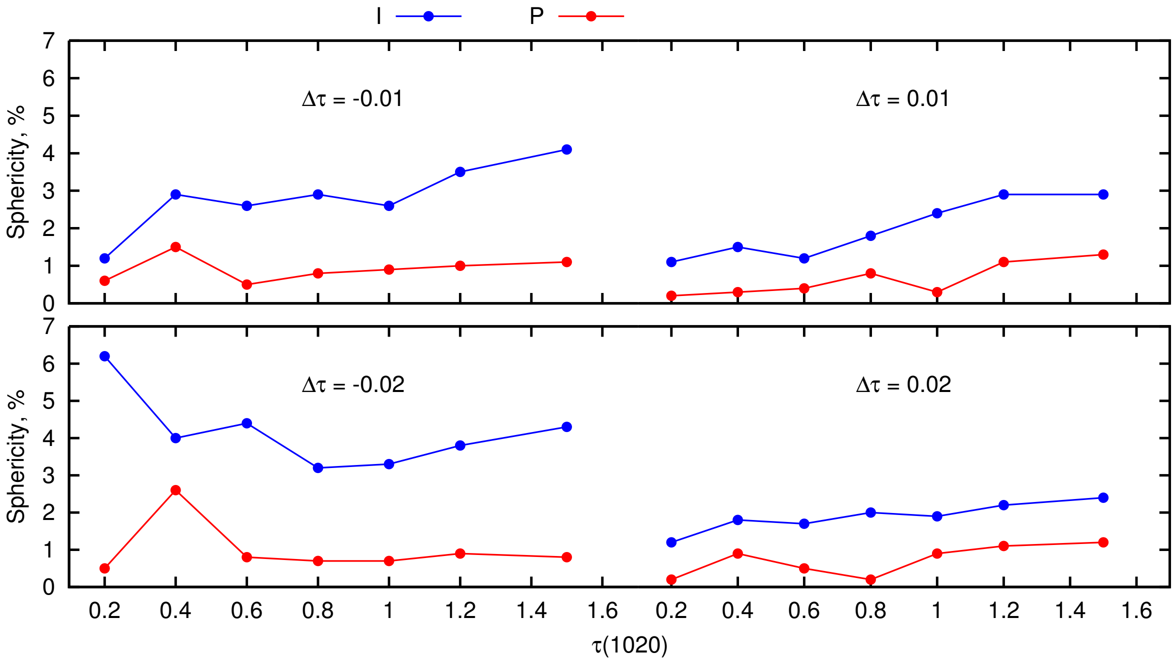

FIGURE A.27: Percentage of the spherical particles retrieved with and without polarization data applying for different AOD levels and with different noises added.

A.2.5 Oceanic aerosol aerosol (Lanai model)

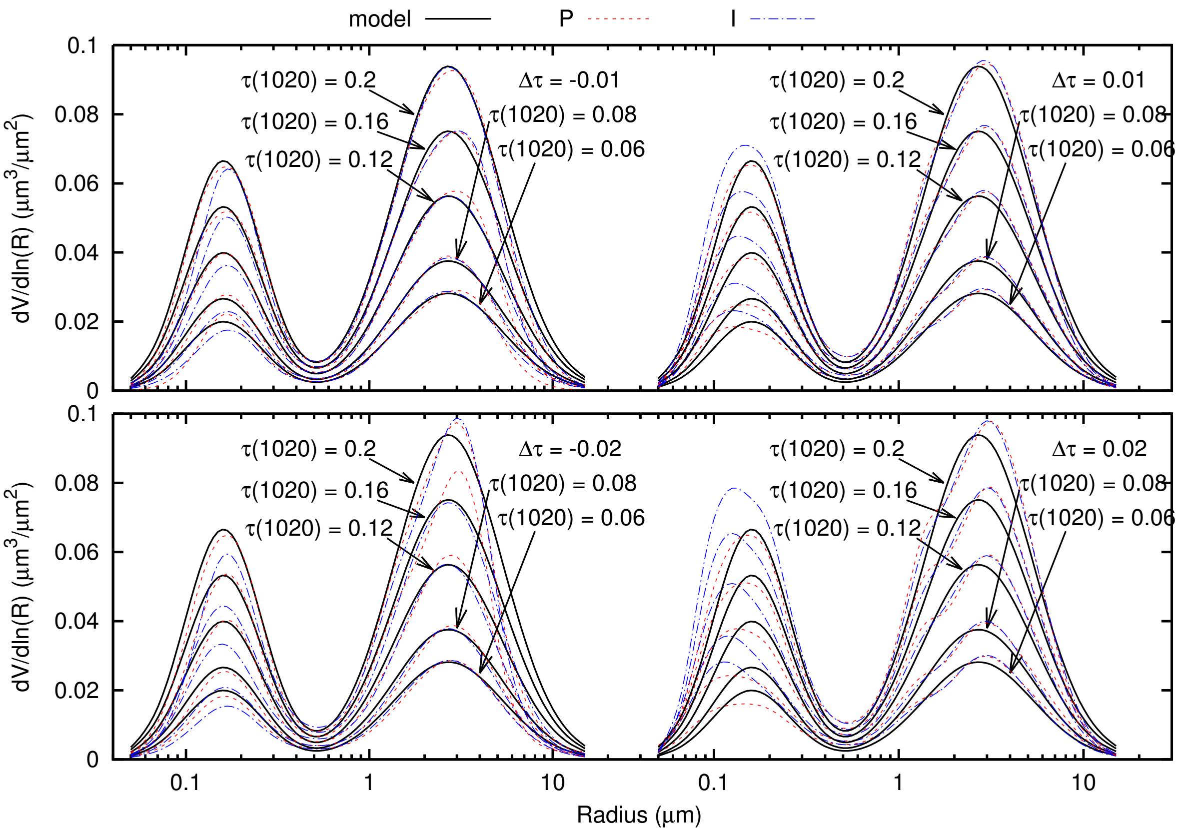

Figure A.28: Volume size distribution retrieved with and without polarization data applying for different AOD levels and with different noises added.

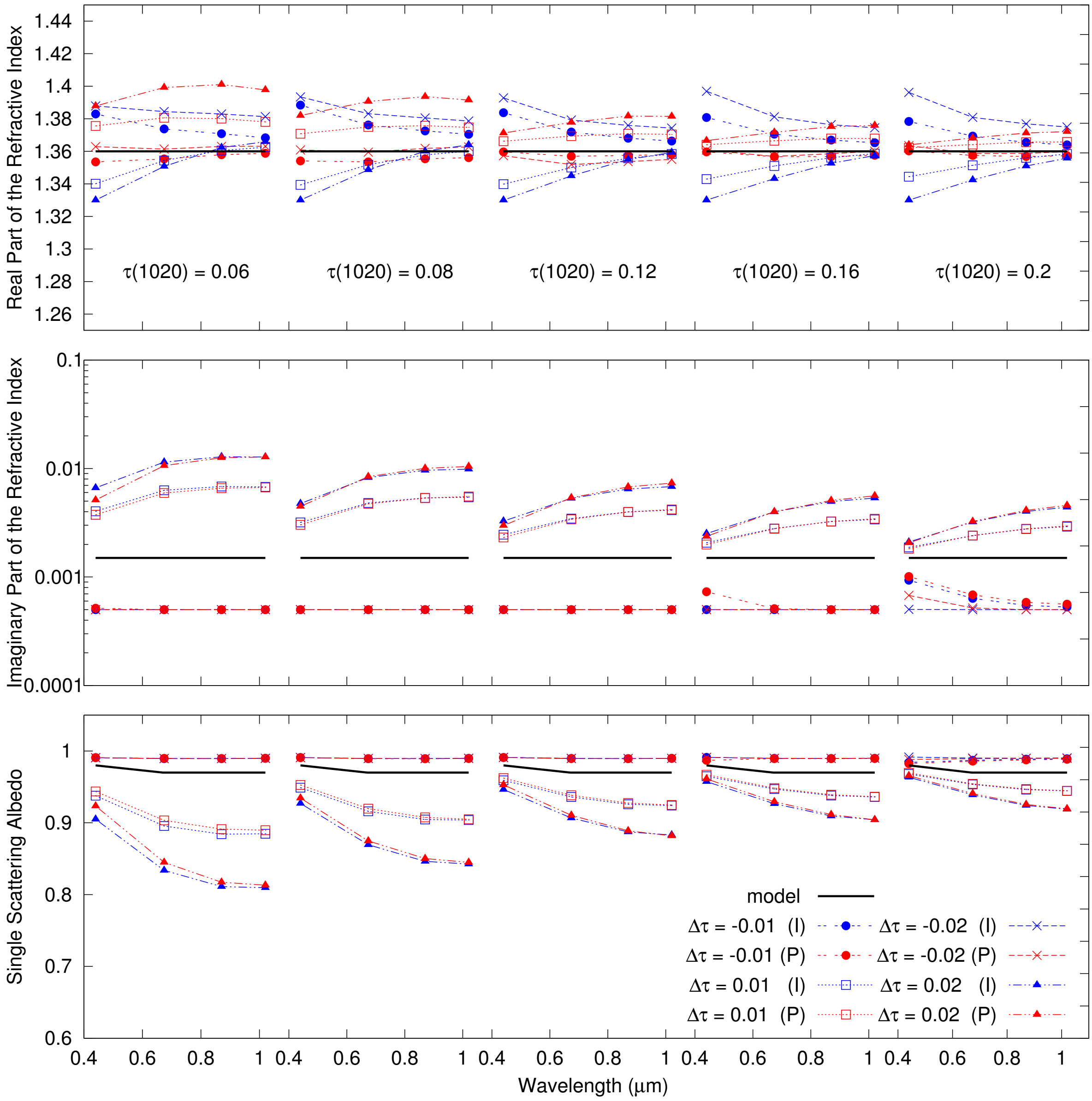

FIGURE A.29: Complex refractive index and single scattering albedo retrieved with and without polarization data applying for different AOD levels and with different noises added.

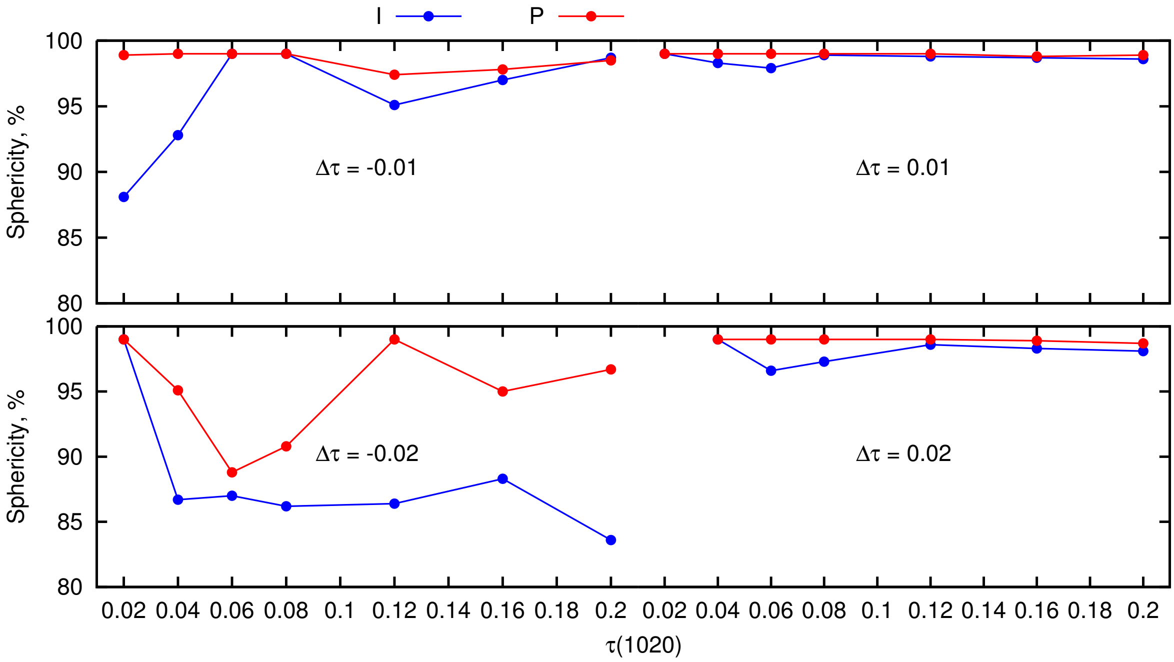

Figure A.30: Percentage of the spherical particles retrieved with and without polarization data applying for different AOD levels and with different noises added.

A.3 Sensitivity to the pointing error

A.3.1 Urban-industrial aerosol (Mexico model)

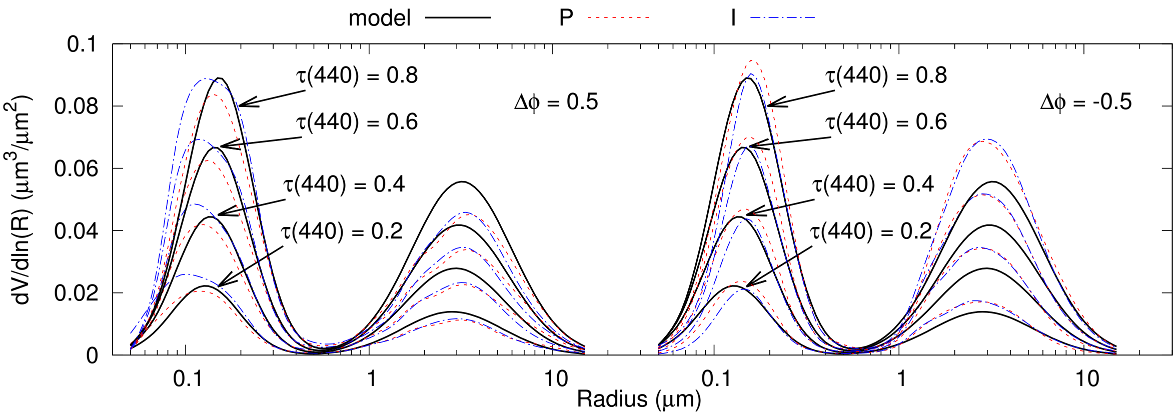

FIGURE A.31: Volume size distribution retrieved with and without polarization data applying for different AOD levels and with different noises added.

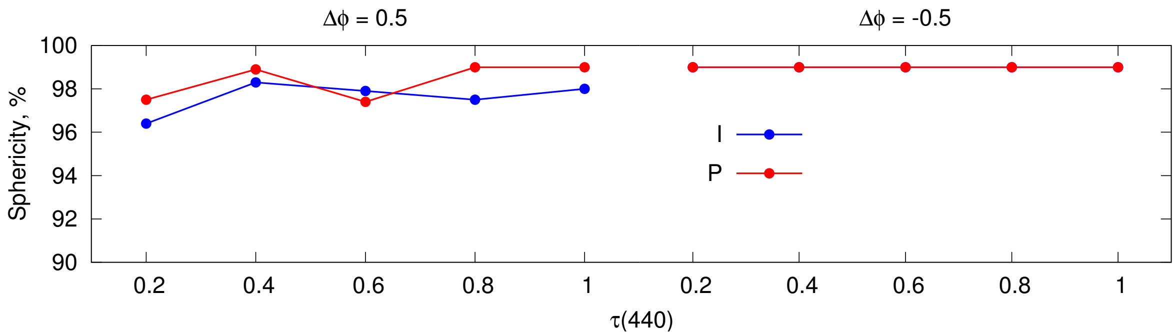

FIGURE A.32: Percentage of the spherical particles retrieved with and without polarization data applying for different AOD levels and with different noises added.

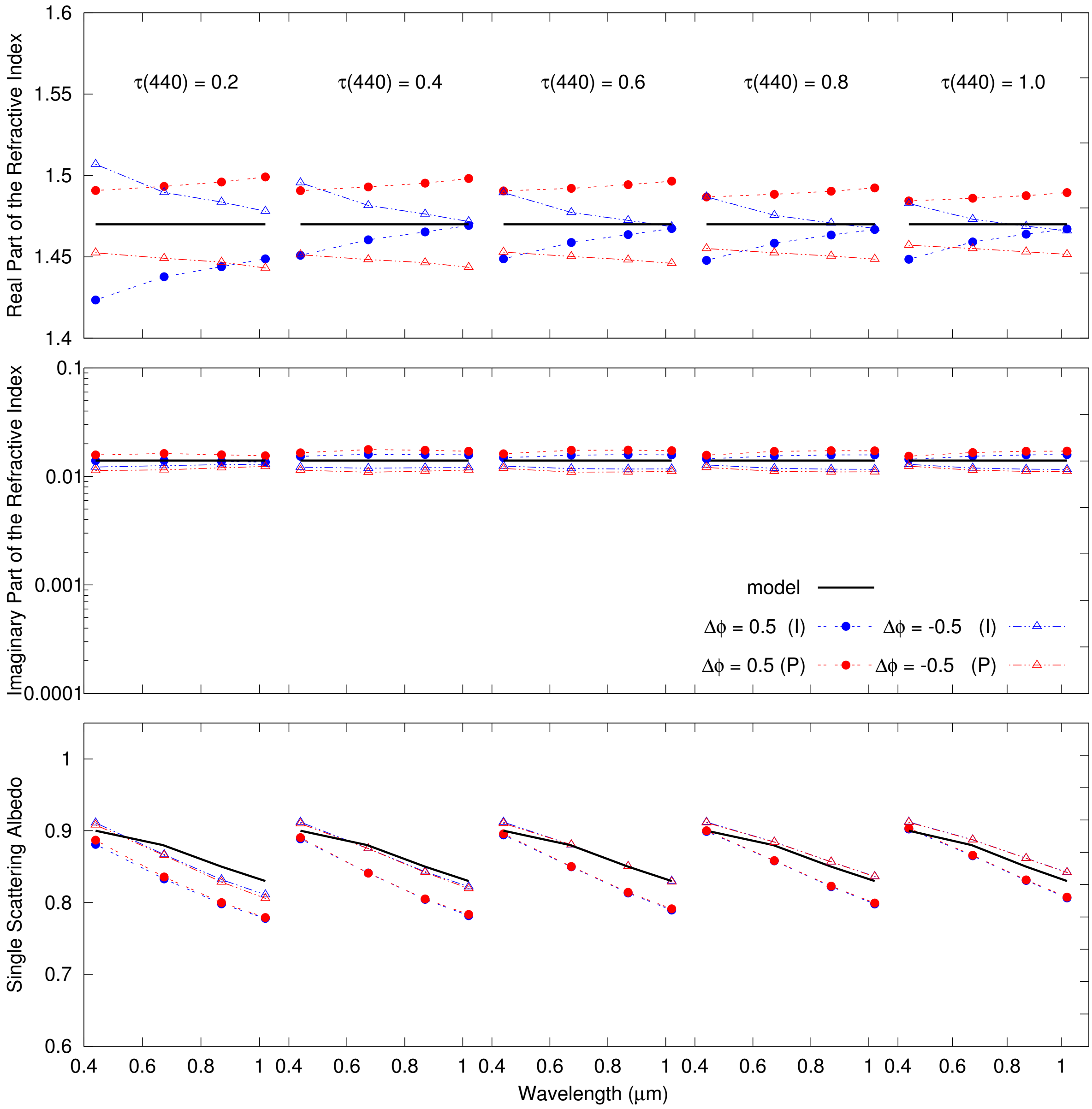

FIGURE A.33: Complex refractive index and single scattering albedo retrieved with and without polarization data applying for different AOD levels and with different noises added.

A.3.2 African savanna aerosol (Mongu model)

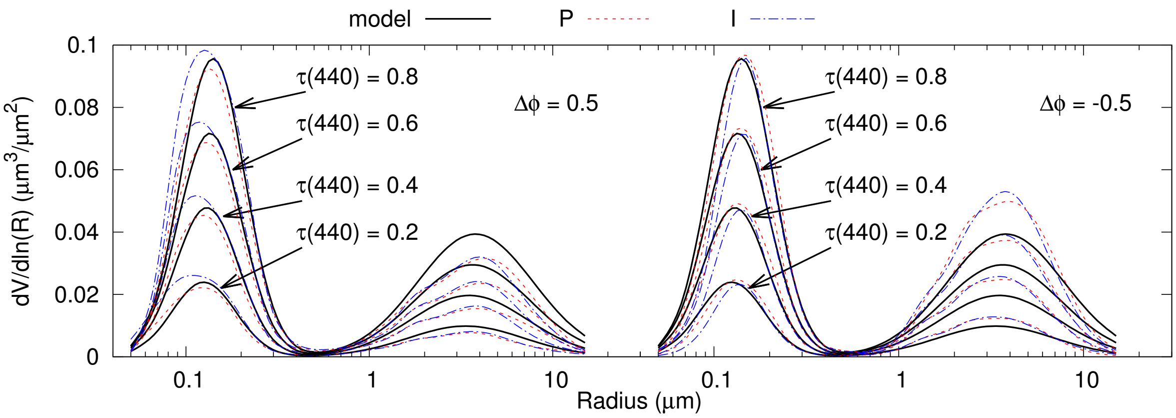

FIGURE A.34: Volume size distribution retrieved with and without polarization data applying for different AOD levels and with different noises added.

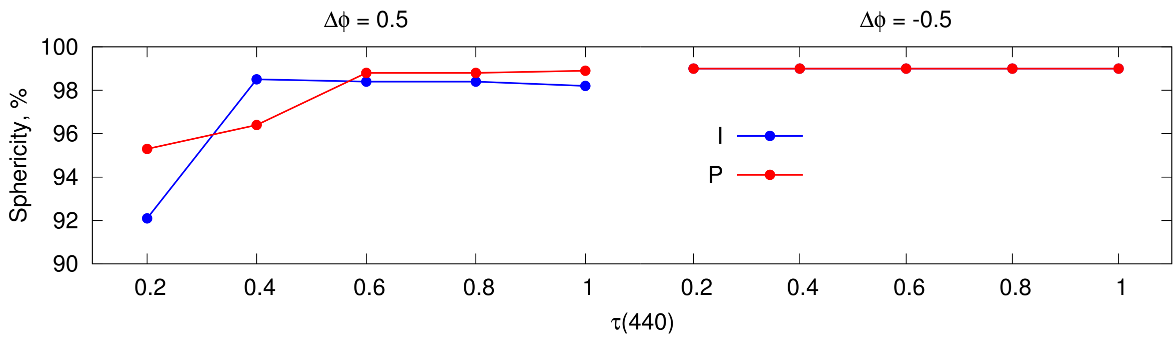

FIGURE A.35: Percentage of the spherical particles retrieved with and without polarization data applying for different AOD levels and with different noises added.

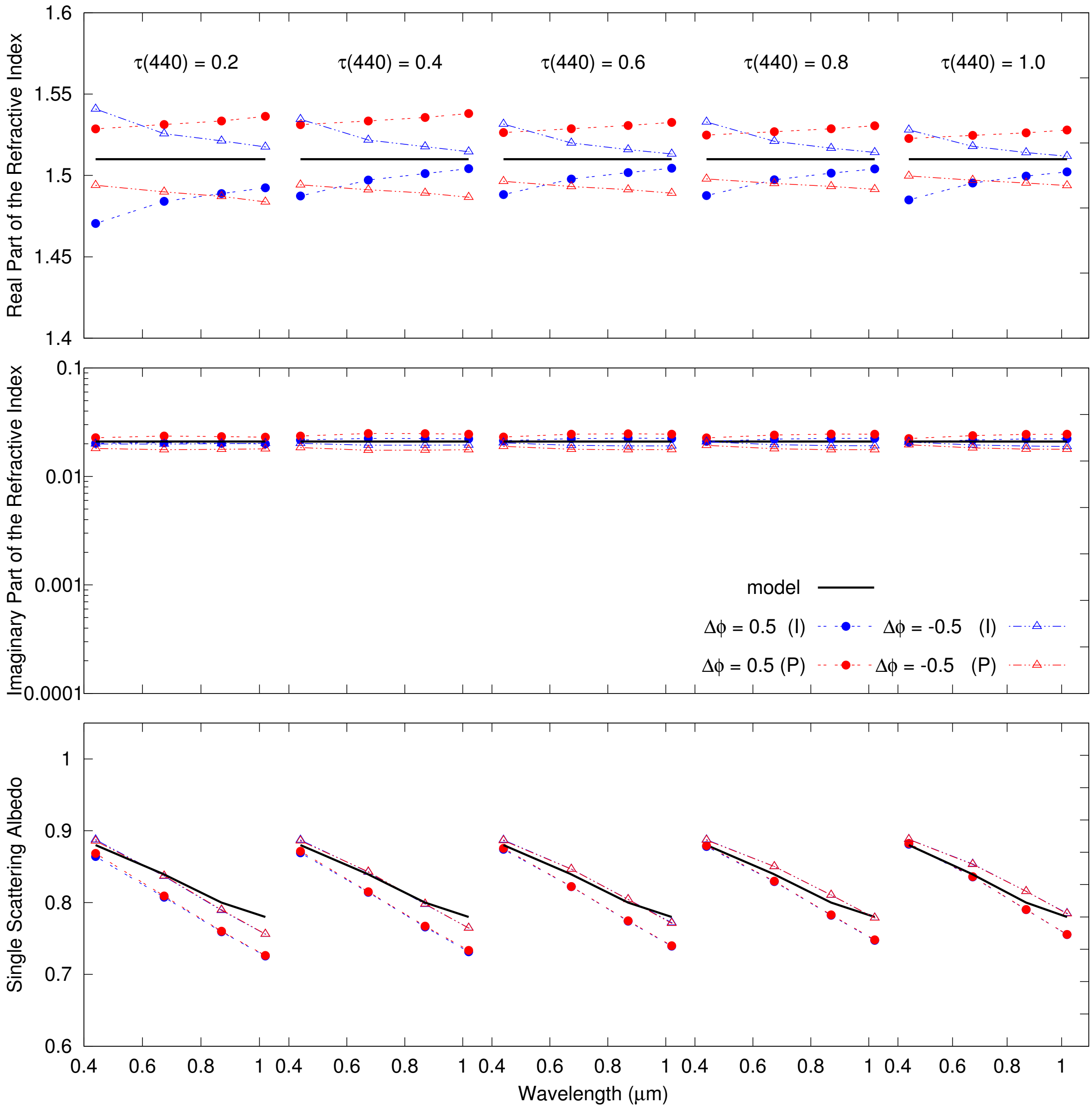

FIGURE A.36: Complex refractive index and single scattering albedo retrieved with and without polarization data applying for different AOD levels and with different noises added.

A.3.3 Urban-industrial aerosol (GSFC model)

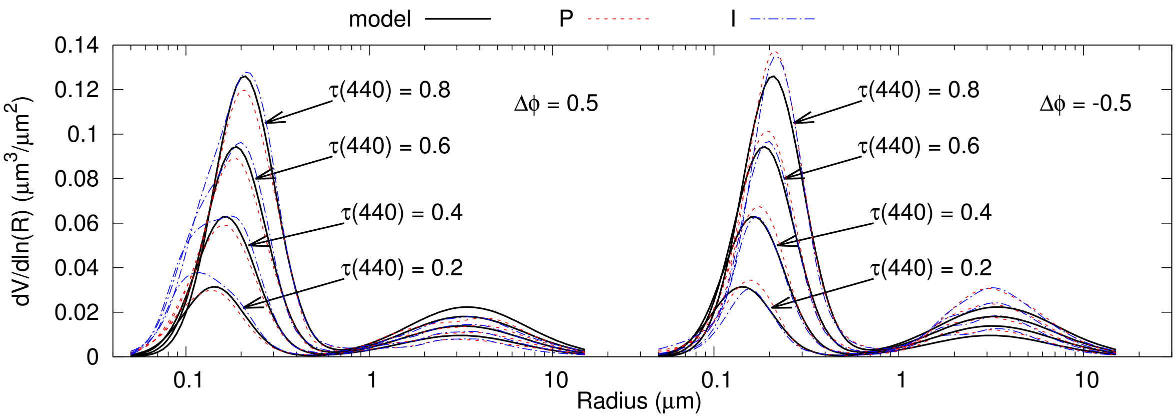

FIGURE A.37: Volume size distribution retrieved with and without polarization data applying for different AOD levels and with different noises added.

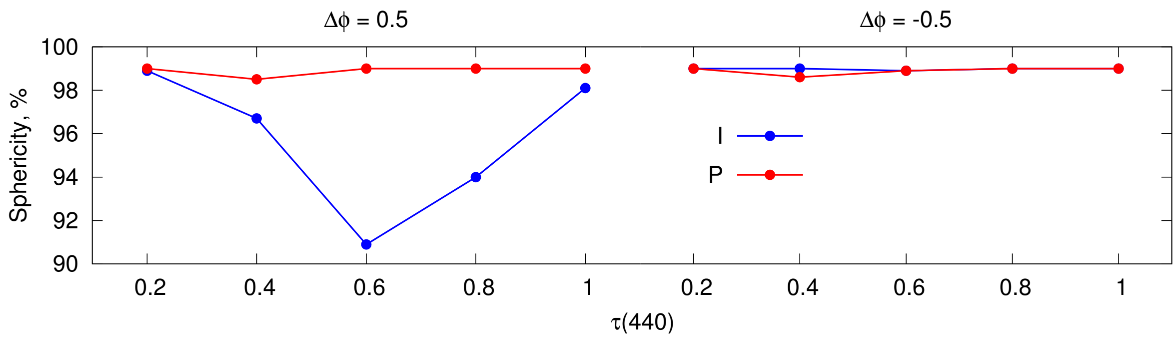

FIGURE A.38: Percentage of the spherical particles retrieved with and without polarization data applying for different AOD levels and with different noises added.

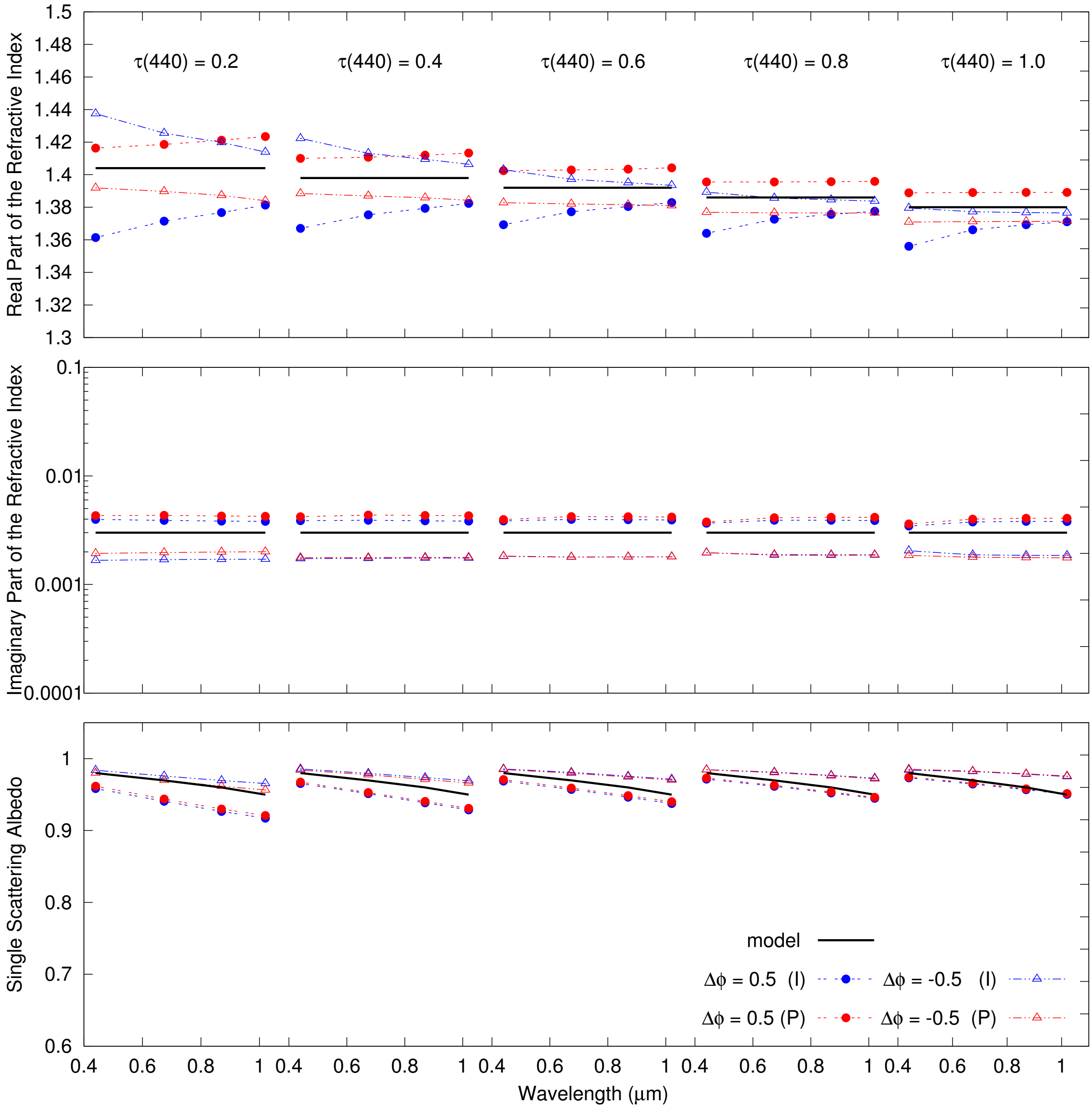

FIGURE A.39: Complex refractive index and single scattering albedo retrieved with and without polarization data applying for different AOD levels and with different noises added.

A.3.4 Desert dust aerosol (Solar Village model)

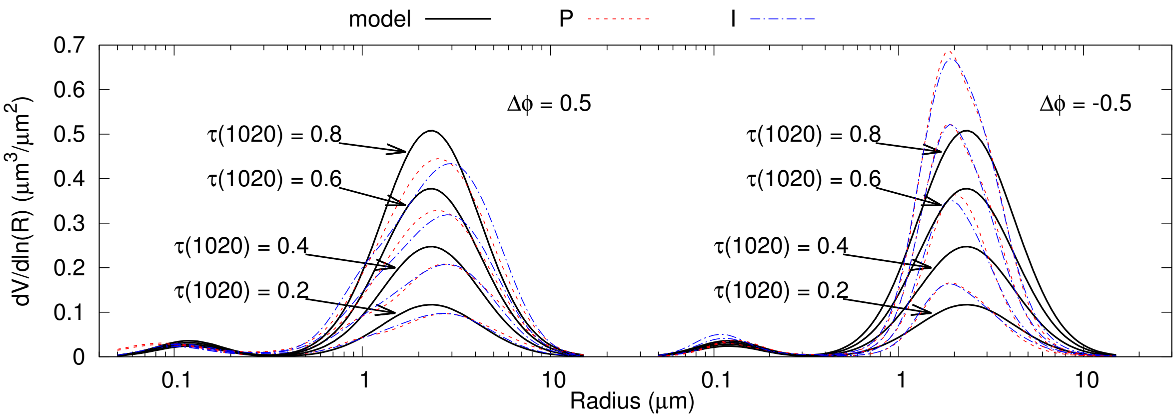

FIGURE A.40: Volume size distribution retrieved with and without polarization data applying for different AOD levels and with different noises added.

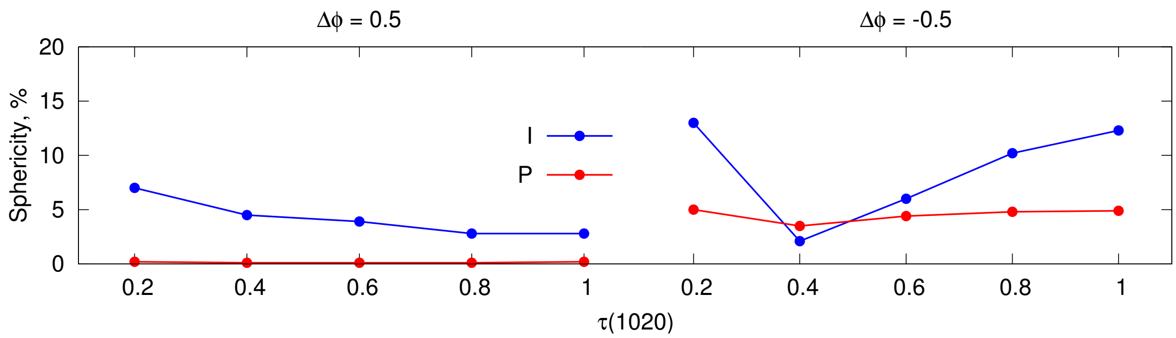

FIGURE A.41: Percentage of the spherical particles retrieved with and without polarization data applying for different AOD levels and with different noises added.

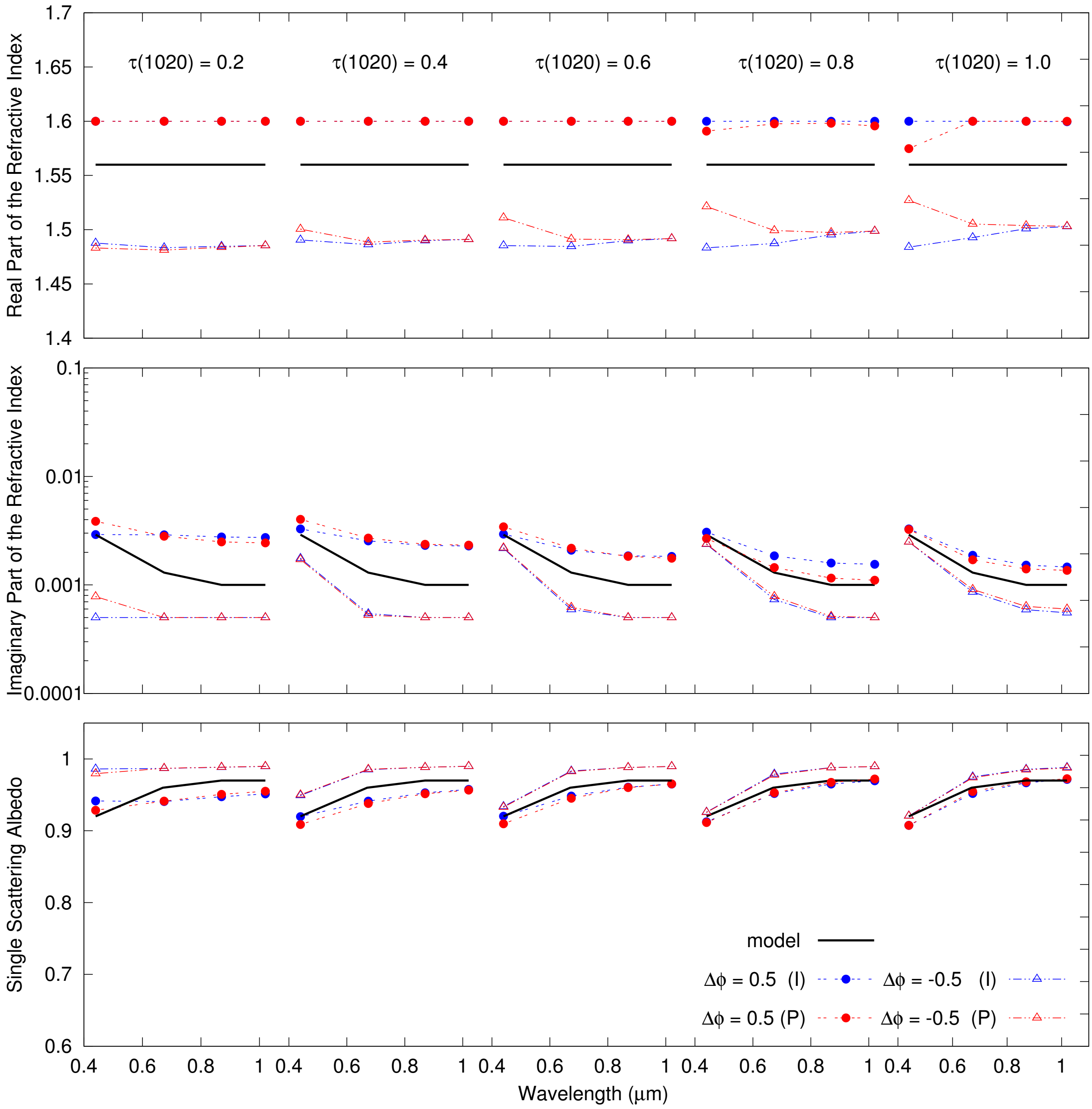

FIGURE A.42: Complex refractive index and single scattering albedo retrieved with and without polarization data applying for different AOD levels and with different noises added.

A.3.5 Oceanic aerosol aerosol (Lanai model)

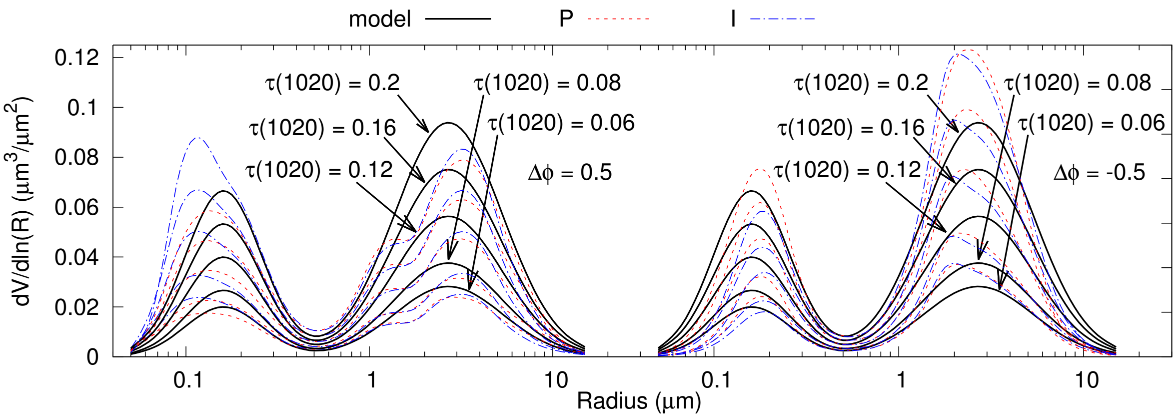

FIGURE A.43: Volume size distribution retrieved with and without polarization data applying for different AOD levels and with different noises added.

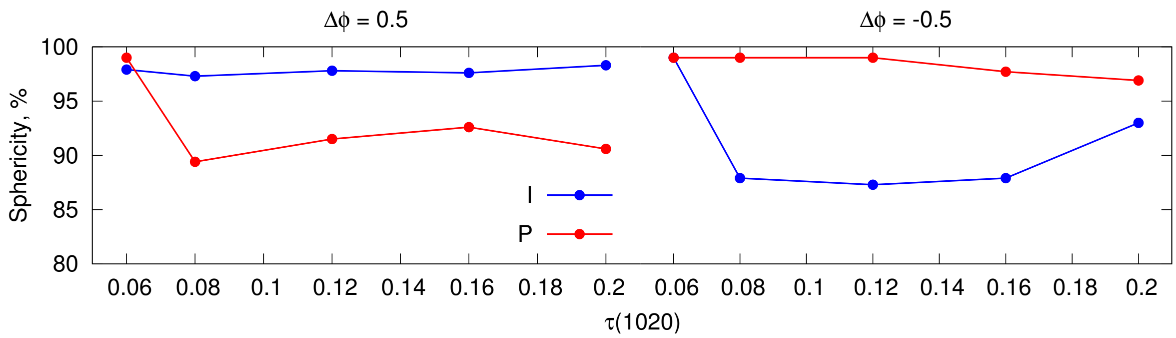

FIGURE A.44: Percentage of the spherical particles retrieved with and without polarization data applying for different AOD levels and with different noises added.

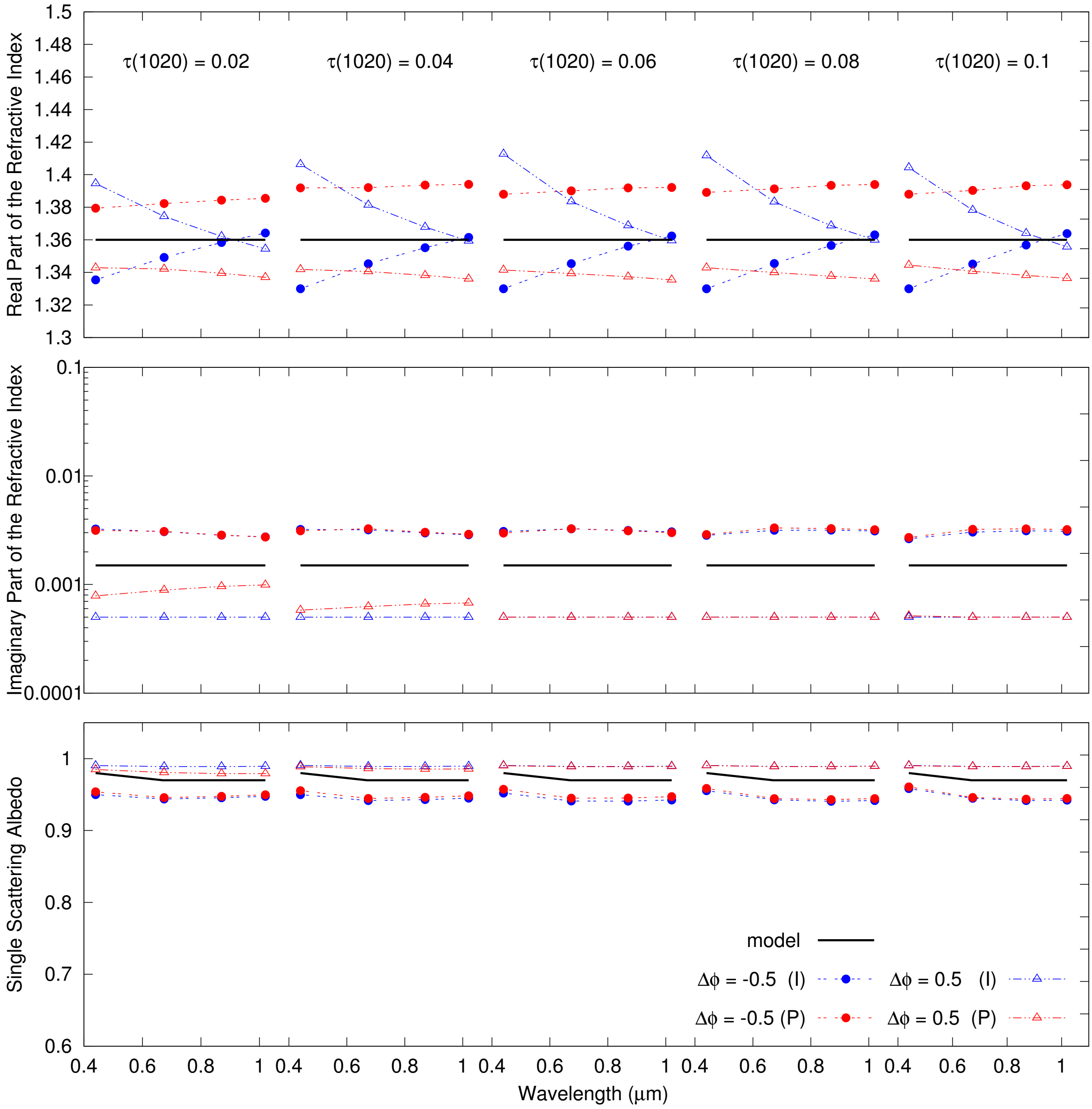

FIGURE A.45: Complex refractive index and single scattering albedo retrieved with and without polarization data applying for different AOD levels and with different noises added.

Appendix B

Inversion examples

B.1 GSFC

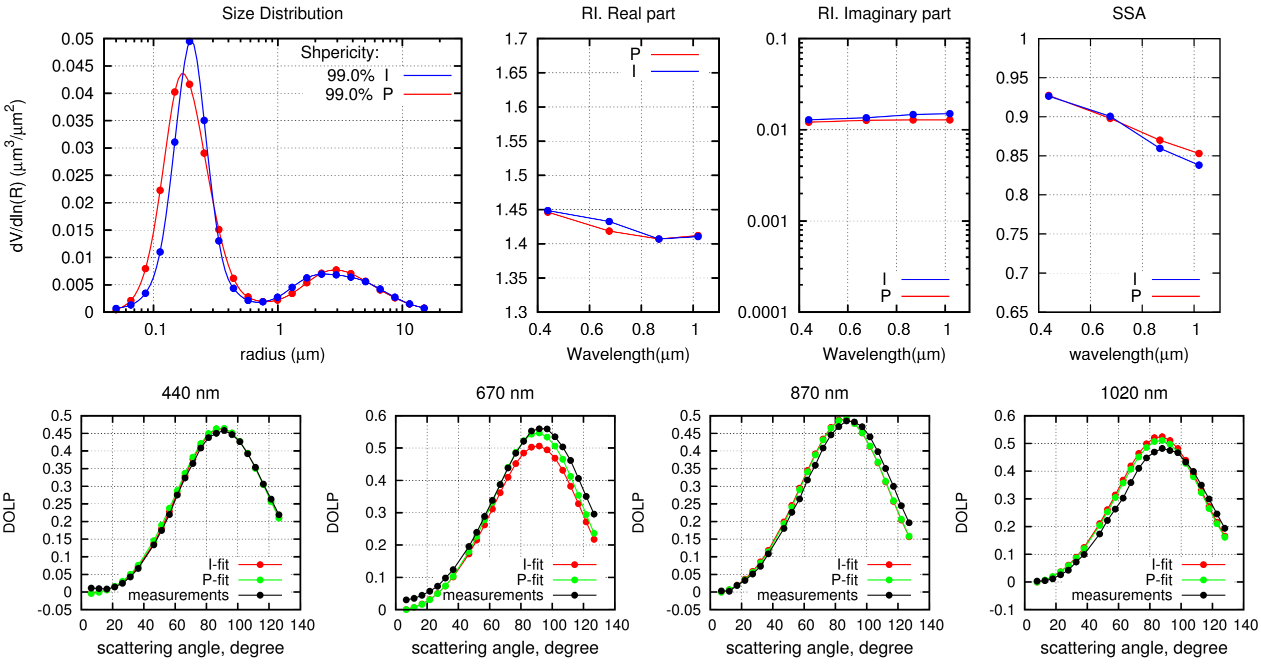

FIGURE B.1: Size Distribution, Refractive Index and Single Scattering Albedo. 09/07/2011, GSFC, $\theta_s = 53.4°$, $\tau_{440} = 0.37$

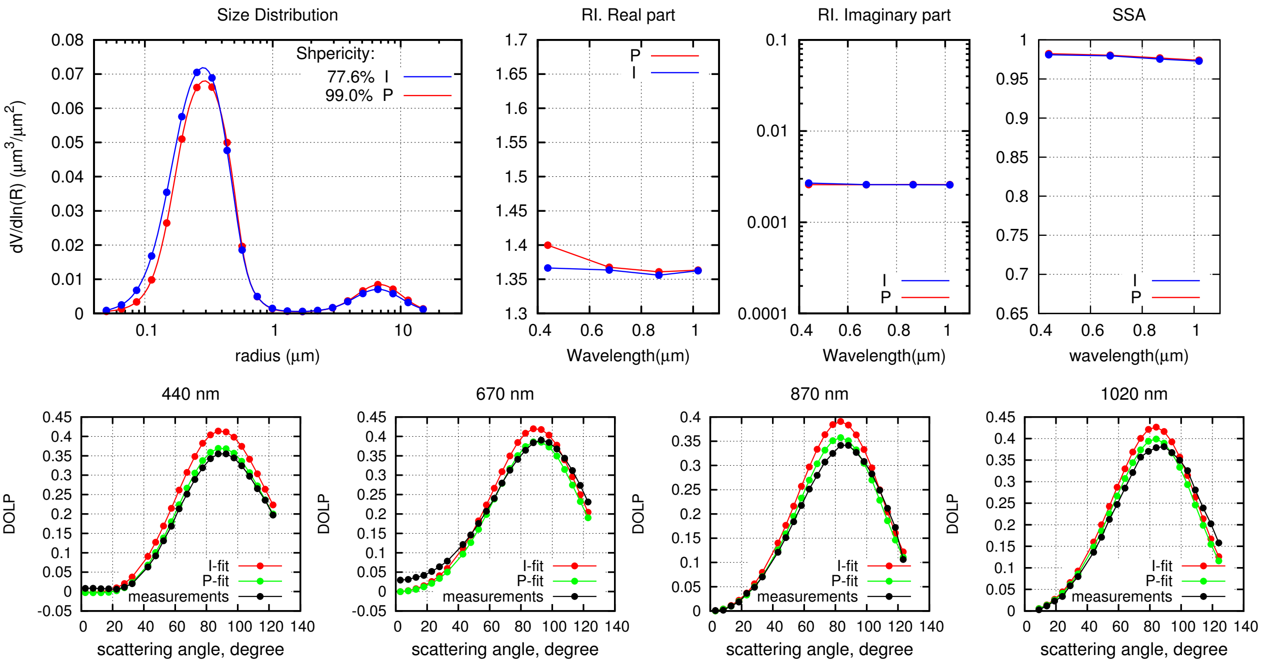

FIGURE B.2: Size Distribution, Refractive Index and Single Scattering Albedo. 11/07/2011, GSFC, $\theta_s = 49.5°$, $\tau_{440} = 0.59$

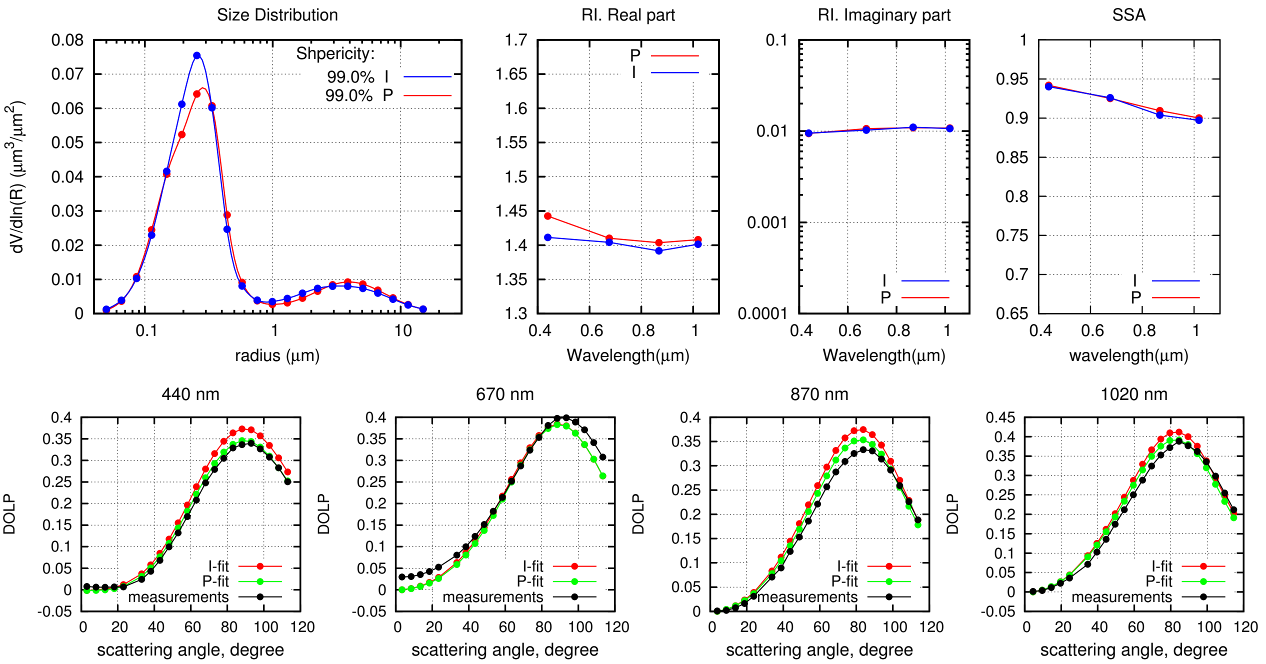

FIGURE B.3: Size Distribution, Refractive Index and Single Scattering Albedo. 20/07/2011, GSFC, $\theta_s = 39.0°$, $\tau_{440} = 0.65$

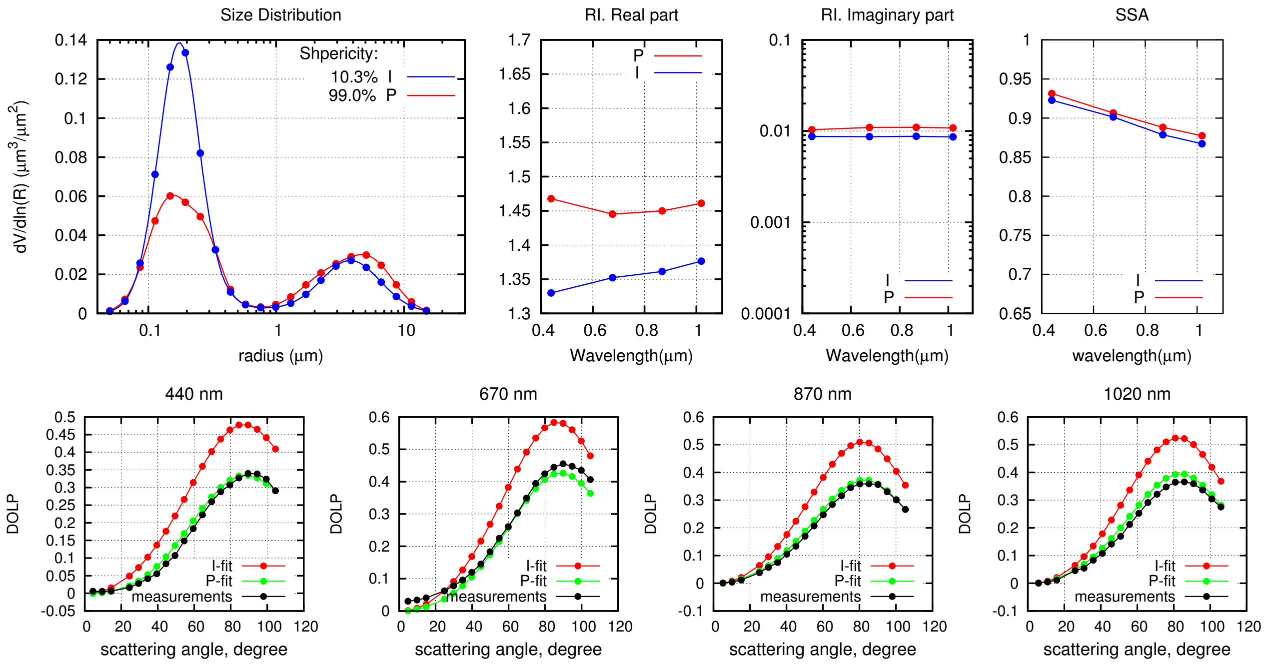

FIGURE B.4: Size Distribution, Refractive Index and Single Scattering Albedo. 22/07/2011, GSFC, $\theta_s = 31.3°$, $\tau_{440} = 0.67$

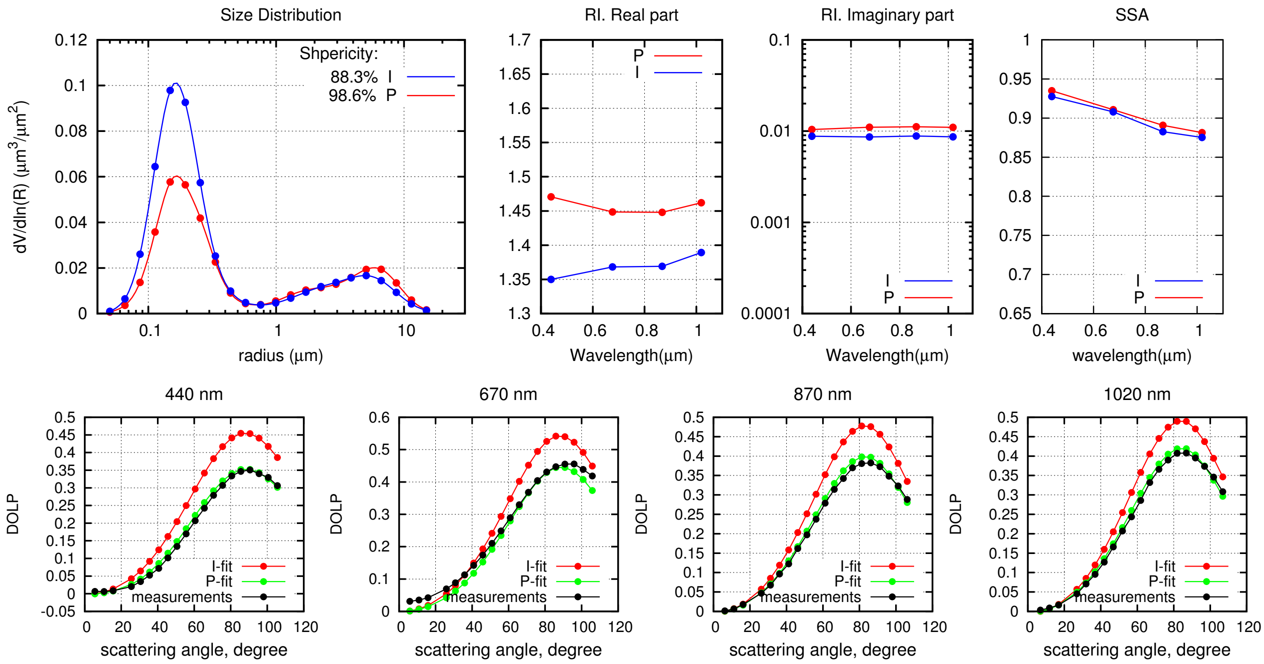

FIGURE B.5: Size Distribution, Refractive Index and Single Scattering Albedo. 29/07/2011, GSFC, $\theta_s = 32.2°$, $\tau_{440} = 0.58$

B.2 Beijing

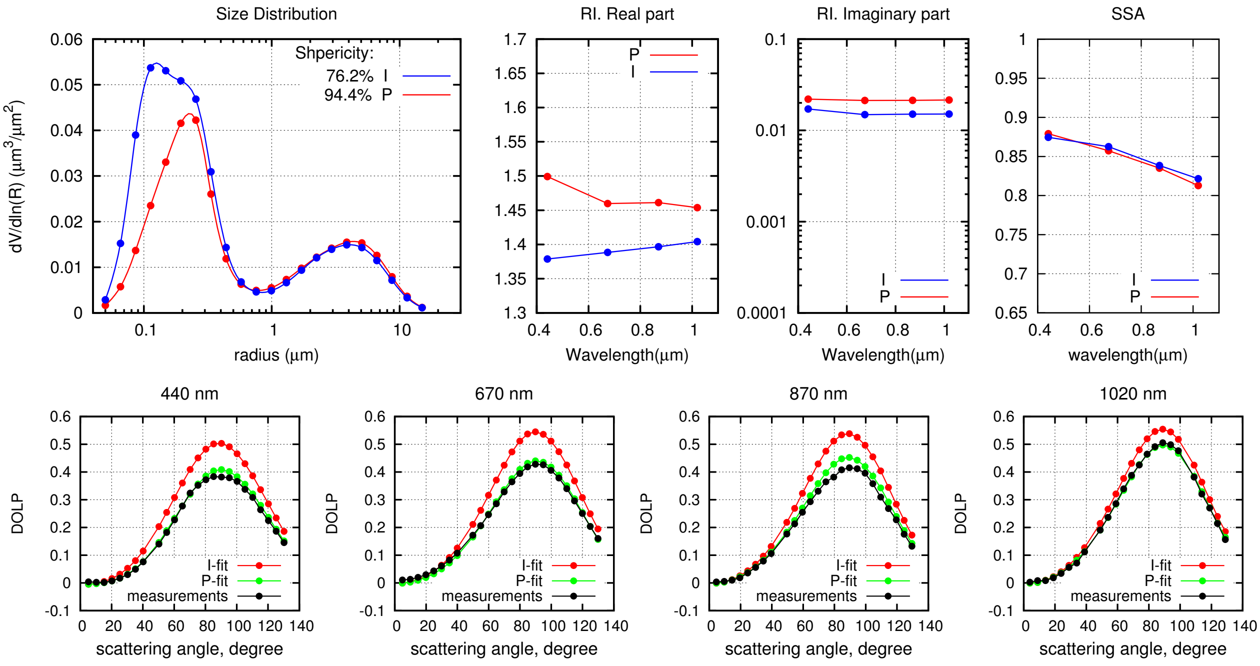

FIGURE B.6: Size Distribution, Refractive Index and Single Scattering Albedo. 10/06/2010, Beijing, $\theta_s = 39.5°$, $\tau_{440} = 2.65$

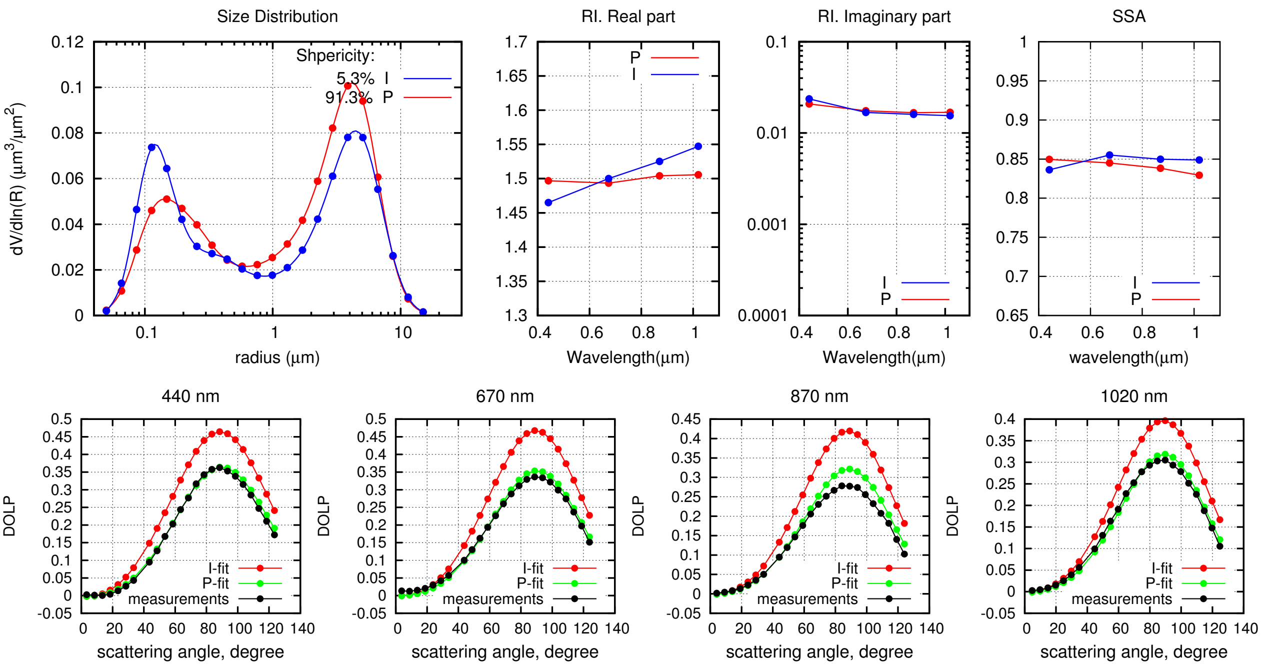

FIGURE B.7: Size Distribution, Refractive Index and Single Scattering Albedo. 21/06/2010, Beijing, $\theta_s = 50.2°$, $\tau_{440} = 0.75$

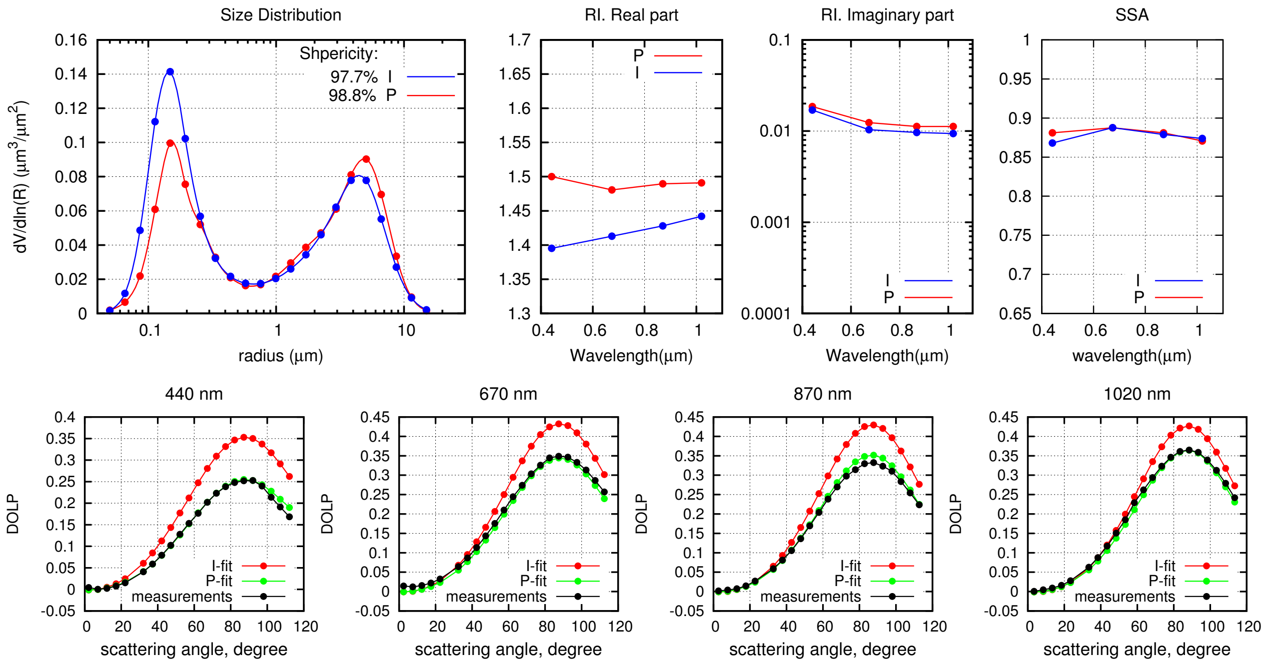

FIGURE B.8: Size Distribution, Refractive Index and Single Scattering Albedo. 23/06/2010, Beijing, $\theta_s = 39.0°$, $\tau_{440} = 1.0$

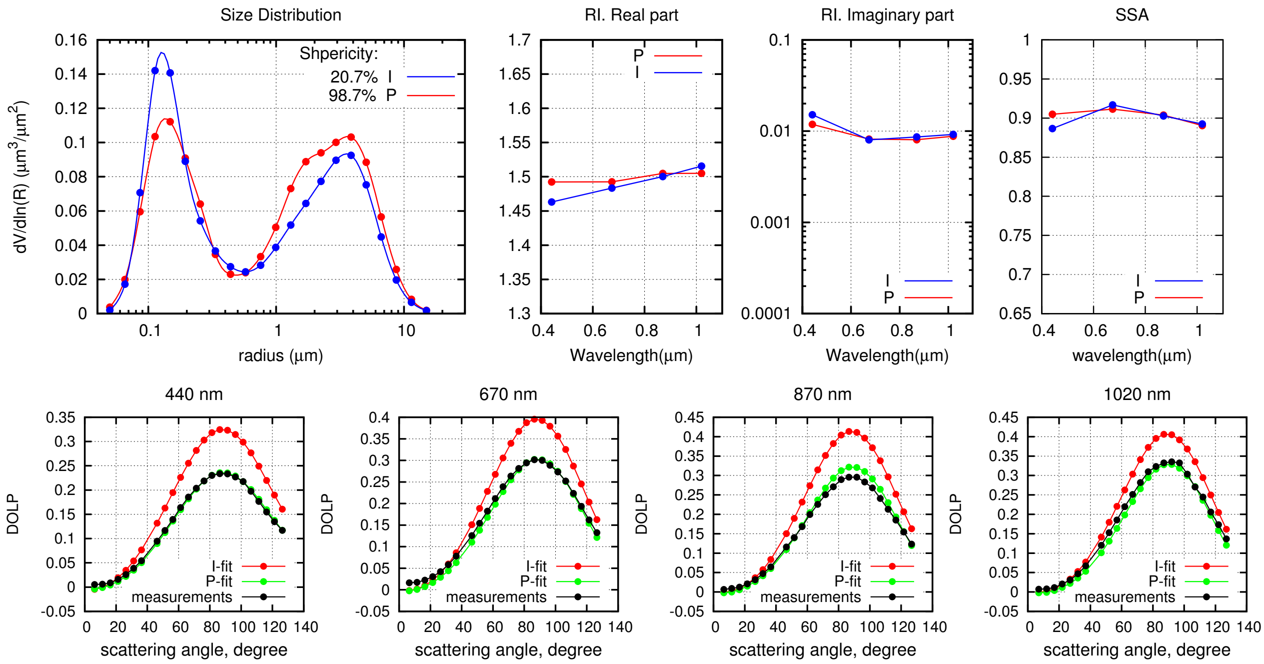

FIGURE B.9: Size Distribution, Refractive Index and Single Scattering Albedo. 05/03/2011, Beijing, $\theta_s = 52.3°$, $\tau_{440} = 1.31$

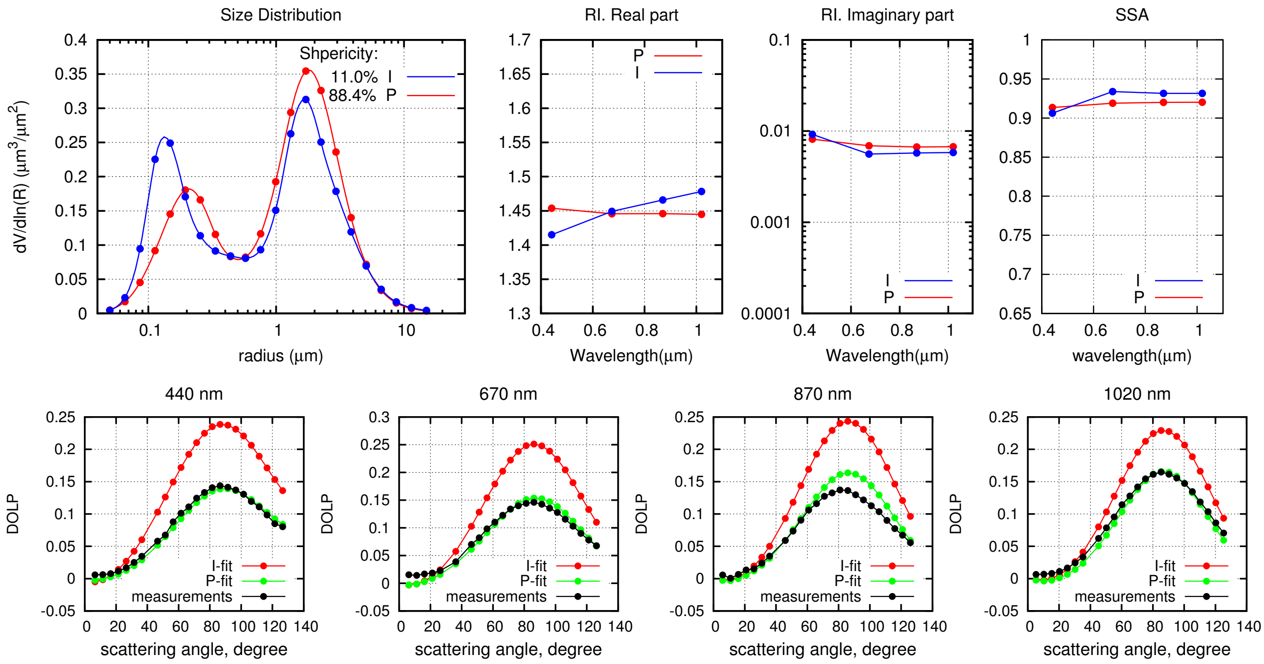

FIGURE B.10: Size Distribution, Refractive Index and Single Scattering Albedo. 25/04/2011, Beijing, $\theta_s = 50.1°$, $\tau_{440} = 2.44$

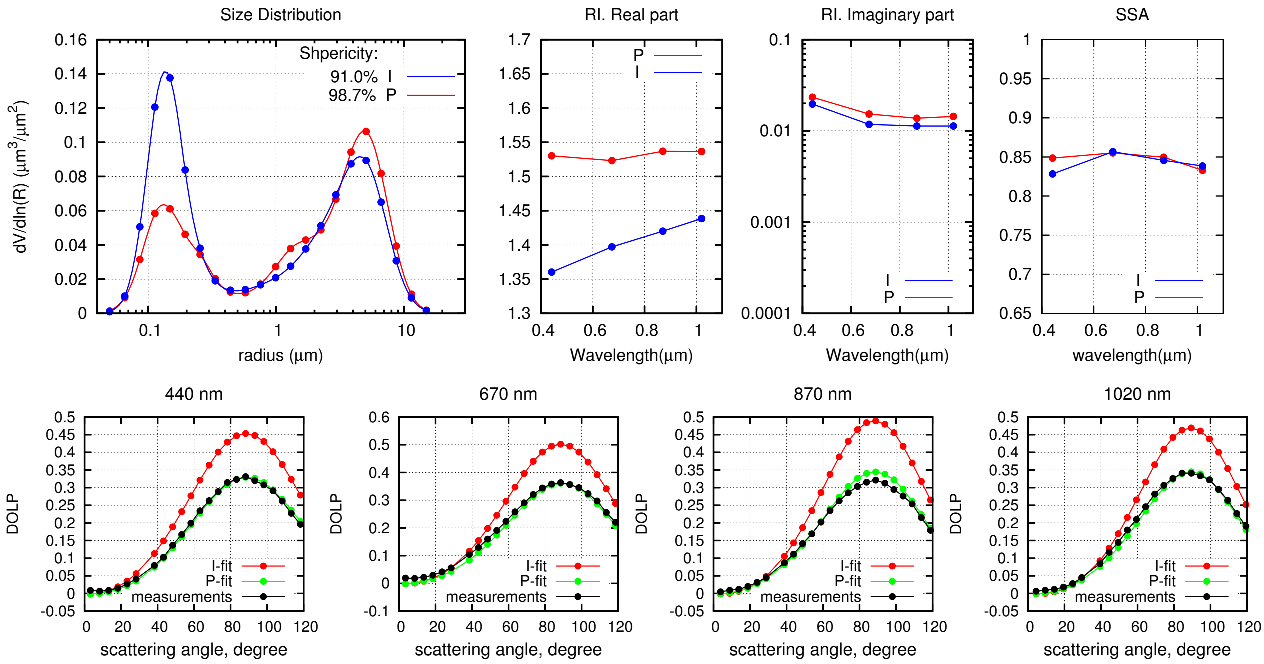

FIGURE B.11: Size Distribution, Refractive Index and Single Scattering Albedo. 28/04/2011, Beijing, $\theta_s = 44.8°$, $\tau_{440} = 0.78$

B.3 Dakar

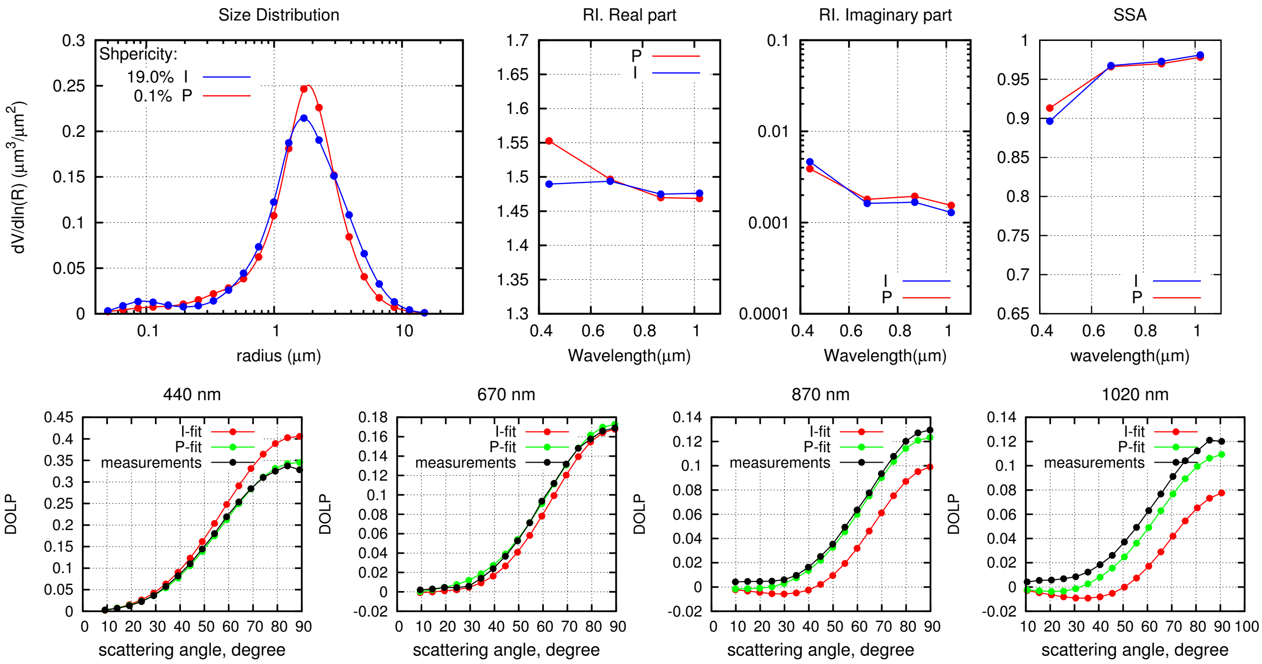

FIGURE B.12: Size Distribution, Refractive Index and Single Scattering Albedo. 02/07/2012, Dakar, $\theta_s = 16.1°$, $\tau_{440} = 0.62$

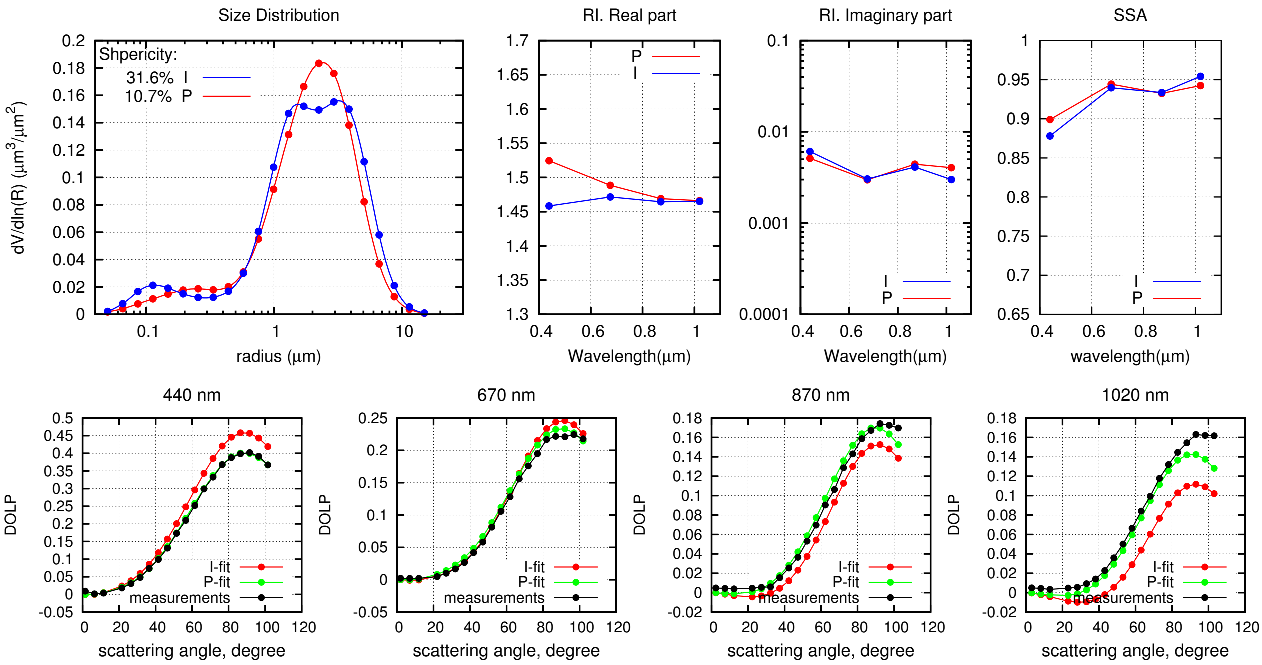

FIGURE B.13: Size Distribution, Refractive Index and Single Scattering Albedo. 14/07/2012, Dakar, $\theta_s = 28.6°$, $\tau_{440} = 0.59$

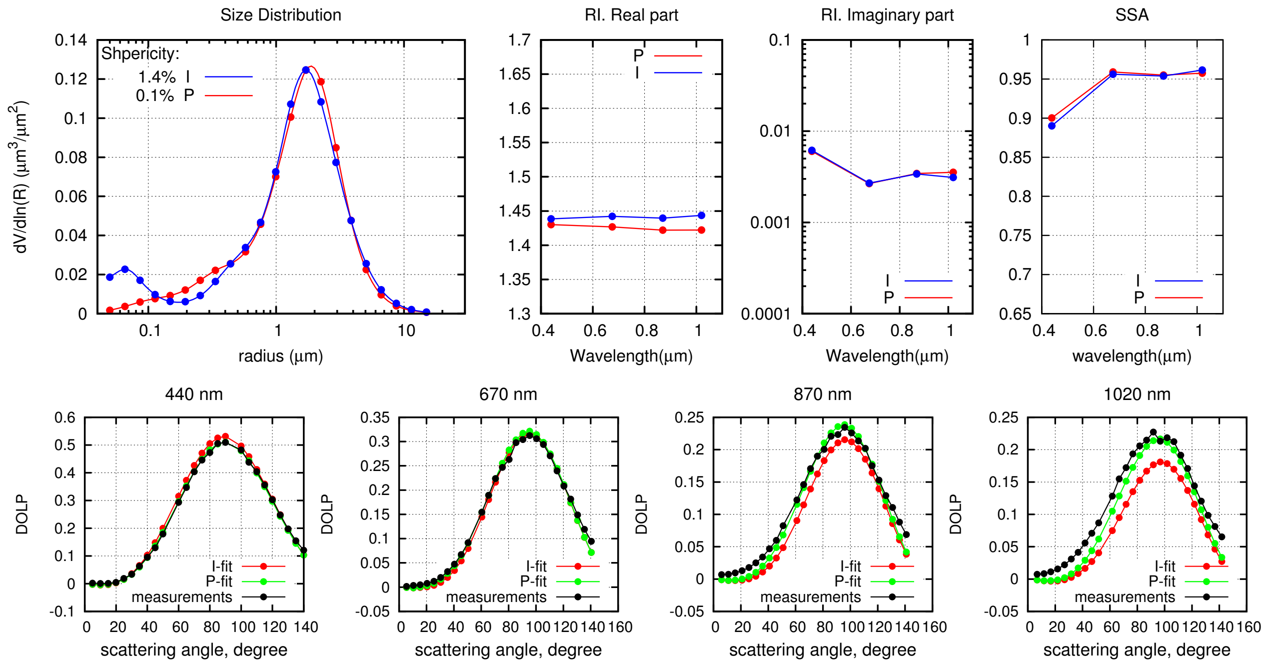

FIGURE B.14: Size Distribution, Refractive Index and Single Scattering Albedo. 16/09/2012, Dakar, $\theta_s = 67.3°$, $\tau_{440} = 0.44$

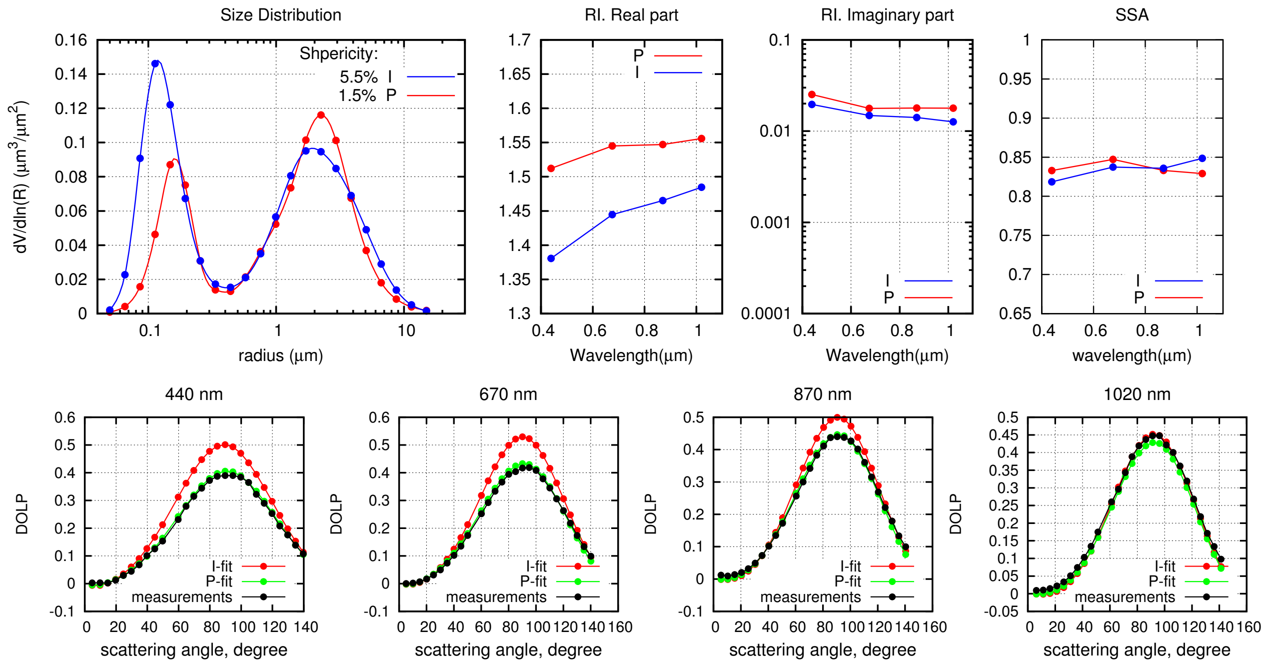

FIGURE B.15: Size Distribution, Refractive Index and Single Scattering Albedo. 11/01/2013, Dakar, $\theta_s = 66.7°$, $\tau_{440} = 0.91$

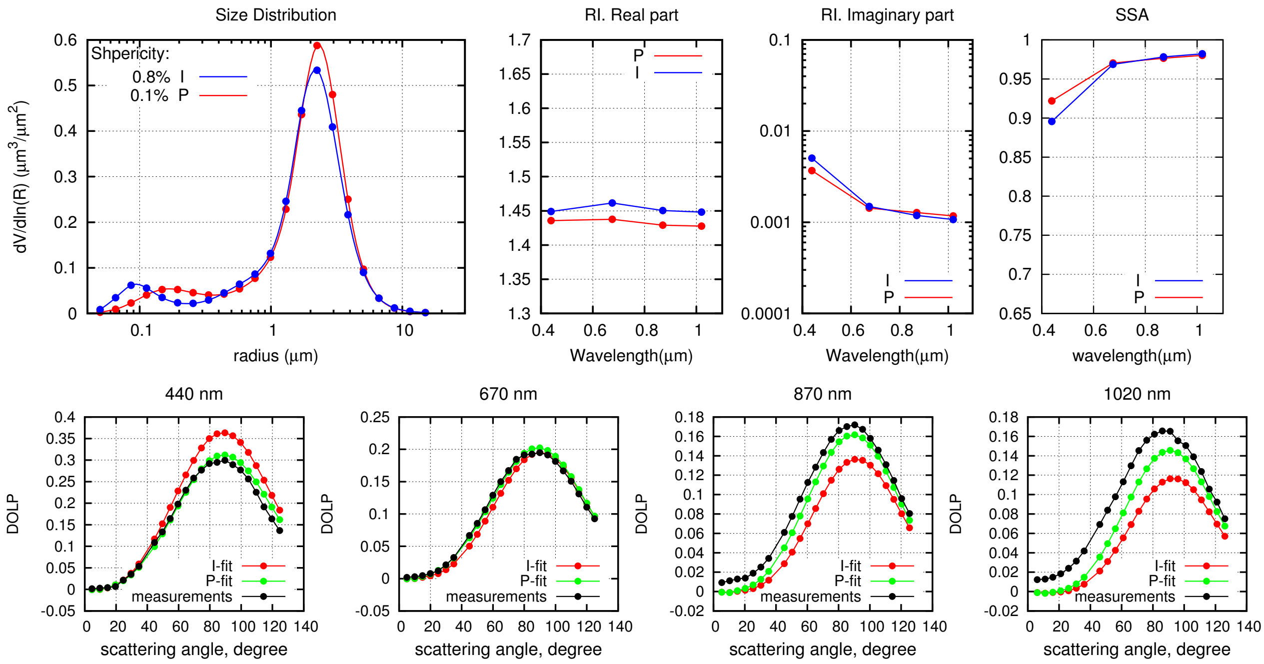

FIGURE B.16: Size Distribution, Refractive Index and Single Scattering Albedo. 01/02/2013, Dakar, $\theta_s = 51.5°$, $\tau_{440} = 1.26$

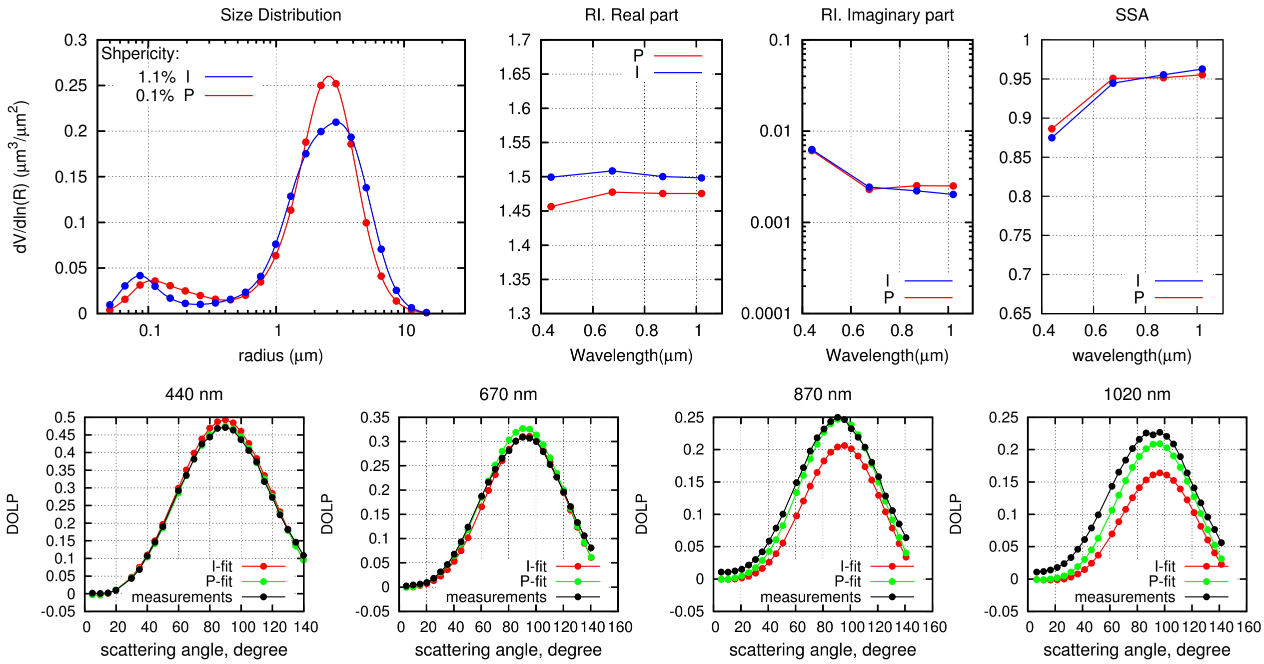

FIGURE B.17: Size Distribution, Refractive Index and Single Scattering Albedo. 05/02/2013, Dakar, $\theta_s = 67.1°$, $\tau_{440} = 0.66$

Bibliography

Standard Atmosphere, ISO 2533:1975, International Organization for Standardization, 1975.

U.S. Standard Atmosphere, 1976, U.S. Government Printing Office, Washington, D.C., 1976.

Manual of the ICAO Standard Atmosphere (extended to 80 kilometres (262 500 feet)), vol. Doc 7488-CD, International Civil Aviation Organization, third edn., 1993.

Ackerman, A. S., Toon, O. B., Stevens, D. E., Heymsfield, A. J., Ramanathan, V., and Welton, E. J.: Reduction of tropical cloudiness by soot, Science, 288, 1042, 2000.

Adams, P., Seinfeld, J., and Koch, D.: Global concentrations of tropospheric sulphate, nitrate and ammonium aerosol simulated in a general circulation model, Journal of Geophysical Research, 104, 13 791–13 823, 1999.

Albrecht, B. A.: Aerosols, Cloud Microphysics, and Fractional Cloudiness, Science, 245, 1227, 1989.

Andreae, M.: Climatic effects of changing atmospheric aerosol levels, in: World Survey of Climatology, edited by Henderson-Sellers, A., vol. 16: Future Climates of the World, pp. 341–392, Elsevier, Amsterdam, 1995.

Ångström, A. K.: On the atmospheric transmission of Sun radiation and on dust in the air, Geogr. Ann., 11, 156–166, 1929.

Antuña, J., Andrade, M., Landulfo, E., Clemesha, B., Quel, E., and Bastidas, A.: Building a Lidar Network in Latin America: Progress and Difficulties, in 23rd International Laser Radar Conference, Nara, Japan, July 24-28, 2006.

Asseng, H., Ruhtz, T., and Fischer, J.: Sun and Aureole Spectrometer for Airborne Measurements to Derive Aerosol Optical Properties, Appl. Opt., 43, 2146–2155, doi:10.1364/AO.43.002146, URL http://ao.osa.org/abstract.cfm?URI=ao-43-10-2146, 2004.

Bevington, P. R.: Data Reduction and Error Analysis for the Physical Sciences, McGraw-Hill, 1969.

Bohren, C. and Huffman, D.: Absorption and Scattering of Light by Small Particles (Wiley science paperback series), Wiley-VCH, 1998.

Bond, T. and Bergstrom, R.: Light Absorption by Carbonaceous Particles: An Investigative Review, Aerosol Science and Technology, 40, 27–67, doi:10.1080/02786820500421521, 2006.

Bösenberg, J.: EARLINET-A European Aerosol Research Lidar Network, Advances in Laser Remote sensing, in: Selected papers 20th Int. Laser Radar Conference (ILRC), Vichi, France, 10-14 July 2000, pp. 155–158, 2000.

Bösenberg, J. and Hoff, R.: Plan for the implementation of the GAW Aerosol Lidar Observation Network GALION, WMO/TD-No. 1443 178, GAW, 2007.

Boucher, O.: Air traffic may increase cirrus cloudiness, Nature, 397, 30–31, 1999.

Chaikovsky, A., Bril, A., Denisov, S., and Balashevich, N.: Algorithms and software for lidar data processing in CIS-LiNet, in: Reviewed and Revised Papers Presented at the 23rd International Laser radar Conference, 24 - 28 July 2006, Nara, Japan, edited by Chikao Nagasava, N. S., pp. 667–670, 2006.

Chanine, M.: Determination of the Temperature Profile in an Atmosphere from its Outgoing Radiance, J. Opt. Soc. Am., 58, 1634–1637, doi:10.1364/JOSA.58.001634, URL http://www.opticsinfobase.org/abstract.cfm?URI=josa-58-12-1634, 1968.

Chowdhary, J., Cairns, B., Mishchenko, M., and Travis, L.: Retrieval of aerosol properties over the ocean using multispectral and multiangle Photopolarimetric measurements from the Research Scanning Polarimeter, Geophysical Research Letters, 28, 243–246, doi:10.1029/2000GL011783, URL http://dx.doi.org/10.1029/2000GL011783, 2001.

Cooke, W. F., Liousse, C., Cachier, H., and Feichter, J.: Construction of a $1° \times 1°$ fossil fuel emission data set for carbonaceous aerosol and implementation and radiative impact in the ECHAM4 model, J. Geophys. Res., 104(D18), 22 137–22 162, 1999.

Davis, D. L., Bell, M. L., , and Fletcher, T.: A look back at the London smog of 1952 and the half century since, Environ. Health Perspect., 110, 734–735, 2002.

Deschamps, P.-Y., Breon, F.-M., Leroy, M., Podaire, A., Bricaud, A., Buriez, J.-C., and Seze, G.: The POLDER mission: instrument characteristics and scientific objectives, Geoscience and Remote Sensing, IEEE, 32, 598–615, 1994.

Diner, D., Beckert, J., Reilly, T., Bruegge, C., Conel, J., Kahn, R., Martonchik, J., Ackerman, T., Davies, R., Gerstl, S., Gordon, H., Muller, J.-P., Myneni, R., Sellers, R., Pinty, B., and Verstraete, M.: Multi-angle Imaging SpectroRadiometer (MISR) description and experiment overview, IEEE Trans. Geosci. Rem. Sens., 36(4), 1072–1087, 1998.

Diner, D. J., Xu, F., Garay, M. J., Martonchik, J. V., Rheingans, B. E., Geier, S., Davis, A., Hancock, B. R., Jovanovic, V. M., Bull, M. A., Capraro, K., Chipman, R. A., and McClain, S. C.: The Airborne Multiangle SpectroPolarimetric Imager (AirMSPI): a new tool for aerosol and cloud remote sensing, Atmospheric Measurement Techniques Discussions, 6, 1717–1769, doi:10.5194/amtd-6-1717-2013, URL http://www.atmos-meas-tech-discuss.net/6/1717/2013/, 2013.

Donaldson, K., Stone, V., Seaton, A., and MacNee, W.: Ambient particle inhalation and the cardiovascular system : potential mechanisms, Environ. Health Perspect., 109, 523–527, 2001.

Draine, B. T. and Flatau, P. J.: Discrete-dipole approximation for scattering calculations, Journal of the Optical Society of America, 11, 1491–1499, doi:10.1364/JOSAA.11.001491, URL http://josaa.osa.org/abstract.cfm?URI=josaa-11-4-1491, 1994.

Dubovik, O.: Optimization of Numerical Inversion in Photopolarimetric Remote Sensing, in: Photopolarimetry in Remote Sensing, edited by: Videen, G., Yatskiv, Y., and Mishchenko, M., Kluwer Academic Publishers, Dordrecht, The Netherlands, p. 65–106, 2004.

Dubovik, O. and King, M. D.: A flexible inversion algorithm for retrieval of aerosol optical properties from Sun and sky radiance measurements, Journal of Geophysical Research: Atmospheres, 105, 20 673–20 696, doi:10.1029/2000JD900282, URL http://dx.doi.org/10.1029/2000JD900282, 2000.

Dubovik, O., Lapyonok, T., and Oshchepkov, S.: Improved technque for data inversion: optical sizing of multicomponent aerosols, Appl. Opt., 34, 8422–8436, 1995.

Dubovik, O., Yokota, T., and Sasano, Y.: Improved technique for data inversion and its application to the retrieval algorithm for adeos/ilas., Adv. Space Res., 21, 397–403, 1998.

Dubovik, O., Smirnov, A., Holben, B. N., King, M. D., Kaufman, Y. J., Eck, T. F., and Slutsker, I.: Accuracy assessments of aerosol optical properties retrieved from Aerosol Robotic Network (AERONET) Sun and sky radiance measurements, Journal of Geophysical Research: Atmospheres, 105, 9791–9806, doi:10.1029/2000JD900040, URL http://dx.doi.org/10.1029/2000JD900040, 2000.

Dubovik, O., Holben, B., Eck, T. F., Smirnov, A., Kaufman, Y. J., King, M. D., Tanré, D., and Slutsker, I.: Variability of Absorption and Optical Properties of Key Aerosol Types Observed in Worldwide Locations, J. Atmos. Sci., 59, 590–608, URL http://dx.doi.org/10.1175/1520-0469(2002)059<0590:VOAAOP>2.0.CO;2, 2002a.

Dubovik, O., Holben, B. N., Lapyonok, T., Sinyuk, A., Mishchenko, M. I., Yang, P., and Slutsker, I.: Non-spherical aerosol retrieval method employing light scattering by spheroids, Geophysical Research Letters, 29, 54–1–54–4, doi:10.1029/2001GL014506, URL http://dx.doi.org/10.1029/2001GL014506, 2002b.

Dubovik, O., Sinyuk, A., Lapyonok, T., Holben, B. N., Mishchenko, M., Yang, P., Eck, T. F., Volten, H., Muñoz, O., Veihelmann, B., van der Zande, W. J., Leon, J.-F., Sorokin, M., and Slutsker, I.: Application of spheroid models to account for aerosol particle nonsphericity in remote sensing of desert dust, Journal of Geophysical Research: Atmospheres, 111, n/a–n/a, doi:10.1029/2005JD006619, URL http://dx.doi.org/10.1029/2005JD006619, 2006.

Dubovik, O., Lapyonok, T., Kaufman, Y. J., Chin, M., Ginoux, P., Kahn, R. A., and Sinyuk, A.: Retrieving global aerosol sources from satellites using inverse modeling, Atmospheric Chemistry and Physics, pp. 209–250, doi:10.5194/acp-8-209-2008, 2008.

Dubovik, O., Herman, M., Holdak, A., Lapyonok, T., Tanré, D., Deuzé, J. L., Ducos, F., Sinyuk, A., and Lopatin, A.: Statistically optimized inversion algorithm for enhanced retrieval of aerosol properties from spectral multi-angle polarimetric satellite observations, Atmospheric Measurement Techniques, 4, 975–1018, doi:10.5194/amt-4-975-2011, URL http://www.atmos-meas-tech.net/4/975/2011/, 2011.

Dubovik, O., Labonnote, L., Litvinov, P., Parol, F., and Mishchenko, M. I.: Electromagnetic and Light Scattering by Nonspherical Particles XIV, Journal of Quantitative Spectroscopy and Radiative Transfer, 2014.

Eck, T. F., Holben, B. N., Reid, J. S., Dubovik, O., Smirnov, A., O'Neill, N. T., Slutsker, I., and Kinne, S.: Wavelength dependence of the optical depth of biomass burning, urban, and desert dust aerosols, J. Geophys. Res., 104, 31 333–31 349, doi:10.1029/1999JD900923, 1999.

Eck, T. F., Holben, B. N., Dubovik, O., Smirnov, A., Goloub, P., Chen, H. B., Chatenet, B., Gomes, L., Zhang, X.-Y., Tsay, S.-C., Ji, Q., Giles, D., and Slutsker, I.: Columnar aerosol optical properties at AERONET sites in Central-eastern Asia and aerosol transport to the tropical mid Pacific, Journal of Geophysical Research, 110, 975–1018, doi:10.1029/2004JD005274, 2005.

Forster, P., Ramaswany, V., Artaxo, P., Bernsten, T., Betts, R., Fahey, D. W., Haywood, J., Lean, J., Lowe, D., Myhre, G., Nganga, J., Prinn, R., Raga, G., Schulz, M., and Dorland, R. V.: Changes in atmospheric constituents and in radiative forcing. Climate change 2007: the physical science basis. Contribution of working group I to the fourth assessment report of Intergovernmental Panel on Climate change, IPCC report, 2007.

Frenkel, J.: A theory of the fundamental phenomena of atmospheric electricity, Journal of Physics, 8, 285–304, 1944.

Gong, S., Barrie, L., Blanchet, J.-P., and Spacek, L.: Modeling size-distributed sea salt aerosols in the atmosphere: An application using Canadian climate models, in: Air Pollution Modeling and Its Applications XII, edited by Gryning, S.-E. and Chaumerliac, N., Plenum Press, New York, USA, 1998.

Gonzalez, L., Breon, F.-M., and Briottet, X.: Construction of a global database of surface reflectance and emissivity at a sub km resolution, PIERS, 6, 195–200, 2010.

Hansen, J. and Travis, L.: Light scattering in planetary atmospheres, Space Science Reviews, 16, 527–610, doi:10.1007/BF00168069, URL http://dx.doi.org/10.1007/BF00168069, 1974.

Hansen, J., Sato, M., and Ruedy, R.: Radiative forcing and climate response, Journal of Geophysical Research, 102, 6831–6864, doi:10.1029/96JD03436, 1997.

Hansen, J., Sato, M., Kharecha, P., and von Schuckmann, K.: Earth's energy imbalance and implications, Atmospheric Chemistry and Physics, 11, 13 421–13 449, 2011.

Hasekamp, O. P. and Landgraf, J.: Linearization of vector radiative transfer with respect to aerosol properties and its use in satellite remote sensing, Journal of Geophysical Research: Atmospheres, 110, n/a–n/a, doi:10.1029/2004JD005260, URL http://dx.doi.org/10.1029/2004JD005260, 2005a.

Hasekamp, O. P. and Landgraf, J.: Retrieval of aerosol properties over the ocean from multispectral single-viewing-angle measurements of intensity and polarization: Retrieval approach, information content, and sensitivity study, Journal of Geophysical Research: Atmospheres, 110, n/a–n/a, doi:10.1029/2005JD006212, URL http://dx.doi.org/10.1029/2005JD006212, 2005b.

Hasekamp, O. P. and Landgraf, J.: Retrieval of aerosol properties over land surfaces: capabilities of multiple-viewing-angle intensity and polarization measurements, Appl. Opt., 46, 3332–3344, doi:10.1364/AO.46.003332, URL http://ao.osa.org/abstract.cfm?URI=ao-46-16-3332, 2007.

Haywood, J. and Boucher, O.: Estimates of the direct and indirect radiative forcing due to tropospheric aerosols: A review, Reviews of Geophysics, 38, doi:10.1029/1999RG000078, 2000.

Haywood, J. M. and Shine, K. P.: The effect of anthropogenic sulfate and soot aerosol on the clear sky planetary radiation budget, Geophysical Research Letters, 22, 603–606, 1995.

Herman, J., Bhartia, P. K., Torres., O., Hsu, C., Seftor, C., and Celarier, E.: Global distributions of UV-absorbing aerosols from Nimbus 7/TOMS data, J. Geophys. Res., 102, 16 911 –16 923, 1997.

Hess, M., Koepke, P., and Schult, I.: Optical Properties of Aerosols and Clouds: The Software Package OPAC., Bulletin of the American Meteorological Society, 79, 831–844, 1998.

Hinds, W.: Aerosol Technology: Properties, Behavior, and Measurement of Airborne Particles (Wiley-Interscience), Wiley-Interscience, 1999.

Hoffmann, T., Odum, J. R., Bowman, F., Collins, D., Klowckow, D., Flagan, R. C., and Seinfeld, J. H.: Formation of Organic Aerosols from the Oxidation of Biogenic Hydrocarbons, Journal of Atmospheric Chemistry, 26, 189–222, 1997.

Holben, B., Eck, T., Slutsker, I., Tanré, D., Buis, J., Setzer, A., Vermote, E., Reagan, J., Kaufman, Y., Nakajima, T., Lavenu, F., Jankowiak, I., and Smirnov, A.: AERONET—A Federated Instrument Network and Data Archive for Aerosol Characterization, Remote Sensing of Environment, 66, 1–16, URL http://www.sciencedirect.com/science/article/pii/S0034425798000315, 1998.

Holben, B., Eck, T., Schafer, J., Giles, D., and Sorokin, M.: Distributed Regional Aerosol Gridded Observation Networks (DRAGON), White Paper, 2011a.

Holben, B., Eck, T., Schafer, J., Giles, D., and Sorokin, M.: Distributed Regional Aerosol Gridded Observation Networks (DRAGON) White Paper, available from http://aeronet.gsfc.nasa.gov/new_web/dragon.html, 2011b.

InVS/Afsse: Estimation de l'impact sanitaire d'une pollution environnementale et évaluation quantitative des risques sanitaires, Tech. Rep. 157 p., Ed. InVS/Afsse, 2005.

IPCC: Climate Change 2007: The Physical Science Basis, Cambridge University Press, 2007.

IPCC: Climate Change 2013 : The Physical Science Basis, Cambridge University Press, 2013.

Jünge, C. E.: The size distribution and aging of natural aerosols as determined from electrical and optical data on the atmosphere, J. Meteorol., 12, 13–25, 1955.

Junge, C. E.: Air chemistry and radioactivity, vol. 4 of *International Geophysics Series*, Academic Press, 1963.

Kacenelenbogen, M.: Application de la télédétection spatiale á la surveillance de la pollution en aérosols, Ph.D. thesis, Université de Lille 1, Villeneuve d'Ascq, France, 2008.

Kalman, R.: A new approach to linear filtering and prediction problems, Journal of Basic Engineering, 82, 35–45, doi:10.1115/1.3662552, 1960.

Kamens, R. M. and Jaoui, M.: Modeling Aerosol Formaiton from α-Pinene + NOx in the Presence of Natural Sunlight Using Gas-Phase Kinetics and Gas-Particle Partitioning Theory, Environmental Science and Technology, 35, 1394–1405, 2001.

Karol, Y., Tanré, D., Goloub, P., Vervaerde, C., Balois, J. Y., Blarel, L., Podvin, T., Mortier, A., and Chaikovsky, A.: Airborne sun photometer PLASMA: concept, measurements, comparison of aerosol extinction vertical profile with lidar, Atmospheric Measurement Techniques, 6, 2383–2389, doi:10.5194/amt-6-2383-2013, URL http://www.atmos-meas-tech.net/6/2383/2013/, 2013.

Kaufman, Y. J., Tanré, D., and Boucher, O.: A satellite view of aerosols in the climate system, Nature, 419, 215–223, URL http://www.nature.com/nature/journal/v419/n6903/full/nature01091.html?lang=en, 2002.

King, M. D., Byrne, D. M., Herman, B. M., and Reagan, J. A.: Aerosol size distributions obtained by inversion of spectral optical depth measurements, J. Atmos. Sci., 21, 2153–2167, 1978.

Kinne, S., Lohmann, U., Feichter, J., Schulz, M., Timmreck, C., Ghan, S., Easter, R., Chin, M., Ginoux, P., Takemura, T., Tegen, I., Koch, D., Herzog, M., Penner, J., Pitari, G., Holben, B., Eck, T., Smirnov, A., Dubovik, O., Slutsker, I., Tanré, D., Torres, O., Mishchenko, M., Geogdzhayev, I., Chu, D. A., and Kaufman, Y. J.: Monthly averages of aerosol properties: A global comparison among models, satellite data and AERONET ground data, Journal of Geophysical Research, 108, doi:10.1029/2001JD001253, 2003.

Kinne, S., Schulz, M., Textor, C., Guibert, S., Balkanski, Y., Bauer, S. E., Berntsen, T., Berglen, T. F., Boucher, O., Chin, M., Collins, W., Dentener, F., Diehl, T., Easter, R., Feichter, J., Fillmore, D., Ghan, S., Ginoux, P., Gong, S., Grini, A., Hendricks, J., Herzog, M., Horowitz, L., Isaksen, I., Iversen, T., Kirkavag, A., Kloster, S., Koch, D., Kristjansson, J. E., Krol, M., Lauer, A., Lamarque, J. F., Lesins, G., Liu, X., Lohmann, U., Montanaro, V., Myhre, G., Penner, J. E., Pitari, G., Reddy, S., Seland, O., Stier, P., Takemura, T., and Tie, X.: An AeroCom initial assessment - optical properties in aerosol component modules of global models, Atmospheric Chemistry and Physics, 6, 1815–1834, 2006.

Koch, D. and Del Genio, A.: Black carbon absorption effects on cloud cover, review and synthesis, Atmospheric Chemistry and Physics, pp. 7685–7696, 2010.

Koch, D., Schulz, M., Kinne, S., McNaughton, C., Spackman, J. R., Balkanski, Y., Bauer, S., Berntsen, T., Bond, T. C., Boucher, O., Chin, M., Clarke, A., De Luca, N., Dentener, F., Diehl, T., Dubovik, O., Easter, R., Fahey, D. W., Feichter, J., Fillmore, D., Freitag, S., Ghan, S., Ginoux, P., Gong, S., Horowitz, L., Kirkevåg, T. I. A., Klimont, Z., Kondo, Y., Krol, M., Liu, X., Miller, R., Montanaro, V., Moteki, N., Myhre, G., Penner, J. E., Perlwitz, J.and Pitari, G., Reddy, S., Sahu, L., Sakamoto, H., Schuster, G., Schwarz, J. P., Seland, Ø., Stier, P., Takegawa, N., Takemura, T., Textor, C., van Aardenne, J. A., and Zhao, Y.: Evaluation of black carbon estimations in global aerosol models, Atmospheric Chemistry and Physics, pp. 9001–9026, 2009.

Lenoble, J., Herman, M., Deuzé, J.-L., Lafrance, B., Santer, R., and Tanré, D.: A successive order of scattering code for solv- ing the vector equation of transfer in the earth's atmosphere with aerosols, Journal of Quantitative Spectroscopy and Radiative Transfer, 107, 479–507, 2007.

Lenoble, J., Remer, J., Remer, L., and Tanre, D.: Aerosol Remote Sensing, Springer Praxis Books, Springer London, Limited, URL http://books.google.by/books?id=QeWvkgEACAAJ, 2011.

Levelt, P. F., Hilsenrath, E., Leppelmeier, G. W., van den Ooord, G. H. J., Bhartia, P. K., de Haan, J. T. J. F., and Veefkind, J. P.: Science objectives of the Ozone Monitoring Instrument, IEEE Trans. Geosci. Remote Sens., 44(5), 1093–1101, 2006.

Li, X. and Strahler, A.: Geometric-optical bidirectional reflectance modeling of the discrete crown vegetation canopy: effect of crown shape and mutual shadowing, Geoscience and Remote Sensing, IEEE Transactions on, 30, 276–292, doi:10.1109/36.134078, 1992.

Li, Z., Blarel, L., Podvin, T., Goloub, P., Buis, J.-P., and Morel, J.-P.: Transferring the calibration of direct solar irradiance to diffuse-sky radiance measurements for CIMEL Sun-sky radiometers, Appl. Opt., 47, 1368–1377, doi:10.1364/AO.47.001368, URL http://ao.osa.org/abstract.cfm?URI=ao-47-10-1368, 2008.

Li, Z., Goloub, P., Dubovik, O., Blarel, L., Zhang, W., Podvin, T., Sinyuk, A., Sorokin, M., Chen, H., Holben, B., Tanré, D., Canini, M., and Buis, J.-P.: Improvements for ground-based remote sensing of atmospheric aerosol properties by additional polarimetric measurements, Journal of Quantitative Spectroscopy and Radiative Transfer, 110, 1954–1961, URL http://www.sciencedirect.com/science/article/pii/S002240730900154X, 2009.

Li, Z., Blarel, L., Podvin, T., Goloub, P., and Chen, L.: Calibration of the degree of linear polarization measurement of polarized radiometer using solar light, Appl. Opt., 49, 1249–1256, doi:10.1364/AO.49.001249, URL http://ao.osa.org/abstract.cfm?URI=ao-49-8-1249, 2010.

Liao, D., Creason, J., Shy, C., Williams, R., Watts, R., and Zweidinger, R.: Daily variation of particulate air pollution and poor cardiac autonomic control in the elderly, Environ. Health Perspect., 107, 521–525, 1999.

Lohmann, U. and Feichter, J.: Global indirect aerosol effects: a review, Atmospheric Chemistry and Physics, 5, 715–737, 2005.

Lohmann, U. and Hoose, C.: Sensitivity studies of different aerosol indirect effects in mixed- phase clouds, Atmospheric Chemistry and Physics, pp. 8917–8934, 2009.

Lohmann, U., Karcher, B., and Timmreck, C.: Impact of the Mount Pinatubo eruption on cirrus clouds formed by homogeneous freezing in the ECHAM4 GCM, Journal of Geophysical Research, 108, 4568, 2003.

Matsumoto, T., Russell, P., Mina, C., Ark, W. V., and Banta, V.: Airborne Tracking Sunphotometer, J. Atmos. Ocean . Tech., 4, 336–339, 1987.

Mishchenko, M., Travis, L., and Mackowski, D.: T-Matrix Computations of Light Scattering by Nonspherical Particles: a Review, Journal of Quantitative Spectroscopy and Radiative Transfer, 55, 1996.

Mishchenko, M. I. and Travis, L. D.: Capabilities and limitations of a current FORTRAN implementation of the T-matrix method for randomly oriented, rotationally symmetric scatterers-Computational Methods, Journal of Quantitative Spectroscopy and Radiative Transfer, 60, 309–324, 1998.

Mishchenko, M. I., Travis, L. D., Kahn, R. A., and West, R. A.: Modeling phase functions for dustlike tropospheric aerosols using a shape mixture of randomly oriented polydisperse spheroids, Journal of Geophysical Research: Atmospheres, 102, 16 831–16 847, doi:10.1029/96JD02110, URL http://dx.doi.org/10.1029/96JD02110, 1997.

Mishchenko, M. I., Hovenier, J. W., and Travis, L. D.: Light scattering by nonspherical particles, Elsevier, New York, 2000.

Mishchenko, M. I., Cairns, B., Hansen, J. E., Travis, L. D., Burg, R., Kaufman, Y. J., Martins, J. V., and Shettle, E. P.: Monitoring of aerosol forcing of climate from space: analysis of measurement requirements, Journal of Quantitative Spectroscopy and Radiative Transfer, 88, 149 – 161, doi:http://dx.doi.org/10.1016/j.jqsrt.2004.03.030, URL http://www.sciencedirect.com/science/article/pii/S0022407304001360, ¡ce:title¿Photopolarimetry in remote sensing¡/ce:title¿, 2004.

Mishchenko, M. I., Cairns, B., Hansen, J. E., Travis, L. D., Kopp, G., Schueler, C. F., Fafaul, B. A., Hooker, R. J., Maring, H. B., and Itchkawich, T.: Accurate Monitoring of Terrestrial Aerosols and Total Solar Irradiance: Introducing the Glory Mission, Bull. Amer. Meteor. Soc., 88, 677–691, doi:10.1175/BAMS-88-5-677, URL http://dx.doi.org/10.1175/BAMS-88-5-677, 2007.

Mishchenko, M. I., Rosenbush, V. K., Kiselev, N. N., Lupishko, D. F., Tishkovets, V., Kaydash, V., Belskaya, I. N., Efimov, Y. S., and Shakhovskoy, N. M.: Polarization remote sensing of solar system objects, Akademperiodyka, Kyiv, Ukraine, 2010.

Moody, E., King, M., Platnick, S., Schaaf, C., and Gao, F.: Spatially complete global spectral surface albedos: value-added datasets derived from Terra MODIS land products, Geoscience and Remote Sensing, IEEE Transactions on, 43, 144–158, doi: 10.1109/TGRS.2004.838359, 2005.

Mortier, A., Goloub, P., Holben, B., Podvin, T., Blarel, L., Verwaerde, C., Karol, Y., Slutsker, I., Balois, J.-Y., Tanre, D., Berkoff, T., Victori, S., and Mathieu, R.: Aerosol Spatial Distribution during DRAGON experiment as seen by a mobile ground-based LIDAR-sunphotometer system-Preliminary results, in: Reviewed and revised papers of the 26th International Lidar Radar Conference, pp. 411–414, Porto Heli, Peloponnesus, Greece, 2012.

Mullot, J. U., Baeza, A., Blanchard, O., Delmas, V., Elichegaray, C., Lefranc, A., Ramel, M., Slama, R., and Vendel, J.: Pollution par les particules dans l'air ambiant. Synthèses des éléments sanitaires en vue d'un appui à l'élaboration de seuils d'information et d'alerte du public pour les particules dans l'air ambiant., Rapport d'expertise collective de l'AFFSET, 2009.

Murayama, T. and et al.: Lidar Network Observation of Asian Dust / Advances in Laser Remote sensing /, in: Selected papers 20th Int. Laser Radar Conference (ILRC), Vichi, France, 10-14 July 2000, pp. 169–177, 2000.

Nakajima, T., Tanaka, M., and Yamauchi, T.: Retrieval of the optical properties of aerosols from aureole and extinction data, Appl. Opt., 22, 2951–2959, 1983.

Nakajima, T., Tonna, G., Rao, R., Kaufman, Y. J., and Holben, B. N.: Use of sky brightness measurements from ground for remote sensing of particulate polydispersions, Appl. Opt., 35, 2672–2686, 1996.

Nakajima, T., Yoon, S. C., Ramanathan, V., Shi, G.-Y., Takemura, T., Higurashi, A., Takamura, T., Aoki, K., Sohn, B.-J., Kim, S.-W., Tsuruta, H., Sugimoto, N., Shimizu, A., Tanimoto, H., Sawa, Y., Lin, N.-H., Lee, C.-T., Goto, D., and Schutgens, N.: Overview of the Atmospheric Brown Cloud East Asian Regional Experiment 2005 and a study of the aerosol direct radiative forcing in east Asia, Journal of Geophysical Research, 112, doi:10.1029/2007JD009009, 2007.

on Climate Control (IPCC), I. P.: Climate Change 2001, the Third Assessment Report of the IPCC, Cambridge Univ. Press, New York, 2001.

Pelon, J., Tanré, D., Garnier, A., and Lifermann, A.: L'apport des nouvelles missions spatiales à sondeurs actifs : Résultats récents de CALIPSO, CloudSat et l'A-Train, La Météorologie, 75, 15–22, 2011.

Penner, J. E., Hegg, D., and Leaitch, R.: Unravelling the role of aerosols in climate change, Environ. Sci. Technol., 35, 332 A–340 A, 2001.

Philips, D.: A technique for the numerical solution of certain integral equations of the first king, J. Assoc. Comp. Mach., 9, 84–97, 1962.

Pincus, R. and Baker, M.: Effect of precipitation on the albedo susceptibility of clouds in the marine boundary layer, Nature, 1994.

Ramanathan, V., Crutzen, P., Lelieveld, J., Mitra, A., Althausen, D., Anderson, J., Andreae, M., Cantrell, C., Cass, G., Chung, C., Clarke, A., Coakley, J., Collins, W., Conant, W., Dulac, F., Heintzenberg, J., Heymsfield, A., Holben, B., Howell, S., Hudson, J., Jayaraman, A., Kiehl, J., Krishnamurti, T., Lubin, D., McFarquhar, G., Novakov, T., Ogren, J., Podgorny, I., Prather, K., Priestley, K., Prospero, J., Quinn, P., Rajeev, K., Rasch, P., Rupert, S., Sadourny, R., Satheesh, S., Shaw, G., Sheridan, P., and Valero, F.: The Indian Ocean Experiment: An integrated assessment of the climate forcing and effects of the great Indo-Asian haze, Journal of Geophysical Research, 106, 28 371–28 393, 2001.

Reid, J. S., Halflidi, H., Maring, H. B., Smirnov, A., Savoie, D. L., Cliff, S. S., Reid, E. A., Livingston, J. M., Meier, M. M., Dubovik, O., and Tsay, S.-C.: Comparison of Size and Morphological Measurements of Coarse Mode Dust Particles from Africa, Journal of Geophysical Research, 108, 8593, doi:10.1029/2002JD002485, 2003.

Remer, L. and Kaufman, Y.: Dynamic aerosol model: Urban/industrial aerosol, Journal of Geophysical Research, 103, doi:10.1029/98JD00994, 1998.

Remer, L., Kaufman, Y., Tanré, D., Mattoo, S., Chu, D., Martins, J., Li, R., Ichoku, C., Levy, R., Kleidman, R., Eck, T., Vermote, E., and Holben, B.: The MODIS Aerosol Algorithm, Products, and Validation, Journal of the Atmospheric Sciences, 62, 947–973, doi:10.1175/JAS3385.1, 2005.

Rodgers, C. D.: Retrieval of Atmospheric Temperature and Composition From Remote Measurements of Thermal Radiation, Rev. Geophys. and Space Phys., 14, 609 – 624, 1976.

Rodgers, C. D.: Inverse methods for atmospheric sounding: theory and practice, World Scientific, Singapore, 2000.

Ross, I.: The radiation regime and architecture of plant stands, Tasks for vegetation science, Dr. W. Junk Publishers, URL http://books.google.by/books?id=w6SogqD0a54C, 1981.

Schmid, B., Redemann, J., Russell, P., Hobbs, P., Hlavka, D., Mcgill, M., Holben, B., Welton, E., Campbell, J., Torres, O., Kahn, R., Diner, D., Helmlinger, M., Chu, D., Robles-Gonzalez, C., and de Leeuw, G.: Coordinated airborne, spaceborne, and ground-based measurements of massive thick aerosol layers during the dry season in southern Africa, Journal of Geophysical Research - Atmospheres, 108, 8496, doi:10.1029/2002JD002297, 2003.

Schuster, G. L., Dubovik, O., and Holben, B. N.: Angstrom exponent and bimodal aerosol size distributions, J. Geophys. Res., 111, D07 207, doi:10.1029/2005JD006328, URL http://dx.doi.org/10.1029/2005JD006328, 2006.

Schutz, B. E., Zwally, H. J., Shuman, C. A., Hancock, D., and DiMarzio, J. P.: Overview of the ICESat Mission, Geophys. Res. Lett., 32, L21S01, doi:10.1029/2005GL024009, URL http://dx.doi.org/10.1029/2005GL024009, 2005.

Shaw, G. E., Reagan, J. A., and Herman, B. M.: Investigations of atmospheric extinction using direct solar radiation measurements made with multiple wavelength radiometer, J. Appl. Meteor., 12 374, 1973.

Shettle, E. P. and Fenn, R. W.: Models of aerosols of lower troposphere and the effect of humidity variations on their optical properties, AFCRL Tech. Rep. 79 0214, 100 pp., Air Force Cambridge Res. Lab., Hanscom, Air Force Base, Mass., 1979.

Sinyuk, A., Dubovik, O., Holben, B., Eck, T. F., Breon, F.-M., Martonchik, J., Kahn, R., Diner, D. J., Vermote, E. F., Roger, J.-C., Lapyonok, T., and Slutsker, I.: Simultaneous retrieval of aerosol and surface properties from a combination of AERONET and satellite data, Remote Sensing of Environment, 107, 90–108, URL http://www.sciencedirect.com/science/article/pii/S0034425706004111, 2007.

Sinyuk, A., Dubovik, O., Holben, B., Schafer, J., Giles, D., Eck, T., Slutsker, I., Sorokine, M., Smirnov, A., Bréon, F., and Khan, R.: Multi-sensor aerosol retrievals using joint inversion of AERONET and satellite observations: concept and applications., Eos Transactions AGU, Fall Meeting Supplements, 53, 2008.

Smirnov, A., Holben, B., Slutsker, I., Welton, E., and Formenti, P.: Optical properties of Saharan dust during ACE 2, Journal of Geophysical Research: Atmospheres (1984–2012), 103, 28 079–28 092, 1998.

Smirnov, A., Holben, B., Eck, T., Dubovik, O., and Slutsker, I.: Cloud-screening and quality control algorithms for the AERONET database., Remote Sensing of Environment, 73, 337–349, 2000.

Stephens, G., Vane, D., Boain, R., Mace, G., Sassen, K., Wang, Z., Illingworth, A., O'Conner, E., Rossow, W., Durden, S., Miller, S., Austin, R., Benedetti, A., and Mitrescu, C.: The CloudSat mission and the A-Train, Bulletin of the American Meteorological Society, 83, 1771–1790, 2002.

Stowe, L. L., Carey, R. M., and Pellegrino, P. P.: Monitoring the Mt. Pinatubo aerosol layer with NOAA/AVHRR data, Remote Sens. Envron., 60, 22–34, 1992.

Strand, O. N. and Westwater, E. R.: Statistical Estimation of the Numerical Solution of a Fredholm Integral Equation of the First Kind, J. Assoc. Comp. Mach., 15, doi: 10.1145/321439.321445, 1968.

Sun, D. and Pinker, R.: Retrieval of surface temperature from the MSG-SEVIRI observations: Part I. Methodology, International Journal of Remote Sensing, 28, 5255–5272, doi:10.1080/01431160701253246, 2007.

Tanré, D., Kaufman, Y. J., Holben, B. N., Chatenet, B., Karnieli, A., Lavenu, F., Blarel, L., Dubovik, O., Remer, L. A., and Smirnov, A.: Climatology of dust aerosol size distribution and optical properties derived from remotely sensed data in the solar spectrum, J. Geophys. Res., 106(D16), 18 205–18 217, 2001.

Tanré, D., Bréon, F. M., Deuzé, J. L., Dubovik, O., Ducos, F., François, P., Goloub, P., Herman, M., Lifermann, A., and Waquet, F.: Remote sensing of aerosols by using polarized, directional and spectral measurements within the A-Train: the PARASOL mission, Atmospheric Measurement Techniques, 4, 1383–1395, doi: 10.5194/amt-4-1383-2011, URL http://www.atmos-meas-tech.net/4/1383/2011/, 2011.

Tanré, D., Bréon, F. M., Deuzé, J. L., Herman, M., Goloub, P., Nadal, F., and Marchand, A.: Global observation of anthropogenic aerosols from satellite, Geophysical Research Letters, 28, 4555–4558, doi:10.1029/2001GL013036, URL http://dx.doi.org/10.1029/2001GL013036, 2001.

Tarantola, A.: Inverse Problem Theory and Methods for Model Parameter Estimation, Society for Industrial and Applied Mathematics, doi:10.1137/1.9780898717921, URL http://epubs.siam.org/doi/abs/10.1137/1.9780898717921, 2005.

ten Brink, H. M., Veefkind, J. P., Waijers-Ijpelaan, A., and van der Hage, J. C.: Aerosol light-scattering in the Netherlands, Atmos. Environ., 30, 4251–4261, 1996.

Textor, C., Schulz, M., Guibert, S., Kinne, S., Balkanski, Y., Bauer, S., Berntsen, T., Berglen, T., Boucher, O., Chin, M., Dentener, F., Diehl, T., Easter, R., Feichter, H., Fillmore, D., Ghan, S., Ginoux, P., Gong, S., Kristjansson, J. E., Krol, M., Lauer, A., Lamarque, J. F., Liu, X., Montanaro, V., Myhre, G., Penner, J., Pitari, G., Reddy, S., Seland, O., Stier, P., Takemura, T., and Tie, X.: Analysis and quantification of the diversities of aerosol life cycles within AeroCom, Atmospheric Chemistry and Physics, 6, 1777–1813, 2006.

Tikhonov, A. N.: On the solution of ill-posed problems and the method of regularization, Dokl. Akad. Nauk SSSR, 151, 1963.

Tomasi, C., Vitake, V., and Santis, L.: Relative optical mass functions for air, water vapour, ozone and nitrogen dioxide in atmospheric models presenting different latitudinal and seasonal conditions, Meteorology and Atmospheric Physics, 65, 11–30, doi:10.1007/BF01030266, URL http://dx.doi.org/10.1007/BF01030266, 1998.

Torres, B., Dubovik, O., Toledano, C., Berjon, A., Cachorro, V. E., Lapyonok, T., Litvinov, P., and Goloub, P.: Sensitivity of aerosol retrieval to geometrical configuration of ground-based sun/sky radiometer observations, Atmospheric Chemistry and Physics, 14, 847–875, doi:10.5194/acp-14-847-2014, URL http://www.atmos-chem-phys.net/14/847/2014/, 2014.

Turchin, V. and Nozik, V.: Statistical regularization of solution of noncorrec problems, Izv. Akad. Nauk SSSR, Ser. Fiz. Atmos. Okeana, 5, 1969.

Twomey, S.: On the numerical solution of Fredholm integral equations of the first kind by the inversion of the linear system pro- duced by quadrature, J. Assoc. Comp. Mach., pp. 97–101, 1963.

Twomey, S.: Pollution and the planetary albedo, Atmospheric Environment, 8, 1251–1256, 1974.

Twomey, S.: Comparison of constrained linear inversion and an iterative nonlinear algorithm applied to the indirect estimation of particle size distributions, Journal of Computational Physics, 18, 188–200, doi:10.1016/0021-9991(75)90028-5, 1975.

Twomey, S.: Introduction to the Mathematics of Inversion in Remote Sensing and Indirect Measurements, Elsevier, New York, 1977a.

Twomey, S.: The influence of pollution on the shortwave albedo of clouds, Journal of the Atmospheric Sciences, 34, 1149–1152, 1977b.

van de Hulst, H. C.: Light scattering by small particles, John Wiley, 1957.

Volten, H., Munoz, O., Rol, E., de Haan, J. F., Vassen, W., Hovenier, J. W., Muinonen, K., and Nousiainen, T.: Scattering matrices of mineral aerosol particles at 441.6 nm and 632.8 nm, Journal of Geophysical Research, 106, 17 375–17 401, 2001.

Wandinger, U., Mattis, I., Tesche, M., Ansmann, A., Bösenberg, J., Chaikovsky, A., Freudenthaler, V., Komguem, L., Linné, H., Matthias, V., Pelon, J., Sauvage, L., Sobolewski, P., Vaughan, G., and Wiegner, M.: Air-mass modification over Europe: EARLINET aerosol observations from Wales to Belarus, Journal of Geophysical Research, 109, 2004.

Wanner, W., Li, X., and Strahler, A. H.: On the derivation of kernels for kernel-driven models of bidirectional reflectance, Journal of Geophysical Research: Atmospheres, 100, 21 077–21 089, doi:10.1029/95JD02371, URL http://dx.doi.org/10.1029/95JD02371, 1995.

Weber, R., McMurry, P., Mauldin III, R., Tanner, D., Eisele, F., Clarke, A., and Kapustin, V.: New particle formation in the remote troposphere: A comparison of observations at various sites, Geophys. Res. Lett., 26, 307–310, 1999.

Welton, E. and et al.: The Micro-pulse Lidar Network (MPL-Net) / Lidar Remote Sensing in Atmospheric and Earth Sciences, in: Reviewed and revised papers at the twenty-first International Laser Radar Conference (ILRC21), pp. 285–288, Quebec, Canada,, 2002.

Whitby, K.: The physical characteristics of sulfate aerosols, Atmospheric Environment, 12, 135–159, 1978.

Winker, D., Pelon, J., Coakley, J., Ackerman, S., Charlson, R., Colarco, P., Flamant, P., Fu, Q., Hoff, R., Kittaka, C., Kubar, T., Le Treut, H., McCormick, M., Mégie, G., Poole, L., Powell, K., Trepte, C., Vaughan, M., and Wielicki, B.: The CALIPSO Mission: A Global 3D View of Aerosols and Clouds, Bulletin of the American Meteorological Society, 91, 1211–1229, doi:10.1175/2010BAMS3009.1, 2010.

Winker, D. M., Couch, R. H., and McCormick, M. P.: An overview of LITE: NASA's Lidar In-space Technology Experiment, Proc. IEEE, 84, 164–180, 1996.

WMO/GAW: Strategic Plan: 2008-2015 - A Contribution to the Implementation of the WMO Strategic Plan: 2008-2011 (WMO TD No. 1384), GAW report 172, World Meteorological Organization, 2007.

Yang, P., Liou, K. N., Mishchenko, M. I., and Gao, B.-C.: Efficient Finite-Difference Time-Domain Scheme for Light Scattering by Dielectric Particles: Application to Aerosols, Applied Optics, 39, 3727–3737, doi:10.1364/AO.39.003727, URL http://ao.osa.org/abstract.cfm?URI=ao-39-21-3727, 2000.

Zieger, P., Ruhtz, T., Preusker, R., and Fischer, J.: Dual-aureole and sun spectrometer system for airborne measurements of aerosol optical properties, Appl. Opt., 46, 8542–8552, doi:10.1364/AO.46.008542, URL http://ao.osa.org/abstract.cfm?URI=ao-46-35-8542, 2007.